PHYSICAL CHEMISTRY 2021

15th International Conference
on Fundamental and Applied Aspects of
Physical Chemistry

Proceedings
Volume I

The Conference is dedicated to the

30th Anniversary of the founding of the Society of Physical Chemists of Serbia

and

100th Anniversary of Bray-Liebhafsky reaction

September 20-24, 2021
Belgrade, Serbia

Title: Physical Chemistry 2021 (Proceedings) **ISBN** 978-86-82475-40-8
Volume I: ISBN 978-86-82475-38-5
Editors: Željko Čupić and Slobodan Anić
Published by: Society of Physical Chemists of Serbia, Studentski Trg 12-16, 11158, Belgrade, Serbia
Publisher: Society of Physical Chemists of Serbia
For Publisher: S. Anić, President of Society of Physical Chemists of Serbia
Printed by: ″Jovan″, <Printing and Publishing Company, 200 Copies
Number of pages: 6+344, Format A4, printing finished in December 2021

Text and Layout: ″Jovan″

200 - *Copy printing*

CONTENT

Volume I

PHYSICAL CHEMISTRY 2021

15th International Conference on Fundamental and Applied Aspects of Physical Chemistry

Organized by

The Society of Physical Chemists of Serbia

in co-operation with

Institute of Catalysis Bulgarian Academy of Sciences

and

Boreskov Institute of Catalysis Siberian Branch of Russian Academy of Sciences

and

University of Belgrade, Serbia:

Faculty of Physical Chemistry
Institute of Chemistry, Technology and Metallurgy
Vinča Institute of Nuclear Sciences
Faculty of Pharmacy

and

Institute of General and Physical Chemistry, Belgrade, Serbia

International Organizing Committee

Chairman: S. Anić (Serbia)
Vice-chairman: M. Gabrovska (Bulgaria)
A. A. Vedyagin (Russia)
S. N. Blagojević (Serbia)

Members: N. Cvjetićanin (Serbia), S. M. Blagojević (Serbia), M. Daković (Serbia), J. Dimitrić Marković (Serbia), T. Grozdić (Serbia), Lj. Ignjatović (Serbia), D. Jovanović (Serbia), M. Kuzmanović (Serbia), D. Marković (Serbia), B. Milosavljević (USA), M. Mojović (Serbia), N. Pejić (Serbia), M. Petković (Serbia), A. Popović-Bjelić (Serbia), B. Simonović (Serbia), M.Stanković (Serbia), B. Šljukić (Serbia), G. Tasić (Serbia), S. Veličković (Serbia), N. Vukelić (Serbia)

International Scientific Committee

Chairman: Ž. Čupić (Serbia)
Vice-chairman: V. Bukhtiyarov (Russia)
S. Todorova (Bulgaria)
B. Adnađević (Serbia)

Members: S. Anić (Serbia), A. Antić-Jovanović (Serbia), A. Azizoğlu (Turky), R. Cervellati (Italy), G. Ćirić-Marjanović (Serbia), V. Dondur (Serbia), I. I. Grinvald (Russia), R. Jerala (Slovenia), M. Jeremić (Serbia), G. N. Kaluđerović (Germany), E. Kiš (Serbia), A.V. Knyazev (Russia), Lj. Kolar-Anić (Serbia), U. Kortz (Germany), T. Kowalska (Poljska), A. Lemarchand (France), G. Lente (Hungary), Z. Marković (Serbia), S. Mentus (Serbia), K. Novaković (UK), N. Ostrovski (Serbia), V. Parmon (Russia), Z. Petkova Cherkezova-Zheleva (Bulgary), M. Plavšić (Serbia), J. Savović (Serbia), G. Schmitz (Belgium), I. Schreiber (Czech), L. Schreiberova (Czech), D. Stanisavljev (Serbia), N. Stepanov (Russia), M. Stojanović (USA), E. Szabó (Slovakia), Zs. Szakacs (Romania), Z. Šaponjić (Serbia), Á. Tóth (Hungary), M. Trtica (Serbia), V. Vasić (Serbia), D. Veselinović (Serbia), V. Vukojević (Sweden)

Local Executive Committee

Chairman: S. N. Blagojević
Vice-chairman: A. Ivanović-Šašić
N. Jović-Jovičić
A. Stanojević

Members: M. Ajduković, I. N. Bubanja, A. Dobrota, J. Dostanić, D. Dimić, S. Jovanović, Z. Jovanović, D. Lončarević, M. Kragović, J. Krstić, B. Marković, S. Maćešić, J. Maksimović, S. Marinović, D. Milenković, T. Mudrinić, M. Pagnacco, N. Potkonjak, B. Stanković, I. Stefanović, G. Stevanović, A. Stoiljković, M. Vasić

SPONSORS

Ministry of Education, Science and Technological Development of the Republic Serbia
Institute of General and Physical Chemistry, Belgrade
Belgrade Analysis d.o.o.

PL- Plenary lecture

DISSIPATIVE STRUCTURES AND BIOLOGICAL RHYTHMS

A. Goldbeter

Unité de Chronobiologie théorique, Service de Chimie physique et Biologie théorique,
Faculté des Sciences, Université Libre de Bruxelles (ULB), Brussels, Belgium

ABSTRACT

Sustained oscillations abound in biological systems. They occur at all levels of biological organization over a wide range of periods, from a fraction of a second to years, and with a variety of underlying mechanisms. They control major physiological functions, and their dysfunction is associated with a variety of physiological disorders. The goal of this presentation is (i) to give an overview of the main rhythms observed at the cellular and supracellular levels, (ii) to briefly describe how the study of biological rhythms unfolded in the course of time, in parallel with studies on chemical oscillations, (iii) to present the major roles of biological rhythms in the control of physiological functions, and (iv) the pathologies associated with the alteration, disappearance, or spurious occurrence of biological rhythms. Among the rhythms discussed are neural and cardiac rhythms, metabolic oscillations such as those occurring in glycolysis in yeast, intracellular Ca^{++} oscillations, cyclic AMP oscillations in *Dictyostelium* amoebae, the segmentation clock that controls somitogenesis, pulsatile hormone secretion, circadian rhythms which occur in all eukaryotes and some bacteria with a period close to 24h, the oscillatory dynamics of the enzymatic network driving the cell cycle, and oscillations in transcription factors such as NF-KB and tumor suppressors such as p53. The concept of dissipative structures applies to temporal oscillations and allows us to unify within a common framework the various rhythms observed at different levels of biological organization, regardless of their period and underlying mechanism.

REFERENCES

[1] Goldbeter, A. (2017) Dissipative structures and biological rhythms. *Chaos* **27**, 104612. doi: 10.1063/1.4990783

[2] Goldbeter, A. (2018) Dissipative structures in biological systems: bistability, oscillations, spatial patterns and waves. *Phil. Trans. R. Soc. A* **376**:20170376. (http://dx.doi.org/10.1098/rsta.2017.0376).

SYNCHRONISATION OF GLYCOLYTIC ACTIVITY IN YEAST CELL POPULATIONS

M.J. B. Hauser

Otto-von-Guericke-Universität Magdeburg,
Institute of Biology, Department of Regulation Biology,
Pfälzer Straße 5, 39106 Magdeburg, Germany.
marcus.hauser@ovgu.de

ABSTRACT

Glycolysis is the central metabolic pathway of almost every cell and organism. We report on glycolytic oscillations of intact yeast cells at the level of the cell population as well as at the level of individual cells. Synchronisation depends on the cell density of a population, because the collective oscillatory behaviour of a yeast cell population ceases when the cell density of the population falls below a threshold. At high cell densities, the dynamics is oscillatory, but below a critical density the collective dynamics becomes quiescent. Whereas cells in stirred cell suspension ceased to oscillate, immobilized cells were found to show glycolytic oscillations, even at very low cell densities. This means, the transition between oscillatory and stationary dynamics in immobilized or suspended cells follows different phase types of transitions.

The pathway to synchrony of originally quiescent, immobilized cells was achieved by a the synchronisation of the frequencies of the cellular oscillations, which was followed by a synchronisation of their phases. The pathway leading to synchronisation involved a narrowing of the frequency distribution in conjunction with a shift in the mean frequency of the glycolytic oscillations to larger values. The population was entrained by those cells that oscillated at higher frequencies; this is typical for synchronisation due to phase advancement.

Two spatial aspects of self-organization observed in extended populations of immobilized yeast cells were addressed: (1) the emergence of regional clusters and (2) the emergence of travelling waves of glycolytic activity. Although the cells were either completely or partially synchronised, travelling glycolytic waves arise due to a phase difference in space. These waves propagated though the field of view; however, the intracellular dynamics of each cell is homogeneous in space, due to the small diameter of the cell.

INTRODUCTION

Glycolysis, i.e., the enzymatic conversion of glucose to pyruvate and ATP, is the central metabolic pathway of almost every cell and organism. Under suitable conditions, glycolytic oscillations may occur in cells as well as in entire cell populations. Oscillations at the population level require the cells to synchronize their metabolism. In fact, yeast cells may achievecomplete synchronisation, where the metabolism of all cells join a common rhythm.

We have studied glycolytic oscillations of intact yeast cells at the level of the cell population as well as at the level of individual cells. Synchronisation is a quorum-sensing phenomenon because the collective oscillatory behaviour of a yeast cell population ceases when the cell density of the population falls below a threshold. At high cell densities, the dynamics is oscillatory, but below a critical density the collective dynamics becomes quiescent. We address the question, under which conditions individual cells in such sparse populations continue or cease to oscillate. Whereas cells in stirred cell suspension ceased to oscillate [1], immobilized cells were found to show glycolytic oscillations, even at very low cell densities [2,3]. This means, the transition between oscillatory and stationary dynamics in immobilized or suspended cells follows different pathways, namely an amplitude death phenomenon in stirred cell suspensions [1] and a so-called Kuramoto transition [2,3,4], respectively. In sparse populations of immobilized cells, the transition in the collective dynamics is caused by the loss of coherence (or desynchronisation) of the oscillations of individual cells.

RESULTS AND DISCUSSION

To identify the pathway how the transition between synchronous and asynchronous behaviour of intact, immobilized yeast cells occurs, we have studied populations of intermediate cell densities [3]. Here, a partially synchronized as well as an asynchronous state were accessible for experimental studies. In the partially synchronized state (Fig. 1), the degree of synchronisation increased substantially, whereas the distributions of the frequencies and phases of the oscillations in the cells narrowed. In fact, the synchronisation of the frequency of the glycolytic oscillations preceded the synchronisation of their phases. The pathway leading to synchronisation involved a shift in the mean frequency of the glycolytic oscillations in the cells: the mean oscillatory frequency was larger than that of the cells in the asynchronous state, suggesting that the cells were entrained by those cells that oscillated more rapidly (at a higher frequency). This is typical for synchronisation due to phase advancement (Fig. 2). However, the cells did not synchronize completely, as the distribution of the oscillatory frequencies only narrowed but failed to collapse on a unique frequency.

When investigating immobilized cell populations of intermediate cell densities, the spatial organization of the dynamics within the population must also be considered. Cells may form regional clusters where they are more densely packed than on average. These clusters may affect the dynamics at the population level because, here, cells may be better synchronized. During partial synchronisation, spatial domains of slightly higher cell density were indeed observed, however, in such clusters a number of cells oscillating at substantially different phases than the bulk of the population were found to be dispersed within the cluster [3,5,6]. Thus, at low and intermediate cell densities, clustering may slightly enhance the degree of synchronisation, but it did not lead to the formation of domains where the cells oscillate homogeneously at distinctively different phases than in other sites of the population.

Another aspect of spatial self-organization observed in populations of immobilized yeast cells is the emergence of travelling waves of glycolytic activity [3,5,6,7] in populations of high and intermediate cell densities. Although the cells were either completely or partially synchronised, travelling glycolytic waves arise due to a phase difference in space (i.e., in the cell population). The waves propagated though the field of view; however, the intracellular dynamics of each cell is homogeneous in space, due to the small diameter of the cell (of 8 – 10µm).

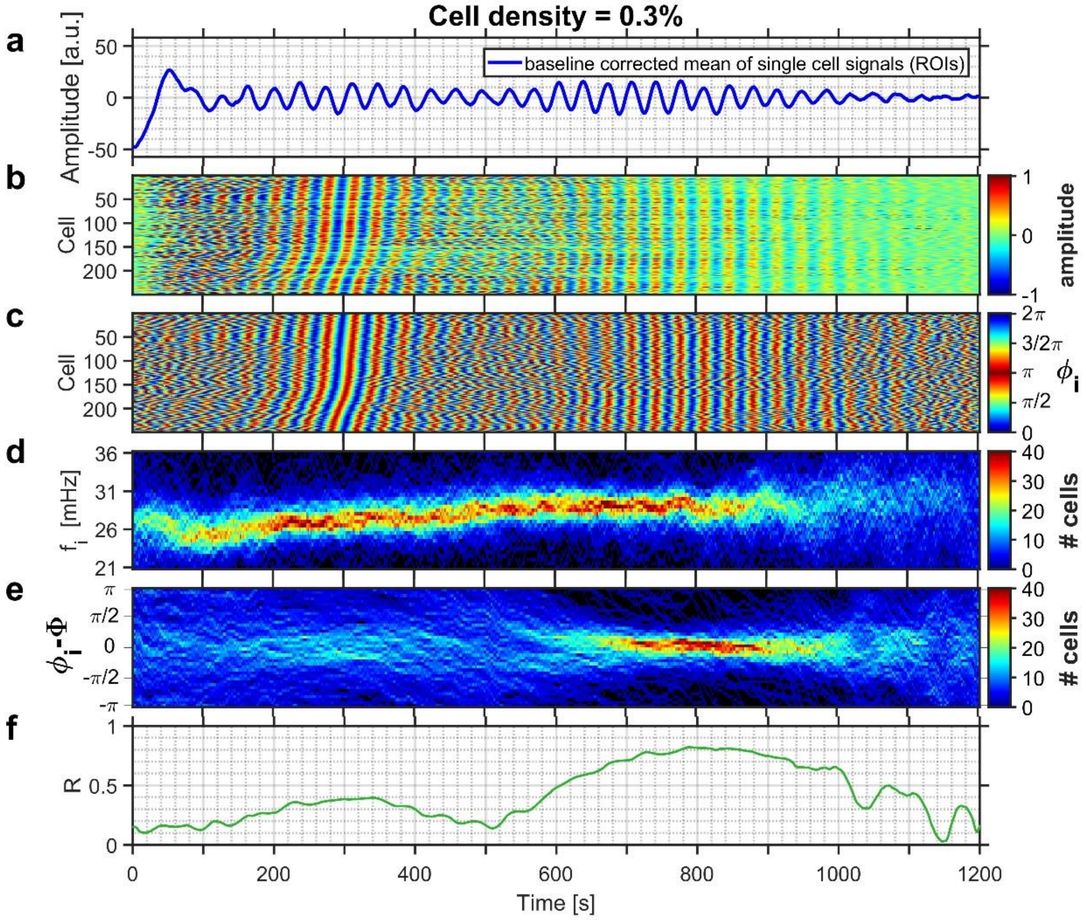

Figure 1. Partial synchronisation in a yeast cell population of intermediate cell density. (a) Time-series of the collective NADH fluorescence signal of immobilized yeast. Partial synchronisation was achieved from 580 s to 1080 s. (b) Relative amplitudes of oscillations and (c) phases of each cell. Time-dependent distributions of (d) the instantaneous frequencies f_i of the cells and (e) of the distribution of the phase difference between the phase φ_i of each cell and the average phase Φ of all cells of the population. (f) Time dependence of the order parameter R, i.e., the degree of synchronisation. Figure taken from ref. [3].

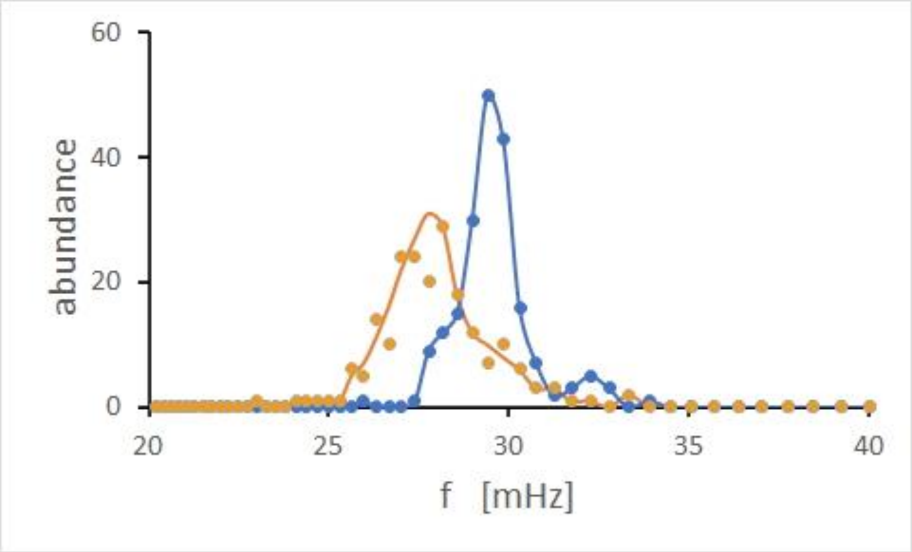

Figure 2. Distribution of oscillation frequencies of individual cells in a population of intermediate cell density. During asynchronous collective behaviour, the cells showed a fairly broad frequency distribution (in orange), whereas during partial synchronisation, the frequency distribution of periods narrowed and was shifted to higher frequencies (in blue). Figure taken from [5].

REFERENCES

[1] S. De Monte, F. d'Ovidio, S. Danø, P. G. Sørensen: Dynamical quorum sensing: Population density encoded in cellular dynamics. Proc. Natl. Acad. Sci. USA **104,** 18377-18381 (2007). https://doi.org/10.1073/pnas.0706089104

[2] A. Weber, W. Zuschratter, M. J. B. Hauser: Desynchronisation of glycolytic oscillations in yeast cell populations. PLoS One 7, e43276 (2012). https://doi.org/10.1371/journal.pone.0043276

[3] A. Weber, W. Zuschratter, M. J. B. Hauser: Partial synchronisation of glycolytic oscillations in yeast cell populations. Sci. Rep. **10** 19714 (2020). https://doi.org/10.1038/s41598-020-76242-8

[4] A.-K. Gustavsson, D. D. van Niekerk, C. B. Adiels, F. B. du Preez, M. Goksör, J. L. Snoep: Sustained glycolytic oscillations in individual isolated yeast cells. FEBS J. **279**, 2837-2847 (2012). https://doi.org/10.1111/j.1752-4658.2012.08639.x

[5] M. J. B. Hauser: Synchronisation of glycolytic activity in yeast cells. A min-review. Curr. Genetics, under consideration.

[6] M. Mojica-Benavides, D. D. van Niekerk, M. Mialkov, J. L. Snoep, B. Mehlig, G. Volpe, M. Goksör, C. B. Adiels: Intracellular communication introduces glycolytic synchronization waves between individually oscillating cells. Proc. Natl. Acad. Sci. **118**, e2010075118 (2021). https://doi.org/10.1073/pnas.2010075118

[7] J. Schütze, T. Mair, M. J. B. Hauser, M. Falcke, J. Wolf: Metabolic synchronization by travelling waves in yeast cell layers. Biophys. J. **100**, 809-813 (2012). https://doi.org/10.1016/j.bpj.2010.12.3704

MAKING NON-BIOCHEMICAL ARTIFICIAL LIFE IN A TEST TUBE

J.Perez-Mercader[1,2]

[1] *Department of Earth and Planetary Sciences and Origins of Life Initiative*
Harvard University, Cambridge, MA 02138, United States (jperezmercader@fas.harvard.edu)
[2] *Santa Fe Institute,1399 Hyde Park Rd., Santa Fe, NM 87501, United States*

ABSTRACT

Living systems on Earth are broadly characterized as complex chemical systems capable of concomitantly (i) process information, (ii) metabolize (including making their own parts from simpler components), (iii) self-reproduce and (iv) evolve. These properties are traditionally associated with the presence in extant living systems of three common universal and interdependent features: the existence of a membrane boundary, metabolism and information-carrying molecules. For each of these there exists an origins-of-life school of thought positing that one of them preceded the others in the path from non-life to proto-life to life. However, their interconnectedness makes exploring any of the three in the absence of the rest extremely difficult.

Notwithstanding the above, we show that properties (i) through (iv) can be described by a small set of unifying equations whose solutions, remarkably, display the above properties. Inspired and guided by these solutions, we present progress in the area of life's origins and its chemical synthesis resulting from experiments on autonomous system boot-up during the chemically controlled non-equilibrium self-assembly of functional, non-biochemical and small molecule-based polymeric vesicles. We follow their dynamical evolution with membrane growth and metabolism working in concert under autonomous chemical control. All this is achieved by implementing a PISA (Polymerization Induced Self-Assembly) polymerization/encapsulation scenario in an aqueous medium, which solves the concentration problem and generates an all-important free-energy gradient which provides the necessary boot-up conditions for these fully artificial systems. By design, our 1-pot chemical system ("test tube") uses reversible addition-fragmentation-chain transfer (RAFT) polymerization and completely avoids bio-chemistry. We monitor the consequences of the on-going active amphiphilic block copolymer synthesis with their resulting molecular self-assembly and evolution using electron and optical microscopy. (We will present actual microscope movies of the resulting active vesicles and their population.) We find that this dissipative self-assembly process leads to vesicles with diameters between 0.5 and 10's of microns which exhibit several emergent, life-like, properties. These include periodic growth and partial collapse, system self-reproduction, together with homeostasis, competition and phototaxis at the population level. We will briefly discuss the extension of the above by executing the PISA process with oscillatory chemical reactions which are actually able to compute as chemical Turing machines and control the assembly sequence and time evolution of their self-generating, entrapping and self-replicating vesicles. Taken together these results offer insights into artificial life, as well as into the formation of small-molecule protocells an route to the earliest living systems on the Earth as precursors to extant life and biochemistry.

REFERENCES

[1] Anders N. Albertsen, Jan K. Szymański, and Juan Pérez-Mercader (2017). "Emergent Properties of Giant Vesicles Formed by a Polymerization-Induced Self-Assembly (PISA) Reaction". *Scientific Reports* 7, 41534. doi:10.1038/srep41534

[2] Bishnu Prasad Bastakoti and Juan Pérez-Mercader (2017). "Autonomous Ex Novo Chemical Assembly with Blebbing and Division of Functional Polymer Vesicles from a "Homogeneous Mixture"". *Advanced Materials*. doi:10.1002/adma.201704368

[3] Kaixuan Ren and Juan Pérez-Mercader (2018). "Light-induced Evolution of Microaggregates: Transformation to Vesicles, Cyclic Growth and Collapse and Vesicle Fusion". *Polymer Chemistry*. doi:10.1039/C8PY00546J (cover of issue)

[4] Gong Chen and Juan Pérez-Mercader (2018). "Polymerization-induced self-assembly for artificial biology: opportunities and challenges". *Macromolecular Rapid Communications*. 40(2). doi:10.1002/marc/201800513. (backcover of issue)

[5] Juan Pérez-Mercader (2020), De novo laboratory synthesis of life mimics without biochemistry, *ALIFE 2020: The 2020 Conference on Artificial Life*. 483-490.doi:10.1162/isal_a_00282

[6] Chenyu Lin, Sai Katla. and J. Perez-Mercader (2021), "Photochemically induced cyclic morphological dynamics via degredation of autonomously produced, self-assembled polymer vesicles", *Nature's Communications Chemistry*. 4, 25. doi:10.1038/s42004-021-00464-8

[7] Marta Dueñas-Diez and Juan Pérez-Mercader (2019). "How Chemistry Computes: Language Recognition by Non-Biochemical Chemical Automata. From Finite Automata to Turing Machines". *iScience*, 19, 514-526. doi:10.1016/j.isci.2019.08.007.

[8] Marta Dueñas-Diez and Juan Pérez-Mercader (2021), "Native Chemical Computation. A Generic Application of Oscillating Chemistry Illustrated with the Belousov-Zhabotinsky Reaction. A Review", *Frontiers in Chemistry*. 9:611120. doi:10.3389/fchem.2021.611120

[9] Besides visiting www.fas.harvard.edu/~topdownsynthbio for more information you can also look at Advanced Science October 2018, https://www.advancedsciencenews.com/mimicking-living-systems-using-polymer-chemistry.

[10] Harvard Gazette, March 2017, "Mimicking life in a chemical soup", https://news.harvard.edu/gazette/story/2017/03/harvard-researcher-creates-chemical-system-that-mimics-early-cell-behavior/

[11] "Scientists Create Self-Replicating Chemicals [Chemical Systems] to Help Explain the Origins of Life" by M. Rorvig in VICE, March 2021 ,https://www.vice.com/en/article/y3g7ev/scientists-create-self-replicating-chemicals-to-explain-the-origins-of-life

DESIGN OF A PHOTOCHROMIC OSCILLATOR TO BE USED AS DYNAMICAL MODEL OF PACEMAKER NEURONS

P. L. Gentili, L. Baldinelli, B. Bartolomei

Department of Chemistry, Biology, and Biotechnology of the Università degli Studi di Perugia (Italy). E-mail: pierluigi.gentili@unipg.it

ABSTRACT

Neuromorphic engineering implements surrogates of neurons to develop Artificial Intelligence. A strategy to devise artificial neuron models is to use non-linear chemical systems that can mimic neural dynamics. This work presents the design of a new photochemical oscillator to be used as a dynamical model of pacemaker neurons. Such photochemical oscillator is based on two photochromic compounds. The spectral and kinetic features required to have oscillations are presented rigorously using numerical integration of non-linear differential equations. The designed artificial pacemaker neuron can communicate with other chemical neuron models through the transmitted and/or emitted light.

INTRODUCTION

A strategy to develop Artificial Intelligence is neuromorphic engineering [1, 2]. Neuromorphic engineering implements surrogates of neurons through non-biological systems either for neuro-prosthesis [3] or to devise brain-like computing machines. Brain-like computing machines are designed to mimic some performances of human intelligence, such as learning, recognizing variable patterns, and computing with words. Brain-like computing machines will have an architecture different from that of our electronic computers, devised by Von Neumann, and having memory physically separated from the processor. It is expected that brain-like computers will have the advantage of requiring much less power and occupying much less space than our best electronic supercomputers. The elementary unit of any brain-like computing machine is the surrogate of the neuron or some of its constitutive parts, such as the synapses. In our brain, neurons are cells specialized in encoding, collecting, processing, and storing information. The synapses constitute the terminal part of a neuron, and they send signals to other neurons or cells. At the cellular level, information is encoded in the values of neurons' transmembrane potentials. Every neuron receiving signals responds by changing its transmembrane potential value. The kind of response depends on the dynamical feature of the neuron. Neurons are non-linear dynamic systems [4, 5] that can work in either oscillatory or chaotic or excitable regimes.

Different methods for engineering surrogates of neurons have been proposed so far. Most of these methods are based on the hardware implementation of neurons and their constitutive element. Such hardware is rigid if it is made of the conventional passive and active circuit elements, either analog [1, 6] or digital [7]. It is also rigid when it consists of two-terminal devices with multiple-valued internal states that can be tuned in either a non-volatile or quasi-stable manner, mimicking synaptic interconnections [8–10]. There is also the possibility of using phase-change devices wherein the actual membrane potential of the artificial neuron is stored in the form of the phase configuration of a chalcogenide-based material, which can undergo phase transition on a nanosecond timescale and at the nanometric level [11]. The hardware might be flexible if it is based on organic film working as artificial synapses [12]. An alternative approach implements neural models in wetware by using liquid solutions of specific non-linear chemical systems [13-17]. Finally, there is the possibility of using hybrid electrochemical systems as surrogates of neurons [18, 19].

In wetware, dynamical models of pacemaker neurons are often implemented by using well-known oscillatory chemical systems, such as the Belousov-Zhabotinsky, Orbán, and Briggs-Rauscher reactions [20]. These reactions can work indefinitely in time, just in open reactors if fresh reagents are constantly introduced, and the products are sucked out. One of our goals is to design photochemical oscillators based on photochromic compounds [21]. Photochromic compounds change structure and colour when they are upon irradiation (see Figure 1). The structural modification is reversible.

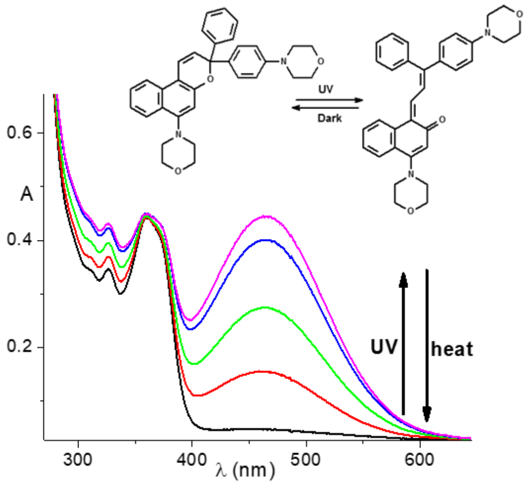

Figure 1. Spectral modification generated by UV irradiation of 6-morpholino-3-(4-morpholinophenyl) -3-phenyl-3H-naphtho[2,1-b]pyran.

Photochromic oscillators give rise to oscillations upon irradiations. When the light is off, the chemical system returns to the original equilibrium state, and it is not a surrogate of a neuron. It is ready to become the dynamical surrogate of a pacemaker neuron as soon as the light is turned on again. If this system is implemented, it will be a breakthrough with respect to the other models of pacemaker neurons in wetware [22].

In this work, we present the design and computational analysis of a new artificial neuron model based on a system of two thermally reversible photochromic compounds. One of them is peculiar because it shows an autocatalytic photo-activation through its intrinsic fluorescence. Together, they give rise to photochemical oscillations when they have specific spectral and kinetic properties.

METHODS

The systems of non-linear differential equations have been solved numerically by using the solver ode15s implemented in MatLab. The linear stability analyses of the steady-state solutions have been performed by MatLab.

RESULTS AND DISCUSSIONS

There is just one theoretical example of photochemical oscillations promoted by light in a batch reactor and isothermal conditions in the scientific literature. This case is based on two direct thermally reversible photochromic compounds presented in reference [21]. This work proposes another brand-new case, which involves two direct thermally reversible photochromic compounds, A and S, as shown in Figure 2a.

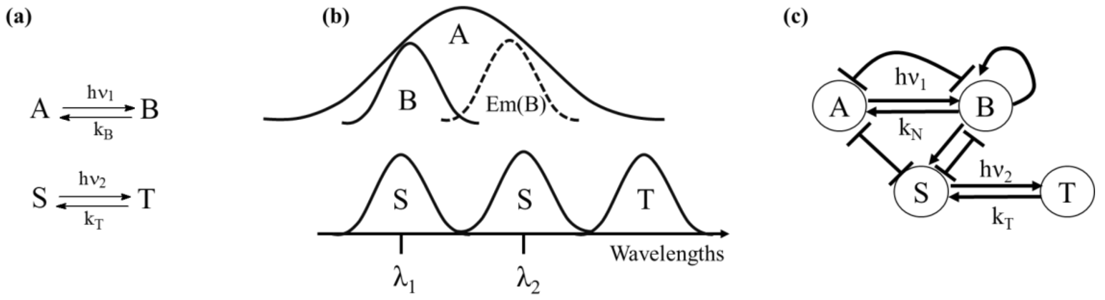

Figure 2. Principal reactions (a), spectral features (b), and reciprocal optical relationships (c) for the chemical system constituted by two thermally reversible photochromic compounds: A and S, which reversibly transform into B and T, respectively. In (c), the flattened arrowheads mean inhibitory actions whereas the traditional arrows represent activating actions.

The species A absorbs at both λ_1 and λ_2, and it jumps to its excited state A* (see steps 1 and 2 of Table 1). A* can transform to B (step 3) that does not absorb appreciably at λ_2. A* can also relax spontaneously to A by internal conversion or other plausible processes, such as fluorescence (step 4). B absorbs at λ_1 and jumps to its excited state B* (step 5). B* relaxes to its ground state B by emitting light with λ_2 as wavelength (step 6) or through internal conversion (step 7). B self-activate its own production, because its emission at λ_2 is re-absorbed by A. B* can also be quenched by A (step 8). Finally, B transforms back to A, thermally (step 9).

Table 1. Elementary steps relative to the direct thermally reversible photochromism of A producing B* when irradiated at ν_1. B* emits at ν_2 that is re-absorbed by A.

Elementary steps	Molecular event	Description	Rate
1	$A + h\nu_1 \rightarrow A^*$	Absorption of $h\nu_1$ by A	$I_1(A)$
2	$A + h\nu_2 \rightarrow A^*$	Absorption of $h\nu_2$ by A	$I_2(A)$
3	$A^* \xrightarrow{k_{RA}} B$	Photo-reaction	$k_{RA}[A^*]$
4	$A^* \xrightarrow{k_{CI(A)}} A + heat\ (+light)$	Deactivation processes	$k_{CI(A)}[A^*]$
5	$B + h\nu_1 \rightarrow B^*$	Absorption of $h\nu_1$ by B	$I_1(B)$
6	$B^* \overset{k_F}{\rightarrow} B + h\nu_2$	Emission of $h\nu_2$ by B*	$k_F[B^*]$
7	$B^* \xrightarrow{k_{CI(B)}} B + heat$	Internal Conversion for B*	$k_{CI(B)}[B^*]$
8	$B^* + A \xrightarrow{k_{EX}} B + A$	Quenching of B* by A	$k_{EX}[B^*][A]$
9	$B \overset{k_B}{\rightarrow} A$	Thermal bleaching	$k_T[B]$

The differential equation describing how the concentration of A changes over time, when it is irradiated at λ_1 is:

$$\frac{d[A]}{dt} = -I_1(A) - I_2(A) + k_{CI(A)}[A^*] + k_T[B] \tag{1}$$

In nondimensionalized form, equation (1) becomes:

$$\frac{dA}{d\tau} = -\frac{i_1 A}{\left(A + EBA(1-A)\right)}\left(1 - e^{-E_1\left(A+EBA(1-A)\right)}\right) - \frac{\phi_F i_1 EBA(1-A)}{(1+\beta' A)\left(A + EBA(1-A)\right)}\left(1 - e^{-E_1\left(A+EBA(1-A)\right)}\right)\left(1 - e^{-E_1 EAA\times A}\right) + (1-A) \tag{2}$$

In (2), $i_1 = \frac{\phi_{RA} I_{0,1}}{k_T[A]_0}$, $\phi_F = \frac{k_F}{k_F + k_{CI(B)}}$, $\beta' = \frac{k_{EX}}{k_F + k_{CI(B)}}[A]_0$, $EAA = \frac{\varepsilon''_A}{\varepsilon'_A}$, $EBA = \frac{\varepsilon'_B}{\varepsilon'_A}$, $E_1 = \varepsilon'_A d[A]_0$, wherein ϕ_{RA} is the photochemical quantum yield of A, $I_{0,1}$ is the intensity at λ_1, ε'_A and ε'_B are the absorption coefficients of A and B at λ_1, ε''_A is that of A at λ_2. $[A]_0$ is the analytical concentration of A, and d is the optical path length. Usually, photochromic compounds exhibit just one stable photo-stationary state. On the other hand, such a system can give rise to bi-stability. When the self-quenching process is faster than the sum of the emissive and internal conversion processes, i.e., when $k_{EX} > \left(k_F + k_{CI(B)}\right)$, and $\beta > 1$, the rate of A's consumption has a maximum as shown by the black curve in Figure 3. For a proper value of i_1, the thermal rate of A's production (see the red straight line of Figure 3) intersects the black curve in three points. The stabilities of the intersection points that appear in Figure 3 can be easily inferred by looking at the relative positions of the two pairs of curves. Among the three intersection points, the intermediate one represents an unstable solution, whereas the other two represent stable states. Therefore, A exhibits bi-stability.

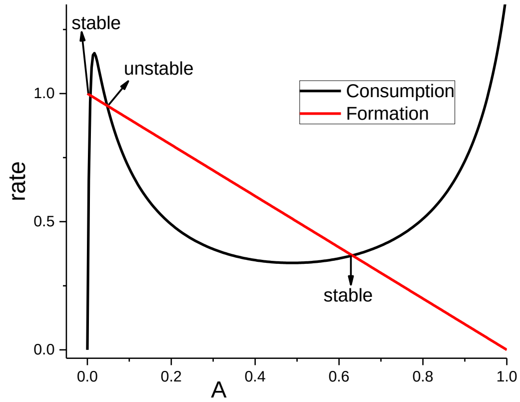

Figure 3. Rates of A's consumption (in black) and A's production (in red) obtained after fixing $i_1 = 1.4$, $EBA = 10$, $E_1 = 20$, $EAA = 10$, $\phi_F = 1$, $\beta' = 10$. There are three intersection points highlighted by the three arrows: the intermediate one represents an unstable photo-stationary state.

An empirical rule for devising oscillatory chemical reactions in open reactors affirms that any bistable system can be transformed in an oscillating one by adding a suitable inhibitory reaction [23]. In this case, the introduction of a second thermally reversible photochromic compound, S=T, which optically interferes with A=B, can originate an oscillatory system. The spectral properties of the photochrome S=T are depicted in Figure 2b. The species S absorbs in the same regions of A and B.

Species T absorbs at longer wavelengths. If the chemical system, constituted by a mixture of A and S, is irradiated at both λ_1 and λ_2, the elementary steps that can occur are not only those reported in Table 1, but also those listed in Table 2. When S absorbs one photon with λ_1 as wavelength is excited to the S** state (step 10), whereas when it absorbs a photon with λ_2 as wavelength is excited to the S* state (step 11). S** relaxes directly to the ground state S by dissipating the absorbed energy (step 12). It also relaxes to S* (step 13). On the other hand, S* can either transform to T (step 14) or relaxes to the ground state S (step 15). The species T can transform back to S, thermally (step 16).

Table 2. Supplementary elementary steps for the chemical system constituted by A=B and S=T irradiated at both λ_1 and λ_2 (see Figure 1).

Elementary steps	**Molecular event**	**Description**	**Rate**
10	$S + h\nu_1 \rightarrow S^{**}$	Absorption of $h\nu_1$ by S	$I_1(S)$
11	$S + h\nu_2 \rightarrow S^{*}$	Absorption of $h\nu_2$ by S	$I_2(S)$
12	$S^{**} \xrightarrow{k_{CI2}} S + heat$	Deactivation processes	$k_{CI2}[S^{**}]$
13	$S^{**} \xrightarrow{k_{CI3}} S^{*} + heat$	Deactivation processes	$k_{CI3}[S^{**}]$
14	$S^{*} \xrightarrow{k_{RS}} T$	Coloration reaction	$k_{RS}[S^{*}]$
15	$S^{*} \xrightarrow{k_{CI1}} S + heat(+light)$	Deactivation processes	$k_{CI1}[S^{*}]$
16	$T \xrightarrow{k_T} S$	Thermal bleaching	$k_T[T]$

The ordinary differential equation describing how [S] changes over time is:

$$\frac{d[S]}{dt} = -I_2(S) - I_1(S) + k_T[T] + k_{CI2}[S^{**}] + k_{CI1}[S^{*}] \tag{3}$$

The introduction of the photochromic S=T does not affect the chemical behavior of A=B. The only form of interaction between the two photochromes is through mutual inner filter effect (see Figure 2c). In nondimensionalized form, the differential equations describing how [A] and [S] change over time are:

$$\begin{aligned}\frac{dA}{d\tau} = &-\frac{\phi_{RA}A}{(A + EBA(1-A) + ESA_1S)}\left(1 - e^{-E_1(A+EBA(1-A)+ESA_1S)}\right) \\ &- \frac{\phi_{RA}i_1EAA_2A}{(EAA_2A + ESA_2S)}\Big(1 \\ &- e^{-E_1(EAA_2A+ESA_2S)}\Big)\left(\left(\frac{\phi_F}{1+\beta' A}\right)\frac{EBA(1-A)}{(A + EBA(1-A) + ESA_1S)}i_1\Big(1\right. \\ &\left.- e^{-E_1(A+EBA(1-A)+ESA_1S)}\Big) + i_2\right) + (1-A)\end{aligned} \tag{4}$$

$$
\begin{aligned}
\frac{dS}{d\tau} = -\frac{\phi_{RS} ESA_2 S}{(EAA_2 A + ESA_2 S)}\Big(1 & \\
& - e^{-E_1(EAA_2 A + ESA_2 S)}\Big)\left(\left(\frac{\phi_F}{1+\beta' A}\right)\frac{EBA(1-A)}{(A + EBA(1-A) + ESA_1 S)} i_1\Big(1\right. \\
& \left. - e^{-E_1(A+EBA(1-A)+ESA_1 S)}\Big) + i_2\right) \\
& - \frac{k i_1 ESA_1 S}{(A + EBA(1-A) + ESA_1 S)}\left(1 - e^{-E_1(A+EBA(1-A)+ESA_1 S)}\right) \\
& + \rho(SA - S) \qquad (5)
\end{aligned}
$$

In equations (4) and (5), $i_1 = \frac{I_{0,1}}{k_B[A]_0}$, $i_2 = \frac{I_{0,2}}{k_B[A]_0}$, $\beta' = \left(\frac{k_{EX}}{k_F + k_{CI(B)}}\right)[A]_0$, $k = \frac{k_{CI3} k_{RS}}{(k_{CI2}+k_{CI3})(k_{RS}+k_{CI1})}$, $SA = \frac{[S]_0}{[A]_0}$, $\rho = \frac{k_T}{k_B}$, $E_1 = \varepsilon'_{A1} d[A]_0$, $EBA = \frac{\varepsilon'_B}{\varepsilon'_{A1}}$, $ESA_1 = \frac{\varepsilon'_{S1}}{\varepsilon'_{A1}}$, $ESA_2 = \frac{\varepsilon'_{S2}}{\varepsilon'_{A1}}$, $EAA_2 = \frac{\varepsilon'_{A2}}{\varepsilon'_{A1}}$, ϕ_{RA} and ϕ_{RS} are the photochemical quantum yields. Such system can give rise to photochemical oscillations. Figure 4 reports two cases.

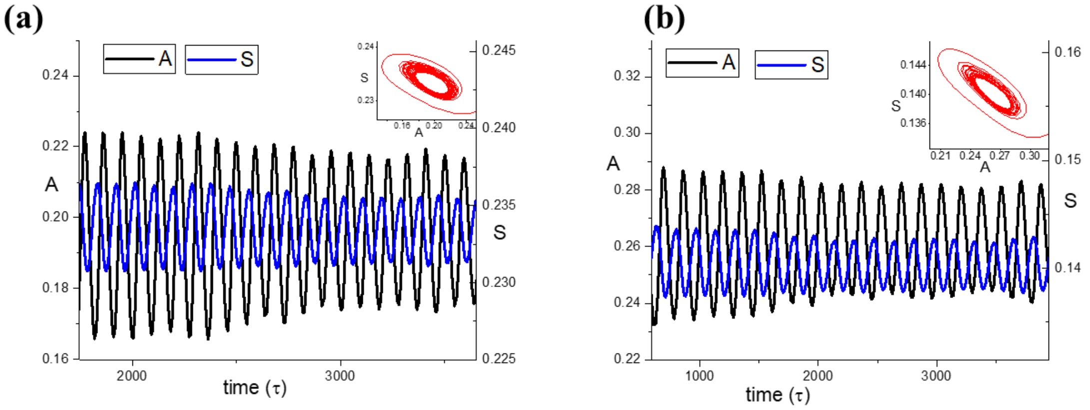

Figure 4. Trends of the relative concentrations A (black traces) and S (blue traces) vs. the relative time τ when $i_1 = 1.755$, $i_2 = 0.1$, $\phi_{RA} = 0.9$, $\phi_{RS} = 0.05$, $\phi_F = 0.9$, $E_1 = 10$, $\beta' = 2.3$, $k = 0.025$, $\rho = 0.02$, $SA = 1$, $EBA = 8$, $ESA_1 = 15$, $ESA_2 = 0.01$, $EAA_2 = 3$ in (a), and $i_1 = 2.75$, $i_2 = 0$, $\phi_{RA} = 0.9$, $\phi_{RS} = 0.05$, $\phi_F = 0.9$, $E_1 = 10$, $\beta' = 6.25$, $k = 0.025$, $\rho = 0.0088$, $SA = 1$, $EBA = 15$, $ESA_1 = 10$, $ESA_2 = 0.001$, $EAA_2 = 1.05$ in (b). The initial conditions in both simulations are $[A; S] = [1; 1]$. The insets report the phase space of the photochemical oscillator.

When ϕ_{RA} is larger than ϕ_{RS} and the thermal recovery of A from B is much faster than that of S from T (i.e., $\rho \ll 1$), then A and S oscillate. Their oscillations are always out-of-phase. The periods are $\approx 100\tau$ in (a) and $\approx 170\tau$ in (b). In a nutshell, it is the mutual optical feedback action between two photochromes, one autocatalytic (i.e., A=B) and the other rather slow in both photochemical and thermal reactions (i.e., S=T), that originates another photochemical oscillator.

CONCLUSIONS

This work shows that photochromic compounds can be used to mimic dynamics of not only phasic [15, 24, 25], and chaotic neurons [26], but also pacemaker neurons. The photochemical oscillator described in this work is based on two photochromic compounds having specific spectral and kinetic properties. Such photochemical oscillator is an alternative to the traditional pacemaker neuron models, which are oscillatory reactions, such as the Belousov-Zhabotinsky (BZ) one [27, 28]. The BZ reaction is powered by chemical affinity, whereas the photochemical oscillator proposed herein is powered by light. Since it is based on two thermally reversible photochromic compounds, it can oscillate indefinitely in time and in a closed reactor as long as the irradiation source is on. On the other hand, the BZ reaction can oscillate indefinitely in time only if it is carried out in an open reactor by constantly feeding reagents. The next challenge is the implementation of photochemical oscillators such as those described in this contribution and a previous paper [21].

REFERENCES

[1] C. Mead; "Neuromorphic Electronic Systems." Proc. IEEE 1990, 78, 1629-1636.

[2] I. K. Schuller, R. Stevens; "Neuromorphic Computing: From Materials to Systems Architecture – Report of a Roundtable Convened to Consider Neuromorphic Computing Basic Research Needs." 2015, US Department of Energy.

[3] J. P. Donoghue; "Bridging the brain to the world: a perspective on neural interface systems neuron." vol. 60. 2008. p. 511–521.

[4] M. Izhikevich; "Dynamical systems in neuroscience." 2007, MIT Press, Cambridge, MA.

[5] M. I. Rabinovich, P. Varona, A. I. Selverston; "Dynamical principles in neuroscience." Rev. Mod. Phys. 2006, 78, 1213-1265.

[6] R. F. Service; "The brain chip." Science 2014; 345: 614–616.

[7] P. A. Merolla, J. V. Arthur, R. Alvarez-Icaza, A. S. Cassidy, J. Sawada, F. Akopyan, B. L. Jackson, N. Imam, C. Guo, Y. Nakamura, B. Brezzo, I. Vo, S. K. Esser, R. Appuswamy, B. Taba, A. Amir, M. D. Flickner, W. P. Risk, R. Manohar, D. S. Modha. "A million spiking-neuron integrated circuit with a scalable communication network and interface." Science 2014; 345: 668–673.

[8] S. D. Ha, S. Ramanathan; "Adaptive oxide electronics: a review." J Appl Phys. 2011; 110: 071101.

[9] M. Di Ventra, Y. V. Pershin; "The parallel approach." Nat Phys 2013; 9: 200–202.

[10] K. Pilarczyk, A. Podborska, M. Lis, M. Kawa, D. Migdal, K. Szacilowski; "Synaptic behavior in an optoelectronic device based on semiconductor-nanotube hybrid." Adv. Electron. Mater. 2016: 1500471.

[11] T. Tuma, A. Pantazi, M. Le Gallo, A. Sebastian, E. Eleftheriou; "Stochastic phase-change neurons." Nat Nanotechnol 2016; 11: 693–699.

[12] Y. Lee, T.-W. Lee; "Organic Synapses for Neuromorphic Electronics: From Brain-Inspired Computing to Sensorimotor Nervetronics." Acc. Chem. Res. 2019, 52, 964-974.

[13] A. Adamatzky, B. De Lacy Costello, T. Asai; "Reaction–diffusion computers." Elsevier, 2005, New York (NY, USA).

[14] P. L. Gentili; "Small steps towards the development of chemical artificial intelligent systems." RSC Adv. 2013, 3, 25523-25549.

[15] P. L. Gentili, M. S. Giubila, R. Germani, A. Romani, A. Nicoziani, A. Spalletti, B. M. Heron; "Optical Communication among Oscillatory Reactions and Photo-Excitable Systems: UV and Visible Radiation Can Synchronize Artificial Neuron Models." Angew. Chem. Int. Ed. 2017, 56, 7535-7540.

[16] V. Vanag; "Hierarchical network of pulse coupled chemical oscillators with adaptive behavior: Chemical neurocomputer." Chaos 2019, 29, 083104.

[17] T. Litschel, M. M. Norton, V. Tserunyan, S. Fraden; "Engineering reaction–diffusion networks with properties of neural tissue." Lab on a Chip 2018, 18, 714-722.

[18] H. Okamoto, N. Tanaka, M. Naito; "Analogy between the stimulus-response characteristics of neuronal and electrochemical cells." Chem. Phys. Lett. 1995, 237, 432-436.

[19] Y. Liu, M. Sebek, F. Mori, I. Z. Kiss, “Synchronization of three electrochemical oscillators: From local to global coupling.” Chaos, 2018, 28, 045104.
[20] P. L. Gentili; “Untangling Complex Systems: A Grand Challenge for Science.” CRC Press, Taylor & Francis Group, 2008, Boca Raton (FL, USA).
[21] P. L. Gentili, B. Bartolomei, J.-C. Micheau; “Light-driven artificial neuron models based on photoswitchable systems.” Dyes and Pigments, 2021; 187: 109086.
[22] P. L. Gentili, J. C. Micheau; “Light and Chemical Oscillations: review and perspectives” J. Photochem. Photobiol. C 2020, 43, 100321.
[23] J. Biossonade, P. De Kepper; “Transitions from bistability to limit cycle oscillations. Theoretical analysis and experimental evidence in an open chemical system” J. Phys. Chem. A 1980, 84, 501-506.
[24] Pier Luigi Gentili, Amanda L. Rightler, B. Mark Heron, Christopher D. Gabbutt; “Extending human perception of electromagnetic radiation to the UV region through biologically inspired photochromic fuzzy logic (BIPFUL) systems.” Chem. Commun. 2016, 52, 1474-1477.
[25] Pier Luigi Gentili, Maria Sole Giubila, Raimondo Germani, B. Mark Heron; “Photochromic and luminescent compounds as artificial neuron models.” Dyes and Pigments 2018, 156, 149-159.
[26] Pier Luigi Gentili, Milos Dolnik, Irving R. Epstein; “Photochemical Oscillator”: Colored Hydrodynamic Oscillations and Waves in a Photochromic System.” J. Phys. Chem. C, 2014, 118, 598-608.
[27] P. L. Gentili, V. Horvath, V. K. Vanag, I. R. Epstein; “Belousov-Zhabotinsky “chemical neuron” as a binary and fuzzy logic processor.” Int. Journ. of Unconventional Computing 2012, 8, 177-192.
[28] V. Horvath, P. L. Gentili, V. K. Vanag, I. R. Epstein; “Pulse-Coupled Chemical Oscillators with Time Delay.” Angew. Chem. Int. Ed. 2012, 51, 6878-6881.

NUCLEOPEPTIDE NETWORKS OUT-OF-EQUILIBRIUM

G. Ashkenasy[1], A.K. Bandela[1], H. Sadihov[1], N. Wagner[1] and A. de la Escosura[2]

[1]*Department of Chemistry, Ben-Gurion University of the Negev, 84105 Beer-Sheva, Israel*
[2]*Department of Organic Chemistry, Universidad Autónoma de Madrid, Campus de Cantoblanco, 28049 Madrid, Spain.*

ABSTRACT

Many fundamental cellular functions, including replication and translation, involve synergistic activity between nucleic acids and proteins/peptides. Yet, studies with synthetic replicators have focused largely on the activity of each class of these molecules separately. We show here that short nucleopeptide chimeras can replicate through autocatalytic and cross-catalytic processes, governed synergistically by nucleobase hybridization and the assembly of peptide segments. Remarkably, within small networks of complementary nucleopeptides, unequal replication kinetics induces clear selectivity toward the formation of a certain species. The selectivity may be maximized to almost extinction of the weakest replicator when the system operates far from equilibrium and manipulated through changes in the physical and chemical conditions.[1] We will discuss how similar processes may have led to the emergence of the first functional nucleic-acid–peptide assemblies prior to the origin of life.

REFERENCES

[1] A.K. Bandela, N. Wagner, H. Sadihov, S. Morales-Reina, A. Chotera-Ouda, K. Basu, R. Cohen-Luria, A. de la Escosura, G. Ashkenasy. "Primitive selection of the fittest emerging through functional synergy in nucleopeptide networks" Proceeding of the National Academy of Sciences USA, **2021**, 118, 9 e2015285118.

COMPETITIVE ADSORPTION AND SELECTIVITY ASPECTS OF CARBON DIOXIDE, WATER VAPOUR, NITROGEN, AND SULFUR DIOXIDE ON ACTIVATED CARBON FOR CAPTURE FROM FLUE GASES

M. Thomas

Wolfson Northern Carbon Reduction Laboratories, School of Engineering, Newcastle University, Newcastle upon Tyne, United Kingdom, mark.thomas@newcastle.ac.uk

ABSTRACT

There is extensive interest in post combustion flue gas treatment for mitigating CO_2 emissions and removal of acid gases. Adsorption on porous materials is a potential low energy method for capturing CO_2. In recent years, many novel porous materials have been synthesized. However, the knowledge of selectivity and competitive adsorption of complex mixtures on porous materials remains superficial. In this study we investigate the adsorption of the main flue gas components (CO_2, N_2, SO_2, and water vapour) on Filtrasorb 400 activated carbon in order to understand adsorption characteristics of the main flue gas components and competitive adsorption effects. The adsorption isotherms of the pure components of flue gas CO_2, N_2, SO_2 and H_2O vapour were investigated. The isosteric enthalpies of adsorption were determined as a function of surface excess. The enthalpies at zero surface coverage have the order: $SO_2 > H_2O > CO_2 > N_2$. However, the SO_2 isosteric enthalpy decreases with increasing surface excess and is lower than that of water vapour at high surface excess uptake values. The temperature range for CO_2 adsorption covers the subcritical to supercritical gas transition. There was no evidence for isosteric enthalpy differences over this temperature range. The adsorption kinetics for SO_2 and H_2O adsorption were measured for each isotherm pressure increment. In both cases the adsorption kinetics followed the linear driving force model. The adsorption mechanisms for both SO_2 and H_2O kinetic trends are discussed in terms of the adsorption mechanisms. The water vapour adsorption kinetics showed a minimum in the region where water molecules form clusters around functional groups, which merge in the pores. The SO_2 adsorption kinetics also show a minimum with increasing surface coverage and this is attributed to dipole-dipole interactions. The activation energies for diffusion of both SO_2 and H_2O into F400 were very low. The adsorption kinetics of both pure N_2 and CO_2 were too fast to be measured accurately by the gravimetric method used in this study. Ideal Adsorbed Solution Theory (IAST) was used to calculate competitive adsorption of SO_2/CO_2 and CO_2/N_2 from the isotherms of the pure components. In the case of CO_2/H_2O adsorption, the adsorption mechanisms of H_2O and CO_2 are different and therefore, IAST was not applicable. The competitive adsorption of CO_2/N_2 was investigated using the Integral Mass Balance (IMB) experimental method and this was used for validation of the IAST. The competitive adsorption of CO_2/H_2O is the most important for CO_2 capture and this was also investigated using the IMB method. The results show that both thermodynamic and kinetic effects are important. The results provide an insight into the role of competitive adsorption in the capture of CO_2 and SO_2 from flue gases by adsorption on porous materials from both thermodynamic and kinetic perspectives.

FUNCTIONAL BIODYNAMICS: THE YIN COMPLEMENT

J. Mau

Chair of Medical Kybernetika, Bashkir State Medical University, Ufa, Russia;
Professor (em) School of Medicine, Heinrich Heine University Duesseldorf, Germany

ABSTRACT

Background

A previous paper elaborated on holistic functional dynamics of human-body system with assumptions about “driving forces” of physiological processes from a phenomenological viewpoint. At the behavioral level of person’s operations in body’s outside world, in particular in interaction with other persons in society, motivations had been considered in more detail though still without attempts to expand the mathematical model accordingly.

AIMS

For an integrative model perspective, in-body resonance of operational decision-making will be incorporated into the holistic modeling of physiological dynamics.

METHODS

From a philosophical viewpoint, one may invoke the Taoist Principle of Shadow-Light (Yin-Yang阴阳) to complement previous axiomatics of Yang. The Yin then appears as a person’s ambitions in pursuit of operational goals within the prevalent life-sphere setting. The holistic approach of a hierarchical drill-down in System Functional Architecture (SFA) is adopted. A generic daily wake-sleep dynamics for a single functional unit is considered first, next extended to a multiplet of functional units, and finally translated one scale upwards to functional aggregate level. Technically, a three-compartment model with charge-transfer intensities is used with any single functional unit.

RESULTS

The Yang dynamics of consumable-charge transfers from ubiquitous ‘source’ to supply-part capacitor and from its content-mirrored demand-part capacitor to the consumer are complemented with an equally ubiquitous ‘drain’ that reflects general desire to consume, the driving force, in order to maintain physiological functions and to pursue operational goals in body’s outside world, the Yin dynamics. By parallel connection of Yin complements of functional units that compose a functional aggregate, the structure can be carried forward consistently to next upper functional level.

CONCLUSION

This extension of axiomatic functional biodynamics within SFA reflects “desire to consume” irrespective of whether generated inside or outside of human body; it then lends itself to investigations in a spectrum of behavioral attitudes and internal disorders, in neuroeconomics, addiction, and metabolism. As mere axiomatics, it provides the feed from person’s surroundings into internal dynamics which was not addressed previously.

COILED-COILS FOR THE DESIGN OF CELLULAR LOGIC CIRCUITS AND NEW PROTEIN FOLDS

R. Jerala

Department of synthetic biology and immunology,
National institute of chemistry, Hajdrihova 19, SI-1000 Ljubljana, Slovenia
roman.jerala@KI.si

ABSTRACT

Coiled-coil (CC) dimers are ubiquitous building modules in natural proteins. Rules that defined interactions in CC dimers are relatively well known which allows us to design new CC dimers with selected stability and selectivity. Although CC dimers have been known since Francis Crick, recently their application in cell regulation and construction of new building modules are experiencing an explosive growth. We have designed new CC pairs that can be fused to and incorporated into other proteins, that enables new type of regulation of biological processes with increased response and fast kinetics (1,2).

CC dimers can be concatenated into longer chains which enables construction of new modular protein folds based on topological principles distinct from natural proteins. Coiled-coil protein origami (CCPO) have interesting properties and we are designing new modalities of their construction that enable multiple use of the same building modules and design of the folding pathways and other properties (3-6).

REFERENCES

[1] Fink T., Lonzarić J… Jerala R. *Nat Chem Biol*. (2018) 15 (2), 115-122.
[2] Lebar T.. Jerala R. Nat. Chem.Biol. (2020) 16 (5), 513-519.
[3] Gradišar H, … Jerala R. *Nat Chem Biol*. (2013) 9:362-6.
[4] Ljubetič A, Lapenta F, .. Jerala R. *Nat Biotechnol*.(2017) 35:1094-1101.
[5] Lapenta F…. Jerala R. *Nat Commun*. (2021) 29:939.
[6] Aupič J…. Jerala R. *Nat Commun*. (2021) 12:940.

HYBRID ORGANIC-INORGANIC PEROVSKITES

A. Stroppa

National Research Council, Italy

ABSTRACT

Hybrid Organic-Inorganic Perovskites (HOIPs) are introducing new directions in the materials science landscape. In this talk, we will discuss the intriguing origin of ferroelectricity in HOIPs. In particular, we highlight the hybrid improper mechanism where Jahn-Teller cooperative distortions are subtly coupled to inversion symmetry breaking giving rise to a switchable electric polarization. Symmetry invariants theory permits to predict a magneto-electric coupling which has been recently confirmed by experiments. We propose further examples of the complex multifunctional behaviour arising from the organic and inorganic dual nature as well as from the interplay between ferroelectricity and spin-related properties in hybrid perovskites. In particular we discuss a recently synthesized ferroelectric layered two-dimensional HOIP, *i.e.* (AMP)PbI_4 (AMP=4-aminomethyl-piperidinium). We report a new effect, *i.e.,* an extraordinarily large Rashba anisotropy that is tunable by ferroelectric polarization: as polarization is reversed, not only the spin texture is inverted, but also the major and minor axes of the Rashba anisotropy ellipse in **k**-space are interchanged, *i.e.* a pseudo-rotation. A **k·p** model Hamiltonian and symmetry-mode analysis reveal a quadrilinear coupling between the cation-rotation modes responsible for the Rashba ellipse pseudo-rotations, the framework rotation, and the polarization.

ANTITUMOR DRUGS IMMOBILIZED INTO MESOPOROUS SILICA SBA-15

G. N. Kaluđerović

Department of Engineering and Natural Sciences, University of Applied Sciences Merseburg, Eberhard-Leibnitz-Strasse 2, DE-06217 Merseburg, Germany.
(goran.kaluderovic@hs-merseburg.de)

ABSTRACT

Conventional therapeutics, such as cisplatin, beside their benefit effects in fight against cancers confronts quite a few challenges [1]. The main goals of chemotherapeutics are to hinder the tumor expansion, reduce growth of tumor cells and increase the patient's survival period. Cisplatin alone or in combined therapy is a first-line agent for several cancers (e.g. testicular, ovarian, lung, head and neck tumors). However, its antitumor efficiency is limited due to dose-dependent toxicities (e.g. nephro- and neurotoxicities) and intrinsic or acquired cellular resistance [2].

Silica-based materials are already highly promising candidates in several fields of medicine including cancer therapy [3,4]. The rationale of loading of highly active anticancer compounds into particles lie in the following: prevention of hydrolysis and accumulation in the healthy tissues/organs, tailorable drug release, as well as local application in tumor tissues in high doses.

SBA-15 or its functionalized forms potentiate and modify mechanism of action of metal-based (e.g. cisplatin, ruthenium(II), organotin(IV) compounds) or natural occurring compounds (e.g. emodin) [3-9]. For instance, SBA-15 loaded with cisplatin induced senescence in survived clones of B16F10 mouse melanoma cells [3]. SBA-15 grafted with $Ph_3Sn(CH_2)_6OH$ triggers apoptosis in B16 cells followed by the development of a nonproliferative melanocyte-like phenotype of surviving cells [5]. Moreover, same nanomaterial almost completely abolished tumor progression *in vivo* in melanoma syngeneic C57BL/6 mouse model without visible side effects. $Ph_3Sn(CH_2)_3OH$ loaded into SBA-15 reduces metastatic potential of highly invasive serous ovarian carcinoma A2780 cells [6]. Importantly, functionalization of SBA-15 has an influence on the mode of action and differentiation inducing properties [7]. SBA-15 potentiates action of $[Ru(\eta^6\text{-}p\text{-cymene})Cl_2\{Ph_2P(CH_2)_3SPh\text{-}\kappa P\}]$ and emodin against B16 cells [8,9]. These approaches present a safer mode in tumor treatment compared to induced apoptosis alone.

REFERENCES

[1] S. Ghosh, Bioorg. Chem. 2019, 88, 102925.
[2] S. Sears, L. Siskind, J. Am. Soc. Nephrol. 2021, ASN.2020101455
[3] D. Edeler, M. R. Kaluđerović, B. Dojčinović, H. Schmidt, G. N. Kaluđerović, RSC Advances 2016, 6, 111031.
[4] D. Drača, D. Edeler, M. Saoud, B. Dojčinović, D. Dunđerović, G. Đmura, D. Maksimović-Ivanić, S. Mijatović, G. N. Kaluđerović, J. Inorg. Biochem. 2021, 217, 111383;
[5] M. Z. Bulatović, D. Maksimović-Ivanić, C. Bensing, S. Gómez-Ruiz, D. Steinborn, H. Schmidt, M. Mojić, A. Korać, I. Golić, D. Pérez-Quintanilla, M. Momčilović, S. Mijatović, G. N. Kaluđerović, Angew. Chem. Int. Ed. 2014, 53, 5982.
[6] C. Bensing, M. Mojić, S. Gómez-Ruiz, S. Carralero, D. Maksimović-Ivanić, S. Mijatović, G. N. Kaluđerović, Dalton Trans. 2016, 45, 18984.
[7] D. Edeler, D. Drača, V. Petković, F. Natalio, D. Maksimović-Ivanić, S. Mijatović, H. Schmidt, G. N. Kaluđerović, Mat. Sci. Eng. C 2019, 100, 315-322.

[8] D. Edeler, S. Arlt, V. Petković, G. Ludwig, D. Drača, D. Maksimović-Ivanić, S. Mijatović, G. N. Kaluđerović, J. Inorg. Biochem. 2018, 180, 155-162.
[9] T. Krajnović, D. Maksimović-Ivanić, S. Mijatović, D. Drača, K. Wolf, D. Edeler, L. A. Wessjohann, G. N. Kaluđerović, Nanomaterials 2018, 8, 322.

CEREBRAL HYPOPERFUSION AND PROGESTERONE TREATMENT ALTER PARAMETERS OF OXIDATIVE STRESS AND ANTIOXIDANT DEFENCE IN MALE RATS

I. Guševac Stojanović[1], A. Todorović[1], S. Pejić[1], N. Tatalović[2], D. Blagojević[2], J. Martinović[1], I. Grković[1], N. Mitrović[1], M. Zarić[1], and D. Drakulić[1]

[1] *University of Belgrade, VINČA Institute of Nuclear Sciences – National institute of the Republic of Serbia, P.O.Box 522, 11001 Belgrade, Republic of Serbia.* (drakulic@vin.bg.ac.rs)
[2] *University of Belgrade, Institute for Biological Research "Siniša Stanković", National Institute of Republic of Serbia, Bulevar despota Stefana 142, 11060 Belgrade, Republic of Serbia.*

ABSTRACT

Numerous natural compounds, like progesterone (P4), a sex steroid hormone, are highlighted as promising agents for treatment of different disorders including prolonged disturbance of blood flow. However, its action on several oxidative stress markers (pro/antioxidant balance, products of lipid peroxidation and phosphatidylcholine to lysophosphatidylcholine intensity ratio) and one of the major components of antioxidant system, superoxide dismutase in rat prefrontal cortex (PFC) following permanent bilateral occlusion of common carotid arteries (2VO) is not completely investigated. According to the obtained results, levels of investigated oxidative stress markers and SOD activity were altered in 2VO animals treated with vehicle, while P4 treatment returned them to control values. Overall, presented data indicate that P4 might manifest antioxidative features in PFC of 2VO rats.

INTRODUCTION

In pathophysiological conditions, including cerebrovascular insufficiency, the imbalance might be created between the generation of reactive species and their abolition by the components of antioxidant system, mostly by superoxide dismutase (SOD), catalase and glutathione peroxidase. Due to their inadequate removal, these over-synthesized highly toxic intermediates are capable of causing structural and functional cellular changes by oxidation of biomolecules, such as lipids, proteins and DNA that may initiate oxidative injury and even cell death in neurons. In the rat two vessel occlusion (2VO), model when both common carotid arteries are permanently ligated, the most prominent neuronal damage is detected in cortical pyramidal neurons in layer III and hippocampal CA1 neurons, as well as in the other vulnerable brain regions and cell types [1].

Different therapeutic strategies are proposed for protecting brain from the deleterious effects of restricted cerebral blood flow that causes limitation of tissue oxygen and nutrients supply. Their aim is to decrease the activation of toxic pathways and increase the activity of endogenous protective mechanisms. Recently, a few neuroprotectants are suggested, including sex steroid hormones, such as progesterone (P4) and its metabolites. Previous reports indicate that P4 treatment in various models of neuronal injury exhibits multiple neuroprotective outcomes by reducing blood-brain barrier leakage, cerebral edema, lesions' volume, thus promoting functional recovery, etc. This pleiotropic hormone might achieve its genomic and non-genomic actions via binding to the appropriate hormone receptors, controlling signalling cascades in neurons, astrocytes and microglia, modulating the inflammatory response, and regulating glutamate excitotoxicity [1, 2]. P4-mediated protection might be also related to membrane stabilization and reactive species scavenging, either of which might attenuate the damage provoked by oxidative stress [3]. However, the additional research is necessary to better analyse the antioxidant mechanisms underlying this hormone's neuroprotective effects in the state of cerebral hypoperfusion and allow its use in preclinical and clinical studies.

To addresses these disputable issues, in the present study, the rat 2VO model and P4 treatment were used to investigate the potential alterations of several parameters of oxidative stress (pro/antioxidative balance (PAB), products of lipid peroxidation (LPO products) and phosphatidylcholine (PC) to lysophosphatidylcholine (LPC) intensity ratio) and one of the major components of antioxidant system, superoxide dismutase (SOD). These changes were evaluated in prefrontal cortex (PFC), a brain region that might be directly affected by mild and prolonged disturbance of blood flow as well as hormone therapy.

METHODS

All research procedures were conducted on adult male Wistar rats (350 – 400 g) and approved by the Ethical Committee for the Use of Laboratory Animals of VINČA Institute of Nuclear Sciences – National institute of the Republic of Serbia, Belgrade (authorization numbers 02/11 and 323-07-04253/2016-05). The animals were randomly divided into three groups: controls subjected to sham operation and treated with vehicle (commercial flaxseed oil, dose 1 mg/kg/day, Sham + V) (n = 5); rats subjected to permanent common carotid artery ligation and vehicle treatment (commercial flaxseed oil, dose 1 ml/kg/day, 2VO + V) (n = 5); and animals with permanently occluded common carotid arteries treated with P4 dissolved in commercial flaxseed oil in dose 1.7 mg/kg/day (2VO + P4) (n = 5). The surgical procedures were conducted by neck ventral midline incision and exposition of both common carotid arteries, followed by their careful separation from carotid sheaths, cervical sympathetic and vagus nerves. In 2VO groups, both common carotid arteries were permanently double-ligated with 5-0 silk suture, while controls underwent the same surgical intervention but without actual occlusion of carotid arteries. The treatments in all experimental groups were administrated in the form of subcutaneous injections for seven consecutive days [2]. On the last day of the experiment, 4 h following the last injection, rats were decapitated with guillotine (Harvard Apparatus, Holliston, USA). PFCs were isolated on the ice, frozen in liquid nitrogen and stored at -70°C until processing.

All analyses were performed on samples homogenized in iced-cold medium (0.25 M sucrose, 1 mM Tris-HCl EDTA buffer pH 7.4) that were then centrifuged two times per 10 min, at 3000 rpm, 4°C (Beckman, Germany). The obtained supernatants were pooled, additionally centrifuged per 20 min, at 10000 rpm, 4°C (Beckman, Germany) and obtained pellets were resuspended in ice-cold 5 mM TRIS HCl pH 7.4 [4].

For PAB assay, as previously reported [5], 10 μl of sample/standard (dilution series of hydrogen peroxide)/blank (dH2O) were incubated with 200 μl of working solution (1 ml TMB (3,3’,5,5’-tetramethylbenzidine) cation solution with 10 ml TMB solution)in a dark place for 12 min, at 37°C. Then, the reaction was stopped by adding 100 μl of 2 N HCl. The absorbencies were read on microplate reader (WALLAC 1420-Victor2 Multilabel Counter, PerkinElmer, USA) at 450 nm.

To estimate the LPO levels, the methane sulfonic acid was added to the reaction mixtures containing samples/standards (dilution series of 10 mM TMOP (1,1,3,3,"-tetramethoxypropane))/blank (acetonitrile:methanol in the ratio 3:1) and working solution. Then the mixtures were heated at 45°C/60 min, centrifuged (15 min, 13000 rpm, 4°C) (Eppendorf 5417, Germany) and the absorbencies were measured at 580 nm in a microplate reader (WALLAC 1420-Victor2 Multilabel Counter, PerkinElmer, USA). The LPO levels were determined using the corresponding standard curve, as described earlier [5].

The activity of total SOD was evaluated by the adrenaline method of Misra and Fridovich, where one SOD unit (U) is defined as the amount of enzyme needed to exhibit 50 % dismutation of the superoxide radical at pH 10.2 [6].

The modified Folch procedure using a chloroform/methanol/water solvent system was used for total lipid extracts preparation. Obtained pallets were subsequently redissolved in matrix solution

(0.5 M DHB (2,5-dihydroxybenzoic acid, Merck Millipore, Germany) in methanol (Merck Millipore, Germany)), applied onto the stainless steel target plate and dried under warm steam of air [7]. All mass spectra were obtained in the reflector mode and “delayed extraction” conditions (delay time was approximately 130 ns) on a commercial matrix assisted laser desorption/ionization time of flight (MALDI-TOF) Voyager-DE PRO mass spectrometer (Sciex, USA).The raw data were processed with the “Data Explorer Software” version 4.9 (Applied Biosystems, USA).

Statistical analysis was performed by one-way analysis of variance (one-way ANOVA) followed by Tukey’s *posthoc* test using GraphPad Prism 5 Software (USA). The significance level was $p < 0.05$, with values expressed as a percentage of the mean of the values in Sham + V group ± SEM (standard error of the mean).

RESULTS AND DISCUSSION

The brain tissue with its elevated metabolic activity, high oxygen consumption, lipid-rich content and low antioxidant capacity is highly prone to oxidative stress. A critically low oxygen supply to the brain in pathophysiological conditions is capable to modulate oxidative phosphorylation by mitochondria and considerably decrease cellular ATP production. As a result of rapid decline in cellular ATP to a level insufficient to sustain the activity of ion pumps, a prompt and widespread membrane depolarization of neurons and astrocytes arise. In parallel, mitochondria increase the production of highly reactive species that enhance lipid peroxidation and protein oxidation and induce the alteration of prooxidant/antioxidant balance in the cerebral tissues and lead to cell death. Although it is reported that reperfusion injury initiates intensive oxidative damage, there are also indications that enduring ischemic/oligemic condition provoked by 2VO creates mild, but permanent oxidative stress, which might be the cause of persistent and progressive neuronal damage [1]. These pathological processes might be prevented or even attenuated by different agents that are shown to exert protective effects in several experimental models, like those that mimic certain pathogenic features of brain dysfunction observed in advanced age- or age-related neurodegenerative diseases. Although P4 is reported to be protective against oxidative insults induced by glutamate, glucose deprivation, and $FeSO_4$/ amyloid β-peptide-provoked toxicity in primary hippocampal cultures [8], its effect in PFC in the state of cerebral hypoperfusion are still unclear. In current experimental setup, a relatively new but well defined assay for estimating the levels of PAB was used. As presented in **Figure 1.**, in 2VO group that received vehicle treatment, PAB level was augmented compared to the controls for 38 % ($p < 0.05$) and it was also increased ($p < 0.05$) regarding to P4 treatment. Previous study has shown a significant elevation of PAB level in acute cerebral ischemia and proposed that it could be used as a predictive marker of disease outcome [9]. To our knowledge, there are no available data about the effect of P4 on PAB levels in 2VO rat model, which makes them unique in the scientific literature.

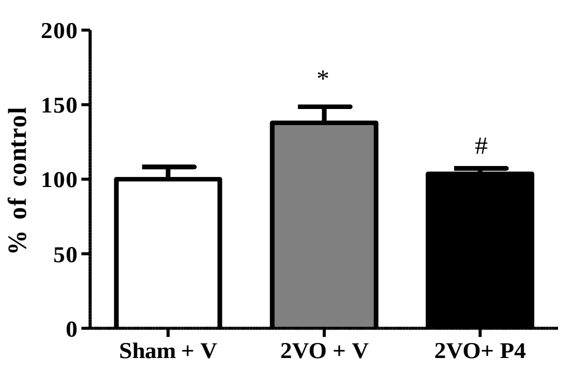

Figure 1. Levels of oxidative stress marker (pro/antioxidative balance (PAB) in prefrontal cortex of sham operated rats treated with vehicle, Sham + V, rats subjected to permanent ligation of common carotid arteries and either vehicle treatment, 2VO + V or P4 treatment, 2VO + P4. Data are presented as the mean ± SEM, whereas the values Sham + V are set as 100%. $^*p < 0.05$, *vs.* control group; $\#p < 0.05$ between 2VO groups.

Moreover, it was found that PAB status was positively correlated with other parameters of oxidative stress, such as LPO products [9]. Thus, in parallel with PAB levels, we estimated the level of LPO products. In comparison to Sham + V, in 2VO + V group the formation of LPO products was increased by 64 % ($p < 0.001$) (**Figure 2.**). Previous reports indicate that elevated levels of prooxidants lead to lipid peroxidation and formation of lipid radicals, like the aldehydes. These most abundant LPO products inactivate many cellular proteins and cause a rapid decrease and inhibition of the enzymatic and nonenzymic components of the antioxidative defense system. This provokes the overproduction of other reactive species and plays an important role in ischemic cell death, which might be associated with our previous findings [2]. Namely, previously we reported that prolonged reduction of cerebral blood flow alters the neuronal morphology, the amount of DNA fragmentation, along with the expression of progesterone receptors and the expression of the key elements of Akt/Erk/eNOS signal pathway. These modifications were attenuated by P4 treatment [2]. Although P4 does not have the characteristic chemical structure of an antioxidant, in the present study, it progressively modulated the levels of LPO products compared to vehicle treatment ($p < 0.01$) and returned them to values observed in controls (**Figure 2.**). This is consistent with literature data on P4 neuroprotective properties that are accomplished via its capacity to mitigate the lipid peroxidation by blocking the formation of free radicals and increasing the efficiency of their elimination by regulating antioxidant defense components [10]. These effects might be also achieved by controlling the isoprostanes production and pro-inflammatory genes activation [3] as detected in models of global cerebral ischemia, traumatic brain injury and subarachnoid hemorrhage [11]. Thus, the observed modulation of investigated parameters promoted by cerebral hypoperfusion might be indicative of a P4-induced reduction of oxidative stress and downregulation of proapoptotic signalling studied earlier [2].

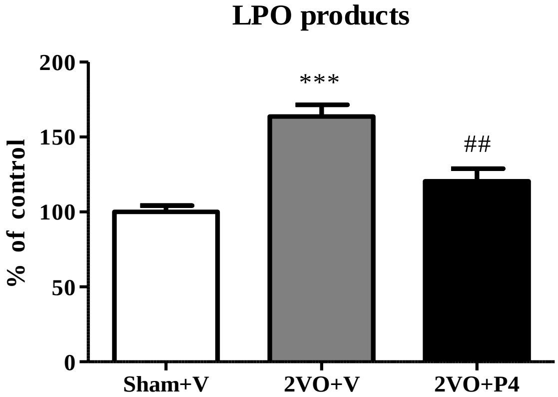

Figure 2. Levels of oxidative stress marker (products of lipid peroxidation (LPO products)) in prefrontal cortex of sham operated rats treated with vehicle, Sham + V, rats subjected to permanent ligation of common carotid arteries and either vehicle treatment, 2VO + V or P4 treatment, 2VO + P4. Data are presented as the mean ± SEM, whereas the values Sham + V are set as 100%. ***$p < 0.001$ *vs.* control group; ##$p < 0.01$ between 2VO groups.

PCs, the most abundant phospholipids, and PC-derived products, including LPCs (lipid species produced by spontaneous hydrolysis or enzymatic degradation of PCs) beside their structural functions and regulation of the physical properties of membranes, act as precursors of various lipid secondary messengers in diverse signalling cascades. The literature indicates that total concentrations of PCs and LPCs, as well as their intensity ratio, might be used as markers positively associated not only with normal aging but also with the onset and progression of different pathological conditions, including cerebrovascular and neurodegenerative diseases [7]. Since there are no available data about the lipid metabolism in PFCs' of 2VO rats treated either with vehicle or P4, this study attempted to add new knowledge about PC/LPC intensity ratio in both groups of hypoperfused animals in comparison to controls by employing MALDI TOF method followed by appropriate statistical analysis.

The observed PCs and LPCs peaks are listed in **Table 1**.

Table 1. List of phosphatidylcholine (PC) and lysophosphatidylcholine (LPC) species identified by MALDI TOF MS detected in positive ion mode.

Phospholipid Class	Adduct	m/z
LPC (16:0)	H	496.5
LPC (16:0)	Na	518.5
LPC (18:1)	H	522.5
LPC (18:0)	H	524.5
LPC (16:0)	K	534.5
LPC (18:1)	Na	544.3
LPC (18:0)	Na	546.4
LPC (22:6)	K	568.5
PC (32:0)	H	734.6
PC (32:0)	Na	756.6
PC (34:2)	H	758.6
PC (34:1)	H	760.6
PC (32:0)	K	772.6
PC (34:1)	Na	782.6
PC (36:4)	H	782.7
PC (36:3)	H	784.6
PC (36:2)	H	786.6
PC (36:1)	H	788.6
PC (34:1)	K	798.6
PC (36:4)	Na	804.6
PC (36:3)	Na	806.6
PC (36:2)	Na	808.6
PC (38:4)	H	810.6
PC (36:1)	Na	810.6
PC (36:4)	K	820.5
PC (36:1)	K	826.7
PC (38:4)	K	848.6

Figure 3. illustrates characteristic PC and LPC peaks observed in all three experimental groups, detected in positive ion MALDI spectra in the presence of DHB.

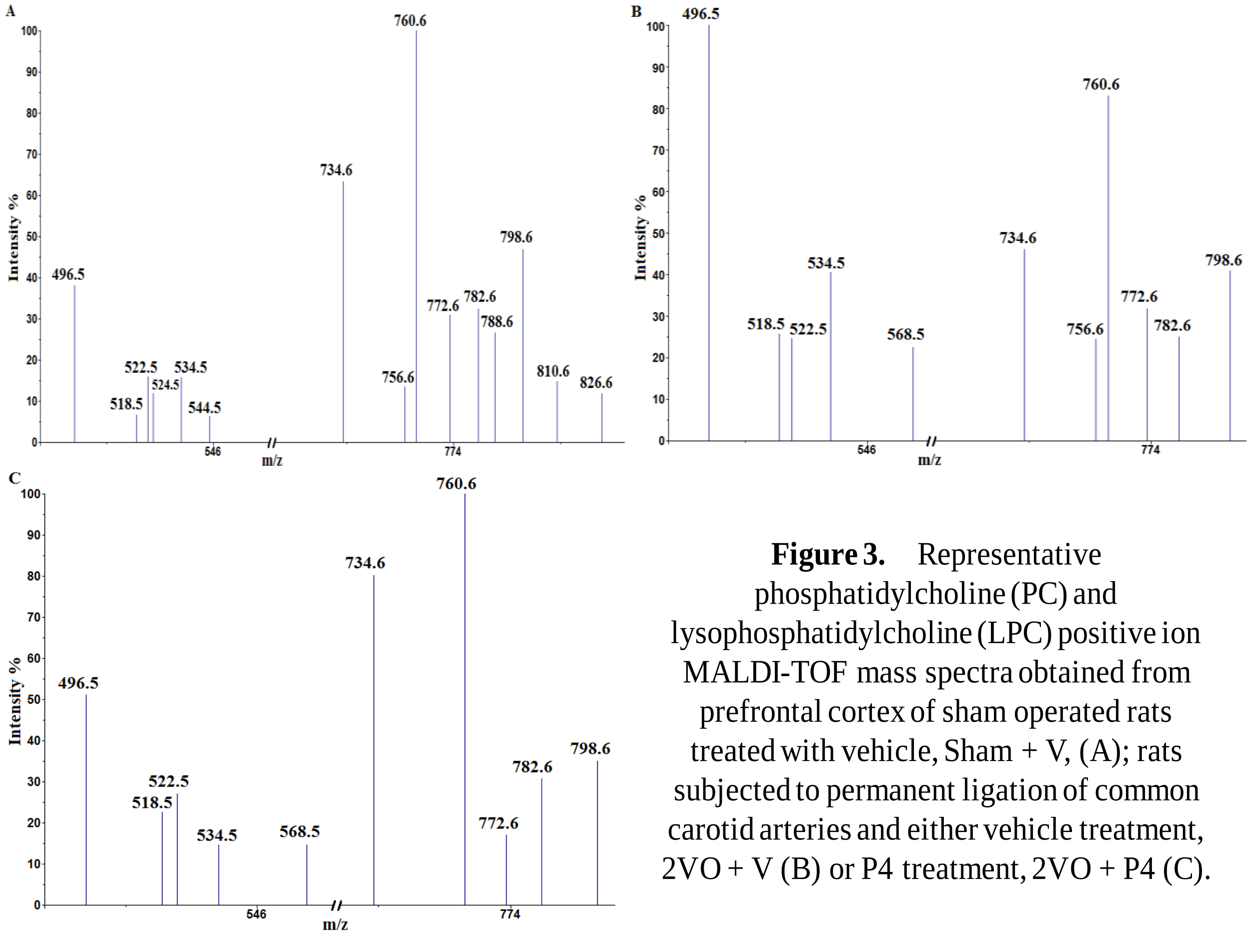

Figure 3. Representative phosphatidylcholine (PC) and lysophosphatidylcholine (LPC) positive ion MALDI-TOF mass spectra obtained from prefrontal cortex of sham operated rats treated with vehicle, Sham + V, (A); rats subjected to permanent ligation of common carotid arteries and either vehicle treatment, 2VO + V (B) or P4 treatment, 2VO + P4 (C).

The most intense peaks that correspond to PC 34:1 [M+H]+ (m/z 760.6), PC 34:1 [M+Na]+(m/z 782.6) and PC 34:1 [M+K]+(m/z 798.6); and LPC 16:0 [M+H]+ (m/z 496.5), [M+Na]+ (m/z 518.5) and LPC 16:0 [M+K]+ (m/z 534.5) were used to calculate the PC/LPC intensity ratio (**Figure 4.**). The other detected PC and LPC peaks detected in samples had much lower intensities and they were not used for further analyses.

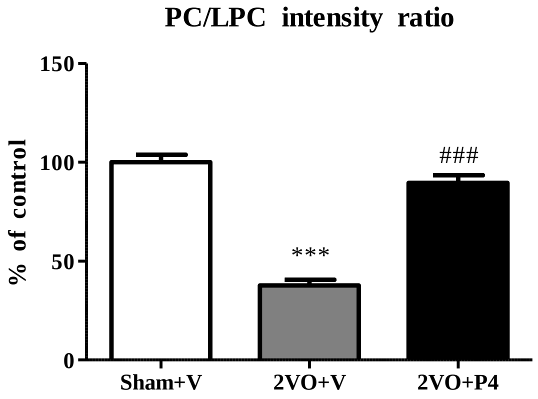

Figure 4. Phosphatidylcholine (PC) to lysophosphatidylcholine (LPC) (PC/LPC) intensity ratio calculated using most intense PC and LPC peaks (D). Intensities obtained from prefrontal cortex of sham operated rats treated with vehicle, Sham + V, rats subjected to permanent ligation of common carotid arteries and either vehicle treatment, 2VO + V or P4 treatment, 2VO + P4. Data are presented as the mean ± SEM, whereas values in Sham + V are set as 100%. ***$p < 0.001$ *vs.* control group; ###$p < 0.001$ between 2VO groups.

The observed decrease of PC/LPC ratio implies the abnormal phospholipid metabolism in 2VO + V group comparing to Sham + V ($p < 0.001$) which is most likely the result of increased activity of phospholipase A2 (PLA2). PLA2 is a lipolytic enzyme responsible for removal of the acyl group from the sn-2 position of PCs initiating the loss of vital membrane phospholipids and generation of free fatty acids and LPCs. These species and products of their metabolism further react with other biomolecules and increase accumulation of lipid peroxides, alter membrane permeability, and ion homeostasis. Aforementioned processes, along with the loss of ATP and massive cellular calcium influx and calcium overload, may provoke the impairment of cellular components, trigger proapoptotic signalling and subsequent changes in neuronal morphology and even cell death [7] that were confirmed in our prior study [2]. Furthermore, in 2VO rats treated with P4, the PC/LPC ratio was increased in comparison to 2VO + V ($p < 0.001$) and returned to the values detected in controls (**Figure 4.**), indicating decline of the intensity of oxidative stress presented herein and amelioration of its downstream prosurvival signalling pathways revealed in our previous report [2].

A detoxification enzyme, SOD, catalyzes dismutation of the superoxide anion radical into less harmful oxygen and hydrogen peroxide. Thus, it contributes to the protection of the cells from detrimental agents that promote cell death [12]. In 2VO + V group the SOD activity was enhanced in comparison to controls ($p < 0.01$) (**Figure 5.**). The observed increased levels of proxidants (**Figure 1., Figure 2., Figure 3.**, and **Figure 4.**) along with previously reported apoptotic events [2], in current experimental setup however, indicate that investigated component of antioxidant system is not capable to completely compensate the overproduction of reactive species. These compounds further oxidize biomolecules, potentiate the accumulation of oxidative cell damage and finally, most likely provoke, at least partially, previously investigated cell death signalling pathway [2]. In contrast, as presented in **Figure 5.**, P4 decreased SOD activity in PFC regarding to vehicle treatment ($p < 0.05$) and returned it to basal values. The unchanged SOD activity along with no alteration of the other tested parameters when compared to controls, indicate that applied hormone might exert neuroprotective effect by attenuating 2VO-induced oxidative stress. The protective outcome in neuronal cells might also arise due to P4-binding to specific receptors in the nucleus and activation of gene transcription. In particular, SOD is one of the P4 target genes implicated in oxidative stress tolerance [11].

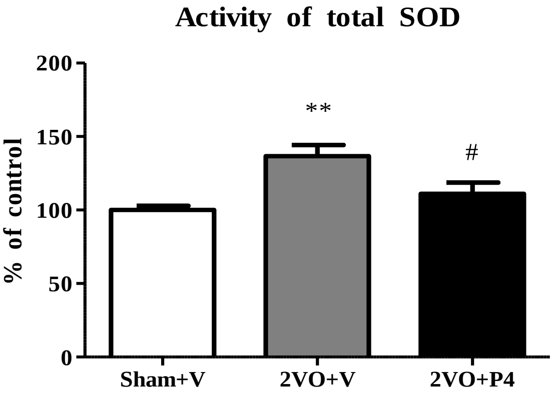

Figure 5. Activity of principal antioxidant marker (total superoxide dismutase (SOD) in prefrontal cortex of sham operated rats treated with vehicle, Sham + V; rats subjected to permanent ligation of common carotid arteries and either vehicle treatment, 2VO + V or progesterone (P4) treatment, 2VO + P4. Data are presented as the mean ± SEM, whereas the values of Sham + V are set as 100%. $^{**}p < 0.01$ *vs.* control group; $^{\#}p < 0.05$ between 2VO groups.

CONCLUSION

Disturbed cognitive and behavioural functions observed in aging, senescence and/or patients with cerebrovascular diseases or cardiovascular pathologies are associated with cerebrovascular insufficiency/hypoperfusion. Even the pathophysiology of this type of brain injury is still ambiguous, the literature highlights that various pathways might be implicated, including the generation of reactive species, inflammation, cell death, and signaling pathway disturbance. Since there is a lack of efficient pharmacotherapy, cerebral hypoperfusion is still a challenging condition in clinical medicine. Among many proposed agents, those preventing the initiation of oxidative stress and targeting the components of antioxidant system might be the promising neurotherapeutic tools.

According to the presented results, hormone treatment modified 2VO-induced increase of investigated prooxidant markers, activity of main component of antioxidant defence system and

PC/LPC intensity ratio that were all restored to control values. Overall, repeated low-dose P4 treatment in PFC of animals subjected to permanent cerebral hypoperfusion, characteristic for elders and patients with cerebrovascular disorders, might exhibit neuroprotective outcome by stimulating its antioxidative capacity.

Acknowledgement

This work is supported by Ministry of Education, Science and Technological Development, Republic of Serbia (grants no. 451-03-9/2021-14/200017-0902102, 451-03-9/2021-14/200017-0902107 and 451-03-9/2021-14/200017-0502110).

REFERENCES

[1] E. Farkas, P.G.M. Luiten, F. Bari, Brain Res Rev., 2007, **54**, 162-180.
[2] M. Stanojlović, I. Guševac Stojanović, M. Zarić, J. Martinović, N. Mitrović, I. Grković, D. Drakulić, Cell Mol Neurobiol., 2019, doi: 10.1007/s10571-019-00777-2.
[3] M. Singh, C. Su, Horm Behav., 2013, **63**, 284-290.
[4] M. Stanojlović, A. Horvat, I. Guševac, I. Grković, N. Mitrović, I. Buzadžić, D. Drakulić, Folia biol (Praha), 2014, **60**, 123-132.
[5] S. Đurašević, G. Nikolić, A. Todorović, D. Drakulić, S. Pejić, V. Martinović, D. Mitić-Ćulafić, D. Milić, T.J. Kop, N. Jasnić, J. Đorđević, Z. Todorović, Food Chem Toxicol., 2020, **140**, 111302-2020.
[6] H.P. Misra, I. Fridovich, J Biol Chem., 1972, **247**, 3170-3175.
[7] J. Miletić Vukajlović, D. Drakulić, S. Pejić, T.V. Ilić, A. Stefanović, M. Petković, J. Schiller, Rapid Commun Mass Spectrom., 2020, **28**, e8595.
[8] A.N. Siddiqui, N. Siddiqui, R.A. Khan, A. Kalam, N.R. Jabir, M.A. Kamal, C.K. Firoz, S. Tabrez, CNS Neurosci Ther., 2016, **22**, 342-350.
[9] J. Kotur-Stevuljevic, N. Bogavac-Stanojevic, Z. Jelic-Ivanovic, A. Stefanovic, T. Gojkovic, J. Joksic, M. Sopic, B. Gulan, J. Janac, S. Milosevic, Atherosclerosis, 2015, **241**, 192-198.
[10] J. Wei, G. Xiao, Acta Pharmacol. Sin., 2013, **34**, 1485-1490.
[11] Ishihara, Y., Takemoto, T., Ishida, A., Yamazaki, T. Oxid. Med. Cell. Longev., 2015, 1-16.
[12] O.M. Ighodar, O.A. Akinloye, Alexandria Med J., 2018, **54**, 287-293.

SELF-CREATION OF COMPLEX CHEMICAL ENTITIES THAT CREATE COMPLEX CELLS, GROWING AND FORMING UNUSUAL STRUCTURES, MOVEMENTS AND MACHINES THAT CAN SWITCH ITSELF TO ANOTHETR

J. Maselko

Technical University, Chemical Department, Wroclaw, Poland, jmaselko2@alaska.edu
University of Alaska, Anchorage, Chemistry Department, USA,

First Law of Thermodynamic describe that everything cannot be -self creator or destroyed in an isolator system. In open systems far from thermodynamic equilibrium. However, they exist systems that exist far from Thermodynamic Equilibriums that are supplied by chemical systems and continuously moving father from equilibrium. They are building chemical cells that can take compounds from outside, react and one compound will stay inside and next move outside. May create very complex towers. Machines cand move in different ways and may produce different complex structures. It is the basic Law of Chemical Self-creation.

Self-Creation chemical cells and theirs functions. $CaCl_2$ – Na_2CO_3.

Here few inorganic compounds will create spontaneously chemical cell. Inorganic chemicals move to cell, produce another chemical that will diffuse outside.

$CaCl_2$ was inversed to solution of Na_2CO_3 producing formation of a cell surrounded by a semi permeable membrane. The water and small molecules diffuse through the membrane. If the $CaCl_2$ is doped with $CuCl_2$ and solution contain NaiI + H_2O_2 the membrane is larger and has violet color from iodine. Iodide and hydrogen H_2O_2 diffuse into a cell, react inside and producing iodine and hydroxy ions. The process is catalyzed by Cu (II) ions

The process is catalyzed by Cu (II) ions inside the cell. The products diffuse out of the cell. Chemical reaction occurs only inside the cell.

The mechanism of iodine formation appears to follow:

$Cu^{2+} + I^- \rightarrow Cu^+ + ½ I_2$

$Cu^+ + H_2O_2 \rightarrow Cu^{2+} + OH\cdot + OH^-$

$OH\cdot + I^- \rightarrow OH^- + ½ I_2$

General reaction is:

$H_2O_2 + 2I^- \rightarrow I_2 + 2OH^-$

Finally, iodine diffuses out of the cell.

Chemical cell is a chemical machine. This sound like an incredible accident but it is the rule in Creation Chemistry. Iodine is essential element of life.

Self-controlling unusually complex tube networks. $AlCl_3$. + NaOH system.

The injection has about 0,01s with 2.5 ml/min, concentration 2-4 M. $AlCl_3$ was saturated.

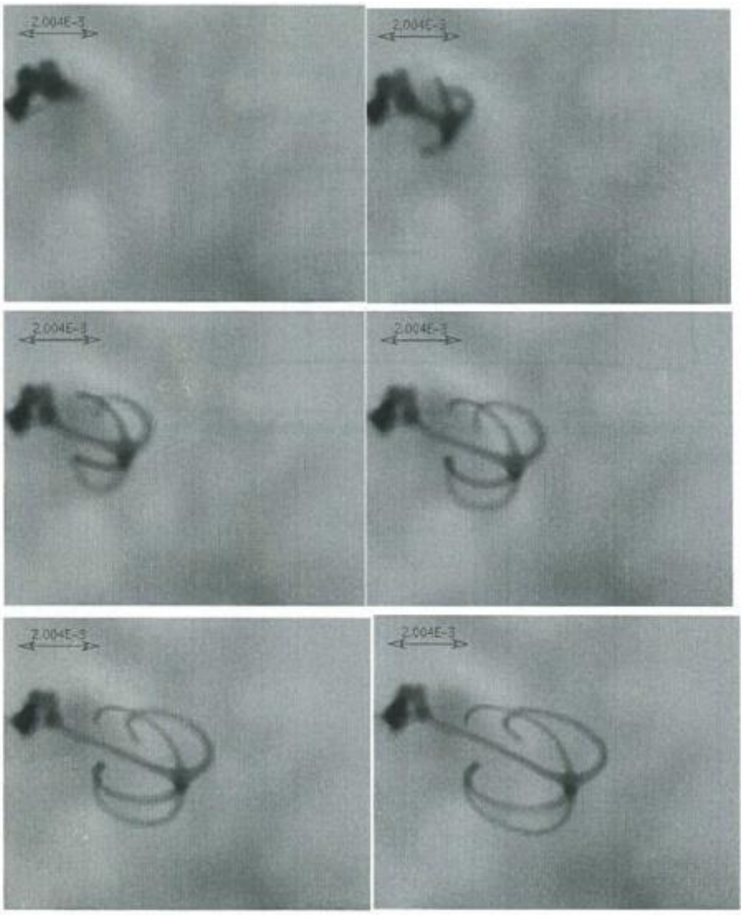

Growing tuba network.

$AlCl_3$ was injected into solution through a needle. The stem is a single tuber from balloon to branchers. Four branches grow at the same time. They distribute symmetrically around the stems at common junction. The number of branches can be from 2 to 5. The single brunch was never observed. Brunches and stem grow together. The circle is constant all the time. Usually from one fluid into another do not move far. The H_2O is controlling chemical compound and chemical compound is controlling H_2O. It may be used in nanotechnology.

Chemical Machines. Self-building complex towers. Al^{3+} - OH – CO_3^{2-}

This system has presented many different structures in time. First is self-formation of Solomonic Columns that climb itself forming spiral. Next step where solution reaches the surface, the different structures are formed. They are channels A and B. Next steps is formation of fingers C and D. The D fingers growth from tip to crescent and from crescent to tip. This process is creating many times. The final structures are streams E with 0.1 mm long and length about few cm.

The next system is a cell that is growth by itself and forming legs that are moving the cell. On the top is jumping. On the bottom is a cell that is creating another attached cell that is moving and become bigger when mother cell is disappearing.

The last cell has membrane with CO_2 bubbles inside. The cells are moving up and down and shrinking in this process. If bubble is released is the cell is moving down and is cell is shrinking is moving up. It is great example of a Chemical Machine. (It is reproduced from Langmuir, 2014, 30, 5727-5731 with permission of American Chemical Society)

In this system we observed self-creations where simple chemical systems may produce many different Chemical Machines. Many Machines can switch many different Machines.

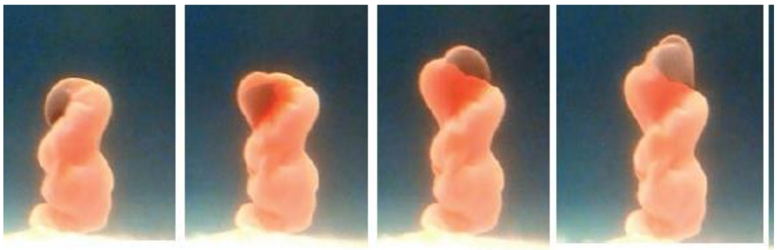

Solomonic Column

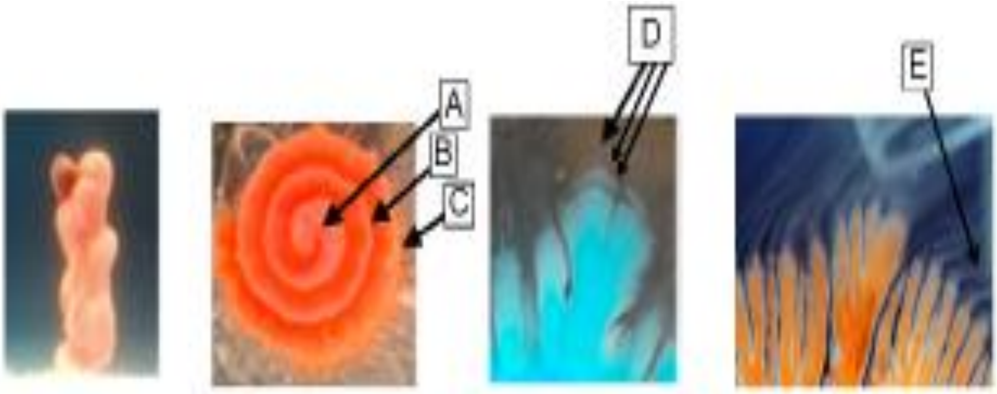

Spirals and Flowers

Chemical Machines

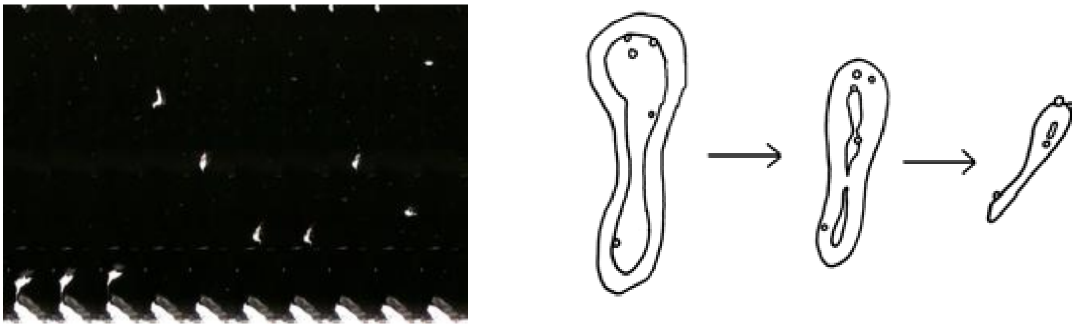

Cell membrane with CO_2 inside

Self-creation of multicellular chemical organism. Behaviors as a whole. $AlCl_3$ - SiO_4
Many towers are building city and metropolis. One tower stop building and new is building itself. At the beginning the new structure growing horizontally, next is growing vertically and it is repeating. When growth is critical then new cell will growth. In the systems always tree cells growth at the same time. The cells communicate between itself. When one is dying then next is growing. It is property of chemical systems.

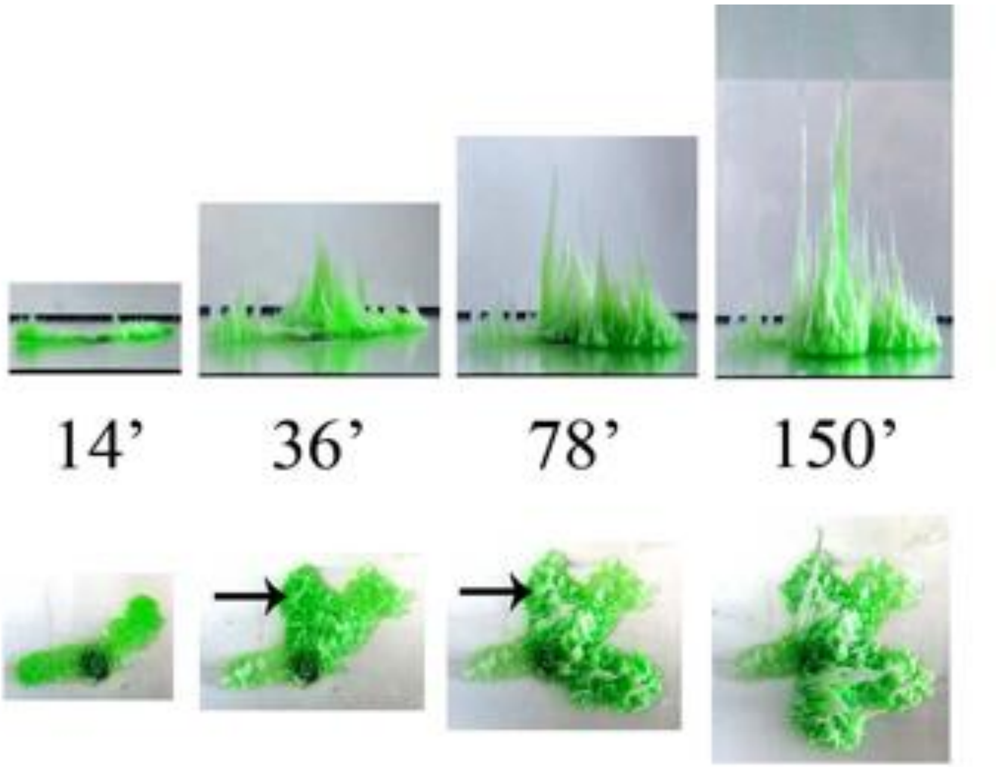

Growth of chemical metropolis from side and top

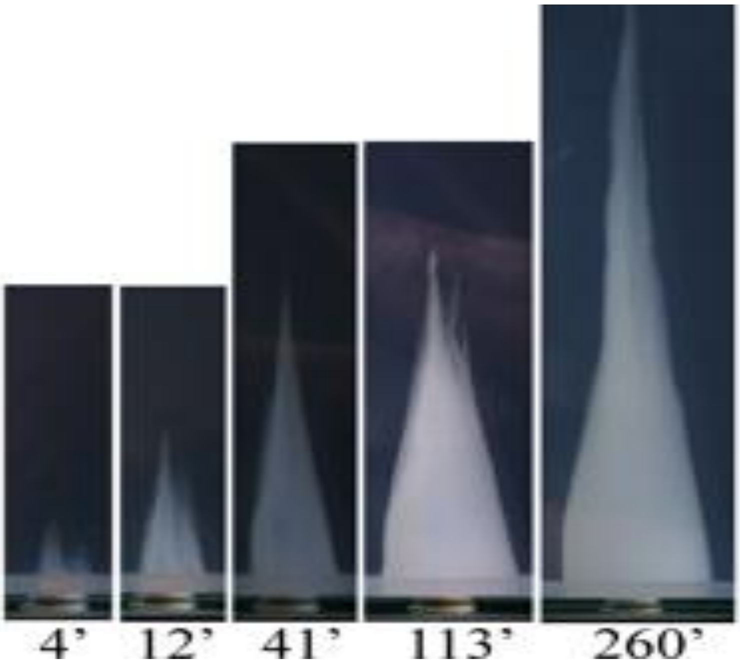

Growth of pyramid

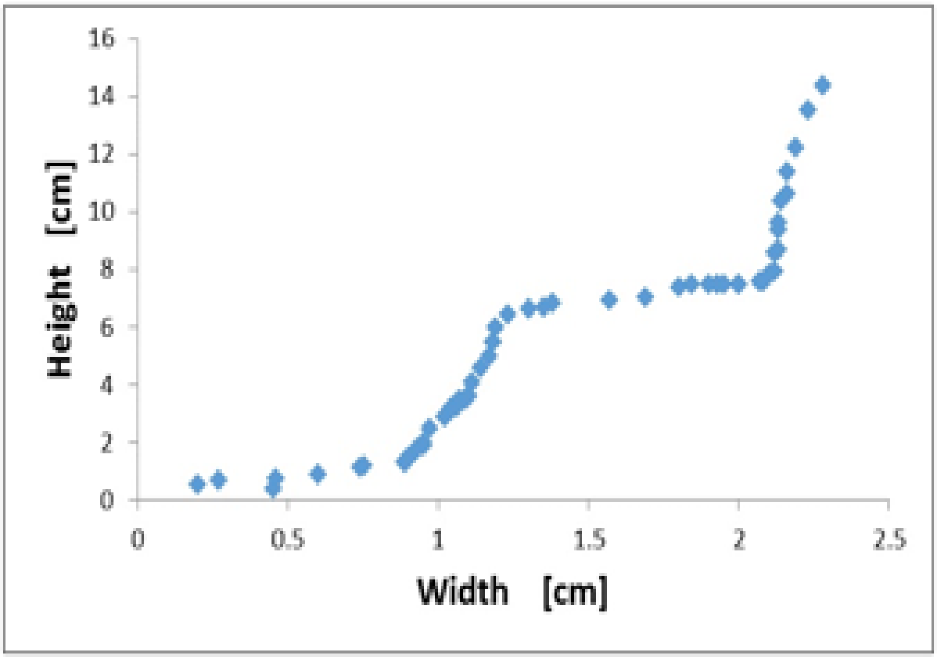

Growth of pyramid

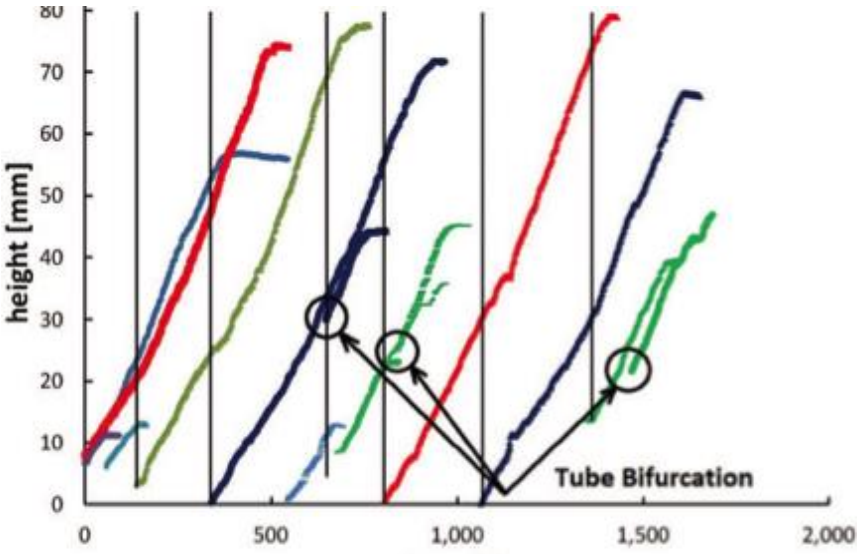

Vertical growth of cells.

The first Law of thermodynamic states: everything cannot be self-creating or destroyed in isolated system. On left are closed systems that are moving to Thermodynamic Equilibrium. On the right, with open systems and with energy and mass, complex structures continuously create itself.

Thermodynamic Equilibrium and Law of Creation.

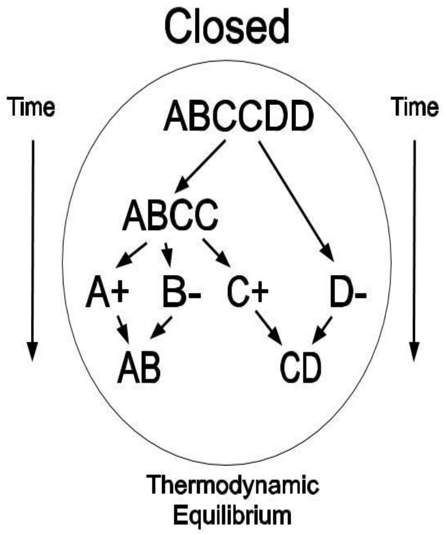

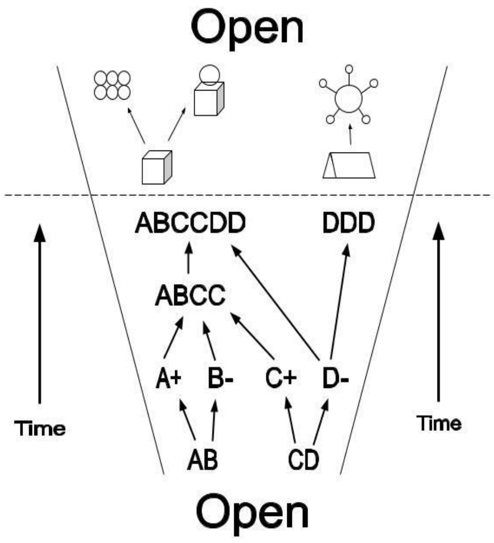

On the let Th. Eq. on write Law of Creation

On the left is Th. Eq. It is closed. On the right-chemical reactions were formed. They can form chemical cells, multicellular structures, chemical Machines, self-growing cities These new chemical complex processes created itself very fast and in simple temperatures.

DISCUSSION

1. Using two simple compounds the self-create will grow to infinity.
2. If there will be no Law of chemistry, there will be no biology.
3. Biology is relatively known. Self-create is known very little.
4. The Law of Self-creation is controlling development of the Universe.

REFERENCES

[1] J. Maselko, J. Pantaleone. Universal Chemical Machine: Continuous Increase of Complexity and Chemical Evolution. Journal of Systems Chemistry. 2019/vol7/ 1-52, 38-51

[2] J. Maselko, Self-creation of chemical structures. Experimental study. Nature Journal, Accepted. May 2021

A - Chemical Thermodynamics

THERMODYNAMIC PROPERTIES OF PURINE

A.V. Knyazev, A.S. Shipilova, S.S. Knyazeva, A.M. Kusutkina,
A.A. Panova, A.S. Logacheva, E.V. Gusarova

Chemistry Department, Lobachevsky State University of Nizhni Novgorod Gagarin Av. 23/2,603950, Nizhni Novgorod, Russia (knyazevav@gmail.com)

ABSTRACT

In the present work the temperature dependence of the molar heat capacity for purine CAS 120-73-0 has been measured for the first time over the temperature range from 5 K to 350 K and p = 0.1 MPa by the precision adiabatic vacuum calorimeter. Based on the experimental data, the thermodynamic functions of the sample have been determined for the range T =(0 – 350) K. Using combination of the adiabatic and combustion calorimetry results the thermodynamic functions of formation of purine at T = 298.15 K and p = 0.1 MPa have been calculated. The low-temperature X-ray diffraction was used for the determination of sample thermal expansion coefficients.

INTRODUCTION

A purine is an aromatic heterocyclic compound composed of carbon and nitrogen. Purines include adenine and guanine, which participate in DNA and RNA formation. Purines are also constituents of other important biomolecules, such as ATP, GTP, and can serve as a cofactors, such as NADH (reduced form nicotinamide adenine dinucleotide) and coenzyme A. [1]. A limited amount of thermodynamic information is available on the fundamental properties of the purine bases. The goals of this work include calorimetric determination of the standard thermodynamic functions of purine with the purpose of improved description of biochemical and industrial processes with its participation.

EXPERIMENTAL

The studied sample of purine (CAS: 120-73-0) was purchased from Sigma-Aldrich. An x-ray diffraction pattern of purine was obtained in the 2θ range from 5 ° to 60 ° on a XRD-6000 X-ray diffractometer from Shimadzu (CuKα radiation, scanning step 0.02 °) to identify the phase. X-ray data and estimation of the impurity content in the studied substance allowed us to conclude that the investigated sample is an individual crystal compound (Pna21, a = 1.555 nm, b = 0.937 nm, c = 0.366 nm) [2].

To measure the molar heat capacity of the studied substances at p = 0.1 MPa in the temperature range from 5 K to 350 K a BKT-3.0 automatic precision adiabatic vacuum calorimeter with discrete heating, was used. The calorimeter design and the operation procedure are described earlier [3].

To study the thermal expansion of studied sample in the temperature range from 150 K to 450 K, a powder diffractometer XRD-6000 Shimadzu described earlier and the low temperature attachment TTK- 450 Anton Paar were used. X-ray diffraction analysis was performed using the XRAY software [4].

RESULTS AND DISCUSSION

Molar heat capacity

The measurements were carried out in temperature range between 5 K and 350 K. The molar heat capacity of the sample varied from 20% to 50% of the total heat capacity of calorimetric ampoule + substance over the investigated temperature range.

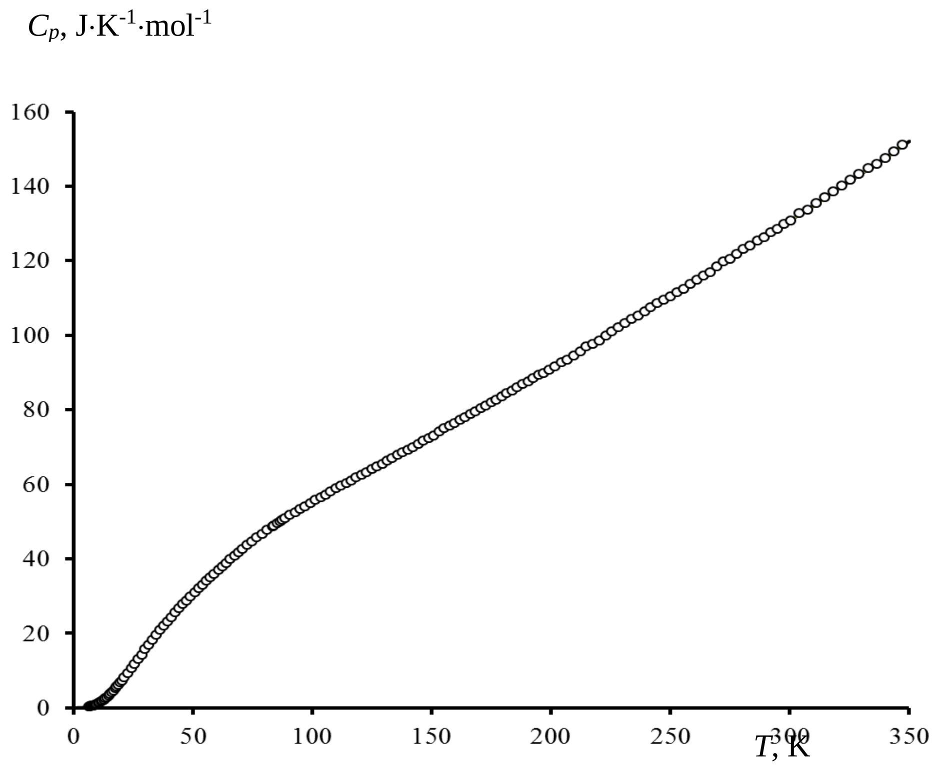

Figure 1. Temperature dependence of molar heat capacity of purine.

The experimental points in the investigated temperature range were fitted by means of the least-squares method and polynomial equations of the molar heat capacity versus temperature.

The experimental values of the molar heat capacity of purine over the range from 5 to 350 K and the averaging $C_p^\circ = f(T)$ plot are presented in Figure 1. The molar heat capacity C_p° of this substance gradually increases with rising temperature and does not show any peculiarities.

The experimental data were used to calculate standard thermodynamic functions, namely the heat capacity, enthalpy $H°(T) - H°(0)$, entropy $S°(T) - S°(0)$ and Gibbs energy $G°(T) - H°(0)$, in the temperature range from 0 K to 350 K. The standard entropy of formation $\Delta_f S°$ of the compounds under study at 298.15 K were calculated from the absolute entropy of the compound and the corresponding simple substances.

Table 1. Thermodynamic properties of formation and absolute entropy of purine (T = 298.15 K. p = 0.1MPa)

$\Delta_f H^o(298)$ (kJ/mol)	$S°$ (J·K^{-1}·mol^{-1})	$\Delta_f S^o(298)$ (J/(mol·K))	$-\Delta_f G^o(298)$ (kJ/mol)
169.41 ± 2.65 [5]	140.9 ± 0.5	−532 ± 7	328 ± 3

Low-temperature X-ray diffraction

*C*alculation of the thermal expansion coefficients was performed in the DTC (Deformation Tensor Computing) software package developed in the St. Petersburg State University [6]. To construct 2D figures of thermal expansion, the software complex KTR-B2 was used.

Table 2. Unit cell parameters and coefficients of thermal expansion of purine.

T (K)	a (nm)	b (nm)	c (nm)	V (nm ^{3})
150	1.5591 (19)	0.9418 (13)	0.3648 (5)	0.5356 (12)
300	1.5598 (16)	0.9408 (12)	0.3655 (5)	0.5363 (10)
450	1.5585 (14)	0.9395 (10)	0.3659 (4)	0.5357 (9)
$\alpha \cdot 10^5$ (K^{-1})	0.06	-0.63	1.01	0.43

The unit cell parameters and the coefficients of thermal expansion of the investigated sample are presented in the Table 2. Thermal expansion of purine is anisotropic, and its coefficient of thermal expansion depends on temperature. The greatest thermal deformations are observed along the crystallographic axis *c*, due to the weakest hydrogen bonds along this direction. The anisotropy of thermal expansion is demonstrated most clearly by the 2D figures of thermal expansion values shown in Fig. 2.

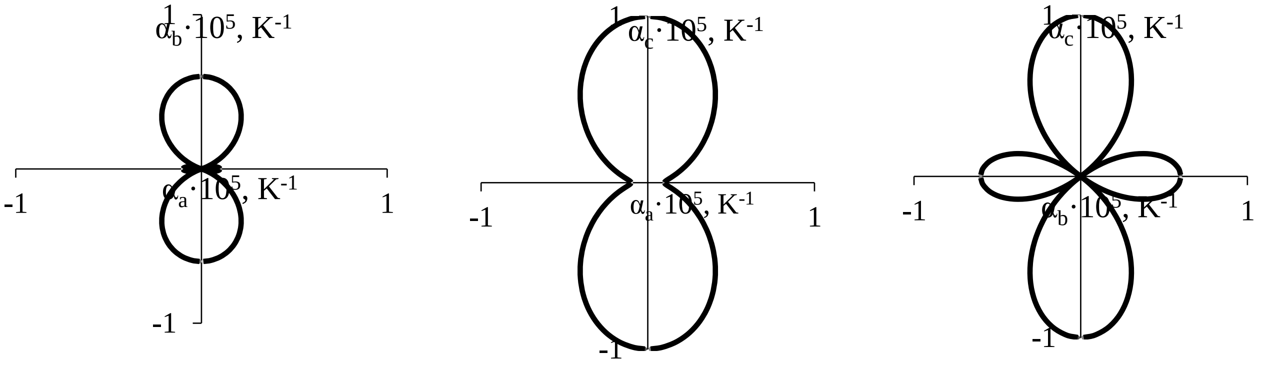

Figure 2. 2D figures of thermal expansion values of purine.

CONCLUSION

The general aim of these investigations was to report the results of the thermodynamic study of purine and to study the thermal expansion of this compound along with calculation of its coefficients. The molar heat capacity of this sample is measured in the temperature range from 5 K to 350 K and the appropriate thermodynamic functions, calculated.

Acknowledgement

The work was supported by the Ministry of Science and Higher Education of the Russian Federation (Project Part of the State Assignment No 0729-2020-0039).

REFERENCES

[1] A. M. Pedley, S. J. Benkovic, Trends in Biochemical Sciences, 2017, 42 (2), 141-154.

[2] D. G. Watson, The crystal and molecular structure of purine, Acta Crystallograhica, 1965, 19, 573-580.

[3] R. H. Stern, Journal of Clinical Lipidology, 2007, 1, 191–193.

[4] L. M Kovba, V.K. Trunov, X-ray analysis. Moscow: Moscow State University (1976).

[5] D. R. Kirklin, E.S. Domalski, J. Chem. Thermodyn., 1984, 16, 633-641.

[6] R. I. Belousov, S.K. Filatov, Glass Physics and Chemistry, 2007, 33(3), 271-275.

LOW-TEMPERATURE STUDIES OF AURIVILLIUS PHASE $Bi_5Ti_3MnO_{15}$

O.V. Krasheninnikova, A.V. Knyazev, E.V. Syrov and A.V. Barykin

Lobachevsky State University of Nizhni Novgorod, Gagarin Prospekt 23/2, 603950 Nizhni Novgorod, Russia (okkraska@gmail.com)

ABSTRACT

Manganese-containing multiferroic Aurivillius layered perovskite was synthesized and characterized by XRD and XRF. The obtained compound is isostructural to its ferrous analog. Second order insulator-metal phase transition was detected at 126 K using low-temperature XRD and DSC. Heat expansion of the material was studied in the temperature range of 80-400 K.

INTRODUCTION

Multiferroics have attracted much attention recently, mostly because of their potential application as detectors, power converters, and memory devices due to their ferroelectric and magnetic properties. Ecological reasons push the development of lead-free ceramic multi-component solid solutions based on relaxor ferroelectrics with special ferroelectric and magnetic properties.

Aurivillius phases are one of the families of layered perovskite structure type, and they have been known for their multiferroic properties [1]. They can be described with general chemical formula $A_{n-1}Bi_2B_nO_{3n+3}$, where A = Na^+, K^+, Ca^{2+}, Sr^{2+}, Ba^{2+}, Pb^{2+}, Bi^{3+} and Ln^{3+}; B = Ti^{4+}, Cr^{3+}, Ga^{3+}, Mn^{4+}, Fe^{3+}, Nb^{5+}, Ta^{5+} and W^{6+}. The crystal structure of Aurivillius phases consists of n perovskite-like layers $[A_{n-1}B_nO_{3n+1}]^{2-}$ stacking between rock-salt-like layers $[Bi_2O_2]^{2+}$. The number of layers n ranges from 1 to 9. The first Aurivillius phase discovered to be ferroelectric was $PbBi_2Nb_2O_9$ in 1962 [2]. Many phases of this family with various electromagnetic properties were discovered since, including multiferroic system $Bi_4Ti_3O_{12}$ – $BiFeO_3$ [3].

In this system, physical properties and stability are varying with the increasing number of layers n. It was established that thermal stability decreases with n increasing [3]. Moreover, orthorhombic – tetragonal phase transitions occur upon heating in the same temperature range as usual perovskites ferroelectric – paraelectric transition (Curie temperature). Curie temperatures in this system increasing for $1 \leq n \leq 3$, decreasing for $4 \leq n \leq 6$ and plateauing for $n > 6$ [3]. Compound $Bi_5Ti_3FeO_{15}$ with $n = 4$ demonstrates quite strong magnetoelectric behavior despite the fact that it is paramagnetic at room temperature. The nature of such electromagnetic properties is yet to be determined. Doping or changing d-elements in various atomic positions can dramatically change the crystal structure and electromagnetic properties of the materials. Even though the structure and properties of Fe-compound are studied, almost no data are available in the literature for the Mn-containing phase, which can be promising multiferroic material. To fill this gap, $Bi_5Ti_3MnO_{15}$ was synthesized and its low-temperature properties were studied.

METHODS

For the synthesis, stoichiometric quantities of Bi_2O_3, TiO_2, and Mn_2O_3 (Sigma-Aldrich) were grounded, pressed into pellets, and annealed at 1173 K for 12 h to perform the following reaction:

$$2.5Bi_2O_3 + 3TiO_2 + 0.5Mn_2O_3 \rightarrow Bi_5Ti_3MnO_{15}$$

The phase purity of the obtained sample was studied using powder XRD on Shimadzu XRD-6000, Cu $K\alpha_{1,2}$ irradiation, 30 kV, 30 mA on the tube; 10-60 ° 2θ range; 0.02 ° step; 2 °/min scan speed.

The chemical composition and purity of the obtained sample were studied using wavelength dispersive X-ray spectroscopy on Shimadzu XRF-1800. Bi Lα, Ti Kα, Mn Kα lines were measured 3 times from sample pellet in a vacuum with 40 kV, 50 mA on Rh-anode tube using SC detector. Fundamental parameters with a single standard calibration method was used for the oxide matrix corrections [4].

Low-temperature XRD studies were carried out using Anton Paar HTK-450 chamber on Shimadzu XRD-6000 diffractometer in the temperature range 80-400 K at 1 °/min scan speed. Cell parameters for every temperature were refined using UnitCell software. Thermal expansion coefficients were calculated using DTC software.

Differential scanning calorimetry measurements were carried out using Netzsch DSC 204 F1 Phoenix in the temperature range 100-400 K in the Ar atmosphere at 10 °/min speed with liquid nitrogen as a cooling agent.

RESULTS AND DISCUSSION

XRD phase analysis proved that the obtained sample is monophasic Aurivillius phase with an orthorhombic *Fmm2* space group with unit cell parameters a = 0.5397(2) nm, b = 0.5425(2) nm, c = 4.213(1) nm. The crystal structure of $Bi_5Ti_3MnO_{15}$ consists of stacking layers of $[Bi_3Ti_3MnO_{13}]^{2-}$ interchanging with $[Bi_2O_2]^{2+}$ slabs (Figure 1). Therefore, the synthesized compound is isostructural to $Bi_5Ti_3FeO_{15}$.

XRF analysis showed that the sample has 99.7 % purity (metal trace basis). The chemical composition of the obtained compound is close to theoretical: 78.1 mass. % Bi_2O_3 (theoretical 78.5); 16.4 mass. % TiO_2 (theoretical 16.2); 5.5 mass. % Mn_2O_3 (theoretical 5.3). Therefore, the measured chemical formula for the obtained compound can be written as $Bi_{4.9\pm0.2}Ti_{3\pm0.2}Mn_{1\pm0.2}O_{14.9\pm0.6}$. A slight lack of bismuth oxide is probably caused by its volatility at a high temperature of synthesis.

Low-temperature XRD studies show a leap of unit cell parameters in the temperature range of 125 – 150 K (Figure 2). Parameters before and after phase transition are fitting well with linear functions. No abrupt changes in the XRD pattern led us to conclude that this transition is happening within orthorhombic symmetry. According to literature data on resistivity measurements, the observed effect can be explained as an insulator-metal phase transition [5]. $Bi_5Ti_3MnO_{15}$ resistivity drops significantly below 126 K, right after the detected phase transition. Heat expansion coefficients were calculated for all measured temperatures. Heat expansion along the c axis is greater than along a or b axes in the temperature range of 80-150 K; anisotropy of heat expansion weakening after the phase transition.

The measured DSC curve corresponds well with XRD and literature data (Figure 3). A slight exo-effect on the curve peaking at 126 K demonstrates the presence of a phase transition. All observations mentioned above led us to conclude that the observed phenomenon is the second-order phase transition.

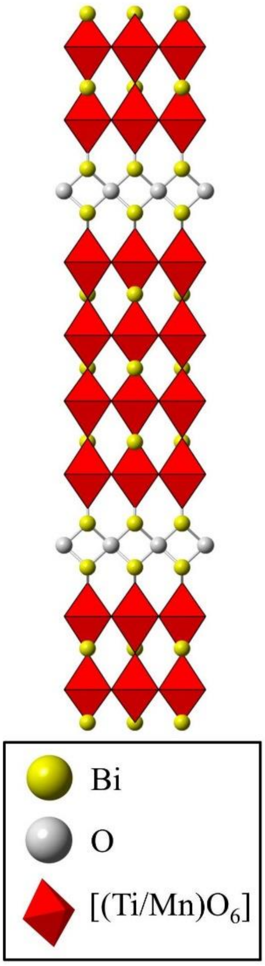

Figure 1. Crystal structure of $Bi_5Ti_3MnO_{15}$

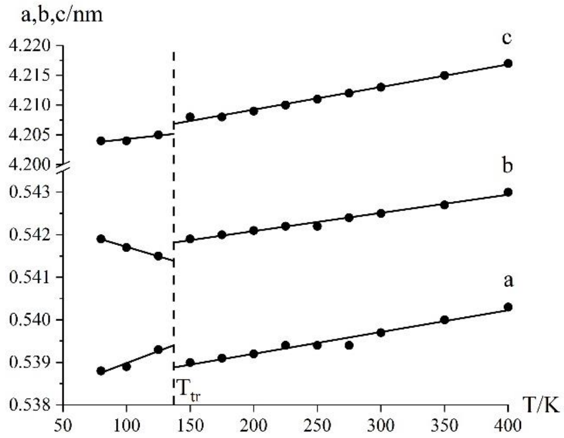

Figure 2. Unit cell parameters vs. temperature of $Bi_5Ti_3MnO_{15}$

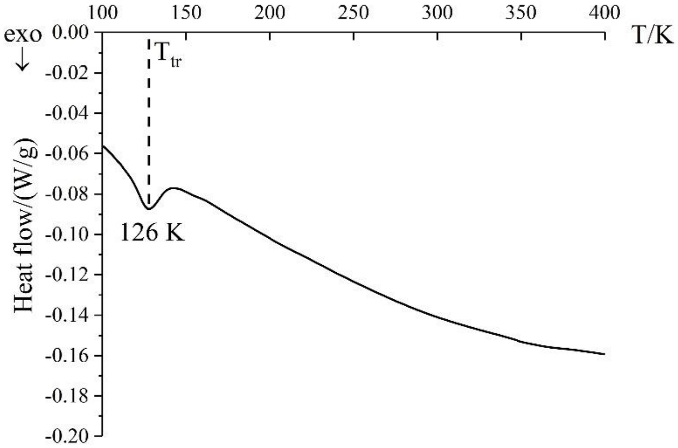

Figure 3. DSC curve of $Bi_5Ti_3MnO_{15}$

CONCLUSION

Therefore, synthesis, characterizing, and low-temperature measurements of Aurivillius phase $Bi_5Ti_3MnO_{15}$ were conducted. Conventional solid state reaction between respective oxides yields monophasic and chemically pure compound, isostructural to $Bi_5Ti_3FeO_{15}$ phase. Low-temperature heat expansion behavior was studied. Low-temperature insulator-metal phase transition within the same symmetry was detected by XRD and DSC measurements at 126 K, corresponding well with literature data on compound resistivity.

Acknowledgement

The work was supported by the Ministry of Science and Higher Education of the Russian Federation (Project Part of the State Assignment No 0729-2020-0039).

REFERENCES

[1] B. Aurivillius, Mixed bismuth oxides with layer lattices. I. The structure type of $CaNb_2Bi_2O_9$, Arkiv för Kemi, V. 1 (1949) 463-480
[2] E.C. Subbarao, A family of ferroelectric bismuth compounds, J. Phys. Chem. Solids, V.23 (1962) 665-676.

[3] M. Krzhizhanovskaya, S. Filatov, V. Gusarov, P. Paufler, Aurivillius phases in the $Bi_4Ti_3O_{12}$/ $BiFeO_3$ system: Thermal behaviour and crystal structure, Z. Anorg. Allg. Chem., V.631 (2005) 1603-1608.

[4] R. Sitko, B. Zawisza, Quantification in X-Ray Fluorescence Spectrometry, Chapter In book: X-Ray Spectroscopy, (2012) 137-162

[5] M. Mahesh Kumar, A. Srinivas, G.S. Kumar, S.V. Suryanarayana, Synthesis and physical properties of $Bi_5Ti_3MnO_{15}$, Solid State Comm., V. 104 No.12 (1997) 741-746

CONTRIBUTION OF DIFFERENT INTERACTIONS TO THE EXCESS GIBBS ENERGY OF MIXING IN AQUEOUS ELECTROLYTE SOLUTIONS

D. Ž. Popović[1], T. Ivanović[2], J. M. Miladinović[3], Z. P. Miladinović[4]

[1] Innovation Centre Faculty of Technology and Metallurgy, University of Belgrade,Karnegijeva 4, 11 001 Belgrade, Serbia (dpopovic@tmf.bg.ac.rs)
[2] Institute for Multidisciplinary Research, University of Belgrade, Kneza Višeslava 1, 11 030 Belgrade, Serbia
[3] Faculty of Technology and Metallurgy, University of Belgrade, Karnegijeva 4, 11 001 Belgrade, Serbia
[4] Institute of General and Physical Chemistry, Studentski trg 12-16, 11 000 Belgrade, Serbia

ABSTRACT

The thermodynamic properties of the mixed electrolyte solutions are conveniently described in terms of excess quantities. The excess Gibbs energy of mixing, presents the difference between the excess free energy of a mixed electrolyte solution and free energies of the individual binary electrolyte solutions at the same temperature, pressure and total ionic strength. In this paper the excess Gibbs energy of mixing is calculated for series of mixed electrolyte solutions and possible pairs, triplets, quads or even higher order multiplets were discussed in respect to Scatchard's mixing parameter values.

INTRODUCTION

In thermodynamics of electrolyte solutions, for aqueous mixture of two electrolytes the excess free energy can be expressed as the sum of the contributions of single electrolyte solutions at the same ionic strength as the mixed one, plus excess free energy of mixing given as an expansion in the ionic strength fractions of electrolyte. The main contribution to the excess free energy of mixing appears due to interactions of pairs and triplets of ions. The contribution of triplet interactions are often considered negligible compared to binary ones. If a solution contains an electrolyte which tends to form complexes or has strong hydrophobic character, the contribution of higher-order multiplets to the excess free energy of mixing must be taken into account, in addition to the contributions due to pairs or pairs and triplets.

THEORY AND MODEL

The model used in calculations is Scatchard's neutral-electrolyte model [1], generally capable of representing osmotic coefficients of mixed electrolyte solutions accurately, given enough mixing parameters. This approach treats all electrolytes present formally as if they were completely dissociated. In the case of mixtures of strong electrolytes, the binary-solution mixing approximation can sometimes provide a fairly reliable estimate of the osmotic coefficients of the ternary solutions. The excess free energy of mixing for the mixed solution of A and B electrolytes, in terms of the Scatchard parameters is given by:

$$\frac{\Delta G_m^{\mathrm{ex}}}{RT} = I y_{\mathrm{A}} y_{\mathrm{B}}\left[B_{\mathrm{AB}}^{(0)} + (y_{\mathrm{A}} - y_{\mathrm{B}}) B_{\mathrm{AB}}^{(1)} + (y_{\mathrm{A}} - y_{\mathrm{B}})^2 B_{\mathrm{AB}}^{(2)} + \cdots + (y_{\mathrm{A}} - y_{\mathrm{B}})^n B_{\mathrm{AB}}^{(n)}\right] \quad (1)$$

where terms B_{AB} represent:

$$B_{\mathrm{AB}}^{(n)} = \sum_{k=n+1}^{k'} \frac{I^k}{k} b_{\mathrm{AB}}^{(n,k)} \quad \text{for } n \geq 0 \quad (2)$$

In previous relations, y is the ionic strength fraction of electrolyte A or B, I is the ionic strength of the mixed solution and b_{AB} are Scatchard's mixing parameters. The b_{AB} parameters are found by least squares method applied to either the osmotic coefficients or the activity coefficient data for the mixed systems containing A and B electrolytes. If we rearrange the terms in excess free energy of mixing through possible pairs, triplets, quads or even higher order multiplets (HOM), we obtain:

$$\frac{\Delta G_m^{ex}}{RT} = \left(\frac{\Delta G_m^{ex}}{RT}\right)_{\text{pairs}} + \left(\frac{\Delta G_m^{ex}}{RT}\right)_{\text{triplets}} + \left(\frac{\Delta G_m^{ex}}{RT}\right)_{\text{quads}} + \cdots + \left(\frac{\Delta G_m^{ex}}{RT}\right)_{\text{HOM}} \quad (3)$$

where:

$$\left(\Delta G_{\mathrm{m}}^{\mathrm{ex}}/RT\right)_{\text{pairs}} = I^2 y_{\mathrm{A}} y_{\mathrm{B}} b_{\mathrm{AB}}^{(0,1)} \quad (4a)$$

$$\left(\Delta G_{\mathrm{m}}^{\mathrm{ex}}/RT\right)_{\text{triplets}} = \left(I^3/2\right) y_{\mathrm{A}} y_{\mathrm{B}} \left[b_{\mathrm{AB}}^{(0,2)} + (y_{\mathrm{A}} - y_{\mathrm{B}}) b_{\mathrm{AB}}^{(1,2)}\right] \quad (4b)$$

$$\left(\Delta G_{\mathrm{m}}^{\mathrm{ex}}/RT\right)_{\text{quads}} = \left(I^4/3\right) y_{\mathrm{A}} y_{\mathrm{B}} \left[b_{\mathrm{AB}}^{(0,3)} + (y_{\mathrm{A}} - y_{\mathrm{B}}) b_{\mathrm{AB}}^{(1,3)} + (y_{\mathrm{A}} - y_{\mathrm{B}})^2 b_{\mathrm{AB}}^{(2,3)}\right] \quad (4c)$$

$$\left(\Delta G_{\mathrm{m}}^{\mathrm{ex}}/RT\right)_{\text{HOM}} = \left(I^{n+2}/n+1\right) y_{\mathrm{A}} y_{\mathrm{B}} \left[b_{\mathrm{AB}}^{(0,n+1)} + (y_{\mathrm{A}} - y_{\mathrm{B}}) b_{\mathrm{AB}}^{(1,n+1)} + \cdots + (y_{\mathrm{A}} - y_{\mathrm{B}})^n b_{\mathrm{AB}}^{(n,n+1)}\right] \quad (4d)$$

RESULTS AND DISCUSSION

Excess Gibbs energy of mixing (Figure 1) was calculated by relation (1), for series of mixed electrolyte solutions at temperature 298.15 K. Scatchard's parameters (Table 1.) for each mixed solution were taken from our previous work on osmotic coefficients treatment[2-7].

Table 1. Scatchard's mixing parameters for different electrolyte systems, standard deviation of fitting the osmotic coefficient data for the system, s.d. (ϕ), the solution ionic strength interval, for which the parameters are valid (m^o stands for standard molality, 1 mol·kg^{-1}).

System	$b_{AB}^{(0,1)}$ (m^o)	$b_{AB}^{(0,2)}$ $(m^o)^2$	*s.d.* (ϕ)·10^3	*Ionic strength interval* (mol·kg^{-1})
{yKCl+(1-y)K_2HPO_4}(aq)[2]	-0.03724	0.047634	7.8	2-12
{$y$$KNO_3$+(1-$y$)$K_2HPO_4$}(aq)[3]	-0.028196	0.081518	4.2	2.5-6.5
{yKBr+(1-y)K_2HPO_4}(aq)[4]	-0.020035	0.020422	8.0	3-10
{$y$$K_2SO_4$+(1-$y$)$K_2HPO_4$}(aq)[5]	-0.010654	0.0062619	8.0	1.2-2
{$y$$KH_2PO_4$+(1-$y$)$K_2HPO_4$}(aq)[6]	-0.0025	0.0122	1.6	0.4-3.4
{$y$$Na_2HPO_4$+(1-$y$)$K_2HPO_4$}(aq)[7]	0.0084145	0.0	0.9	0.9-1.06

If pairwise interactions are truly the only interactions occurring in a mixed solution, then $b_{\mathrm{AB}}^{(0,1)}$ parameter will be the only one required to fit the data, and the total excess free energy of mixing will be equal to $\left(\Delta G_m^{ex} / RT\right)_{pairs}$. This is the case with the system {*y*Na_2HPO_4+(1-*y*)K_2HPO_4}(aq) where standard deviation of the fit is of 10^{-4} order even with only one mixing parameter.

If the sole use of $b_{\mathrm{AB}}^{(0,1)}$ is found to be inadequate in fitting the data, then there must also be triplet interactions in the solution. Therefore, both $b_{\mathrm{AB}}^{(0,2)}$ and $b_{\mathrm{AB}}^{(1,2)}$ as well as $b_{\mathrm{AB}}^{(0,1)}$ must be used in fitting the data, as it is the case for the systems {*y*KCl+(1-*y*)K_2HPO_4}(aq), {*y*KBr+(1-*y*)K_2HPO_4}(aq) and {*y*K_2SO_4+(1-*y*)K_2HPO_4}(aq) where the standard deviation of the fit by using just two mixing parameters $b_{\mathrm{AB}}^{(0,1)}$ and $b_{\mathrm{AB}}^{(0,2)}$ is still relatively, high. Gibbs energy of mixing for these systems, specially with {*y*KCl+(1-*y*)K_2HPO_4}(aq), changes evidently with the increase of solution ionic strength reflecting possible triplet interactions.

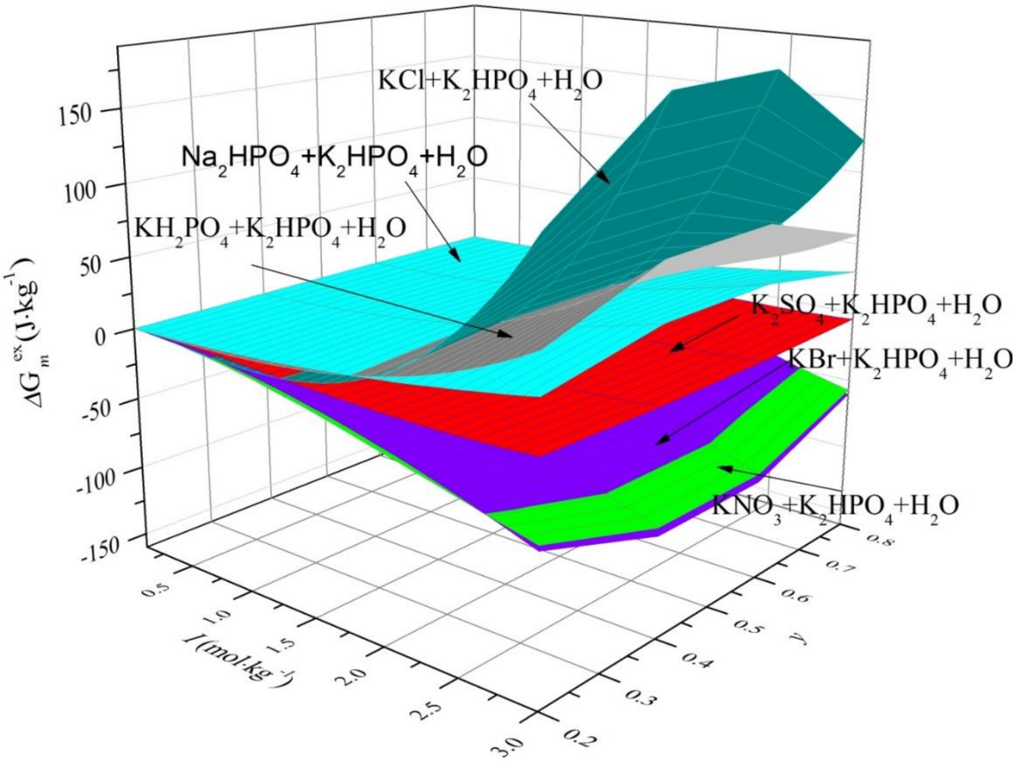

Figure 1.: Excess Gibbs energy of mixing per kilogram of solvent (water) for different mixed electrolyte solutions at *T* = 298.15 K in respect to solution ionic strength, *I*, and ionic strength fraction, *y*.

CONCLUSION

By obtaining detailed thermodynamic data on excess Gibbs energy of mixing for the aqueous electrolyte systems, using Scatchard's parameters, significant information regarding specific ion interactions can be obtained.

Acknowledgement

This work was supported by the Ministry of Education, Science and Technical Development of the Republic of Serbia (Contract No. 451-03-9/2021-14/200287).

REFERENCES

[1] G. Scatchard, J. Phys. Chem., 1961, 83, 2636-2642.

[2] Daniela Z. Popović, Jelena Miladinović, Milica D. Todorović, Milorad M. Zrilić, Joseph A. Rard, J. Chem. Thermodyn., 2011, 43, 1877-1885.

[3] Daniela Z. Popović, Jelena Miladinović, Zoran P. Miladinović, Branislav B. Ivošević, Milica D. Todorović, Joseph A. Rard, J. Chem. Thermodyn., 2012, 55, 172-183.

[4] Daniela Z. Popović, Jelena Miladinović, Zoran P. Miladinović, Snežana R. Grujić, Milica D. Todorović, Joseph A., J. Chem. Thermodyn., 2013, 62, 151-161.

[5] Daniela Ž. Popović, Jelena Miladinović, Joseph A. Rard, Zoran P. Miladinović, Snežana R. Grujić, J. Chem. Thermodyn., 2014, 79**,** 84-93.

[6] T. Ivanović, Daniela Ž. Popović, Jelena Miladinović, Joseph A. Rard, Zoran P. Miladinović, Ferenc T. Pastor, J. Chem. Thermodyn., 2020, 142, 105945.

[7] Daniela Ž. Popović, Jelena Miladinović, Joseph A. Rard, Zoran P. Miladinović, Snežana R. Grujić, J. Solution Chemistry, 2016, 45, 1261-1287.

B - *Spectroscopy,*
Molecular Structure,
Physical Chemistry of Plasma

INSIGTHS FROM NUMERICALLY EXACT APPROACHES FOR THE CALCULATION OF THE ROVIBRATIONAL ENERGY STRUCTURE OF TRI- AND TETRATOMIC MOLECULES

M. Mladenović

MSME, Univ Gustave Eiffel, CNRS UMR 8208, Univ Paris Est Créteil,
F-77454 Marne-la-Vallée, France (mirjana.mladenovic@univ-eiffel.fr)

ABSTRACT

Numerically exact rotation-vibration solutions to the molecular Schrödinger equation for tri- and tetratomic molecules are applied. As a first example, the torsional structure of HOCO is analyzed using several adiabatic projection techniques. The torsional structure is found to exhibit two limiting cases associated with oscillator and rotor spectral patterns. Combining full-dimensional rovibrational calculations for N_2H^+ with the available experimental values for B_0, the r_α and r_e structures of the ion are additionally determined and analyzed.

INTRODUCTION

Numerical approaches for full-dimensional rovibrational calculations are valuable tools for achieving a complete full-dimensional physical description of molecular behavior for a given potential energy surface (PES) constructed within the Born-Oppenheimer approximation. To obtain the maximum information possible in such a calculation, a good functional representation for the potential is desirable, satisfying at least the fundamental symmetries [1]. This request is not fulfilled by commonly used quartic force fields, based on near-equilibrium arrangements. With the help of full-dimensional rovibrational calculations, we may not only assess the validity of traditional methods, but also provide a hint at possible causes for their limitations.

METHODS

Methods for full-dimensional rovibrational calculations, which I have been developing for general tri- and tetratomic molecules, use the exact body-fixed kinetic energy operator in combination with flexible basis sets and efficient computational strategies [2,3]. The computation makes no approximation beyond the concept of the potential energy surface, involving no dynamical approximations and no re-expansion of the potential energy function. The computed rovibrational energy levels are quantitatively analyzed by several adiabatic projection techniques, which provide detailed information on anharmonic and coupling/mixing effects, allowing also for automatic quantum number assignments. The quantum state character correlation scheme is employed to monitor the evolution of the adiabatic representation [3].

RESULTS AND DISCUSSION

The hydrocarboxyl radical, HOCO, is an intermediate in the reaction between hydroxyl radical, HO, and carbon monoxide, CO, known to exhibit a significant nonstatistical (non-Arrhenius) behavior. The internal dynamics of HOCO is dominated by the torsional (out-of-plane) motion.

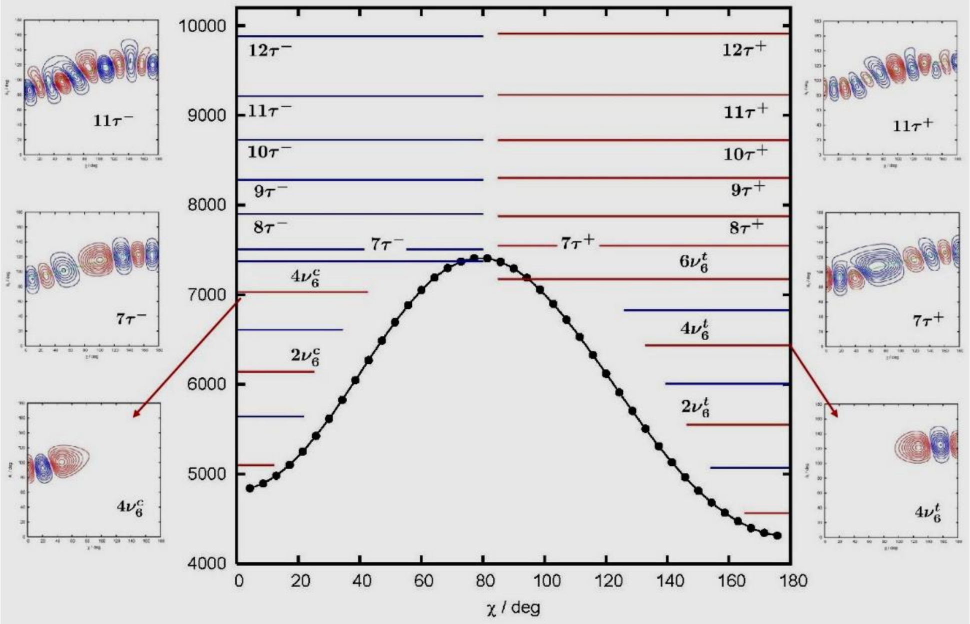

Figure 1. Two limiting cases associated with oscillator and rotor spectral patterns identified for the torsion in HOCO.

The torsional structure of HOCO is studied in great detail using the RCCSD(T)/cc-pVQZ PES developed earlier [4]. The torsion is described by a double-minimum anharmonic potential with a nonplanar barrier between the *trans* and *cis* arrangements. The electronic torsional saddle point is 3270 cm^{-1} above the *trans* form. The torsional saddle point $^{adi}V^0$ on the effective ground-state profile is at 7410 cm^{-1}, as seen in Figure 1. The pure torsional states below $^{adi}V^0$ follow the oscillator pattern associated either with the *trans* or *cis* form and described by the quantum number ν_6. The first states having a nonzero wave function probability amplitude in both well regions occur in the vicinity of $^{adi}V^0$. The states above $^{adi}V^0$ exhibit the free-rotor behavior, with the even-parity and odd-parity levels of similar energies. The rotor states are described by the quantum number τ^p, where the parity label p is + or – for even or odd parity. The expectation value of the torsional angle in the first excited torsional state is about 25° for *trans*-HOCO and 20° for *cis*-HOCO. Due to this, alternative approaches to vibrational calculations based on the normal mode description (such as the vibrational configuration interaction approach) encounter difficulties in treating even the fundamental torsional transition of *trans*-HOCO and *cis*-HOCO [5].

Vibrational second-order perturbation theory is commonly used to derive effective spectroscopic constants from *ab initio* energy points, which typically cover only a narrow portion of the potential energy surface around the minimum. This traditional approach has been integrated into several popular quantum chemistry program packages with the motivation to routinely provide reference data for experimental measurements. However, the standard perturbational approach is not always sufficient to reliably predict all experimentally required spectroscopic properties. Huang *et al.* [6] strongly questioned the attribution of the transition at 11244 MHz to C_3H^+ on the basis of large discrepancies between the calculated equilibrium centrifugal distortion constants D_e and the experimentally derived D_0 value. Using their quartic force field in combination with our numerically exact rovibrational treatment, we found that the PES from Ref. [6] in fact supports the experimental identification of C_3H^+ [1]. Another example is provided by the protonated nitrogen molecule, N_2H^+. The experimentally derived sextic centrifugal distortion constant is reported to be H_0=73.5 mHz for N_2H^+ and H_0=71.6 mHz for N_2D^+ [7]. The vibrational second-order perturbational results are much smaller, given by H_e= 48.8 mHz for N_2H^+ and H_e= 34.2 mHz for N_2D^+ [7]. Our rovibrational calculations using a CCSD(T) PES of Ref. [8] provide H_0=73.3 mHz N_2H^+ and H_0=65.8 mHz N_2D^+, in good agreement with the experimental findings.

Microwave rotational spectroscopy measures the energies of rotational transitions, frequently with stunning precision. The experimental observations are usually fitted to effective spectroscopic Hamiltonians and applied to find the molecular structure at equilibrium. In real vibrating-rotating molecules, corresponding to actual experimental situation, the ground vibrational state is described by a wave function, extended over other-than-equilibrium arrangements. The effects of zero-point vibrational motion produce an effective rotational constant B_0, which is different from the equilibrium B_e value. Based on numerically exact rovibrational energy levels, we have designed a new two-step experimental/theoretical procedure for the derivation of molecular equilibrium structures [9,10]. This method has been applied on the formyl cation, HCO^+, a key species in ion-molecule chemistry with a central role in astrochemical models [11].

Information about the correction $\Delta B_0=B_e-B_0$ is not easily accessible experimentally. The zero-point B_0 constant is usually corrected by the vibration-rotation α constants. The estimates for B_e obtained in this fashion produce the so-called r_α structure. On the other hand, the concepts of B_0 and B_e are both well founded in theoretical approaches based on numerically exact full-dimensional rovibrational calculations. The full correction $\Delta B_0=B_e-B_0$ only allows to derive the equilibrium r_e structure.

In Figure 2, we see the pairs of the bond distances r(NH) and r(NN) reproducing the estimates B^{est} modeled as B_0+S_0 and $B_0+\Delta B_0$ for eight isotopologues of N_2H^+, involving H, D, ^{14}N, and ^{15}N. The intersection of the horizontal and vertical dashed lines shows the r_e and r_α parameters, computed by nonlinear least-squares methods. Two bond distances, describing a linear triatomic molecule such as N_2H^+, are anti correlated.

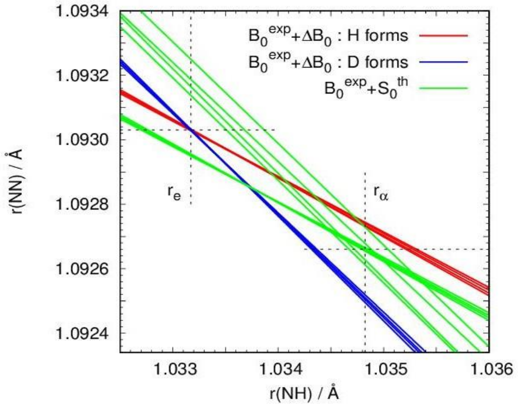

Figure 2. Parameters of N_2H^+.

The spectroscopic α corrections S_0 for eight isotopic variants of N_2H^+ are approximately 200 MHz. They provide the dominant contribution to the full corrections ΔB_0. The higher-order corrections ΔB_0-S_0 are in order of several MHz and much small than S_0. In spite of that, the higher-order contributions are found to be essential for the determination of the molecular structure. To access the higher-order contributions experimentally, measurements on vibrational overtones and combination bands are required. But, this is not an easy task. In electronic-structure program packages, the spectroscopic correction S_0 from second-order vibrational perturbation theory is routinely used to obtain the zero-point rotational constant B_0 from the calculated equilibrium rotational constant B_e. However, the correction S_0 has its own fundamental deficiency due to neglecting higher-order effects.

In theoretical spectroscopy, quartic internal coordinate force fields are sometimes employed for the determination of spectroscopic parameters by perturbation methods. In rovibrational calculations beyond the perturbation treatment, they are commonly subjected to a Morse transformation. The quartic force fields are, however, often found to be insufficient to properly capture the angular behavior, important for describing the underlying physics of the system. In our study on N_2H^+, we use the global three-dimensional PES of Schmatz [8] and the quartic force field of Huang *et al.* [12], both designed for this ion in its ground electronic state. The minimum energy paths V_{MEP} and the ground state adiabatic profile $^{(0,0)}V_{opt}$ along the bending angle θ computed for the two PESs are

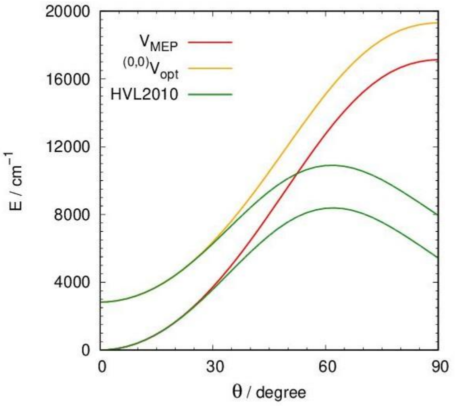

Figure 3. Minimum energy path V_{MEP} and effective bending potential $^{(0,0)}V_{opt}$ along the Jacobi angle θ computed for N_2H^+ using the PES of Ref. [8] (red and yellow) and the PES of Ref. [12] (green).

compared in Figure 3. The minimum energy paths are constructed by minimization of the potential energy with respect to the radial coordinates. The adiabatic (effective) bending profile is obtained by adding the zero-point energy of the stretching vibrations to the minimum energy path. Figure 3 clearly shows that the quartic force field of Ref. [12] provides a good description of the bending motion only for angles θ smaller than 30°.

CONCLUSION

The issues concerning the potential energy representations and numerically exact full-dimensional rovibrational calculations in combination with exact kinetic energy operators are not simply a technical matter: they are essential ingredients for achieving good, reliable results from high-level/high-accuracy *ab initio* points and for generating data to support/assist detailed spectroscopic studies. In connection with this, triatomic molecules are still important for examining the effect of the orientation of the axis system on the kinetic energy operator and tetratomic molecules for examining the effect of the out-of-plane motion in the internal molecular dynamics. Only full-dimensional rovibrational calculations are capable of providing the full correction ΔB_0 to the rotation constant B_0 in the ground vibrational state for the effects of zero-point motion in the molecule.

REFERENCES

[1] M. Mladenović, J. Chem. Phys., 2014, 141, 224304.
[2] M. Mladenović, J. Chem. Phys., 2000, 112, 1070-1081.
[3] M. Mladenović, Spectrochim. Acta, Part A, 2002, 58, 795–807.
[4] M. Mladenović, J. Phys. Chem. A, 2013, 117, 7224−7235.
[5] M. Mladenović, J. Chem. Phys., 2012, 137, 014306.
[6] X. Huang, R. C. Fortenberry, T. J. Lee, Astrophys. J. Lett. 2013, 768, L25.
[7] L. Dore, L. Bizzocchi, E. S. Wirström, C. Degli Esposti, F. Tamassia, S. B. Charnley, Astron. Astrophys., 2017, 604, A26.
[8] S. Schmatz, M. Mladenović, Ber. Bunsenges. Phys. Chemie 1997, 101, 372-386.
[9] M. Mladenović, J. Chem. Phys., 2017, 147, 114111.
[10] M. Mladenović, M. Lewerenz, Mol. Phys., 2018, 116, 3607-3620.
[11] M. Mladenović, E. Roueff, Astron. Astrophys. 2014, 566, A144.
[12] X. Huang, E. F. Valeev, T. J. Lee, J. Chem. Phys., 2010, 133, 244108.

STUDY OF NONCOVALENT INTERACTIONS USING CRYSTAL STRUCUTRE DATA AND QUANTUM CHEMICAL CALCULATIONS

M. R. Milovanović[1], J. M. Živković[1], D. B. Ninković[1], J. P. Blagojević Filipović[1], D. Z. Vojislavljević–Vasilev[1], I. S. Veljković[2], I. M. Stanković[2], D. P. Malenov[3], V. B. Medaković[3], D. Ž. Veljković[3], S. D. Zarić[3]

[1]Innovation center of the Faculty of Chemistry, Studentski trg 12-16, Belgrade, 11000, Serbia,
[2]Institute of Chemistry, Technology and Metallurgy, University of Belgrade, Njegoševa 12, 11000 Belgrade, Serbia,
[3]Faculty of Chemistry, University of Belgrade, Studentski trg 12-16, Belgrade, 11000, Serbia
(szaric@chem.bg.ac.rs)

ABSTRACT

The analysis of the crystal structures in the CSD was used to recognize and characterize new types of noncovalent interactions. It was also used to study already known noncovalent interactions. Based on the data from the CSD we can determine existence of the interactions, frequency of the interactions, and preferred geometries of the interactions in the crystal structures [1,2].

The quantum chemical calculations were performed to evaluate the energies of the interactions. For the preferred geometries in the crystal structures we can calculate the interaction energies. By calculating potential energy surfaces for the interactions, we can determine the most stable geometries, as well as stability of various geometries [1,2].

Using this methodology our group recognized stacking interactions of planar metal-chelate rings; stacking interactions with organic aromatic rings, and stacking interactions between two chelate rings. The calculated energies showed that the stacking of metal-chelate rings is stronger than stacking between two benzene molecules. Studies of interactions of coordinated ligands indicate stronger noncovalent interactions that interactions of noncoordinated molecules [2].

REFERENCES

[1] Ninković, D. B., Blagojević Filipović, J. P., Hall, M. B., Brothers, E. N., Zarić, S. D. (2020) *ACS Central Science*, **6**, 420

[2] Malenov, D. P., Zarić, S. D. (2020) *Cood. Chem. Rev.* **419**, 213338

FORMATION OF THE METHANE HALIDES FLUID-LIKE LAYERS AT AMBIENT CONDITIONS

I.I. Grinvald, R.V. Kapustin

Nizhny Novgorod State Technical University n.a. R.E. Alekseev
Minin str. 24, 603950 Nizhniy Novgorod, Russia
(grinwald@mts-nn.ru)

ABSTRACT

The work presents the IR-study of fluid-like methane halides (methyl iodide, carbon tetrachloride, chloroform, and methane dichloride) layers formation in the near-surface area at ambient conditions. It was shown that at vapors compression-expansion procedure in variable-thickness spectral cell, the phase state of matter, exhibiting both gas and liquid spectral properties appears. The reversible and continuous transition of gas-like and liquid-like shapes, not depending on thermodynamic characteristics of studied substances, was revealed.

INTRODUCTION

Fluids represent a unique phase state of matter generating under supercritical conditions and combining the properties of gas and liquid. It is conventional to divide fluids into gas-like and liquid-like states depending on which properties prevail in them, however, this definition is ambiguous due to the continuous nature of the transition between these two states.

Supercritical fluids have many applications as industrial solvents, largely due to their tunable density, and can be used as an environmentally friendly solvent for hazardous waste cleanup. However, the same properties that make fluids useful also make their generation quite difficult. Aside from the high pressures and temperatures required, fluids can be chemically active and corrode many components of experimental apparatus. Therefore, the formation of supercritical fluids is generally limited to the simplest compounds – water and carbon dioxide. FTIR studies of their behavior and the liquid-like to gas-like fluid transition are presented in a few of works to date. The spectral manifestations shown there are similar to FTIR observations of some organic liquids at ambient conditions. [1; 2]

In the present work, we set the aim to generate a fluid-like state of matter at ambient conditions and reveal it with FTIR methods by fixing a combination of gaseous and liquid properties and their transitions for methyl iodide, carbon tetrachloride, chloroform, and methane dichloride.

EXPERIMENTAL

To generate fluid-like layers, a variable thickness optical cell (VTC), shown in Figure 1, was used. At the first step, organic components were evaporated into the cell at atmospheric pressure and 295K during 20 – 70 hours. At the second step, the fluid-like state was formed by compressing of interwindow space in vapor-filled VTC. For the estimating of fluid-like layers, their IR bands were compared with the ones recorded in a 100-mm gas cell at 295K for gases and between optical windows for liquid state.

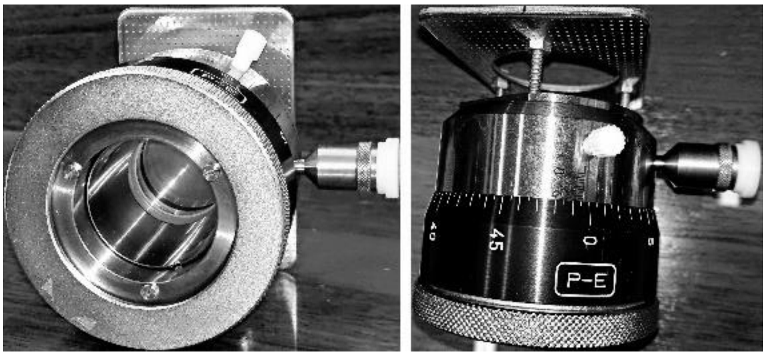

Figure 1. Spectral cell (VTC) used for generating the fluid-like layers.

IR-spectra were recorded by IR-Fourier spectrometer FSM 1202 (InfraSpec Co.) in 500-4000 cm^{-1} range with resolution 2 cm^{-1} and 60 scans. The VTC was manufactured by Perkin-Elmer Co. The purity of halides was not less than 99 perc as it was confirmed by chromato-mass spectrometry data obtained by GCMS - QP2010 Plus spectrometer (Shimadzu Co. Inc.).

RESULTS AND DISCUSSION

In the IR spectra of methyl iodide in the region of bending (H-C-H) vibrations, recorded at 6 mm thickness of VTC, the gas phase band at 1263 cm^{-1} (**B**, in the Fig. 2) and the liquid phase band at 1240 cm^{-1} (**C**, in the Fig. 2) were observed. Besides, a broad band with a rotational structure at 1426 cm^{-1}, assigning to gas phase, is revealed.

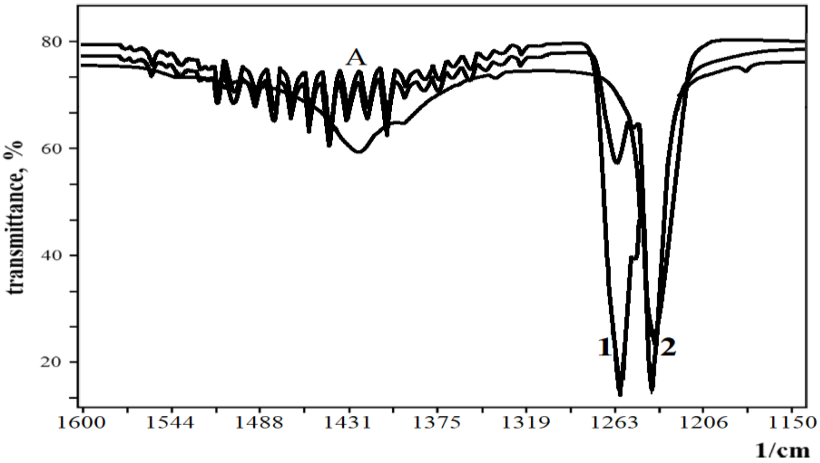

Figure 2. Fragment of methyl iodide spectra in H-C-H bending region.

The spectrum 2, recorded at 1 mm distance between the optical windows, demonstrates the presence of both gaseous and liquid phase components. At the distance 0.5 mm, the relative intensity of the gas state band decreases, and the intensity of the liquid state band grows (spectrum 3, Fig. 2). Since the IR spectra of gases cannot be observed at such distances, the mentioned bands can be assigned to the generated fluid-like layer.

The spectra of carbon tetrachloride (Fig. 3) show similar changes under the vapor compression procedure. The gas phase bands (**A**, **B**) at 795 and 779 cm^{-1} in spectrum 1 (at the 6 mm optical distance) are observed. In spectrum 2 the gas band **A** and liquid bands **C**, **D** at 784 and 761 cm^{-1} are observed. These data indicate that the formed “gas-liquid” state of carbon tetrachloride can also be determined as a fluid-like layer.

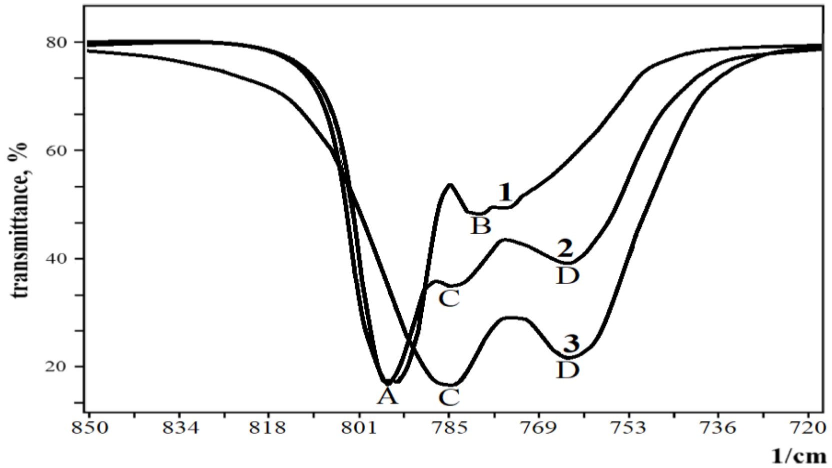

Figure 3. Fragment of carbon tetrachloride spectra in C-Cl stretching region.

In the spectra of methane dichloride (Fig. 4) the gas phase bands (bands **A**, **B,** spectrum 1) at 764 and 750 cm^{-1} at the optical distance 6 mm are revealed. At 1 mm thickness of VTC in the spectrum (Fig. 2, spectrum 2) both gas bands (**A**, **B**) and liquid band **C** at 738 cm^{-1} were observed. Under reduction of interwindow distance to 0.5 mm, the gas phase bands disappear, and only the liquid phase band remains. This transition is reversible: at the optical distance expansion to 6 mm, the gas phase bands appear again while liquid phase bands are absent. Since similar changes cannot be caused at these conditions by condensation or evaporation of the substance only, the presented data reasonably justify the formation of a layer with fluid-like properties.

The spectra of chloroform and chloroform-d (Fig. 5), manifesting similar behavior under the vapor compression procedure, at the same time have some differences.

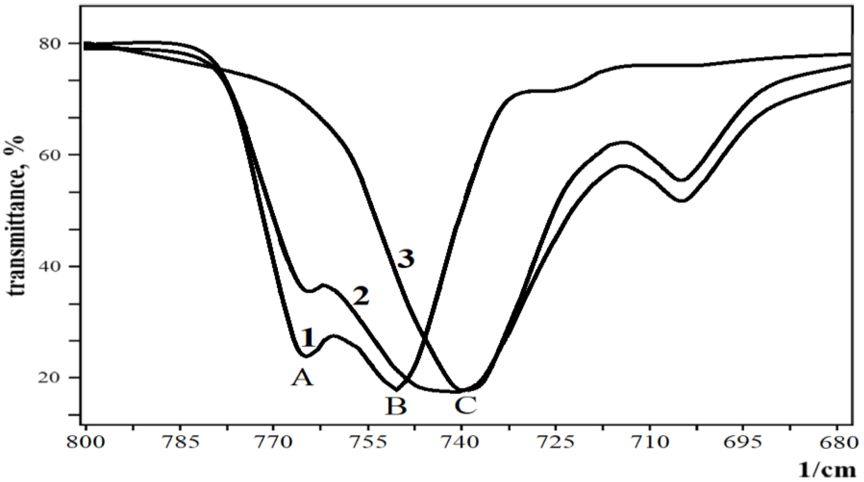

Figure 4. Fragment of methane dichloride spectra in C-Cl stretching region.

The gas and liquid bands of fluid-lake layer locate much closer to each other than in spectra of other halides. Two overlapped components of liquid band, which are well-visible in chloroform-d spectrum, indicate on the symmetry breaking of (CCl_3)-group. This can be explained by the formation of intermolecular hydrogen bond in the fluid-like system.

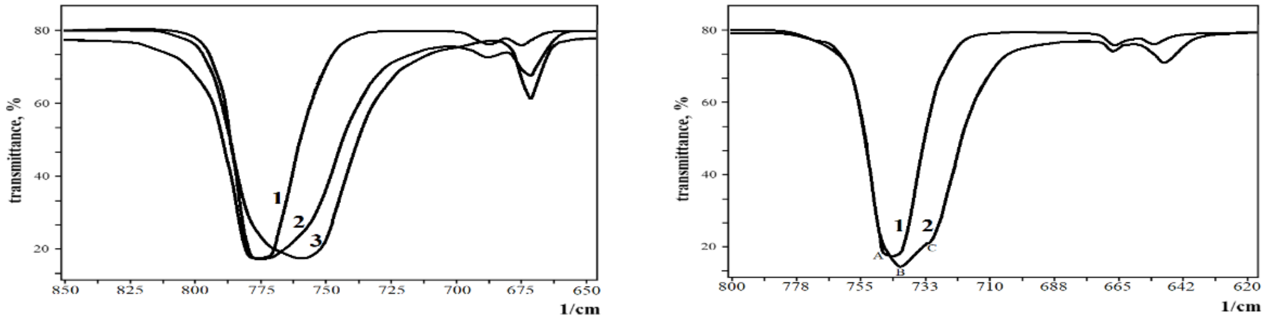

Figure 5. The fragment of chloroform and chloroform-d spectra in C-Cl stretching region.

CONCLUSION

As the reversible transition from gaseous to liquid properties occurs very quickly and does not depend on the thermodynamic characteristics of the substance, this phenomenon cannot be assigned to the process of evaporation-condensation only. Therefore, these systems, having the duality of phase state properties, were defined as fluid-like state. Since in the space of VTC ambient conditions remain, the solid surface should play a crucial role in fluid-like state arising mechanism.

REFERENCES

[1] E.S. Alekseev, A.Yu. Alentiev et al., Russ. Chem. Rev. 89 (2020) 1337
[2] N. J. Hestand, S.E.Strong et al., J. Chem. Phys. 150 (2019) 054505

STRUCTURAL TRANSFORMATIONS OF DICHLORO-ALKANES AT THE LIQUID-TO-GAS TRANSITION

I.I. Grinvald, R.V. Kapustin

Nizhny Novgorod State Technical University n.a. R.E. Alekseev
Minin str. 24, 603950 Nizhniy Novgorod, Russia
(grinwald@mts-nn.ru)

ABSTRACT

The work discusses the data obtained by IR study referring to the dual gas-liquid properties of thin layers forming in the cell near-surface (optical windows) area for dichloromethane, 1,2-dichloroethane and 1,2-dichloropropane. These layers represent the combination of gas-like and liquid-like states, which can be considered as the intermediate stage of the phase transition from gas to liquid. It was shown that the molecular interactions in dual gas-liquid systems of chloroalkanes are changing due to the restructuring of Cl···H hydrogen bonding.

INTRODUCTION

The problem of gas-liquid systems formation, considering different properties of substances, was studied by several methods from thermodynamic and molecular light scattering to quantum-chemical and dynamic simulation, The IR spectroscopy was used for these investigations as well. Some recent works devoted to the interactions in gas and liquid phases of organic species can be quoted [1].

It was revealed that at the formation of liquid phase a non-valence intermolecular bonding appears, which leads to supramolecular systems with shifted hydrogen or halogen atoms. However, the role of this transformations in the mechanism of phase-to-phase transitions at ambient conditions was not considered.

An attempt to use this phenomenon to interpret the processes occurring in the interfacial space during evaporation and condensation led to the idea of generating thin molecular layers in an optical cell and detecting their features by IR spectroscopy methods. As part of this study, results for dichloromethane, 1,2-dichloroethane and 1,2-dichloropropane are discussed here. The main reason for this choice is the assumption that the stretching vibrations of C-Cl in these systems can clearly demonstrate the existence of intermolecular bonds and its changing in the gas and liquid phases [2].

EXPERIMENTAL

The following procedure was used to create a thin layer in the spectral cell during the evaporation of organic liquids. The sample was placed under a Teflon gasket (1 mm thick) on a KBr optical window so that it did not fall into the optical beam. Then the gasket is closed with another window, and both windows are placed in the holder for spectra recording. Before spectral measurement, the sample was left between the windows at ambient conditions for 5-30 minutes, depending on the type of chloroalkanes.

IR-spectra were recorded for liquid sample between KBr windows, and for gas phase – in 100 mm gas cell, by IR-Fourier spectrometer FSM 1202 (InfraSpec Co.) in 500-4000 cm^{-1} range with 2 cm^{-1} resolution and 60 scans. The purity of dichloroalkanes was not less than 99 perc as it was confirmed by chromato-mass spectrometry data obtained by GCMS - QP2010 Plus spectrometer (Shimadzu Co. Inc.).

RESULTS AND DISCUSSION

Dichloromethane. In the IR spectra of liquid dichloromethane in the region of C-Cl stretching vibrations the bands at 740 and 706 cm^{-1} (labeled as **A**, **B** in the spectrum 1, Fig. 1) were observed. These bands can be assigned, taking the conception that they assign to two types of intermolecular binding. The first of them is attributed to (Cl···H) hydrogen bonds in chains having (H-C-Cl) fragments and another one to (Cl···H) bonds in chain with (Cl-C-Cl) fragments. The second binding option should be stronger, but less likely to form. Consequently, the intensity of band **B** is considerably lower.

In gas phase spectrum instead of bands **A, B** the two-components band (components at 763 and 750 cm^{-1}) is revealed (spectrum 2, Fig.1). Therefore, it can be assumed that the bands of C-Cl bond stretching in molecules bound in the chain, transform into a pair of isomers C-Cl bond stretching, the first with (Cl-C-Cl) fragment and the second with two (H-C-Cl) structural elements attributed to unbound shape of dichloromethane in the gas phase (Fig 1, bands **C, D**).

When a liquid sample was evaporated into the space between the optical windows at ambient conditions, complex bands containing both gas non-resolved (**C, D**) and liquid (**A**) bands were observed, while the band **B** was absent (spectrum 3, Fig. 1). Since a real gas spectrum cannot be obtained in such a thin cell, it can be assumed that the spectrum of the thin layer demonstrates the appearance of intermediate molecular shape arising at the liquid-to-gas phase transition.

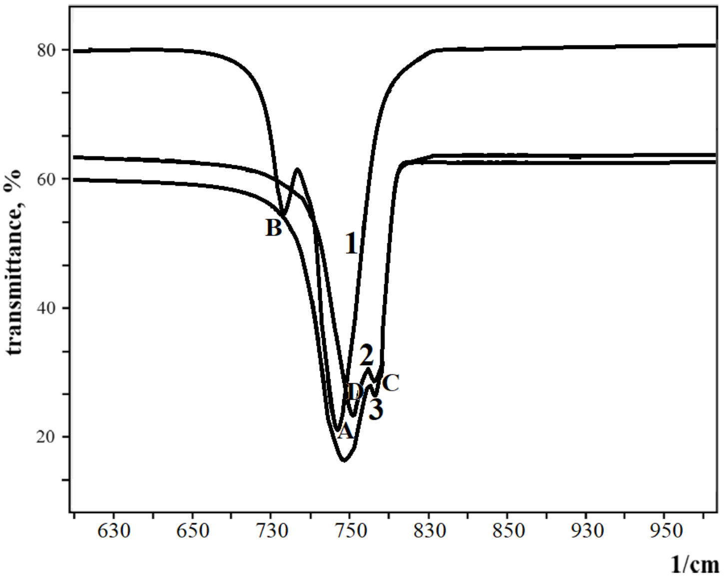

Figure 1. Fragment of dichloromethane IR spectra in C-Cl stretching region.

1,2-dicloroethane. The spectra of 1,2-dichloroethane in C-Cl stretching region (Fig. 2) exhibit two kinds of intermolecular binding as well: the shape with intermolecular (Cl···H) bonds of *sin*-isomer (bands **A, B** at 766 and 655 cm^{-1} in spectrum 1, Fig.2) and the shape with (Cl···H) bond of *anti*-isomer (band **C** at 711 cm^{-1}, spectrum 1, Fig.2)

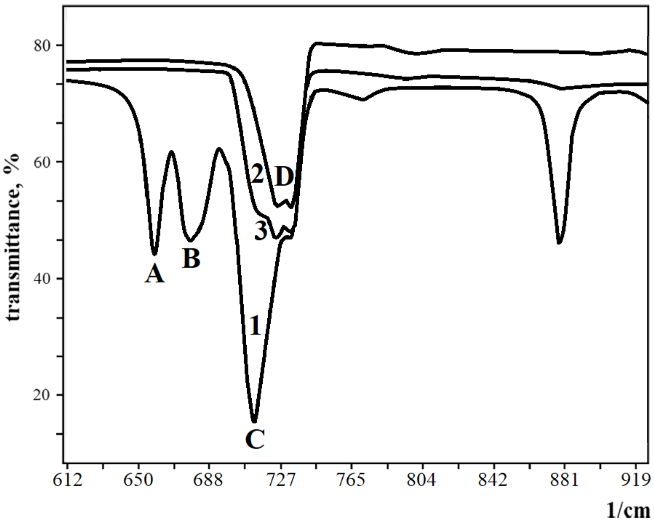

Figure 2. Fragment of dichloroethane spectra in C-Cl stretching region.

In the gas phase spectrum, band **D** has two components, at 731 and 724 cm^{-1} (spectrum 2, Fig. 2). These components can be assigned to the staggered and eclipsed conformers, which have a low barrier of transformation in the gas phase. The spectrum of the thin layer (spectrum 3, Fig.2) has the combination of gas and liquid phase bands. However, band **C** here is assigned to *anti*-isomer only, and bands **A, B** are absent at all. It can be assumed that such a molecular form is a transitional one at the transformation of a liquid into a gas within the system.

1,2-dicloropropane. In the spectra of liquid 1,2-dichloropropane (spectrum 1, Fig. 3) two pair of bands are shown – one at 742, 745 cm^{-1} (spectrum 1, pair **A**) and another one – at 670, 620 cm^{-1} (spectrum 1, pair **B**). Such a complication of the spectrum for the considered dichloroalkane can be caused by the appearance of two structures with different spatial arrangement of CH_3-group in each chlorine conformer. In the thin layer spectrum recorded after 15 minutes of evaporation procedure, two types of bands were observed–one with liquid components at 685 cm^{-1} (Fig.3, spectrum 2, band **C)** and another one with two gas components – at 744, 757 cm^{-1} (Fig.3, spectrum 2, components **D**). After the 30-minuts of evaporation procedure instead of double-component gas band **D** the single band at 747 cm^{-1} remains.

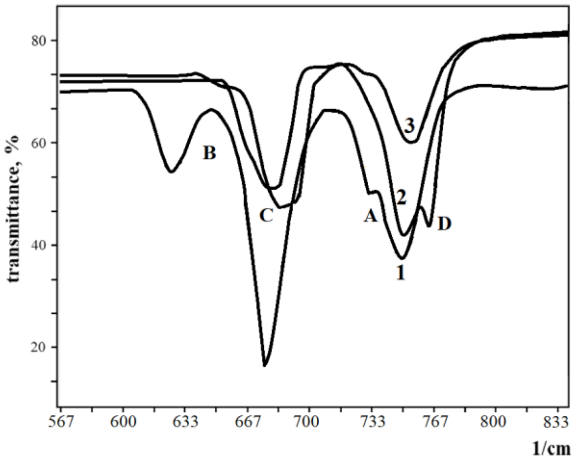

Figure 3. Fragment of 1,2-dichloropropane spectra in C-Cl stretching region.

CONCLUSION

The presented data show that during the phase liquid-to-gas transition the thin layer having combination of both gas and liquid phase properties, unambiguous manifesting in their IR spectra, arises. Therefore, it can be assumed that the detected dual-phase state is a transitional substance shape formed when a liquid is converted into a gas at ambient conditions. In this state molecular binding is weaker than in the initial liquid bulk, and gas is also present inside it.

REFERENCES

[1] I. I. Grinvald, I. Yu. Kalagaev, et al, Rus. J. Phys. Chem. A 93 (2019) 69
[2] I. Grinvald, I. Kalagaev, et al, Struct. Chem. 30 (2019) 1659

A THEORETICAL CALCULATION OF THE RAMAN SPECTRUM OF INDIGO CARMINE

J. Senćanski[1], J. Maksimović[2] and M. Pagnacco[3]

[1]University of Belgrade, Institute of General and Physical Chemistry,
Studentski trg 12-15, 11000 Belgrade, Serbia.(sencanskijelena@yahoo.com)
[2]University of Belgrade, Faculty of Physical Chemistry, Studentski trg 12-15, 11000 Belgrade, Serbia.
[3]University of Belgrade, Institute of Chemistry, Technology and Metallurgy, Njegoševa 12,11000 Belgrade, Serbia.

ABSTRACT

This paper presents the B97D functional added to the Hamiltonian in order to calculate Raman spectrum of indigo carmine. The experimental spectrum of the compound was recorded from indigo carmine, a commercial dye sold for use in food processing when used in a mixture with D-glucose. The Raman spectrum was calculated using the B97D/cc-pVTZ level of theory. The results obtained show lower deviation from 1000 cm^{-1} to 2000 cm^{-1} for the main bands compared with the data found in the literature.

INTRODUCTION

Synthetic dyes are commonly used across consumable goods. Indigo carmine (indigotine, E132) is a blue dye that is used in the food, pharmaceutical, medical and cosmetic industries [1]. Indigo carmine is an organic compound that has the chemical formula $C_{16}H_8N_2Na_2O_8S_2$[2].

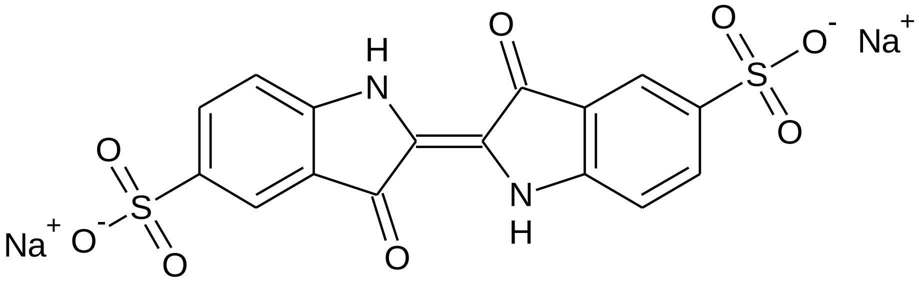

Figure 1. The structural formula of indigo carmine[2]

To calculate the Raman spectrum, Volkov et al [3] performed their calculation using a 6-31++g(d,p) basis set and the restricted B3LYP functional. Peica et al [2] optimized indigo carmine by BPW91/6311++G**, B3PW91/LANDL2DZ, B3LYP/6311++G** and B3LYP/LANL2DZ.

The aim of the results presented here was to examine a method of calculation that had not already been used in the literature and to compare the results obtained by a theoretical calculation with an experimental one.

METHODS

An experimental spectrum of the compound was recorded for indigo carmine (E132), a commercial dye sold for use in food production as a dye in a mixture with D-glucose. The spectrum was recorded by a Thermo Scientific DXR Raman Microscope. The recording of the spectrum is done at λ=532 nm, laser strength 8mW, magnification 10x, and 2.1 µm laser spot size.

The geometry of the indigo carmine was optimized using the B97D/cc-pVTZ level of theory. After optimizing the geometry, the Raman spectrum was calculated to be the same level of theory. The calculations were carried out in *Gaussian* 09, Revision D.01[4].

RESULTS AND DISCUSSION

In order to simulate the Raman spectrum, firstly, geometrical optimization of the molecule was carried out. The optimized structure of the indigo carmine molecule is presented in **Fig. 2.**

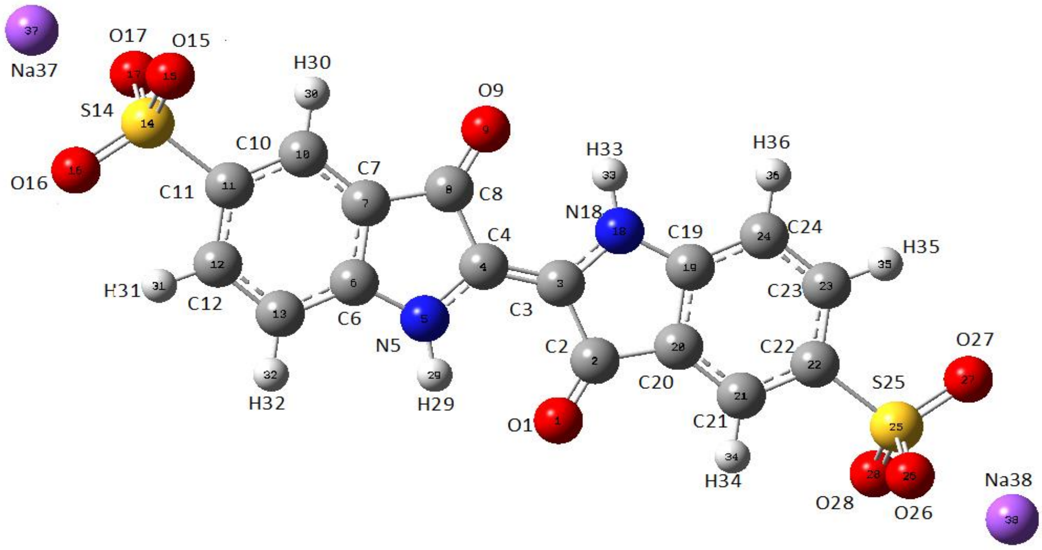

Figure 2. The optimized geometry of Indigo carmine

Table 1. The theoretical and experimental values of the vibration bands [2]

This study		Literature [2]				
	B97D		B3PW91		B3LYP	
experimental	cc-pVTZ	experimental	LANL2DZ	6-311G++G**	LANL2DZ	6-311++G**
1039	**1051**	1036	1022	1074	1023	1068
1136	1155	1130	1164	1152	1157	1139
1248	1234	1240	1239	1243	1265	1244
1293	**1291**	1290	1288	1280	1288	1296
1347	**1347**	1344	1357	1345	1343	1352
1473	1457	1472	1472	1486	1482	1482
1577	**1586**	1576	1511	1509	1621	1616
1625	**1623**	1623	1640	1632	1635	1634
1698	**1702**	1698	1687	1701	1669	1681

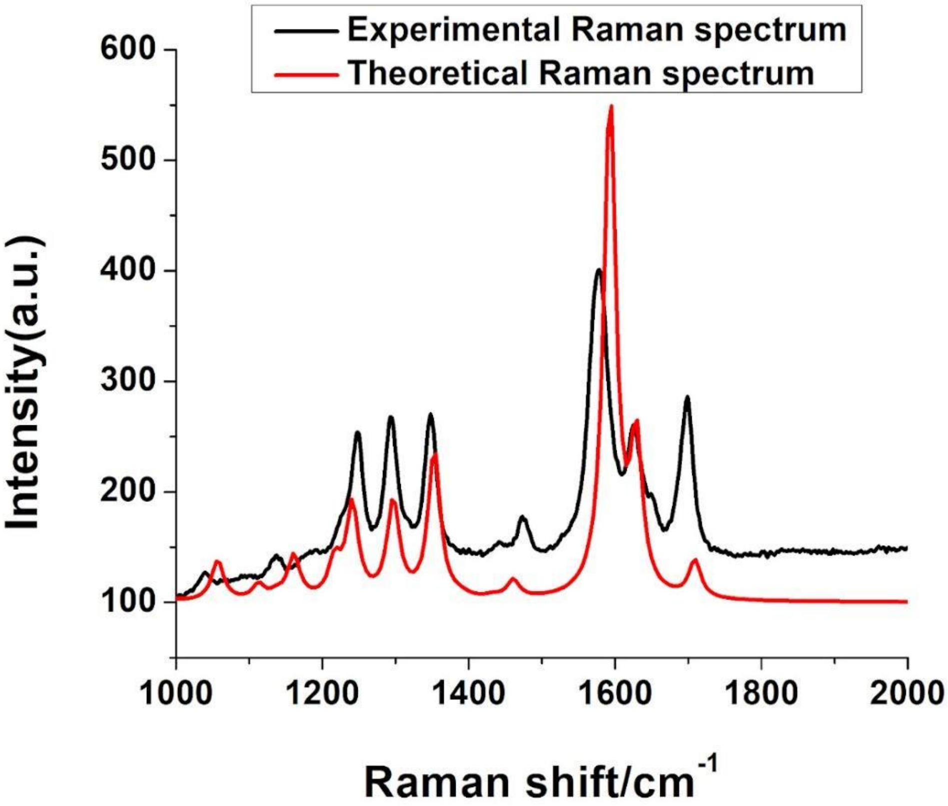

Figure 3. The experimental and calculated spectra

Fig. 3. lists the calculated and experimental spectra, whose good agreement is evident. The bands that have a lower or the same deviation compared to the data found in literature are marked in bold. The results obtained in terms of a lower deviation compared to the data in the literature were anticipated due to the fact that a higher basis set is taken to calculate the spectrum compared to the reference [2].

CONCLUSION

The data obtained for the simulated Raman spectrum of the indigo carmine indicates good agreement with the experimental spectrum as well as better agreement compared to the data found in literature. Therefore, the use of the B97D functional and the correlation consistent basis set may be applied to achieve a satisfactorily precise calculation of the vibrational spectra of indigo carmine.

Acknowledgement

This work was partially supported by the Ministry of Education, Science and Technological Development of the Republic of Serbia,no: 451-03-9/2021-14/200026, 451-03-9/2021-14/200051, 451-03-9/2021-14/200146.

REFERENCES

[1] EFSA Panel on Food additives and Nutrient Sources added to Food (ANS), Scientific Opinion on the re-evaluation of Indigo Carmine (E 132) as a food additive, EFSA Journal 12, 2014, 12(7), 3768.

[2] N. Peica, W. Kiefer, Journal of Raman Spectroscopy: An International Journal for Original Work in all Aspects of Raman Spectroscopy, Including Higher Order Processes, and also Brillouin and Rayleigh Scattering, 2008, 39, 47-60.
[3] V. V. Volkov, R. Chelli, R. Righini, C. C. Perry, Dyes and Pigments 2020, 172, 107761.
[4] M. J. Frisch, et al, *Gaussian* 09, Revision D.01, Gaussian Inc., Wallingford CT, 2009.

LIBS HYDROGEN DETECTION: TEA CO_2 LASER - POLYMETHYL METHACRYLATE INTERACTION

M. Trtica [1], M. Kuzmanovic [2], J. Savovic [1] and D. Rankovic [2]

[1] University of Belgrade, VINCA Institute of Nuclear Sciences - National Institute of the Republic of Serbia, Mike Petrovica Alasa 12-14, 11001 Belgrade, Serbia. (etrtica@vin.bg.ac.rs)
[2] Faculty of Physical Chemistry, University of Belgrade, Studentski trg 12-16, 11158 Belgrade, 118, PAC 105305, Serbia

ABSTRACT

Laser-Induced Breakdown Spectroscopy (LIBS) was applied to detect hydrogen in solid polymer - polymethyl methacrylate (PMMA). A pulsed Transversely Atmospheric Excited (TEA) CO_2 laser was used as the excitation source. Using a low laser intensity of ∼58 MW/cm^2 and fluence of ∼16.5 J/cm^2, the plasma above the PMMA was studied in a vacuum ambiance (0.01 mbar). Under the applied experimental conditions, the plasma could be induced only in the presence of a metal sub-target, after a cavity in a PMMA was created by multipulse laser ablation. The spectrum of the plasma generated on a PMMA-metal sub-target system was dominated by the emission of intensive hydrogen, carbon, and oxygen atomic lines and molecular bands of C_2 and CN. The characteristics of laser-induced plasma were analyzed by evaluating the plasma parameters, such as the electron number density and temperature.

INTRODUCTION

Hydrogen detection and quantification in solids are of great importance in contemporary science and technology applications. Of particular importance is the detection of hydrogen in nuclear fission and fusion technology. Focusung only on the fusion area the significance can be twofold: (i) Consideration of the laser-polymer interaction is essential from the aspect of the fuel capsule design [1]. Namely, in laser-based direct-drive inertial confinement fusion, the D-T fuel is placed inside a capsule where the outer layer is typically the plastic forming the ablator and, (ii) the PMMA as a hydrogen-bearing material can be used to test and optimize the LIBS apparatus for hydrogen detection before analyzing an authentic reactor plasma facing material that has been exposed to H-isotope atoms fluxes, e.g., tungsten with incorporated hydrogen [2].

This paper describes the interaction of a pulsed IR laser with a polymethyl methacrylate (PMMA - $(C_5O_2H_8)_n$) target, focused on the detection of hydrogen by the TEA CO_2 laser-based Laser-Induced Breakdown Spectroscopy. The PMMA is a promising polymer for use in various fields such as electronics and biomedicine, and also in nuclear technology [3].

EXPERIMENTAL

The LIBS set-up used in this study is described in detail in Ref. [4,5]. The experimental apparatus, Figure 1, includes a pulsed laser, focusing and collecting optics, and a spectrometer coupled with a CCD detector. In order to provide conditions for the generation of plasma, a PMMA sample was placed on a steel sub-target.

A pulsed TEA CO_2 laser is a commercial version of a laser constructed at the VINCA Institute of Nuclear Sciences, having a pulse energy of up to 170 mJ at a wavelength of 10.6 µm. The typical laser/optical pulse form is shown in Fig. 1(a). A sample, PMMA-steel sub-target system, was placed in a chamber evacuated to 0.01 mbar. The laser beam was transmitted through a NaCl window of the chamber and focused on the PMMA surface with a ZnSe lens (f=13.0 cm). Optical emission from the plasma was viewed in a direction parallel to the sample surface. The image of a plasma plume was projected along a horizontal axis on the entrance slit of a spectrograph using a lens (f=9.5 cm). The spectrograph was coupled with a CCD detection system (Apogee Alta F1007 camera), and spectra were recorded using a time-integrated space-resolved method [4,5]. The typical integration time was 60 seconds.

RESULTS AND DISCUSSION

Initially, CO_2 laser-PMMA-steel sub-target interaction was accompanied by absorption of laser radiation by PMMA, resulting in its melting and vaporization without inducing the plasma. Repeated laser shots hitting the same spot on the PMMA surface created a channel/cavity through PMMA. For PMMA thickness of 5 mm and applied laser energy of 160 mJ, the laser radiation reached the steel sub-target surface after accumulation of 150 laser pulses. At that point, plasma was induced on the steel sub-target, and a plasma plume appeared over the PMMA surface. A series of complex phenomena were involved in plasma creation and propagation. A simplified description includes two main processes: (i) absorption of laser radiation by steel, causing its ablation, vaporization, and plasma generation; (ii) propagation of the plasma through previously created PMMA channel causing PMMA heating, vaporization, and decomposition.

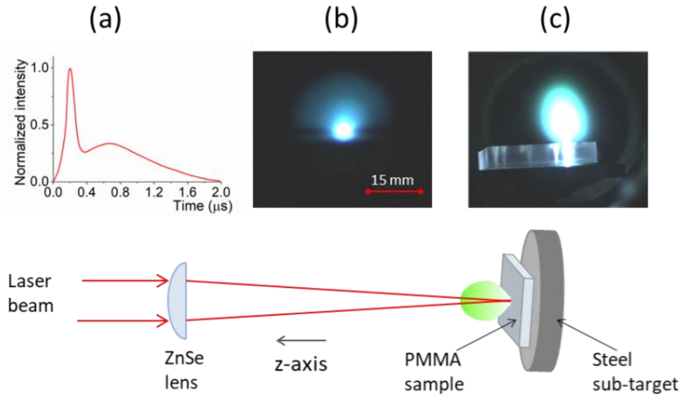

Figure 1. Schematic illustration of PMMA irradiation by CO_2 laser. (a) CO_2 laser pulse shape; (b) and (c) View of plasma created over the steel sub-target and PMMA-steel sub-target system, respectively. Experimental conditions: vacuum ambience, 0.01 mbar; laser output pulse energy 165 mJ (intensity ~58 MW/cm^2, fluence ~16.5 J/cm^2).

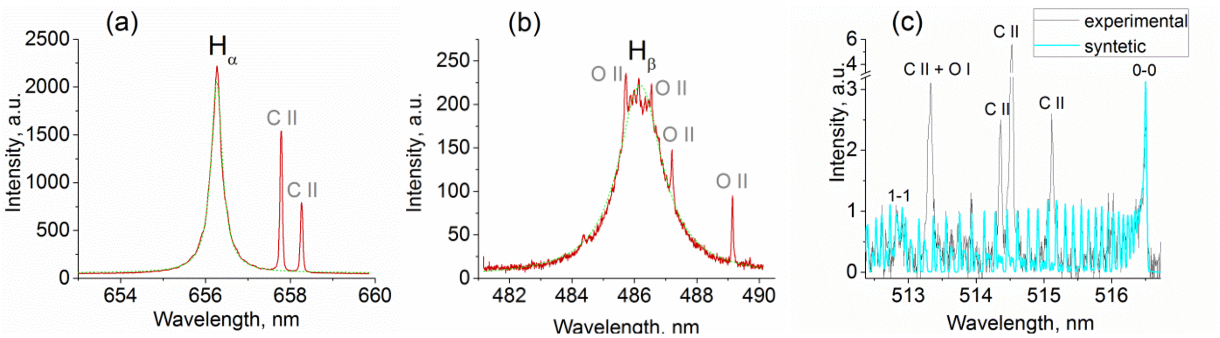

The plasma emission consisted of the spectral lines of the PMMA constitutive elements

Figure 2. LIBS spectra recorded 2 mm above the PMMA-steel sub-target system: (a) H_α 656.27 nm line; (b) H_β 486.13 nm line, and (c) C_2 Swan-band emission. Experimental conditions: vacuum ambiance, 0.01 mbar; laser output pulse energy 165 mJ.

(hydrogen, carbon, and oxygen), Fig. 2 (a,b), and a band spectra of small molecular species created in the plasma, such as C_2 (Fig. 2(c)), and CN. For all atomic species, the highest emission intensity was recorded in the vicinity of the PMMA surface, at a distance 2 mm above the sample surface.

Estimation of the plasma parameters, electron number density (N_e), and ionization temperature (T) was done to characterize the excitation conditions in the laser-induced plasma. The electron density was inferred from the Stark broadened H_α (656.27 nm) and $H_\square$ (486.13 nm) linewidths [6]. Estimated from the spectra recorded from a plasma slice 2 mm above the PMMA surface, *N*e was 1.6 x 10^{16} cm^{-3}. The FWHM of both hydrogen lines decreased with increasing distance from the PMMA surface. For example, at a distance of 7 mm, the estimated N_e was 4.9 x 10^{15} cm^{-3}.

The ionization temperature was determined from the measured intensity ratio of carbon ionic and atomic line pair (C II 250.9 nm/C I 247.9 nm) and previously obtained *N*e. Depending on the distance from the PMMA surface, the temperature varied from 16500 K (at 2 mm) to 13600 K (at 7 mm).

Apart from atomic lines of H, C, and O, intensive molecular emission could be observed in the plasma. Figure 2 (c) shows LIBS spectra of the C_2 Swan band, recorded 0.5 mm above the PMMA surface. By increasing the air pressure to 0.1 mbar, a CN violet system could also be registered. The maximum CN emission intensity was located 2 mm above the PMMA surface. Formation of the CN molecules required recombination of atomic carbon or the C_2 molecules from the plasma with the atmospheric nitrogen. The rotational temperature of 4500 K was estimated by comparison of the experimental and simulated C_2 emission spectra.

CONCLUSION

In this work, TEA CO_2 laser-based LIBS was successfully applied to detect hydrogen from a solid polymer – PMMA. The low laser intensity of ∼58 MW/cm^2 and fluence of ∼16.5 J/cm^2 could not induce plasma on the PMMA under vacuum conditions. The plasma above the sample was created only when a sub-target made of steel was employed. The possible mechanism of plasma creation in a PMMA-steel sub-target system was proposed. Apart from hydrogen, the species like C, O, C_2 and CN were registered in the emission spectra.

Furthermore, the electron number density and the ionic, vibrational, and rotational temperatures were evaluated to characterize the laser-induced plasma. Depending on the observation distance, estimated N_e was in the range 1.6 x 10^{16} cm^{-3} to 4.9 x 10^{15} cm^{-3}, at a distance of 2 mm, and 7 mm above the sample surface, respectively. The corresponding ionization temperature was 16500 K (2 mm) and 13600 K (7 mm). The rotational temperature of 4500 K was estimated by comparing the experimental and synthetic C_2 Swan bands.

Acknowledgment

This work was partially supported by: (i) International Atomic Energy Agency (IAEA), through contract, “Contemporary and New IF Structural-First Wall Materials: Conditions of High Thermal and Electromagnetic Fluxes“, Contract no. 24076, and (ii) The Ministry of Education, Science and Technological Development of the Republic of Serbia through Contract No. 451-03-9/2021-14/200017.

REFERENCES

[1] G. McCracken, P. Stott, Inertial-Confinement Fusion, in: Fusion, Elsevier, 2013: pp. 82–83.

[2] N. Moral, R.S. Hontoria, J. Alvarez, D. Garoz, M. Perlado, HiPER Fellows Meeting, Bordeaux, 3rd Feb. 2012. Book of abstracts, p. 10/37.

[3] International Atomic Energy Agency - Contract 24076, “Contemporary and New IF Structural-First Wall Materials: Conditions of High Thermal and Electromagnetic Fluxes“, 2020-2024.

[4] M. Momcilovic, M. Kuzmanovic, D. Rankovic, J. Ciganovic, M. Stoiljkovic, J. Savovic, M. Trtica, Applied Spectroscopy, 2015, **69**, 419-429.
[5] M. Kuzmanovic, D. Rankovic, M. Trtica, J. Ciganovic, J. Petrovic, J. Savovic, Spectrochimica Acta Part B, 2019, **157**, 37–46.
[6] N. Konjević, M. Ivković, N. Sakan, Spectrochimica Acta Part B, 2012, **176**, 16–26.

LASER-INDUCED BREAKDOWN SPECTROSCOPY STUDY OF ARCHEOLOGICAL GLASS SAMPLES

A. Šajić[1], M. Kuzmanović[1], D. Ranković[1], I. Stojić[3], M. Stoiljković[2] and J. Savović[2]

[1] *University of Belgrade, Faculty of Physical Chemistry, Strudentski Trg 12-16, 11000 Belgrade, Serbia.*
[2] *University of Belgrade, INN Vinca, Mike Petrovića Alasa 12-14, 11001 Belgrade, Serbia. (lelas@vinca.rs)*
[3] *University of Belgrade, Institute of History, Knez Mihailova 36/II, 11000 Belgrade, Serbia.*

ABSTRACT

Two unclassified glass samples of medieval origin found in Belgrade were examined by the laser-induced plasma spectroscopy (LIBS) technique. Measurements were performed with a LIBS system based on a compact TEA CO_2 laser with low pulse energy (E <170 mJ). The threshold energy required to induce plasma on a glass sample was 80 mJ per pulse. Depending on the sample, spectral lines of Si, Al, Ca, Fe, Ti, Mg, Mn, Sr, Cu, K, Ba, Na, and Ni were detected. Detection limits (LODs) were also estimated for several elements: Ni (18 ppm), Cu (2.5 ppm), Ti (25 ppm), Mn (32 ppm), and K (205 ppm). The plasma diagnostics was performed to determine plasma temperature and electron concentration. The excitation temperature of 8700 K was evaluated using a Boltzmann plot, constructed from the measured relative integral intensities of iron spectral lines. The electron number density, determined using the intensity ratio of Ti ionic and atomic lines, was $2\cdot10^{17}$ cm^{-3}.

INTRODUCTION

Glass is a material that is unsuitable for the analysis by standard analytical techniques because the sample preparation of aluminosilicate glass matrix is complex. Moreover, glass as a sample is not convenient for X-ray fluorescence spectrometry (XRF) either, because essential elements that make up the glass are light elements that cannot be accurately determined using this method. On the other hand, Laser-Induced Breakdown Spectroscopy (LIBS) has characteristics that make it a suitable technique for the elemental analysis of glass [1]. Most elements of the periodic table, usually without the need for sample preparation, could be analyzed by LIBS.

The commonly used laser as a radiation source in LIBS is Nd:YAG laser. However, due to the high transparency of Nd:YAG laser radiation in the visible spectral region, it is hard to induce plasma on a glass sample. In addition, irradiation by high-energy laser pulses very often produces cracks in the sample. The mid-infrared lasers are more convenient for glass analysis because laser radiation is well absorbed, and LIBS plasma is easily created. This paper aims to demonstrate the analytical potential of LIBS for the chemical analysis of glass. For that purpose, two fragments of archaeological glass were used as samples. The first was a fragment of a bottom of a vessel made of dark green glass (Figure 1. a), the other was a fragment of a more delicate vessel in the shape of a vase made of opaque, pearly glass (Figure 1. b).

EXPERIMENTAL

Experiments were conducted using a setup based on the Transversely Excited Atmospheric pressure (TEA) CO_2 laser. It is a small, compact, laboratory-made laser. A working gas mixture in the laser chamber was $CO_2/N_2/He$ in the volume ratio of 2:2:9. The energy of the laser pulse is up to 160 mJ. The laser emits radiation of 10.6 μm in the form of short pulses. The pulse repetition frequency is usually 1-2 Hz. The laser pulse of a TEA CO_2 laser consists of two parts, the initial peak and the tail. The initial peak has a full width at half maximum (FWHM) of 100 ns and contains about 35% of the total radiated laser energy. The rest of about 65% is contained in the pulse tail, whose duration is over 2 µs. The initial peak causes ablation of the target and initiation of plasma, while the pulse tail additionally and prolonged heats the plasma. These facts are responsible for the favorable properties of TEA CO_2 laser-induced plasma excitation conditions [2,3].

The laser beam was focused by a ZnSe lens of 125 mm focal length, while achromatic lenses were used to projected plasma optical emission on the entrance slit of a Carl Zeiss PGS-2 spectrometer. The spectrometer was equipped with a diffraction grating with 631 lines/mm, blazed at 290 nm. The U2C-16H11850 CCD camera (SOL Instruments.) with 2048 × 64 chip (pixel size 14 × 14 µm) was used as a detection system. The spectral range of the camera is 200–1100 nm, with maximum spectral sensitivity at 600 nm. The target was set on the X-Y-Z translation stage and moved between two laser pulses to ensure that each laser pulse interacts with a new surface area. In this way, a stable plasma was produced. The camera was synchronized with the laser pulse, and the signal detection time was 10 ms.

Measurements were performed mainly using a laser pulse energy of 140 mJ, with the laser beam focused on the target. The radiation was detected from a plasma slice 1 mm above the target surface. Each measurement represents the mean value of at least ten consecutive individual spectra, whereby the spectra that deviated significantly in intensity from the mean value were discarded, after which the spectra were averaged again.

RESULTS AND DISCUSSION

Figure 1. c shows a part of the spectrum rich in narrow spectral lines of single-charged titanium ions. The lines of Mn, Cu, and Ni are also seen in the spectrum, together with spectral lines of the atmospheric air constituents (nitrogen and oxygen). The N II and O II lines emission originates from the early phases of plasma evolution, characterized by high temperature and electron number density. Because of that, these lines and very intense and broad. By carefully optimizing the laser focus, the observed plasma area, and delaying emission signal detection relative to the plasma generation, the emission of N and O lines can be eliminated. In this way, spectral lines of sample elements could be obtained with an even better signal-to-noise ratio.

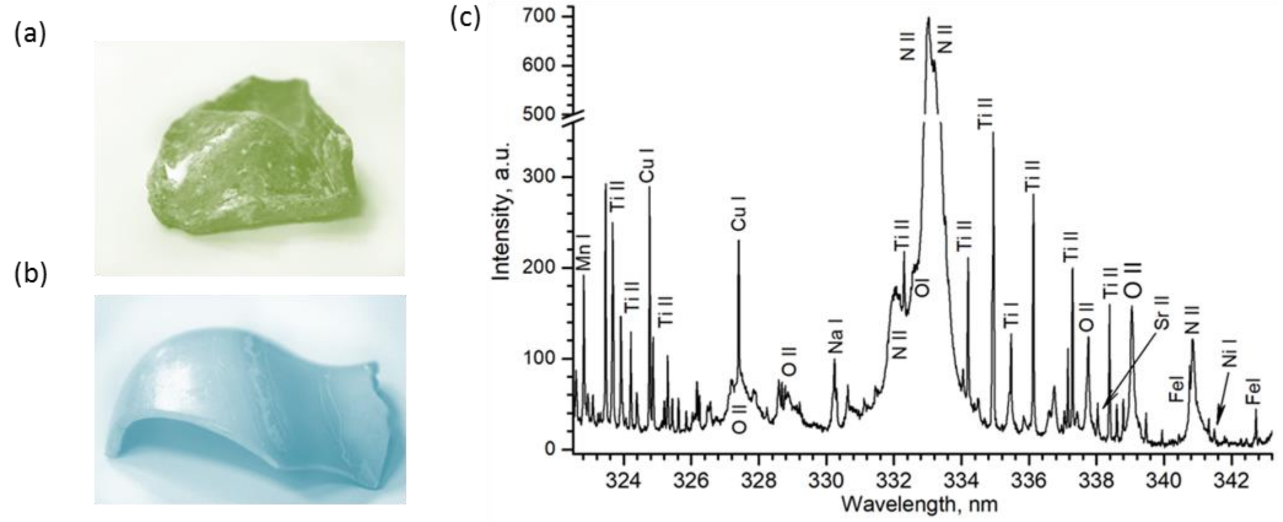

Figure 1. a) A green glass sample (flask bottom fragment); (b) Pearlescent glass sample (fragment of a vase); (c) Part of the UV spectra of the green glass sample.

In addition to the lines of elements that most often characterize ordinary (soda-lime-silica) glass (Si, Na, K, Ca, Al and Mg), high contents of Mn and Fe were registered in both samples, which were probably added in order to color the glass. Typically for non-modern glass samples, both samples have high concentrations of potassium, which was previously used instead of sodium for lowering the temperature necessary to produce glass. As known, the ordinary soda-lime glass appears colorless. Pigments (usually in a form of powdered metal oxides) are added in the manufacturing process to change the glass color. Although the elements identified in both samples were almost the same, the line intensities of characteristic elements were quite different. For instance, LIBS spectra of pearlescent glass were characterized by higher intensities of Ca and K and lower intensities of Fe and Mn lines compared to a green glass sample. In addition to the mentioned elements, Ti, Ba, Sr, and Cu were also detected.

In order to determine the limits of detection of the LIBS technique for glass analysis, elemental analysis of samples by X-ray fluorescence (XRF) was performed. The sensitivity of the LIBS technique was demonstrated for several elements, Ni, Cu, Ti, Mn, and K. The obtained LODs were 18, 2.5, 25, 32, and 205 ppm, respectively. LODs were determined as the concentration of an element whose spectral line intensity is equal to three times the standard deviation of the nearby background signal. The high LOD for K is a consequence of its low ionization energy and the fact that the most sensitive potassium lines were not used for the analysis as they are prone to self-absorption.

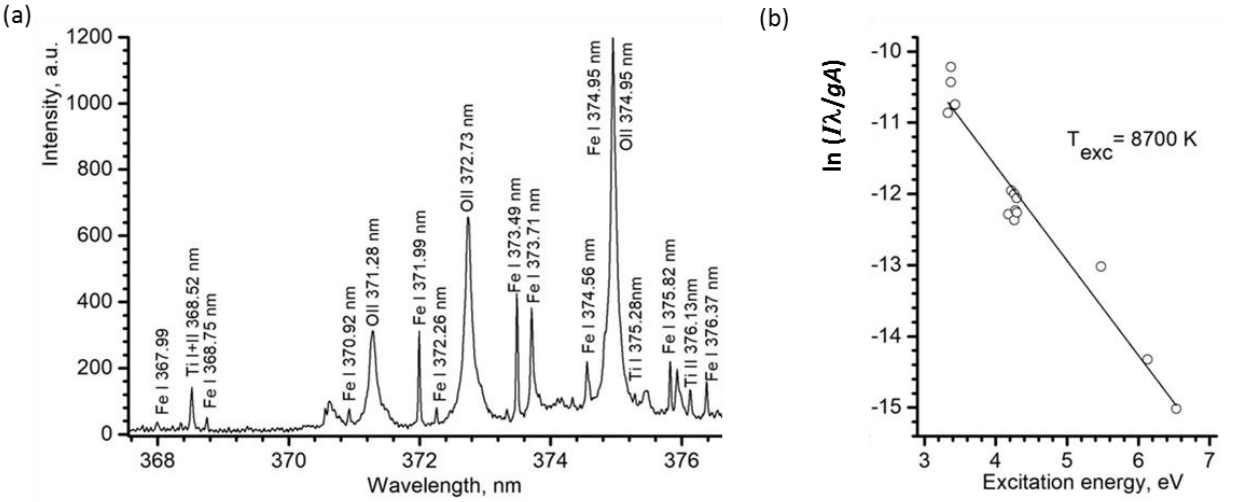

Figure 2. (a) Part of LIBS spectra of green glass sample; (b) The Boltzmann plot for the iron atomic spectral lines. The evaluated excitation temperature was 8700 ± 900 K.

Plasma diagnostics was performed using the spectral lines shown in Figure 2. a. Boltzmann plot method was used to evaluate the excitation temperature (Figure 2. b). The plot was constructed using suitable iron atomic lines, which in this spectral region have many spectral lines with a favorable distribution of excitation energies, and transition probabilities determined with high accuracy. A satisfactory linear fit was obtained from which the excitation temperature of 8700 K was determined, with a roughly estimated error of 900 K. The excitation temperature determined in this way was used to estimate the electron concentration using the intensity ratio of two spectral lines (ionic and atomic) of the same element [4]. For this purpose, the ratio of Ti II 376.13 nm and Ti I 375.28 nm lines were used. An electron concentration of $2 \cdot 10^{17}$ cm^{-3} was obtained, with a relative error of about 30%. It should be underlined that the plasma parameters obtained in this way refer to the time interval and the volume of plasma from which the spectral lines of metal elements are predominantly emitted.

CONCLUSION

In this work, a potential of LIBS based on a TEA CO_2 laser for the spectrochemical analysis of glass has been demonstrated. The LIBS spectra consisted of sharp emission lines of main and minor glass constituents were obtained with a good signal-to-noise ratio. Limits of detection for Ni, Cu, and Ti were in the range of 2.5 to 32 ppm. The main parameters, temperature, and electron number density were determined to characterize excitation conditions in the plasma. The values of the excitation temperature and the electron number density were 8700 K and $2 \cdot 10^{17}$ cm^{-3}, respectively.

Acknowledgement

This work was partially supported by the Ministry of Education, Science and Technological Development of the Republic of Serbia through Contract No. 451-03-68/2020-14/200146, 451-03-9/2021-14/200017 and ИИИ 47025.

REFERENCES

[1] M. Oujja, M. Sanz, F. Agua, J. Conde, M. García-Heras, A. Dávila, Pilar Oñate, J. Sanguino, J. R. V. D. Aldana, P. Moreno, M. Villegas, M. Castillejo, J. Anal. At. Spectrom. 2015, **30**, 1590-1599.

[2] M. Momcilovic, M. Kuzmanovic, D.Rankovic, J.Ciganovic, M.Stoiljkovic, J. Savovic, M. Trtica, Appl. Spectrosc. 2015, **69**, 419-429.

[3] J. Savovic, M.Stoiljkovic, M.Kuzmanovic, M.Momcilovic, J.Ciganovic, D.Rankovic, S.Zivkovic, M.Trtica, Spectrochim. Acta Part B 2016, **118**, 127-136.

[4] E. Tognoni, M. Hidalgo, A. Canals, G. Cristoforetti, S. Legnaioli, A. Salvetti, V. Palleschi, Spectrochim. Acta Part B 2007, **62**, 435-443.

OPTICAL SPECTROSCOPY OF PLASMA INDUCED BY IRRADIATION OF ANIMAL BONE WITH TEA CO_2 LASER

M. Marković[1], D. Ranković[1], M. Savić Biserčić[2], M. Trtica[2], J. Savović[2] and M. Kuzmanović[1]

[1] *University of Belgrade, Faculty of Physical Chemistry, Strudentski Trg 12-16, 11000 Belgrade, Serbia. (miroslav@ffh.bg.ac.rs)*
[2] *University of Belgrade, INN Vinca, Mike Petrovića Alasa 12-14, 11001 Belgrade, Serbia.*

ABSTRACT

The application of laser-induced breakdown spectroscopy (LIBS) for the elemental analysis of pig shoulder bone samples is reported. Measurements were performed using a compact laboratory-made TEA CO_2 laser with low pulse energy. The recorded spectra consisted of well-defined lines of atoms and single charged ions of Ca, Mg, P, and other constituent elements, with a good signal-to-noise ratio suitable for spectrochemical analysis. Based on the ICP quantitative analysis of the bone sample, the limits of detection of LIBS analysis were estimated for Mg (16 ppm) and Na (940 ppm). Plasma parameters, temperature, and electron number density were determined by measuring Stark widths and relative intensities of the C and Mg ionic and atomic spectral lines.

INTRODUCTION

In forensic and archeological contexts, identifying isolated or fragmentary bones is essential since many non-osseous materials, like plastic, wood, or stones, can be mistaken for human/animal bone. Bones can be generally identified on three levels: gross skeletal anatomy, bone macrostructure, and bone histology (microstructure).

As a versatile, non-contact, multi-elemental, non-destructive sampling, powerful atomic spectrometry method LIBS provides elemental composition data of practically any forensic sample. LIBS utilizes a high power density laser pulse to ablate a sample and create a localized plasma plume. Plasma plume emits wavelengths characteristic of the elemental composition of the investigated sample.

TEA CO_2 laser has several advantages over the most common commercially used laser in LIBS, Nd:YAG laser. Unlike Nd:YAG laser, TEA CO_2 laser does much less damage to samples which is a benefit in applications such as forensics, archeology, or art where tolerance to damage and sample consumption is minimal. Its temporal pulse profile of the order of hundred nanoseconds, followed by a few μs tail, produces a plasma plume with good analytical characteristics.

In this work, the applicability of a TEA CO_2 laser-based LIBS for qualitative analysis of the elemental composition of a pig shoulder bone was tested. The paper aims to demonstrate LIBS potential for relatively simple, fast, and sensitive analysis of complex organic matrices such as bones. The selection of a pig bone was based on its likeness with the human bones, i.e., only minor bone composition differences [1]. In addition, to characterize the excitation conditions in the laser-induced plasma, two main plasma parameters, electron number density and temperature were determined using standard spectroscopic methods. The calculated plasma parameters may be used to normalize the line intensities by intrinsically correcting for shot-to-shot fluctuations and are essential for quantitative LIBS analysis using a calibration-free approach.

EXPERIMENTAL

The Transversely Excited Atmospheric pressure carbon dioxide (TEA CO_2) laser, developed at the VINCA Institute of Nuclear Sciences, was used as the radiation source in the applied LIBS setup [2]. The operating laser wavelengths were 10.5709 and 10.5909 μm, and the pulse repetition rate up to 2

Hz when in a multimode regime. The initial laser peak, which lasted around ~100 ns, carried approximately 35% of the total pulse energy. The initial peak was followed by a decaying tail which lasted around ~ 2 µs.

The optimized measurement parameters were: laser pulse energy of 155 mJ, laser beam focused at the sample surface, acquisition of plasma emission from a plasma slice 1 mm above the sample surface. ZnSe lens was used for laser beam focusing. A plasma image was projected on the entrance slit of a Carl Zeiss PGS2 spectrograph by an achromatic quartz lens. U2C-16H11850 CCD camera with enhanced sensitivity in UV range was used to capture plasma emission spectra. The CCD camera was triggered at a minimal exposure time of 10 ms to reduce dark current and noise.

A preliminary quantitative analysis of samples was performed using the ICP OES technique (iCAP 6000, Thermo Scientific). Digestion procedure using mineral acids was performed to prepare bone samples for ICP analysis. Multi-element standard soultions were prepared from 1000 ppm ICP standard stock solution (Merck) and used for calibration. Concentrations of the phosphorus determined in the bone sample was 12.8 %. Other elements detected in ppm concentrations were Mg (3440 ppm), Na (4330 ppm) and Al (214 ppm).

RESULTS AND DISCUSSION

Part of the spectrum obtained by irradiating the bone sample with TEA CO_2 laser pulses is shown in Fig. 1. In the spectral region around 250 nm, atomic and ionic carbon lines and strong atomic phosphorus lines dominate the spectrum. In addition, oxygen and nitrogen ion lines from the atmosphere were observed in the spectrum.

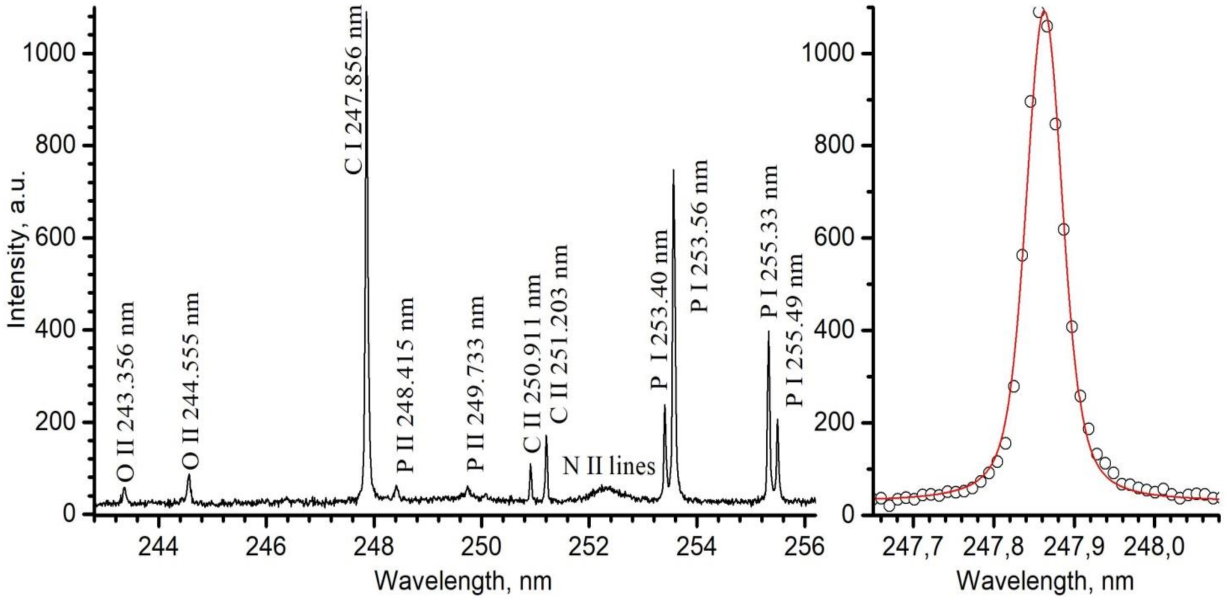

Figure 1. a) Part of UV spectra of the pig shoulder bone sample, b) Profile of C I 247.856 nm line fitted with Voit profile (fixed Gaussian width of 0.040 nm)

The measurement of the ionic to atomic carbon line intensity ratio is a very suitable method for determining the ionic temperature (T_{ion}) in plasma [3]. Determination of temperature using the C II/C I intensity ratio required knowledge of the electron concentration, N_e. The electron number density was determined from the Stark-broadened profile of the C I 247.86 nm line. The experimental line profile was deconvolved to extract Lorentz width, assuming that the Stark broadening dominates the Lorentz profile. The ion broadening coefficient for the C I 247.86 nm line is very small (0.033 at 10^{16}

cm^{-3}) and due to considerable Gaussian width the Stark width was determined by deconvolution using Voigt fitting. The Gaussian component of the profile was fixed to the predetermined instrumental width (0.040 nm). The Stark width of carbon 247.86 nm line was 0.024 nm which corresponds to the electron number density of 2.9×10^{17} cm^{-3} [4]. The ionic temperature of T_{ion} =18100 K was calculated from the measured intensity ratio of C II 250.91 nm and C I 247.86 nm lines (0.077) and the predetermined value of N_e.

An intense C I line at 247.86 nm is suitable for the determination of the carbon concentration. Using the measured intensity to background noise ratio of the carbon line and assuming the typical carbon concentration in bones (mainly in the form of $CaCO_3$) is about 5%, the detection limit (LOD) for carbon was estimated at 0.07%. Similarly, using the Na I line 330.23 nm line, LOD for sodium was estimated at 940 ppm. Despite a low sensitivity, this line is still usable for detecting Na in samples with larger quantities of this element, as our bone sample (4330 ppm). The Na I line at 588.00 nm is suitable to determine Na with higher sensitivity, but only in samples with low Na concentrations since this line is highly prone to self-absorption.

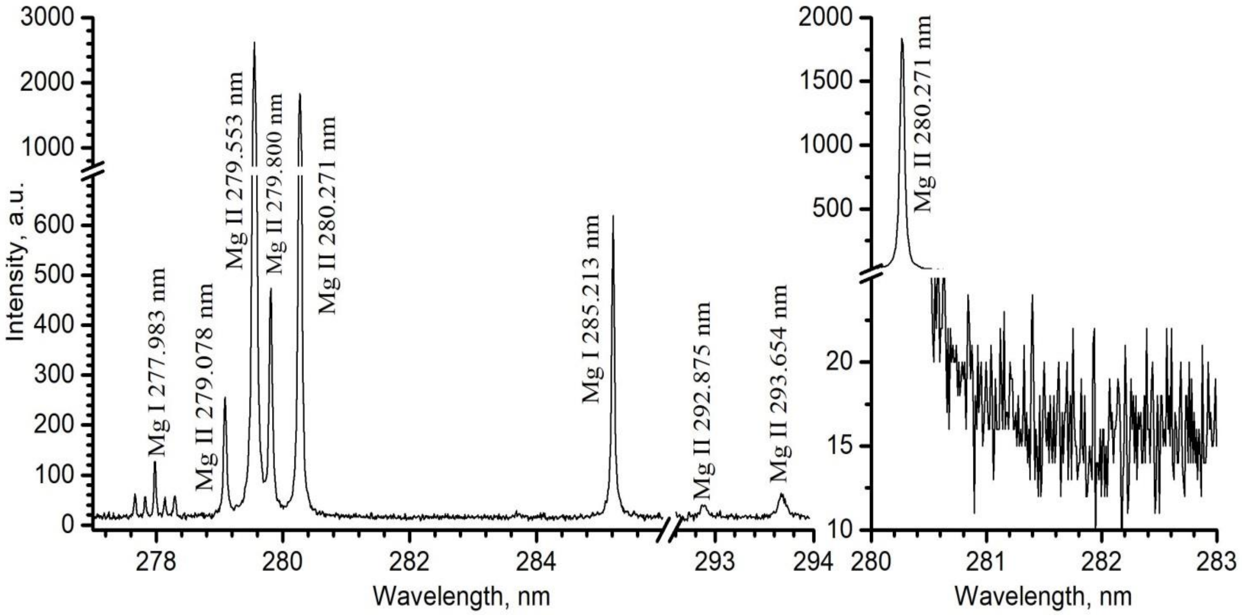

Figure 2. a) Part of LIBS spectra of the pig shoulder bone sample: Mg I and Mg II lines, b) Illustration of the determination of LOD for magnesium.

In Fig. 2a, a group of magnesium ionic and atomic lines suitable for plasma diagnostics is shown. Using the predetermined electron concentration, from the ratio of Mg II 280.27 nm and Mg I 285.21 nm line integral intensities [5], the ionization temperature of 10500 K was calculated. The difference in temperatures determined from carbon and magnesium lines is caused by the fact that the predominant emission of these lines comes from different plasma regions. Due to the significantly higher ionization and excitation energy of carbon regarding magnesium, the maximum carbon emission is located in the hotter plasma zones. The lines shown in Fig. 2 are also suitable for determining the magnesium content. Magnesium is present in the bones in a significant concentration, e.g., the Mg concentration in our sample was 0.344%. Figure 2b illustrates the determination of LOD using the Mg II ionic line at 280.27 nm. The obtained LOD for Mg was 16 ppm.

CONCLUSION

The applicability of the LIBS technique based on low pulse energy TEA CO_2 laser for the elemental analysis of bone samples was demonstrated. LIBS can be used to detect most metals in bones with detection limits between 10-100 ppm, as illustrated by the Mg example. The possibility of using Mg and C lines for plasma diagnostics was also demonstrated. Apparent values for electron concentration of 2.9×10^{17} cm^{-3} and ionization temperature in the range from 10500 to 18100 K were determined, depending on the properties of the element whose lines were used for diagnostics.

Acknowledgement

This work was partially supported by the Ministry of Education, Science and Technological Development of the Republic of Serbia through Contract No. 451-03-68/2020-14/200146 and 451-03-9/2021-14/200017.

REFERENCES

[1] K. Franke, F. Schöne, A. Berk, M. Leiterer, G. Flachowsky, Eur. J. Nutr. 2008, **47**, 40–46.

[2] M. Momcilovic, M. Kuzmanovic, D.Rankovic, J.Ciganovic, M.Stoiljkovic, J. Savovic, M. Trtica, Appl. Spectrosc. 2015, **69**, 419-429.

[3] M. Kuzmanovic, D. Rankovic, M. Trtica, J. Ciganovic, J. Petrovic, J. Savovic, Spectrochim. Acta 2019, **157**, 37-46.

[4] H. Griem, Spectral Line Broadening by Plasmas, Academic Press, New York, 1974.

[5] E. Tognoni, M. Hidalgo, A. Canals, G. Cristoforetti, S. Legnaioli, A. Salvetti, V. Palleschi, Spectrochim. Acta Part B 2007, **62**, 435-443.

CONFORMATIONAL AND SPECTROSCOPIC ANALYSES OF 2-(4-FLUOROPHENYL)-2-HYDROXYPROPANOIC ACID

V. Vitnik and Ž. Vitnik

Department of Chemistry, Institute of Chemistry, Technology and Metallurgy, University of Belgrade, Njegoševa 12, 11000 Belgrade, Serbia. (vesnak@chem.bg.ac.rs)

ABSTRACT

The conformational and vibrational spectroscopic analyses of 2-(4-fluorophenyl)-2-hydroxypropanoic acid (FHPA) are represented in this research. Theoretical calculations were performed by density functional theory (DFT) with B3LYP method using 6-311++G(d,p) basis set. The FT-IR and Raman spectra of FHPA were recorded and analyzed. The comparison between the experimental and calculated spectra showed good agreement. Molecular electrostatic potential map (MEP) of the compound was calculated to predict chemical reactivity of the title molecule.

INTRODUCTION

Fluoro compounds are widely used in medicinal chemistry. Compounds with a C-F bond are well known drugs such as: cholesterol-absorption inhibitor Ezetimibe [1], Celecoxib [2] inhibitor of the cyclo-oxygenase 2, antimalarial drug Mefloquine and anticancer drug 5-fluorouracil. Fluoxetine [3] is approved as the drug for use in the treatment of both obsessive-compulsive disorder and bulimia. Many fluoroquinolones are highly active antibacterial agents that are widely used [4]. Fluoro compounds have broad spectrum of industrial applications like refrigerants fluoropolymers and fire extinguishants. Some fluoro compounds containing OCF_3-group have application in electro-optical materials and are used for the development of liquid crystal displays.

In an attempt to give our contribution to the structural analysis of fluoro compounds, in the present study, the stability of different possible conformers of monomer and dimmer of FHPA are determined. The vibrational spectra of FHPA are analyzed to confirm the molecular structure. MEP surface is plotted over the optimized geometry to find out the reactivity of FHPA molecule.

EXPERIMENTAL DETAILS

The chemical structure and purity of the synthesized compound was confirmed by its melting point, ^{1}H and ^{13}C NMR, FT-IR and UV spectra. FT-IR spectrum was recorded on a Bomem MB 100 spectrophotometer. The Raman spectrum of FHPA was recorded in the region of 50–3500 cm^{-1} using Thermo DXR Raman microscope with the 532 nm laser excitation line, with a constant power of 10 mW and exposure time of 10.00 s.

COMPUTATIONAL DETAILS

All the calculations were performed using Gaussian 09 Revision D.01 program package. Geometry of FHPA was fully optimized at DFT/B3LYP/6-311++G(d,p) level of theory. The harmonic frequencies were calculated with the same method and scaled by 0.967. The assignments of the calculated wavenumbers were aided by the animation option of Gauss View 3.0 graphical interface from Gaussian programs. To investigate the reactive sites of FHPA, MEP for the 0.002 a.u. isosurfaces of electron density was evaluated using the B3LYP/6-311++G(d,p) level of theory.

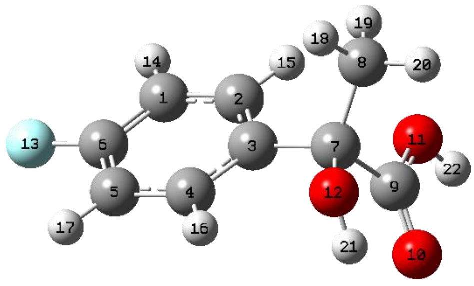

Figure 1. Optimized geometry of FHPA

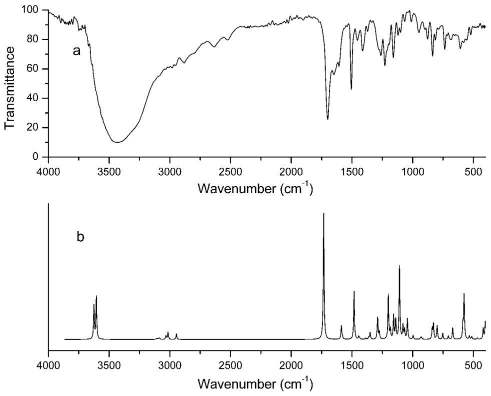

Figure 2. Experimental and predicted IR spectra of FHPA

RESULTS AND DISCUSSIONS

Detailed conformational analysis was evaluated to find all stable conformers of FHPA. Analysis shows that orientation of phenyl, OH and COOH groups attached in position C7 defines conformational characteristics of molecule. The position and different orientations of these groups give rise to eleven stable conformers. The DFT energy and the statistical Boltzmann distribution reveal that the two isomers acquire dominant stability among other isomers with 84.35 and 12.97 of percentage contribution. The stability of conformers highly depends on the orientation of phenyl ring and possibility to form intramolecular hydrogen bond. The phenyl ring in most stable conformers is in the same plane with α-OH group while in the least stable one is in the plane of COOH group. The optimized molecular structure of the most stable conformer with the atom numbering scheme of the title molecule is shown in Fig. 1.

In order to estimate the barrier height and confirm the transitions between conformers for the rotation around single bonds potential energy scan (PES) is done. The energy for rotation of phenyl ring when passing through a plane of C1-COOH bond is 2.5 kcal/mol while the rotation of COOH group requires 5.5 and 7.0 kcal/mol of energy when the group is in the plane of C7-C(Ph) bond.

Since FHPA possesses three groups that can form an intermolecular hydrogen bonds, in an additional part of the conformational analysis, the stability of potential dimers is investigated. Also the atom C7 represents stereocenter and two types of dimers can be formed: centrosymmetric (*R*/*S* or *S*/*R*) and with C_2 symmetry (*R*/*R* or *S*/*S*). From the DFT calculations it is evident that the most stable dimer is centrosymmetric dimer with intermolecular hydrogen bond between carboxyl groups of two molecules with different configuration of stereocenters (*R*/*S* or *S*/*R*).

As the exact geometrical parameters of the investigated molecule are not available, the literature data on crystal of the similar compound, 2-(4-fluorophenyl)-2-hydroxyacetic acid, are used for comparison. In the crystal structure of racemic form of this molecule the centrosymmetric dimer formed with intermolecular hydrogen bond between carboxyl group of one molecule and α-OH group of the other molecule is found (CCDC 1292366). Also, the dimer formed via intermolecular hydrogen bonds between carboxyl groups of two molecules is not found in the literature. Instead of that combined hydrogen bonding is found in crystal of optically active molecule a.i. pure enantiomer form (CCDC 131621) in a form of asymmetric trimer with α-OH···O=C, OH···O=C and α-OH···α-OH hidrogen bonds.

In FT-IR spectrum of FHPA the broad absorption bands at 3425 and 3295 cm^{-1} are assigned to O11-H22 and O12-H21 stretching vibrations, respectively. In FT-Raman spectrum these vibrations are appeared as sharp peaks at 3230 and 3200 cm^{-1}. The bands at 3010/3010 cm^{-1} and 2984/3092 cm^{-1} (FT-IR/FT-Raman) are assigned to asymmetric and symmetric stretching vibrations of aromatic C-H groups, respectively. The bands observed at 2952/2989 and 2882/2944 cm^{-1} (FT-IR/FT-Raman) are assigned to asymmetric and symmetric C-H stretching vibrations of C8H_3 group, respectively. The C=O stretching vibrations appeared as very sharp and intense band at 1735 cm^{-1} in FT-IR and weak band at 1696 cm^{-1} in FT-Raman spectrum. The strong bands observed at 1649 and 1608 cm^{-1}in FT-IR spectrum are assigned as C-C stretching vibrations of the phenyl ring. In FT-Raman spectrum the band corresponding to the same vibrations appears as a weak band at 1606 cm^{-1}. The bands at 813, 1229/773, 1195 cm^{-1} (FT-IR/FT-Raman) are assigned to C-F stretching vibrations.

The medium to strong bands observed in the FT-IR/FT-Raman spectra at 1229/1165 and 1262/1220 cm^{-1} are assigned to aromatic C–H in-plane bending vibrations, and weak and medium bands at 836, 900, 949 cm^{-1}, and strong band at 815 cm^{-1} (FT-IR/FT-Raman) are assigned to C–H out-of-plane deformation modes. In-plane bending vibrations of O11–H22 group lead to two bands at 1121 and 1160 cm^{-1} in FT-IR (1100 and 1128 cm^{-1} in Raman) and bands centered at 461 and 785 cm^{-1} in FT-IR (728 cm^{-1} in Raman) are assigned to out-of-plane bending vibrations. The O12–H21 in- and out-of-plane bending vibrations appear as weak bands at 1338/1294 cm^{-1} and 415, 420, 468/420 cm^{-1} (FT-IR/FT-Raman), respectively. Bands of the in- and out-of-plane bending vibrations of C9=O10 bond appear at 1160/1128, 1121/1100 cm^{-1} and at 461/ 785 cm^{-1} (FT-IR/FT-Raman), respectively. The weak bands at 522/612 and 411, 480/500 cm^{-1} (FT-IR/FT-Raman) are assigned to in- and out-of-plane bending vibrations of C–F bond, respectively. All the calculated wavenumbers show excellent agreement with the experimental data.

The maximum negative region of MEP (possible site for electrophilic attack) is spread over oxygen atoms O10, O11 and O12 of carboxyl and α-hydroxyl group, respectively. The maximum positive region (possible site for nucleophilic attack) is mainly localized on the hydrogen atom H22.

CONCLUSION

The structural, vibrational properties and chemical reactivity of FHPA were studied with DFT/B3LYP/6-311++G(d,p) method. The calculated results correlate well with the experimental values.

Acknowledgement

This work was financially supported by Ministry of Education, Science and Technological Development of the Republic of Serbia (Grant No. 451-03-68/2020-14/200026).

REFERENCES

[1] J. W. Clader, J. Med. Chem. 2004, 47, 1-9.
[2] D. Clemett, K. L. Goa, Drugs, 2000, 59, 957–980.
[3] D. L. Roman, C. C. Walline, G. J. Rodriguez, E. L. Barker, Eur. J. Pharmacol., 2003, 479 (1-3), 53-63.
[4] P. Ball, J. Antimicrob. Chemother., 2000, 46, 17-24

SPECTROSCOPIC AND COMPUTATIONAL STUDY OF NOVEL DIHYDROPYRIMIDINE AZO PYRIDONE DYE

Ž. Vitnik [1], J. Tadić [2], D. Mijin [3] and V. Vitnik [1]

[1] *Department of Chemistry, ICTM, University of Belgrade, Belgrade, Serbia,*
(*vesnak@chem.bg.ac.rs*)
[2] *Innovation Center, Faculty of Technology and Metallurgy, University of Belgrade, Belgrade, Serbia*
[3] *Department of Organic Chemistry, Faculty of Technology and Metallurgy, University of Belgrade, Belgrade, Serbia*

ABSTRACT

Structural, vibrational, electronic, NMR and reactivity properties of ethyl 4-(4-((5-cyano-2-hydroxy-4-methyl-6-oxo-1-propyl-1,6-dihydropyridine-3-yl)diazenyl)phenyl)-6-methyl-2-oxo-1,2,3,4-tetrahydropyrimidine-5-carboxylate (PPD) were investigated by using density functional theory (DFT). Theoretical calculations were performed with B3LYP/6-311++G(d,p) method. The calculated data correlated well with the experimental ones. HOMO-LUMO energy gap for the title molecule confirmed the high reactivity of dye. The obtained results verified the hydrazone form as *more stable one.* In addition, molecular electrostatic potential (MEP) map of the dye was used to test its activity.

INTRODUCTION

The heterocyclic azo dyes have been *extensively* studied because of their significant coloration properties [1]. Also, some of arylazo pyridone dyes possess antibacterial [2] and anticancer [3] activity. It is well known that compounds based on the 3,4-dihydropyrimidine-2(1*H*)-one (DHPM) core have broad spectrum of activities like antibacterial, antiviral, antioxidant, anti-inflammatory and antitumor [4].

In this paper the structural and spectroscopic properties of newly synthesized DHPM azo pyridone dye were calculated. Also, azo-hydrazone tautomerism of dye PPD was analyzed.

EXPERIMENTAL DETAILS

The structure of the newly synthesized compound was elucidated by melting point and FT-IR, UV-Vis, MS, ^{1}H and ^{13}C NMR spectral data. FT-IR spectrum was recorded on the Nicolet™ iS™ 10 FT-IR spectrometer in the region 500–4000 cm^{-1} using ATR technique. The ultraviolet absorption spectrum of PPD was examined in the range of 200-600 nm using Shimadzu 1700 spectrophotometer. The UV pattern was taken from a 10^{-5} molar solution of ethanol. ^{1}H and ^{13}C NMR spectra were recorded on a Bruker Ascend 400 instrument at 400 Hz and 100 MHz, respectively, in DMSO-d_6. Quadrupole ion trap mass spectrometer LCQ Advantage (Thermo Fisher Scientific, USA) was used for the compounds detection.

COMPUTATIONAL DETAILS

All the calculations were performed using Gaussian 09 program package. Geometry of PPD was fully optimized with DFT/B3LYP/6-311++G(d,p) method. The calculated harmonic frequencies are scaled by 0.968. ^{1}H and ^{13}C NMR chemical shifts are calculated with GIAO approach. UV absorption energies of this compound in ethanol were calculated by TD-DFT method. The frontier molecular orbital energies and HOMO-LUMO energy gap are calculated with B3LYP/6-311++G(d,p) method.

The molecular electrostatic potentials for the 0.002 a.u. isosurfaces of electron density was evaluated using the same method.

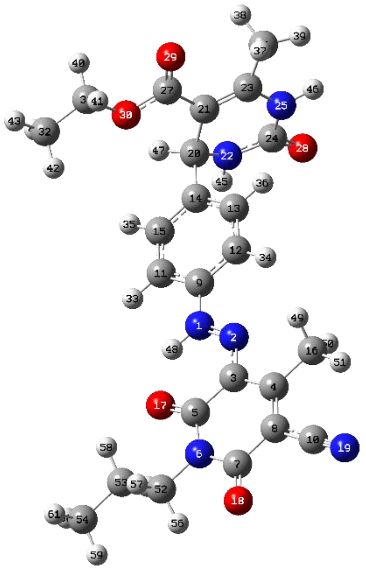

Figure 1. Optimized geometry of PPD

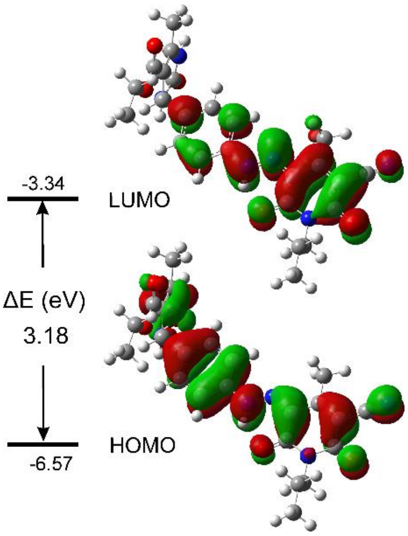

Figure 2. HOMO-LUMO plot of PPD

RESULTS AND DISCUSSIONS

The calculated energy data of possible tautomeric forms confirm that the most stable form of the dye is hydrazone one. The phenylazo pyridone part of PPD molecule is planar while the DHPM group is normal to that plane which prevents electron delocalization between these two parts of the molecule. The largest conformational difference in the molecule results from the rotation of the DHPM group around the C14-C21 bond. The calculation showed that the energy barrier for this rotation is just 2.0 kcal/mol and that the rotation produces two conformers with almost identical energies. The optimized geometry of the most stable conformer obtained with B3LYP method is presented in Fig. 1 with numbering of atoms. To the best of our knowledge, exact experimental structure data of PPD are not yet known in the literature.

In calculated IR spectrum of PPD, weak and broad absorption bands at 3513 and 3499 cm^{-1} are assigned to N25-H46 and N22-H45 stretching modes of the dihydropyrimidinone ring, respectively. These bands appear at 3593 and 3507 cm^{-1} in experimental FT-IR spectrum, respectively. The band at 3181 cm^{-1} is assigned to N1-H48 stretching mode of hydrazone group. The bands of symmetric and asymmetric C-H stretching modes of the phenyl group are at 3076 and 3061 cm^{-1}, respectively. The band calculated at 2255 cm^{-1} belongs to stretching vibration of nitrile group. The sharp and intensive bands observed at 1728 and 1687 cm^{-1} in calculated IR spectrum are assigned to C24=O28 and C27=O29 stretching vibrations of dihydropyrimidinone ring and ethoxycarbonyl group, respectively. For two polar carbonyl groups, C7=O18 and C5=O17, of pyridone ring the calculated energy values of stretching vibrations are 1682 and 1617 cm^{-1}, respectively. The band of the combined mode of C3=N2 stretching vibration and in-plane bending N1-H18 vibration appears at 1519 cm^{-1} in calculated spectrum and correlate well with experimental value of 1514 cm^{-1}. The shapes of the calculated and experimental infrared spectra reveal that hydrazone tautomer is predominant form of the dye in the solid state.

Additional evidence of hydrazone tautomeric form of PPD are characteristic signals of hydrogen of N-H groups in ^{1}H NMR spectrum as well as ^{13}C NMR signals of carbon atoms of carbonyl groups.

In ^{1}H NMR spectrum signal at 14.62 ppm marks hydrogen H48 which belongs to hydrazone group. The predicted value is 14.68 ppm. Two signals that appear at 9.23 and 7.77 ppm, assigned to H46 and H45, respectively, indicate the presence of two N-H groups as part of dihydropyrimidinone ring. In predicted ^{13}C NMR spectrum of the investigated dye, resonance maximum at 174.67 ppm, assigned to ethoxycarbonyl group, correlates with the experimental value of 165.72 ppm. Resonance maxima of C7 and C5 of carbonyl groups of pyridone ring are at 169.67 and 168.71 ppm while the experimental values are 161.18 and 160.66 ppm, respectively. The chemical shift value of C24 atom of carbonyl group in dihydropyrimidinone ring is observed at 152.46 ppm while the corresponding computed value is 158.1 ppm. The carbon atom C3 resonates at 123.48 ppm in the ^{13}C NMR spectrum and the computed value is 130.58 ppm. The chemical shift values predicted by TD-DFT are in close agreement with the experimental ones.

Density plots over the highest occupied molecular orbital (HOMO) and lowest unoccupied molecular orbital (LUMO) energy surface identifies the donor and acceptor groups in the molecule. However, it provides information about the intramolecular charge transfer (ICT) through the molecule. As can be seen from the Fig. 2, HOMO is spread over dihydropyrimidinone and phenyl rings. LUMO is mainly located over pyridone ring and support ICT through investigated molecule. The frontier orbital energy gap for PPD is 3.18 eV and reveals the high reactivity of molecule.

In attempt to predict reactive sites of electrophilic or nucleophilic attack for molecule PPD, the MEP at the B3LYP/6-311++G(d,p) optimized geometry is calculated. PPD molecule has tree possible sites for electrophilic attack because negative regions in the studied molecule are found around the O28 and O18 atoms of carbonyl groups as well as nitrile group. The maximum positive region is localized on the H45 and H46 atoms of two N-H groups of dihydropyrimidinone ring indicating the possible sites for nucleophilic attack.

CONCLUSION

Detailed DFT and experimental analyzes of structural and spectroscopic properties of PPD have shed light on the existence of its hydrazone tautomeric form as the most stable form of the molecule.

Acknowledgement

This work was financially supported by Ministry of Education, Science and Technological Development of the Republic of Serbia (Grant No. 451-03-68/2020-14/200026, 451-03-68/2020-14/200135 and 451-03-68/2020-14/ 200287).

REFERENCES

[1] M. A. Metwally, E. Abdel-Galil, A. Metwally, F. A. Amer, Dyes Pigm. 2012, 92(3), 902-908

[2] S. M. Ashkar, M. A. El-Apasery, M. M. Touma, M. H. Elnagdi, Molecules 2012, 17, 8822-8831.

[3] D. Mijin, B. Božić Nedeljković, B. Božić, I. Kovrlija, J. Lađarević, G. Ušćumlić, Turk. J. Chem. 2018, 42, 896-907.

[4] Â. de Fátima, T. C. Braga, L. da S. Neto, B. S. Terra, B. G. F. Oliveira, D. L.da Silva, L. V. Modolo, J. Adv. Res. 2015, 6, 363-373.

EXPERIMENTAL AND THEORETICAL UV-VIS SPECTRAL STUDY OF SOME ARYLAZO PYRIDONE DYES IN AMIDE SOLVENTS

J. Lađarević [1], Ž. Vitnik [2], V. Vitnik [2], B. Božić [3] and D. Mijin [1]

[1] Faculty of Technology and Metallurgy, University of Belgrade, Karnegijeva 4, Belgrade, Serbia
[2] Institute of Chemistry, Technology and Metallurgy, University of Belgrade, Njegoševa 12, 11000 Belgrade, Serbia. (vesnak@chem.bg.ac.rs)
[3] Institute of Physiology and Biochemistry "Ivan Đaja", Faculty of Biology, University of Belgrade, Studentski trg 16, Belgrade, Serbia

ABSTRACT

Spectral properties of ten 5-(substituted phenylazo)-3-cyano-1-ethyl-6-hydroxy-4-methyl-2-pyridones were investigated in formamide and *N,N*-dimethylformamide (DMF) by combining experimental study and density functional theory (DFT). In these two solvents, equilibrium between hydrazone and anionic forms is confirmed both experimentally and theoretically. Relative position of the absorption maxima of hydrazone and anion forms is highly affected by the substitution pattern in the phenyl ring. Theoretical absorption energies showed good agreement with experimental data.

INTRODUCTION

Arylazo pyridone dyes comprise a significant class of disperse dyes composed of pyridone ring, as coupling component, and carbocyclic and heterocyclic ring as diazo component. Their use in the textile industry have been known for a long time and is highly affected by their good wash and light fastness properties, vigorous colors and molar extinction coefficients [1,2]. In recent years, they are also utilized as suitable compounds for liquid crystal displays (LCD), ink-jet printing, hot melt or phase change inks [3]. One of the most interesting features of these dyes is the possibility of the azo-hydrazone tautomerism for the dyes bearing –OH group in *ortho*- and *para*-position to the azo bridge. This phenomenon has attracted a considerable attention since tautomers possess different physical, optical and toxicological properties, and most important different tinctorial strengths [4].

In this work, UV-Vis spectral properties of ten 5-(substituted phenylazo)-3-cyano-1-ethyl-6-hydroxy-4-methyl-2-pyridones of diverse substituents (R = –OMe, –NO_2, –Cl, H) in different positions of the phenyl moiety (*ortho*-, *meta*- and *para*-) have been analyzed in formamide and DMF both from theoretical and experimental standpoints (Sheme 1).

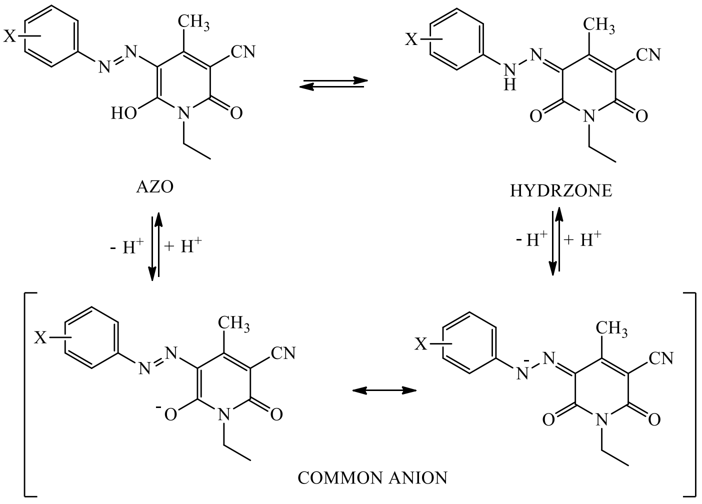

	X
1	4-OMe
2	3-OMe
3	2-OMe
4	4-NO_2
5	3-NO_2
6	2-NO_2
7	4-Cl
8	3-Cl
9	2-Cl
10	H

Scheme 1. Possible forms of the investigated dyes in solutions.

METHODS

UV-Vis spectra were collected on a Shimadzu 1700 spectrophotometer at a concentration of 5×10^{-5} mol dm^{-3}. All spectra are recorded at room temperature.

Geometries of all investigated dyes have been calculated using the Gaussian 09 program package on M06-2X/6-311++G(d,p) method using a conductor-like polarisable continuum model (CPCM) for inclusion of solvent effects. UV absorption energies in formamide and DMF were calculated by TD-DFT approach on the same level of theory.

RESULTS AND DISCUSSION

DFT study show that investigated dyes adopt hydrazone form in the solid state and most of the solvents [5]. Intramolecular hydrogen bond between carbonyl group of pyridone ring and hydrogen of N–H hydrazone bond is considered to be the main reason for high stability of this form. In proton-accepting solvents, deprotonation takes place and equilibrium between hydrazone and common anion has been established (Sheme 1).

UV-Vis spectra of the dyes 1-10 in formamide and DMF clearly show the existence of two forms in the solution. Furthermore, all spectra exhibit bands in the region between 300–340 nm which have been proven to be an indicator of the anionic form in DMF [5]. In order to determine the position of the hydrazone form, acetic acid is added to the solution to eliminate the present anionic form, while the position of anionic form is confirmed upon addition of the solid NaOH (Table 1). It can be observed that the relative positions of the hydrazone and anionic form are dependent on the substitution pattern. Anion form appears at lower wavelength with respect to hydrzone form, except in the case of 4 whose anion form show bathochromic shift.

Table 1. Experimental and theoretical UV-Vis maxima of hydrazone and anionic forms and their differences ($\Delta\lambda = \lambda_{anion} - \lambda_{hydrazone}$) in formamide.

	Experimental			theoretical (scaled)[a] M06-2X		
	$\lambda_{hydra.}$, nm	λ_{anion}, nm	Δλ, nm	$\lambda_{hydra.}$, nm	λ_{anion},nm	Δλ, nm
1	465.5	404.0	–61.5	463.83	432.87	-30.96
2	441.0	400.0	–41.0	443.79	433.75	-10.05
3	463.0	405.0	–58.0	461.69	429.49	-32.20
4	443.0	508.0	65.0	441.58	491.48	49.90
5	426.5	406.0	–20.5	426.38	439.80	13.42
6	450.0	410.0	–40.0	448.39	442.66	-5.73
7	440.5	405.0	–35.5	442.20	437.52	-4.69
8	433.5	403.0	–30.5	433.54	437.25	3.71
9	438.5	413.0	–25.5	438.67	438.27	-0.39
10	438.0	396.5	–41.5	438.28	430.78	-7.51

[a] scaled by 1.16

Table 2. Experimental and theoretical UV-Vis maxima of hydrazone and anionic forms and their differences ($\Delta\lambda = \lambda_{anion} - \lambda_{hydrazone}$) in DMF.

	Experimental			theoretical (scaled) M06-2X [5]		
	$\lambda_{hydra.}$, nm	λ_{anion}, nm	$\Delta\lambda$, nm	$\lambda_{hydra.}$, nm	λ_{anion},nm	$\Delta\lambda$, nm
1	458.0	420.5	–37.5	457.08	427.21	–32.87
2	437.0	408.0	–29.0	437.59	428.26	–9.33
3	454.5	408.5	–46.0	454.96	423.97	–30.99
4	438.0	483.0	45.0	435.26	485.55	50.29
5	421.5	414.0	–7.5	420.44	434.42	13.98
6	442.0	426.5	–15.5	441.88	437.31	–4.57
7	433.5	415.0	–18.5	436.03	432.00	–4.03
8	426.5	416.0	–10.5	427.48	431.81	4.33
9	431.5	418.0	–13.5	432.52	432.73	0.21
10	433.0	406.0	–27.0	432.11	425.37	–6.74

[a] scaled by 1.1456

It is known that the TD-DFT M06-2X method gives underestimated wavelengths of absorption maxima so it is necessary to scale the calculated values. The best scaling factors for formamide and DMF of 1.16 and 1.1456 were determined by fitting. The scaled values show excellent agreement with the experimentally determined values for the hydrazone form. However, the calculated values for the anionic form show a significant overestimation of the maxima as well as a significant underestimation of the difference between maxima of anion and hydrazone forms.

CONCLUSION

In proton-accepting solvents, equilibrium between hydrazone and common anion has been established. The position of absorption maxima of the hydrazone and anionic forms are determined. The calculated values for the anionic form show significant overestimation of the maxima and underestimation of the difference between maxima of anion and hydrazone forms.

Acknowledgement

This work was financially supported by Ministry of Education, Science and Technological Development of the Republic of Serbia (Grant No. 451-03-68/2020-14/200026, 451-03-68/2020-14/200135 and 451-03-68/2020-14/200178)

REFERENCES

[1] K. Hunger, Industrial Dyes Chemistry, Properties, Applications, Wiley-VCH, Weinheim, Germany, 2003.
[2] H. Qian, X. Zhao, Y. Dai, W. Huang, Dyes Pigm. 2017, 143, 223-231.
[3] J. M. Park, C. Y. Jung, W. Yao, C. J. Song, J. Y. Jaung, Col. Tech. 2017, 133, 158-164.
[4] X. Zhao, F. Chang, Y. Feng, H. Qian, W. Huang, Dyes Pigm. 2017, 140, 286–296.
[5] J. Mirković, B. Božić, V. Vitnik, Ž. Vitnik, J. Rogan, D. Poleti, G. Ušćumlić, D. Mijin, Color. Technol., 2018, 134, 33-43.

CRYSTALOGRAPHIC AND DFT STRUCTURAL ANALYSIS OF OCTOPAMINE-COUMARIN DERIVATIVE

D. Dimić[1], E. Avdović[2], D. Sretenović[3], Ž. Milanović[2], G. Kaluđerović[4] and J. Dimitrić-Marković[1]

[1] University of Belgrade, Faculty of Physical Chemistry, Studentski trg 12-16, 11000 Belgrade, Republic of Serbia. (ddimic@ffh.bg.ac.rs)
[2]Institute of Information Technologies, Department of Science, University of Kragujevac, Jovana Cvijića bb, 3400 Kragujevac, Serbia.
[3]Lehrstuhl für Molekulare Physikalische Chemie, Heinrich-Heine-Universität Düsseldorf, Universitätsstraße 1, D 40225 Düsseldorf, Germany.
[4]Department of Engineering and Natural Sciences, University of Applied Sciences Merseburg,Eberhard-Leibnitz-Straße 2, DE-06217 Merseburg, Germany

ABSTRACT

Octopamine is a norepinephrine analog in invertebrates and acts as a neurotransmitter. The crystal structure of a novel octopamine-coumarin derivative is described in this contribution. The density functional theory optimization of a structure by several common functionals (APFD, B3LYP-D3BJ, M05-2X, and M06-2X) was performed. Based on the bond lengths and angles, B3LYP-D3BJ proved to be the most reliable functional with the lowest values of mean absolute error. The experimental and theoretical UV-Vis transition wavelengths are also discussed.

INTRODUCTION

Coumarin and its derivatives have gained much attention due to their significant antibacterial, antifungal, anticoagulant, anti-HIV, antioxidant and cytotoxic activities. These compounds consist of fused benzene and pyrone rings with a variety of active positions which are important for their biological functions, such as signaling and hormonal role, as well as defense functions. Octopamine is a phenol analog of norepinephrine. It is included in the signal transduction, neurotransmission, neuromodulation, recovery after high energy demand, and modulation of cellular immune responses [1].

In this contribution, the synthesis under mild conditions of an octopamine-coumarin derivative is described. The experiments were performed because similar derivatives between coumarin and dopamine showed promising anti-tumor activity. The crystallographic structure was solved and presented. This structure was later used as a starting structure for geometry optimization by employing common functionals (APFD, B3LYP-D3BJ, M05-2X, and M06-2X). Based on the difference in experimental and theoretical bond lengths and angles, the suitable method for structure description was determined.

EXPERIMENTAL/THEORETICAL METHODS

Octopamine hydrochloride, methanol, toluene, acetone, and 96% ethanol were purchased from Sigma Aldrich (Munich, Germany). The synthesis of 3-(1-((2-hydroxy-2-(4-hydroxyphenethyl)amino)ethylidene)-chroman-2,4-dione (D1) followed the Scheme 1. The experimental UV-Vis spectrum was recorded on the Evolution 220 Thermo Scientific spectrophotometer in the region between 200 and 400 nm for the 6.25×10^{-5} M solution in methanol. The NMR spectra were obtained on the Varian Gemini Spectrometer with $CHCl_3$ as solvent and TMS as internal standard.

The data collection for the crystallographic structure was performed on the Oxford Diffraction Xcalibur2 diffractometer equipped with a Sapphire2 CCD detector with graphite-monochromatized

MoKα radiation (wavelength 0.71073 Å). CrysAlis CCD was used for data collection while CrysAlis RED was used for cell refinement, data reduction, and absorption correction. The structure was solved by SHELXT and subsequent Fourier series using SHELXL, implemented in the WinGX program suit. The anisotropic displacement parameters were refined for all non-hydrogen atoms. The analysis of bond distances, angles, and non-bonding interactions was performed in programs SHELX, PLATON, and DIAMOND.

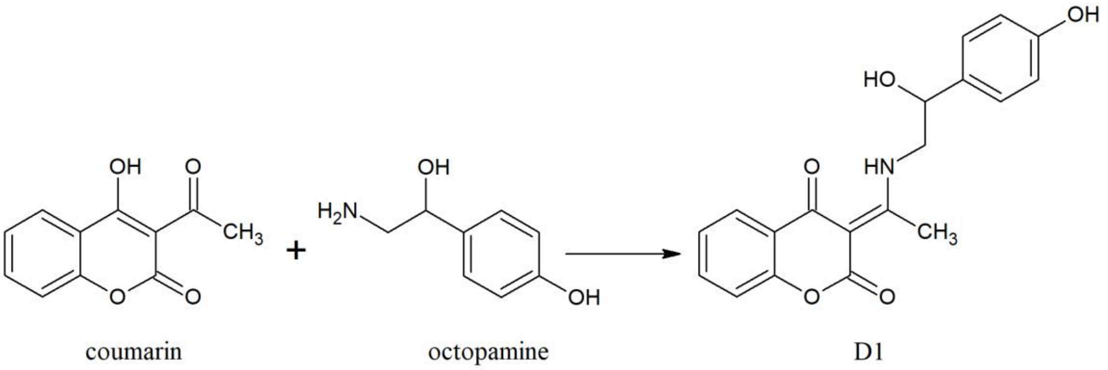

Scheme 1. The synthesis route of the octopamine-coumarin derivative.

The optimization of the structure was done based on the crystallographic data in the Gaussian program package [2]. Several common functionals were used for the optimization, namely APFD, B3LYP-D3BJ, M05-2X, and M06-2X, in conjunction with the 6-311++G(d,p) basis set. These functionals are recommended for the calculation of the thermodynamic parameters and structural features (bond lengths and angles) of organic compounds. The absence of imaginary frequencies showed that the local minimum was found. The optimization was performed without any geometrical constraints. The parameter used for the comparison of the experimental and calculated bond lengths and angles was the mean absolute error (MAE). The Time-Dependent Density Functional Theory (TD-DFT) was applied for the theoretical analysis of possible electronic transitions for structure optimized at B3LYP-D3BJ level of theory. The ^{1}H and ^{13}C NMR chemical shifts were calculated within the Gauge Independent Atomic Orbital (GIAO) approach for previously mentioned optimized structure.

RESULTS AND DISCUSSION

The crystallographic structure of **D1** is presented in Figure 1.

The obtained substance consists of two rings of the coumarin core, aliphatic chain, hydroxyl group attached to the aliphatic chain, aromatic ring, and a phenolic hydroxyl group. The structure is additionally stabilized by the presence of an intramolecular hydrogen bond that encloses six-membered ring O−C−C−C−N−H. This ring determines the keto-amine tautomeric form of the molecule. This hydrogen bond leads to the equalization of two carbon-carbon bonds due to the delocalization of the π-electron system.

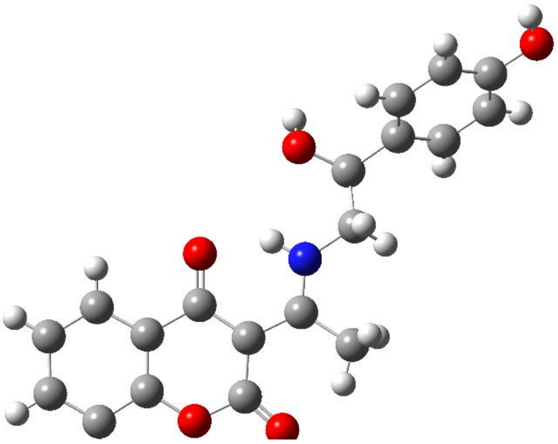

Figure 1. The crystallographic structure of **D1**.

The overall crystal structure also contains hydrogen bonds formed by the hydroxyl groups in the structure.

Table 1. Parameters R and MAE for the comparison of the experimental and theoretical bond lengths and angles.

	Funct.	APFD	B3LYP-D3BJ	M06-2X	M05-2X
Bond length [Å]	MAE	0.014	0.015	0.013	0.014
Bond angles [^{o}]	MAE	0.819	0.779	0.882	0.868

The parameter MAE for the investigated functionals, given in Table 1, shows that all of the functionals describe well the experimental structure. The values for bond lengths were reproduced better in comparison to the values for bond angles. Therefore, parameters for bond angles can be used for the precise comparison of functionals. The values of MAE for bond lengths were between 0.013 and 0.015 Å, while for bond angles these values were in a range from 0.779 to 0.882^o. Based on these two values, it can be concluded that the structure optimized at B3LYP-D3BJ/6-311++G(d,p) resembles the most experimental one.

Additionally, UV-Vis spectra were used to verify the applicability of the chosen level of theory. The experimental spectrum consists of three closely positioned peaks between 280 and 320 nm and one at 240 nm. The calculated values, at B3LYP-D3BJ level of theory, are 315 nm (HOMO→LUMO), 308 nm (HOMO-1→LUMO), 292 nm (HOMO-2→LUMO), and 245 nm (HOMO-1→LUMO+1). These results prove that the experimental wavelengths are well reproduced. The differences can be attributed to the specific interactions with the solvent as they change the energy of electronic levels.

The experimental NMR spectra were also well-reproduced with parameters R and MAE being 0.994 and 0.15 ppm for ^{1}H NMR and 0.999 and 7.37 ppm for ^{13}C NMR. The lowest differences in values were obtained for aromatic and coumarin hydrogen and carbon atoms due to the rigidity of these moieties. The noticeable differences are observed for the methyl group and aliphatic chain because atoms in these parts are more flexible and there is a possibility of free rotation.

CONCLUSION

In this contribution, the synthesis under mild conditions of the octopamine-coumarin derivative is presented, together with the crystallographic structure. The bond lengths and angles were well-reproduced by the optimization employing common functionals, although, the lowest mean average errors were obtained for the structure optimized at the B3LYP-D3BJ/6-311++G(d,p) level of theory. The theoretical wavelengths of electronic transitions are very close to the experimental ones. High values of R (0.994 and 0.999) and low values of MAE (0.15 and 7.37 ppm) were obtained when theoretical and experimental ^{1}H and ^{13}C NMR spectra were compared.

Acknowledgement

The authors acknowledge the Ministry of Education, Science and Technological Development of the Republic of Serbia for the financial support (Agreement No. 451-03-9/2021-14/200146 and 451-03-9/2021-14/200378) and the Science Fund of the Republic of Serbia (Serbian Science and Diaspora Collaboration Program: Knowledge Exchange Vouchers, No. 6388843, Project Acronym: TumorSelCoum)

REFERENCES

[1] D. Dimić, Ž. Milanović, G. Jovanović, D. Sretenović, D. Milenković, Z. Marković, J. Dimitrić Marković, Comput. Biol. Chem, 2019, 84, 107170

[2] M.J. Frisch, G. W. Trucks, H. B. Schlegel, et al. Gaussian 09, Revision C. 01, Gaussian Inc. Wallingford, CT. USA, 2010.

DFT OPTIMIZATION AND FUKUI ANALYSIS OF SELECTED 1,4-BENZODIAZEPIN-2-ONE DRUGS

D. Dimić[1], N. Ristivojević[1], J. Đorović-Jovanović[2] and A. A. Rakić[1]

[1]*University of Belgrade, Faculty of Physical Chemistry, Studentski trg 12-16, 11000 Belgrade, Republic of Serbia. (ddimic@ffh.bg.ac.rs)*
[2]*Department of Science, Institute of Information Technologies, University of Kragujevac, Jovana Cvijića bb, 34000 Kragujevac, Republic of Serbia*

ABSTRACT

1,4-Benzodiazepin-2-ones are an important class of drugs with a variety of structural modifications. Five of them (nordiazepam, diazepam, oxazepam, temazepam, and nitrazepam) were optimized at the M06-2X/6-311++(d,p) level of theory based on the crystallographic structure. After the comparison, quantified by the correlation coefficient and mean average error, these structures underwent the Natural Bond Orbital (NBO) analysis and the Condensed Fukui functions (CFFs) were calculated. The most reactive positions for electrophilic, nucleophilic, and radical attach were determined.

INTRODUCTION

Benzodiazepin-2-ones are a class of drugs that are in use for over 50 years for various conditions, such as epilepsy, alcohol withdrawal, depression, and insomnia [1,2]. Various other beneficial physiological effects are also known. The plethora of structural modifications led to the refinement of their physicochemical properties, stabilities, and activities. Besides extensive experimental investigations, quantum-chemical methods have proven to be important for the analysis, reactivity, and prediction of drug behavior [1].

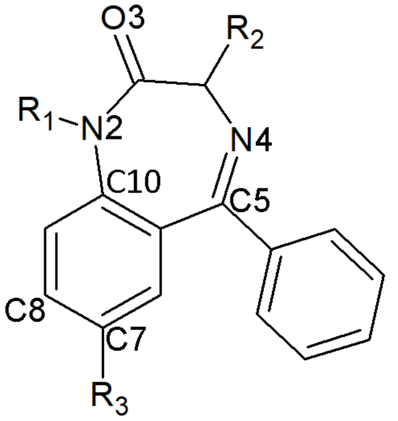

	R_1	R_2	R_3
(NO)nordiazepam	H	H	Cl
(DI)diazepam	CH_3	H	Cl
(OX)oxazepam	H	OH	Cl
(TE)temazepam	CH_3	OH	Cl
(NI)nitrazepam	H	H	NO_2

Figure 1. Structures of investigated 1,4-benzodiazepin-2-one drugs

In this contribution five of the 1,4-benzodiazepin-2-one drugs, namely nordiazepam (NO), diazepam (DI), oxazepam (OX), temazepam (TE), and nitrazepam (NI) (Figure 1) are optimized by DFT methods based on the crystallographic structures. After the comparison of bond lengths and angles of experimental and theoretical structures, the NBO analysis is performed to calculate the Fukui functions. These molecules were selected so that the influence of the specific substituents could be examined.

THEORETICAL METHODS

The crystallographic structures were obtained from the Cambridge Crystallographic Data Centre (CCDC) (CCDC: 149151 (NO), 1142317 (DI), 1226369 (OX), 1317863 (TE), and 1219355 (NI)) and later reoptimized at the M06-2X/6-311++G(d,p) level of theory as implemented in the Gaussian program package [3]. This functional was suggested by the authors since it adequately described the thermodynamic parameters and structure of various molecules. The Natural Bond Orbital (NBO) analysis, implemented in the Gaussian program package, was performed to obtain the natural charges so that Condensed Fukui functions (CFFs) can be calculated as follows:

$$f_A^+ = q_N^A - q_{N+1}^A \tag{1}$$

$$f_A^- = q_{N-1}^A - q_N^A \tag{2}$$

$$f_A^0 = [q_{N-1}^A - q_{N+1}^A]/2 \tag{3}$$

The given equations can be used for the determination of the affinity of atom A towards nucleophilic, electrophilic, and radical attack. The values of $q_N{}^A$, $q_{N-1}{}^A$, and $q_{N+1}{}^A$ represent the NBO charges for the neutral, anionic, and cationic species, respectively.

RESULTS AND DISCUSSION

The experimental and theoretical bond lengths and angles were compared based on two parameters, namely the correlation coefficient (R) and mean average error (MAE). These values for each of the analyzed drugs are given in Table 1.

Based on the results presented in Table 1, it can be concluded that the chosen level of theory, M06-2X/6-311++G(d,p) describes well the experimental structures. The values of R are above 0.99 for bond lengths and above 0.93 for bond angles. On the other hand, MAE values for bond lengths and angles are below 0.01 Å and 0.06° for all of the investigated structures. It should be kept in mind that the optimization of the structure was performed for an isolated molecule in a vacuum and some discrepancy is expected. Nevertheless, this result proved that these structures could be used for further analysis. From the structural point of view, these molecules represent rigid structures with extended delocalization between aromatic ring and heterocycle. The only rotatable part is the aromatic ring without substituents.

Table 1. The correlation coefficient and mean average error for investigated structures.

Molecule		NO	DI	OX	TE	NI
Bond lengths (Å)	R	0.99	0.99	0.99	0.99	0.99
	MAE	0.01	0.01	0.01	0.01	0.01
Bond angles (°)	R	0.98	0.93	0.99	0.98	0.96
	MAE	0.58	0.65	0.51	0.55	0.68

The reactivity of molecules is investigated by calculating the CFFs. The structural differences between these molecules are substituents on the aromatic ring (Cl, NO_2, and Br), presence of methyl group on N1 (DI, and TE), and presence of OH group in structures of OX and TE. It is not expected that the values of CFFs of atoms in the rotatable aromatic ring will be influenced by the substituents, therefore only atoms with the three highest values of CFFs are discussed in the proceeding paragraphs.

The most reactive position for the electrophile attack is the nitrogen atom in position 2, with the following values ND (0.160 *e*), DI (0.193 *e*), OX (0.136 *e*), TE (0.171 *e*), and NI (0.183 *e*). This position is not influenced by the presence of various substituents. The O3 atom is another active position in ND, DI, OX, and TE. The electronegative atom Cl is very reactive towards electrophile attack. The f_A^- values are between 0.128 and 0.145 *e*. In NI third most reactive position is C7 (0.138 *e*) due to the presence of the electron-withdrawing NO_2 group.

The reactive positions for nucleophile attack include N4, C5, and C8 of NO, DI, OX, and TE. This result shows that the interactions with amino acids in proteins can occur both with the aromatic ring and heterocycle. In mentioned molecules, these values are around 0.160 *e* for N4, 0.130 *e* for C5, and 0.120 *e* for C8. The carbon atoms of the aromatic ring are slightly negatively charged (-0.2 *e*) except for C10 which is a neighboring atom of N2. The atoms of the nitro group in the structure of NI have negative charges as well, with values -0.494, 0.390, and -0.390 *e* for nitrogen and two oxygen atoms, respectively. These atoms are a very potent position for nucleophilic attack, with f_A^+ being 0.121 *e* (N), 0.198 *e* (O), and 0.198 *e* (O).

The attack of radical species can be expected for the atoms in positions O2, N4, and Cl of NO, DI, OX, and TE. It is important to mention that the electron delocalization in investigated species includes all of these atoms except for Cl. The values for f_A^0 are around 0.1 *e* for all mentioned atoms, which shows no difference in their reactivity. On the other hand, the NI molecule differs since N4 and oxygen atoms of the NO_2 group are the most reactive sites, with oxygen atoms being more probable with f_A^0 of around 0.13 *e*.

Based on the presented values, the most reactive positions in investigated structures are the electronegative atoms (N2, N4, O3, and Cl), electronegative group (NO_2), the carbon atom in position 8 of the aromatic ring, and the carbon atom of heterocycle in position 5. This analysis leads to the conclusion that these atoms and groups are most likely to form the interactions in the active positions of proteins. The choice of substituents allows the introduction of new active positions, therefore careful selection is needed for the desired pharmacological effects and further experimental and theoretical analyses are needed.

CONCLUSION

The theoretical analysis of 1,4-benzodiazepin-2-one molecules is an effective way for the prediction of their reactivity and interactions with proteins. Structures of nordiazepam, diazepam, oxazepam, temazepam, and nitrazepam were optimized at the M06-2x/6-311++G(d,p) level of theory and compared with crystallographic data. The correlation coefficients between experimental and theoretical bond lengths and angles are higher than 0.99 and 0.93. The mean average error is below 0.01 Å and 0.6°. The values of Condensed Fukui Functions (CFFs) showed various active positions including hetero- and carbon atoms of heterocycle, carbon atoms of the aromatic ring, and substituents (Cl and NO_2).

Acknowledgement

The authors acknowledge the financial support by the Ministry of Education, Science and Technological Development of the Republic of Serbia (Agreement No. 451-03-9/2021-14/200146 and 451-03-9/2021-14/200378)

REFERENCES

[1] B. Pem, V. Vrček, Int. J. Qunatum. Chem., 2018, 118, e25523.
[2] J. Spencer, R.P. Rathnam, B.Z. Chowdhry, Future Med. Chem., 2010, 2, 1441.
[3] M.J. Frisch, G. W. Trucks, H. B. Schlegel, et al. Gaussian 09, Revision C. 01, Gaussian Inc. Wallingford, CT. USA, 2010.

THE NATURE OF STACKING INTERACTIONS OF THE RESONANCE-ASSISTED HYDROGEN-BRIDGED RINGS

J. P. Blagojević Filipović [1], S. D. Zarić [2]

[1] *Innovation Centre of the Faculty of Chemistry,*
Studentski trg 12-16, 11000 Belgrade, Serbia, (jbfilipovic@chem.bg.ac.rs)
[2] *University of Belgrade, Faculty of Chemistry, Studentski trg 12-16, 11000 Belgrade, Serbia*

ABSTRACT

The Symmetry Adapted Perturbation Theory (SAPT) energy decomposition analysis is applied for studying the nature of stacking interaction occurring in homodimers of resonance-assisted hydrogen-bridged (RAHB) rings and heterodimers of RAHB and benzene rings. The contribution of various energy terms is dependent on the composition of a RAHB ring and can be rationalized based on electrostatic potential maps.

INTRODUCTION

The existence of mutual stacking interaction between Resonance-Assisted Hydrogen-Bridged (RAHB) rings (Figure 1a), as well as stacking interactions between RAHB and C_6-aromatic rings is confirmed by analysing the crystal structures from the Cambridge Structural Database (CSD) and by quantum-chemical calculations in the gas phase [1,2]. It is observed that both RAHB/RAHB and RAHB/C_6-aromatic rings form parallel layers in the crystal structures and that these layers are in both cases separated by 3.0-4.0 Å in the majority of the structures. Thus, contacts between the layers can be assigned to stacking interactions. Namely, we used malonaldehyde molecule (Figure 1b), its mononitrogen (Figure 1c) and dinitrogen analogue (Figure 1d) as prototypes for the RAHB rings, since these rings are the most frequently present in both sets of structures in the CSD (RAHB/RAHB rings and RAHB/C_6-aromatic rings) [1,2]. We used benzene molecule as a prototype for a C_6-aromatic molecule. In this work, we present a Symmetry Adapted Perturbation Theory (SAPT2+3, [3]) energy decomposition, calculated for RAHB/RAHB and RAHB/benzene stacking interactions and discuss the nature of these interactions.

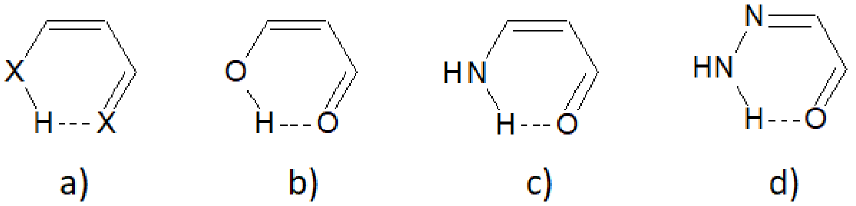

Figure 1. Examples of the RAHB rings; a) general formula, electronegative atoms, usually N, O and S forming intramolecular hydrogen bond are connected by a π-system; b) malonaldehyde; c) the mononitrogen analogue of malonaldehyde; d) the dinitrogen analogue of malonaldehyde

METHODS

On the basis of the SAPT energy decomposition scheme the interaction energy is consisted of the electrostatic, induction, dispersion and exchange-repulsion terms. Dispersion and exchange-repulsion terms are sometimes combined into a net dispersion term [4]. A SAPT2+3 energy decomposition analysis was performed in this work on structures corresponding to the lowest minima on the RAHB/RAHB and the RAHB/benzene potential energy curves [1,2]. The SAPT2+3 calculations were performed at cc-pVQZ level, since it was shown to be in good agreement with CCSD(T) method at the Complete Basis Set limit (CCSD(T)/CBS) [1,2]. To perform SAPT2+3 calculations we used PSI4 program package [5]. The electrostatic potential maps were calculated at the outer contour of electron density of 0.001 a. u. using Wavefunction Analysis Surface Analysis Suite (WFA-SAS) program [6] by the wavefunctions calculated in Gaussian09 [7] at MP2/cc-pVTZ level.

RESULTS AND DISCUSSION

The dispersion term is dominant in all studied systems (Table 1), but it is significantly cancelled or even surpassed by the exchange-repulsion term. Thus, when we compare RAHB/RAHB stacked systems [1] we can see that the electrostatic term is dominant in $H_4C_3O_2/H_4C_3O_2$ and H_5C_3NO/H_5C_3NO systems, since net dispersion is quite small (in $H_4C_3O_2/H_4C_3O_2$ system) or even repulsive (in H_5C_3NO/H_5C_3NO system). The main reason for significantly smaller total interaction energy in $H_4C_2N_2O/H_4C_2N_2O$ system, compared to the other two RAHB /RAHB stacking interactions is a smaller electrostatic contribution. On the other hand, in this system, net dispersion contribution is almost equal to the electrostatic contribution (Table 1).

Similar observations apply to RAHB/benzene stacked dimers [2]. Dispersion terms are almost cancelled in $H_4C_3O_2$/benzene and H_5C_3NO/benzene systems, while net dispersion significantly contributes to the interaction in $H_4C_2N_2O$/benzene system. However, even in this system the electrostatic contribution is more pronounced than net dispersion (Table 1). Electrostatic contribution is dominant in $H_4C_3O_2$/benzene and H_5C_3NO/benzene. Induction energy term contributes to the interaction energy in all studied RAHB/RAHB and RAHB/benzene systems, but to a smaller extent (Table 1).

We can observe that differences occur in the nature of RAHB stacking interactions for the three rings. These differences can be explained by electrostatic potential maps (Figure 2). It can be seen that $H_4C_3O_2$ and H_5C_3NO molecules both have a dipole moment. At the other hand, a clearly pronounced dipole moment can not be observed in case of $H_4C_2N_2O$ molecule. Thus, significant contribution of electrostatic interaction in antiparallel $H_4C_3O_2/H_4C_3O_2$ and H_5C_3NO/H_5C_3NO can be attributed to antiparallel dipole-dipole interactions. Benzene molecule does not possess a dipole moment, but it possesses a quadrupole moment, thus a smaller electrostatic term in $H_4C_3O_2$/benzene and H_5C_3NO/benzene systems than in the corresponding RAHB/RAHB systems is a consequence of a dipole-quadrupole interaction. For that reason, the overall interaction is stronger in $H_4C_3O_2/H_4C_3O_2$ and H_5C_3NO/H_5C_3NO systems than in $H_4C_3O_2$/benzene and H_5C_3NO/benzene systems. Since $H_4C_2N_2O$ molecule does not possess a clearly pronounced dipole moment, the electrostatic terms are less dominant than in systems involving $H_4C_3O_2$ and H_5C_3NO molecules. Also, net dispersion is significant, which can be attributed to the smaller exchange-repulsion term (Table 1).

Table 1. SAPT2+3 energy decomposition analysis; all energy values are in kcal/mol. Net dispersion is a sum of exchange-repulsion and dispersion terms.

Model system	ELST	EXCH	IND	DISP	NET DISP	SAPT 2+3
$H_4C_3O_2/H_4C_3O_2$	−3.55	5.92	-0.60	-6.10	-0.18	-4.32
H_5C_3NO/H_5C_3NO	−4.81	7.86	-1.12	-6.74	1.12	-4.81
$H_4C_2N_2O/H_4C_2N_2O$	-0.89	3.76	-0.33	-4.64	-0.88	-2.09
$H_4C_3O_2$/benzene	-2.68	6.51	-0.80	-6.63	-0.12	-3.60
H_5C_3NO/benzene	-2.60	6.51	-0.92	-6.52	-0.01	-3.53
$H_4C_2N_2O$/benzene	-1.61	4.70	-0.51	-5.69	-0.99	-3.11

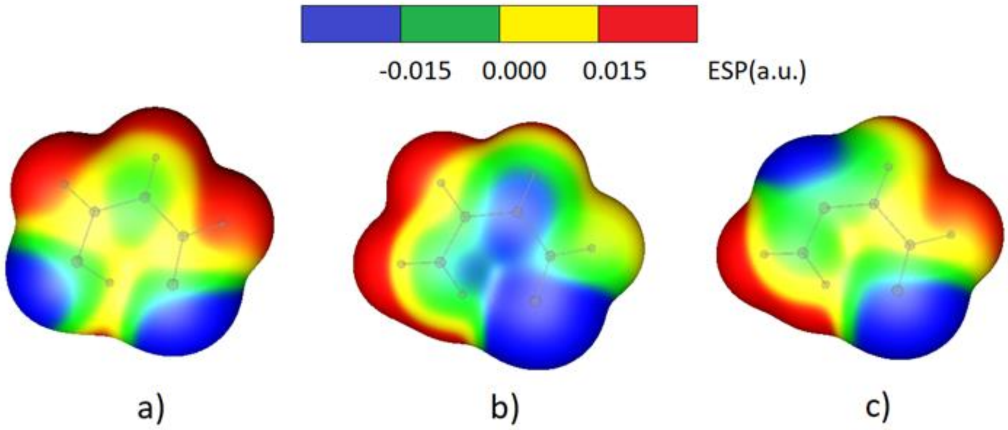

Figure 2. The electrostatic potential maps of a) malonaldehyde; b) the mononitrogen analogue of malonaldehyde; c) the dinitrogen analogue of malonaldehyde (Figure 1)

CONCLUSION

The SAPT2+3 energy decomposition analysis is performed on RAHB/RAHB and RAHB/benzene model systems. The dispersion contribution is dominant in all studied systems. Depending on the dipole moment intensity, the electrostatic term is dominant or comparable with a net dispersion term, which is often presented as a sum of dispersion and exchange-repulsion terms. In a system that does not possess a pronounced dipole moment, the electrostatic contribution is smaller than in systems with a pronounced dipole moment. Also, exchange-repulsion term is smaller, which leads to a more significant net dispersion term. The induction energy term contributes to the stacking interaction energy in all systems, but not to a large extent.

Acknowledgement

This work was supported by the Serbian Ministry of Education, Science and Technological Development (Contract numbers: 451-03-9/2021-14/200168 and 451-03-9/2021-14/200288).

REFERENCES

[1] J. P. Blagojević Filipović, M. B. Hall, S. D. Zarić, Cryst. Growth Des. 2019, 19, 5619-5628.

[2] J. P. Blagojević Filipović, M. B. Hall, S. D. Zarić, Phys. Chem. Chem. Phys. 2020, **22**, 13721-13728.

[3] T. M. Parker, L. A. Burns, R. M. Parrish, A. G. Ryno, C. D. Sherrill, J. Chem. Phys. 2014, 140, 094106.

[4] E. G. Hohenstein, C. D. Sherrill, J. Phys. Chem. A, 2009, 113, 878-886.

[5] R. M. Parrish, L. A. Burns, D. G. A. Smith, A. C. Simmonett, A. E. DePrince, E. G. Hohenstein, U. Bozkaya, A. Y. Sokolov, R. Di Remigio, R. M. Richard, et al. J. Chem. Theory Comput., 2017, 13, 3185-3197.

[6] F. A. Bulat, A. Toro-Labbé, T. Brinck, J. S. Murray, P. J. Politzer, Mol. Model. 2010, 16, 1679−1691.

[7] M. J. Frisch, G. W. Trucks, H. B. Schlegel, G. E. Scuseria, M. A. Robb, J. R. Cheeseman, G. Scalmani, V. Barone, G. A. Petersson, H. Nakatsuji, et al. Gaussian 09, Revision D.01; Gaussian, Inc., 2016.

C - *Kinetics, Catalysis*

ROLE OF MECHANOCHEMISTRY IN ECO-FRIENDLY AND SUSTAINABLE PREPARATION AND RECYCLING OF CATALYSTS

Z. Cherkezova-Zheleva

Institute of Catalysis, Bulgarian Academy of Sciences,
Acad. G. Bonchev St., Bldg. 11, 1113 Sofia, Bulgaria
*E-mail: zzhel@ic.bas.bg, fax: +359 2 971-29-69

ABSTRACT

Ensuring a secure, reliable and unhindered supply of raw materials is crucial for the competitiveness and growth of the European Union (EU) economy. The EU is taking actions to secure the access of all raw materials, but some of them are defined as ‘critical’. Difficulties in the access to critical raw materials (CRMs) are expected to depress industrial sectors vital to European Union. The current conditions of material supply and their evolution in EU and international markets strongly affect the present-day list of CRMs. The current Fourth list of CRMs was published in 2020 and covers a larger number of materials. The sustainable solution of the CRM problem is design of advanced CRM-free or low content materials, but also the optimal use, enhanced recycling and sustainable mining. In this context, the European Commission set up a number of initiatives to promote innovative solutions and accelerate the innovations in the field of raw materials. A lot of efforts are concentrated on the substitution of CRMs together with preservation and improvement of the advanced properties of the respective materials. However, the more realistic option relates to optimisation of CRM life cycle covering extraction and processing of the raw materials, manufacturing, distribution, use, recycling, and final disposal, as well as the environmental impact of a product through its life cycle.

Currently preparation of heterogeneous catalysts with advanced properties is strongly related to the use of one or more CRM such as Cr, rare earths, platinum group metals, etc. Criticality assessment of some raw materials in regard of catalysts preparation will be presented.

Mechanochemical treatment can be successfully used as a method for CRM recovery and recycling. On the other hand, the role of Mechanochemistry in synthesis and/or activation of CRM-free catalysts is a large and growing field of research and innovations. The research activities in this fast-moving area are focused on the development of new concepts for design and synthesis of non-CRM catalysts with the same or better activity and selectivity compared to the current ones. Improvement of full material life cycle of obtained non-CRM catalysts together with better recycling, reuse and repair of CRM-based catalysts are open areas for new ideas, scientific and innovative projects.

Acknowledgement

The authors gratefully acknowledge the financial support of the Bulgarian National Science Fund at the Ministry of Education and Science - Project № КП-06-КОСТ/18/ 2019. This article is based on the project activities of COST Action CA 18112 “Mechanochemistry for Sustainable Industry” (Mech@SustInd), supported by COST (European Cooperation in Science and Technology).

Keywords: Mechanochemistry, Catalysis, Critical Raw Materials (CRM), CRM-free Catalysts, Material preparation and characterization.

ARTIFICIAL SECONDARY STRUCTURES IN THE DESIGN OF NEW CATALYSTS AND NEW MATERIALS

S. I. Kirin

Ruđer Bošković Institute, Bijenička 54, HR-10000 Zagreb, Croatia
(Srecko.Kirin@irb.hr)

ABSTRACT

In this conference paper, an author's review in the field of bioinorganic chemistry, stereochemistry, homogeneous catalysis and medicinal inorganic chemistry is presented, with particular emphasis on physical chemistry aspects. Within this work, bioconjugates of amino acid containing phosphine or nitrogen ligands were utilized for metal coordination. The metal complexes were extensively characterized by a number of instrumental spectroscopic or crystallographic techniques and by DFT calculations. The metal complexes were used as catalysts in the selective preparation of intermediates in the synthesis of active pharmaceutical ingredients. Special attention was paid to the formation of specific supramolecular artificial secondary structures formed by the amino acid moieties that control the stereochemical outcome of the catalytic reactions. In addition, the metal complexes served as building blocks for supramolecular architectures as well as potent anticancer agents.

INTRODUCTION

Proteins and nucleic acids are natural macromolecules that contain a large number of amino acid or nucleotide monomers, respectively. The secondary structures of these macromolecules are particularly important for their function in a biological environment. In nature, out of the wide variety of potentially possible secondary structures, proteins and nucleic acids are known to adopt only a very small number of secondary structures. Those privileged secondary structures are for example α-helix and β-sheet for proteins, or B-DNA for nucleic acids.

Ferrocenes 1,n'-disubstituted with amino acids are an interesting class of compounds that adopt only a limited number of secondary structures as well.[1] Most commonly, a *Herrick* conformation is found, with two inter-strand hydrogen bonds forming two formal 10-membered rings, Figure 1. Also known are the *van Staveren* conformation, with one inter-strand hydrogen bond forming a formal 7-membered ring and the *Xu* conformation (or open conformation) without any hydrogen bonds.[1] If the amino acids in these ferrocene bioconjugates are chiral, the inter-strand hydrogen bonding induces a new chiral element, namely helical chirality of the central ferrocene moiety. Most importantly, in both the *Herrick* and the *van Staveren* conformation, L-chirality of the pendant amino acids induced a *P*-helix at the ferrocene, Figure 1. The working hypothesis of our research is that this specific induction of chirality can find applications, for example in asymmetric catalysis.

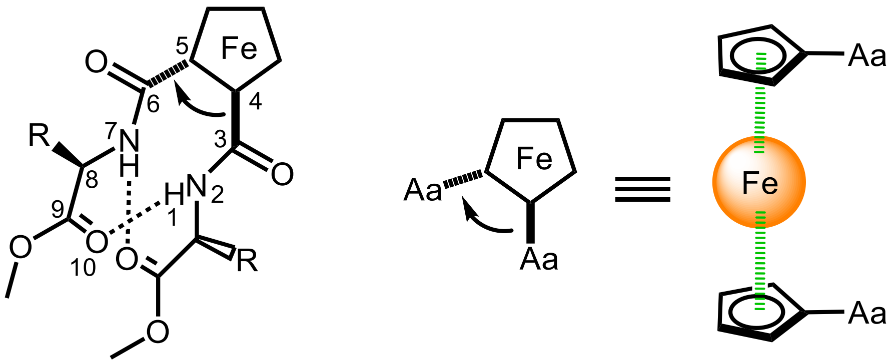

Figure 1. Herrick conformation (left), helical chirality of ferrocene (right). Aa = amino acid(s), curved arrows indicate sign of helical chirality.

RESULTS AND DISCUSSION

Metalloenzymes are in general very selective catalysts with high reaction rates, but work often only with a limited number of substrates and their application can be expensive. On the other hand, if a small metal complex is catalytically active, it can have a rather broad substrate scope and it can be much cheaper, but selectivity and reaction rates are far behind enzymes. The difference between metalloenzymes and small metal complexes is the outer-coordination sphere present in the metalloenzymes. Consequently, in order to model the catalytic function of an enzyme, it is not enough to consider only the active site, but at least some of the outer-coordination sphere should be included as well. However, this approach can only be efficient, if the outer-coordination sphere of the small metal complex is very well defined, for example as shown for ferrocene amino acids, Figure 1.

Prominent examples of small metal complexes with a well-defined outer-coordination sphere are rhodium triphenylphsophines substituted with chiral amino acids or chiral diamines, Figure 2.

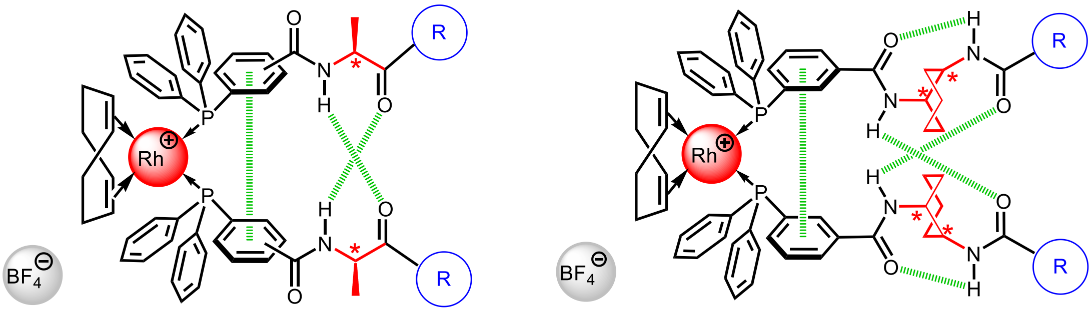

Figure 2. Schematic repre-sentation of rhodium cata-lysts, amino acid based (left) and diamine based (right).

These complexes can be used as catalysts in asymmetric hydrogenation reactions of α,β-unsaturated amino acids or as model compounds of intermediates in the synthesis of active pharmaceutical ingredients.[2,3] While optimized amino acid derivatives achieve up to 84% ee, the selectivity of diamine derivatives is up to 97% ee. Moreover, these catalytic systems are particularly interesting because they feature "backdoor induction" of chirality. The coordination sphere of the catalytic metal is only prochiral, while the chirality is transmitted from the distant chiral amino acids or diamines forming a *Herrick-like* conformation.

The higher selectivity of the diamine catalysts, if compared to the amino acid derivatives, prompted a study of 1,n'-disubstituted ferrocene diamines, Figure 3 (left), as opposed to their amino acid derivatives, Figure 3 (right).[4] Diamine ferrocenes expectedly showed a high stability of a *Herrick-like* conformation in DCM solution. In addition, it was surprisingly found that they could act as chirooptical switches between two stable states. The ferrocene absorption in the visible part of the CD spectrum can be inverted by solvent exchange or acid addition. The inversion is achieved through a change of the hydrogen-bonding pattern.

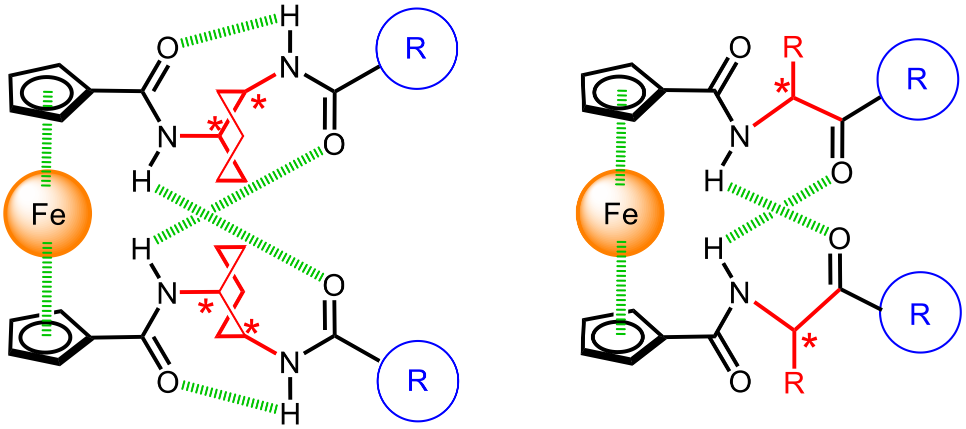

Figure 3. Schematic representations of ferrocene diamines (left) and ferrocene amino acids (right).

As shown in the previous paragraphs, in order to define the outer-coordination sphere of the metal complex by hydrogen bonding, spatial proximity of the two organic ligands in a *cis*-isomer is beneficial. An example where a *trans*-arrangement of the ligands results in a tightly bound dimer is provided by a palladium complex with amino acid substituted triphenylphosphines, Figure 4.[5] The self-assembly of the dimer is governed by the *cis-trans* isomerisation of the palladium metal centre. The dimer has a molecular mass of about 3000 g mol^{-1} and is held together by 16 hydrogen bonds and aromatic stacking.

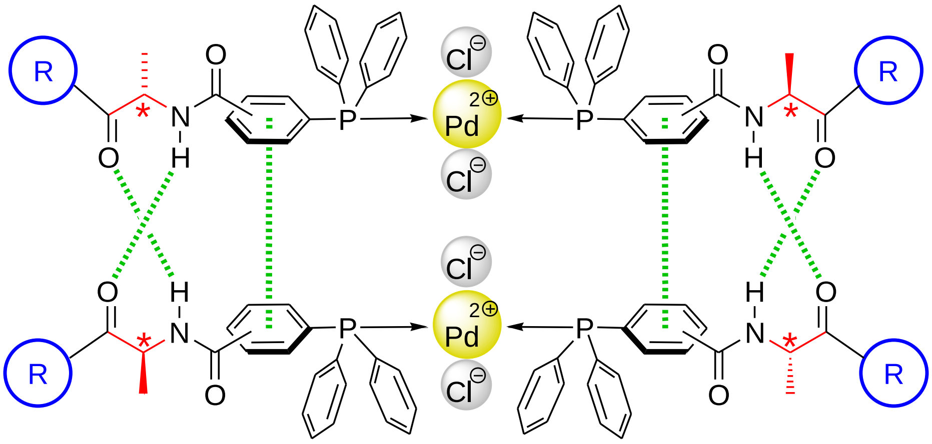

Figure 4. Schematic representation of a palladium complex dimer.

So far, organometallic and inorganic examples were discussed in this review. However, for the selective formation of a *Herrick-like* conformation, the presence of a metal cation is not required, Figure 5 (left).[6] An aminopyridine ligand exhibits supramolecular chirality in solution, based on self-assembly of the building blocks. Interestingly, this is the first reported system where the supramolecular chirality is completely inverted by addition of metal ions, e.g. zinc.

Finally, (*p*-cymene)-ruthenium bioconjugates with *Herrick-like* secondary structures have significant anticancer activity. An investigation using human cervical carcinoma cell lines revealed IC_{50} values as low as 5 μM, Figure 5 (right).[7] These metal complexes have been shown to cause non-oxidative protein damage and induce autophagy.

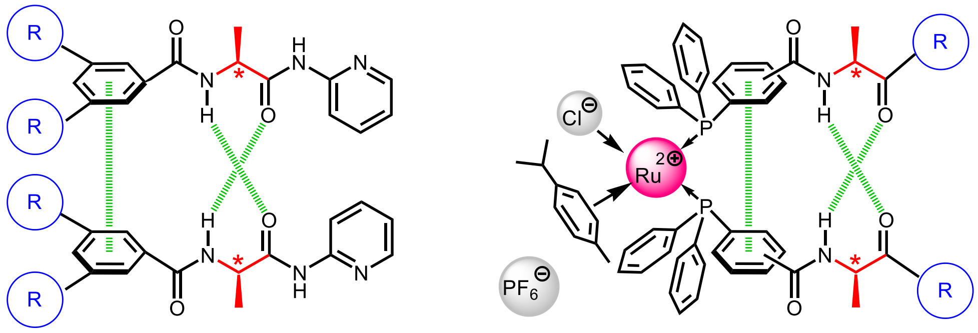

Figure 5. Schematic represen-tations of an all-organic deri-vative (left) and a ruthenium complex (right).

CONCLUSION

Herein, a number of amino acid bioconjuates is discussed, including their metal complexes with rhodium(I), iron(II), palladium(II), zinc(II) and ruthenium(II). A common feature of these rather different compounds is the superior stability of a small number of secondary structures. Obviously, the concept of privileged secondary structures does apply not only to natural macromolecules like proteins and nucleic acids, but also to significantly smaller artificial systems forming *Herrick-like* conformations. The general goal of this research is to study these systems and to find appropriate applications in catalysis, activity in biological environment and beyond. Current efforts are directed towards the development of amino acid bioconjugates of tridentate nitrogen ligands, potentially capable of forming similar artificial secondary structures. [8,9]

Acknowledgement

This work was partially supported by CAT Pharma (KK.01.1.1.04.0013), a project co-financed by the Croatian Government and the European Union through the European Regional Development Fund – the Competitiveness and Cohesion Operational Programme.

REFERENCES

[1] S. I. Kirin, H.-B. Kraatz, N. Metzler-Nolte, Chem. Soc. Rev., 2006, 35, 348-354.
[2] Z. Kokan, Z. Glasovac, M. Majerić Elenkov, M. Gredičak, I. Jerić, S. I. Kirin, Organometallics, 2014, 33, 4005-4015.
[3] S. Opačak, Z. Kokan, Z. Glasovac, B. Perić, S. I. Kirin, Eur. J. Org. Chem. 2019, 2115-2128.
[4] S. Opačak, B. Perić, D. Babić, Ž. Marinić, V. Smrečki, B. Pem, I. Vinković Vrček, S. I. Kirin, Dalton Trans., 2021, 50, 4504-4511.
[5] Z. Kokan, B. Kovačević, Z. Štefanić, P. Tzvetkova, S. I. Kirin, Chem. Commun., 2018, 54, 2094-2097.
[6] Z. Kokan, B. Perić, M. Vazdar, Ž. Marinić, D. Vikić-Topić, E. Meštrović, S. I. Kirin, Chem. Commun., 2017, 53, 1945-1948.
[7] M. Pernar, Z. Kokan, J. Kralj, Z. Glasovac, L.-M. Tumir, I. Piantanida, D. Eljuga, I. Turel, A. Brozovic, S. I. Kirin, Bioorg. Chem., 2019, 87, 432-446.
[8] N. Pantalon Juraj, G. I. Miletić, B. Perić, Z. Popović, N. Smrečki, R. Vianello, S. I. Kirin, Inorg. Chem., 2019, 58, 16445-16457.
[9] N. Pantalon Juraj, S. I. Kirin, Coord. Chem. Rev., 2021, accepted.

VISIBLE LIGHT PROMOTED PHOTOREDOX CATALYSIS IN MICROFLOW SYSTEMS

B. P. Bondžić

University of Belgrade, Institute of Chemistry, Technology and Metallurgy – National Institute of the Republic of Serbia, Njegoševa 12, 11000 Belgrade, Serbia.
(bbondzic@chem.bg.ac.rs)

ABSTRACT

Lately, the application of microfluidic devices has been a very promising strategy in organic chemistry, and one of the research fields in which microfluidics have shown great potential is visible light photochemistry. There are several advantages when conducting transformations in flow compared to the batch reactions, in particular: a more predictable reaction scale-up, decreased safety hazards, improved reproducibility and yields, shorter residence time, higher reaction selectivity and product purity and lower catalyst loading. In addition, for photochemical transformations, the high surface-area-to-volume ratios typical of flow reactors allow for improved light efficiency. Light penetration in batch reactors is limited by decreasing light transmission over distance in a liquid medium.

Having all these advantages in mind, it comes as no surprise that visible light promoted photoredox chemistry in flow has been applied in functionalizations biologically active organic molecules.

A merger of organocatalysis and visible light photoredox catalysis performed in flow allowed access to a wide range of functionalized N-aryl-substituted tetrahydroisoquinolines (THIQs) in a formal C–H oxidation/Mannich reaction. Strecker type functionalization and copper-catalyzed alkynylation of several *N*-aryl-substituted THIQs were also successfully performed in flow, giving valuable products with high efficiencies. Three types of microreactors i.e., PFA microtube flow reactor, PDMS polymeric microreactor and glass/silicon reactor were designed and applied in these model reactions. The application of custom-made porous polymeric type microreactors proved to be crucial regarding the C–H oxidation step and overall reaction performance.

METAL DUSTING AS A KEY ROUTE TO PRODUCE FUNCTIONALIZED CARBON NANOFIBERS

A. Vedyagin , I. Mishakov and Yu. Bauman

Department of Materials Science and Functional Materials,
Boreskov Institute of Catalysis SB RAS,
Pr. Lavrentieva 5, 630090 Novosibirsk, Russia. (vedyagin@catalysis.ru)

ABSTRACT

The catalytic chemical vapor deposition (CCVD) method is frequently used to produce carbon nanomaterials, which are characterized by unique properties. Such materials are applied in various fields of science and technology, and their attractiveness grows year by year. Both the size and chemical, and phase composition of the catalysts are responsible for their activity and stability. In some cases, amorphous carbon being formed blocks the active sites and thus interrupts the CCVD process. On the other hand, the metal dusting process, known as a negative phenomenon causing the destruction of the industrial metal reactors, has started to be considered as a preparative route to obtain active and stable CCVD catalysts from bulk metal precursors. The present paper is aimed to demonstrate the current state of art in the claimed field of science.

INTRODUCTION

Carbon nanomaterials are a class of materials composed of carbon atoms. Due to their unique and easily tunable properties, they are widely used in numerous fields of application, including composite materials, lubricants, capacitors, adsorbents, catalysts, biomedical delivery systems, etc. Among them, carbon nanofibers (CNF) are of special interest due to the variety of their morphologic structure and relative cheapness. The exact area of application of CNF is also determined by the presence of functional groups on the fibers' surface. The introduction of heteroatoms into the structure of CNF, as usual, noticeably modifies their properties.

One of the most commonly used approaches to obtain CNF is the catalytic chemical vapor deposition (CCVD) method. The process undergoes in accordance with the so-called carbide cycle mechanism [1]. Initially, hydrocarbon molecules (methane, ethane, propane, etc.) serving as the carbon source are decomposed into carbon and hydrogen. During this stage, the formation along with the subsequent degradation of intermediate surface carbide-like compounds on the frontal facets of the dispersed particles of iron-subgroup metals (Fe, Co, and Ni) or their alloys takes place. The second physical stage is connected with the diffusion transfer of carbon atoms through the bulk of a metal particle from the frontal facet to the rear facet. Carbon atoms reach the rear facet and initiate the formation of a graphite phase nucleus followed by the growth of graphite-like fibers of different morphology and texture. Such a complex mechanism imposes special requirements on the composition and size of metal particles. Non-compliance with these requirements turns the CCVD process to the formation of amorphous carbon, blockage of the frontal facets, and deactivation of the catalyst. Therefore, the synthesis of the catalyst's particles with the required characteristics is an actual challenge.

On the other hand, one of the major problems of the modern chemical industry is the self-destruction of metal reactors working under the carburizing atmosphere. The phenomenon underlying this process is called metal dusting or carbon erosion. Quite recently, this generally negative process was considered as a possible route for the preparation of dispersed metal particles of uniform size and chemical composition [2-6]. As reported, in the case of Ni-based systems, the induction period of the metal dusting process can be effectively shortened by using halogenated hydrocarbons as a carbon source. Moreover, the addition of alloying metals to nickel also affects the activity and efficiency of the catalyst [7-10].

The present paper summarizes all the experimental data accumulated during the last decade. The fundamental aspects of the metal dusting process were studied using the McBain balances, while the batch production of the CNF via the CCVD process was performed in a pilot-scale tubular reactor. 1,2-dichloroethane was used as the main carbon source. One-pot functionalization was provided by the addition of heteroatom-containing substances into the reaction mixture. The collected samples of CNF were characterized by a number of physicochemical techniques.

METHODS

Nickel-chrome alloy (80% Ni, 20% Cr, nichrome wire) was used as a bulk Ni-based precursor. Model Ni1-xMx (where M is Cr, Cu, Co, Fe, Pt, Mo, W, or Pd) bulk alloys were synthesized via the co-precipitation method. Thus, obtained sediments were filtered, dried, heated in hydrogen flow at a ramping rate of 20 °C/min up to 800 °C and calcined at this temperature for 30 min. The samples are labeled as *Ni-M (cp)*. The formation of alloys was confirmed by the powder X-ray diffraction (XRD) analysis, which was performed at room temperature on a Shimadzu XRD-7000 diffractometer (CuKα radiation, Ni filter on the reflected beam).

The kinetics experiments on the metal dusting process were carried out at 600 °C in a quartz flow reactor equipped with McBain microbalance, which allowed measuring of the sample's weight during the process. The volume of the produced CNF was limited by the volume of the quartz basket that corresponds to the CNF weight of a few mg. The batch production of CNF samples (a few kg) for their detailed characterization was realized in a tubular quartz reactor placed inside a high-temperature furnace. Photos of both reactors as well as carbon products are shown in Figure 1.

The CCVD experiments were arranged as follows. The specimen of the alloy was loaded inside one of the reactors. The reactor was purged with argon and hydrogen and heated up to the reaction temperature. Then, the reaction gas feed containing argon and hydrogen was passed through the saturator filled with 1,2-dichloroethane (DCE). The excess of hydrogen (37.5 vol.%) in the reaction mixture was required to promote chemical corrosion of the metallic surface and prevent it from complete chlorination. In order to provide a one-pot synthesis of CNF and their functionalization with nitrogen-containing groups, acetonitrile (8 vol.%) was added to the reaction mixture.

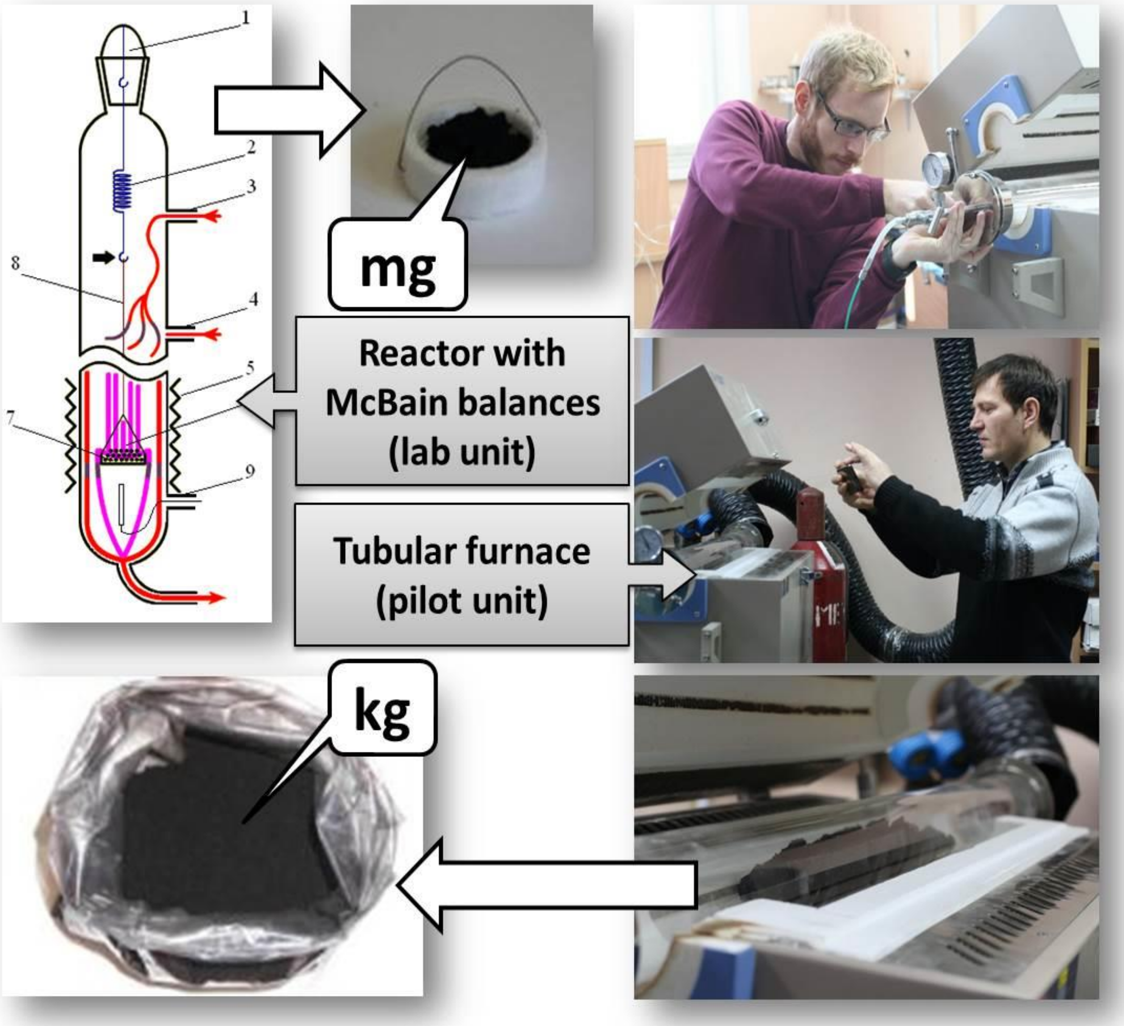

Figure 1. Experimental equipment used in the present research: McBain balances for the kinetics studies of the CCVD process (left); tubular furnace for batch production of CNF (right).

The structure and morphology of the CNF samples were studied by scanning electron microscopy (SEM) on a JSM-6460 scanning electron microscope (JEOL, Japan) at magnification factors from 8 to 300000. The transmission electron microscopy (TEM) studies were performed on a JEM-2010CX instrument (JEOL, Japan) with an accelerating voltage of 100 kV, an objective lens spherical aberration coefficient of 2.8 mm, and a line resolution of 1.4 Å. The instrument is equipped with XFlash (Bruker, Germany) X-ray energy dispersion spectrometer (EDX) having the Si-detector with an energy resolution of 130 eV. The test samples were applied as a suspension in ethanol to perforated carbon base layers fixed on a copper grid. The genesis of surface changes happening under the influence of the reaction medium at different times of exposure was also monitored by the TEM method. The measurements were carried out at 80 kV accelerating potential (JEM-1400, JEOL, Japan). The sample of NiCr wire was fixed in a standard grid holder. Then, a piece of wire was arc-curved in order to assure that the sample is fixed properly within the TEM holder. The beam was focused on the same edge of the wire.

The textural characteristics of the CNF samples were studies by a nitrogen adsorption method. The isotherms were obtained at 77.4 K on an Autosorb-iQ (Quantachrome Instruments, USA) instrument. The samples were degassed under an oil-free vacuum using a step-wise procedure, including treatment at 90 °C for 5 h and 300 °C for 10 h.

RESULTS AND DISCUSSION

Initially, the metal dusting process was studied for the bulk nichrome alloy subjected to the action of DCE vapors. For this purpose, the same piece of nichrome wire was treated under the reaction conditions for a varied period of time and then fixed in a standard grid holder of the microscope. It should be mentioned that the process starts with a prolonged induction period when no noticeable changes in the sample's weight can be registered. However, during the induction period, the surface of the nichrome wire undergoes significant alteration. As presented by a set of TEM images in Figure 2, the surface of the initial wire is relatively smooth. After just 1 minute of interaction with DCE vapor, it became evidently rough. Already after 10 minutes of the metal dusting process, the formation of dispersed metal particles accompanied by the growth of CNF takes place. 20 minutes of interaction is enough for the process to go deep inside the bulk of the wire. After 3 h of the experiment, as demonstrated by the SEM image in Figure 2, the initial wire does not exist anymore. The sample is represented by agglomerates composed of CNF with evenly distributed metal particles. Carbon yield achieves the value of 67.5 g/g_{cat}, while the specific surface area of CNF product exceeds 400 m^2/g (see Table 1).

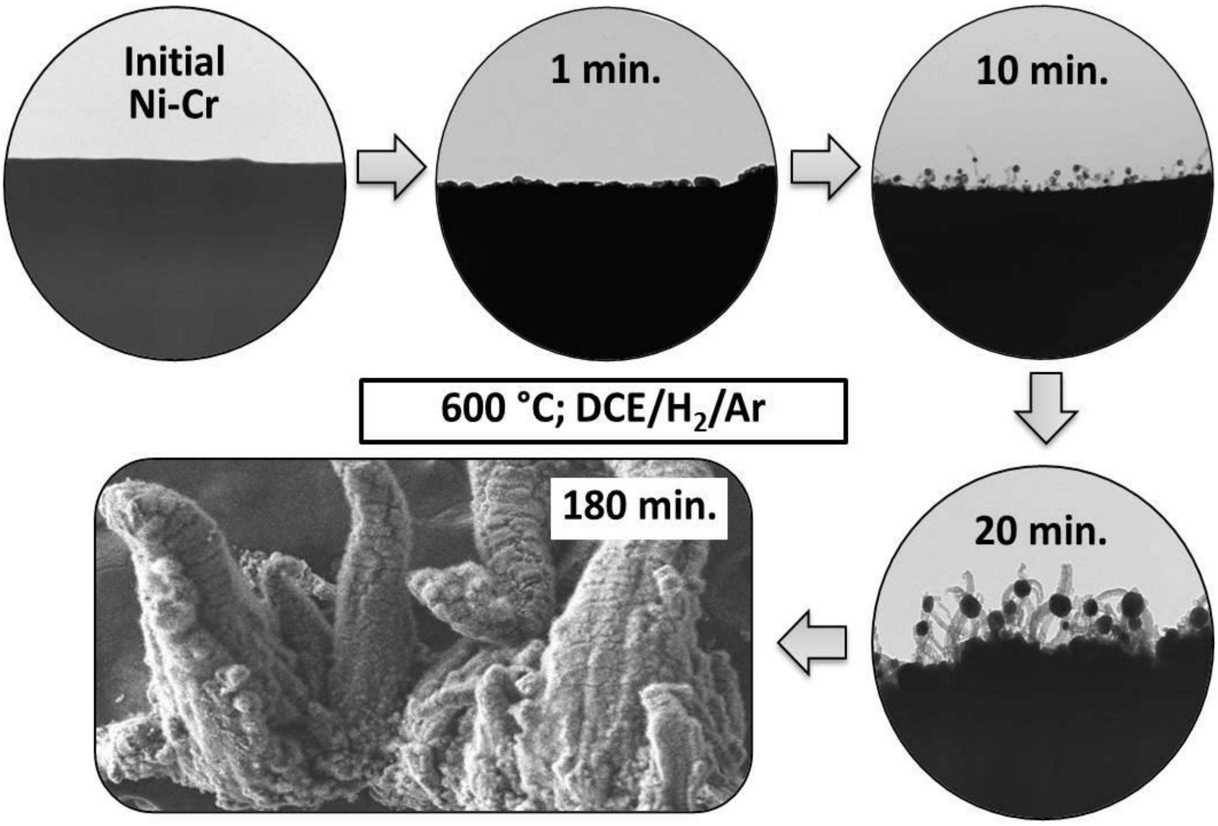

Figure 2. Scheme demonstrating the metal dusting process for the Ni-Cr wire exposed to the DCE/H_2/Ar reaction mixture at 550 °C.

Based on the detailed results of the TEM study, the general process scheme consisting of the following stages was proposed: i) adsorption and decomposition of DCE on the NiCr surface; ii) diffusion of carbon atoms to the bulk through the grain boundaries; iii) nucleation of the graphite phase; iv) disintegration of the alloy and appearance of the active nanoparticles catalyzing the CNF growth. It should be emphasized that the metal dusting process is significantly promoted by the use of chlorinated hydrocarbons in combination with H2 excess that can be explained by the action of an aggressive corrosive medium generated by the decomposition of DCE. Therefore, the controllable metal dusting process of the bulk Ni-based alloys can be considered as a new platform for the synthesis of efficient catalysts for CNF production.

Table 1. Yield and specific surface area (SSA) of the obtained CNF over Ni-based catalysts of different compositions.
Reaction conditions: DCE/H_2/Ar; 600 °C; 2 h.

Catalyst	Carbon yield, g/g_{cat}	SSA, m^2/g
Ni-Cr (wire)	67.5*	401
Ni (cp)	22.6	325
Ni-Cr (1%, cp)	29.7	280
Ni-Cu (1%, cp)	23.6	320
Ni-Co (1%, cp)	24.8	330
Ni-Fe (1%, cp)	4.1	-
Ni-Pt (4%, cp)	27.0	380
Ni-Mo (4%, cp)	33.7	311
Ni-W (4%, cp)	26.1	307
Ni-Pd (5%, cp)	24.0	382
Ni-Pd (5%, cp)	50.9**	454

*Duration of the experiment was 3 h.

**Reaction mixture contained 8 vol.% acetonitrile.

The effect of the alloying metal on the efficiency of the overall CCVD process was investigated on a series of specially prepared Ni-M alloys. It should be noted here that the concentration of each studied metal was varied in a wide range from 1 to 25 wt%, and only the samples with optimal concentration showing the best performance are compared below. The obtained data are summarized in Table 1. A monometallic Ni sample prepared via the same precipitation approach was used as a reference. As seen, the effect of the alloying metal can as positive as negative. For instance, the addition of iron (1 wt%) almost deactivates the catalyst. The corresponding carbon yield hardly reaches 4.1 g/g$_{cat}$. The addition of other metals improves the performance and significantly shortens the induction period of the metal dusting stage. The highest SSA values (380 m^2/g and above) were obtained in the case of samples Ni-Pt (4%, cp) and Ni-Pd (5%, cp).

Finally, it was found that the addition of acetonitrile to the reaction mixture doubles the carbon yield value, increases the SSA value to 454 m^2/g, and allows incorporation of almost 2 wt% of nitrogen atoms into the CNF structure.

CONCLUSION

It was established that the metal dusting process of bulk metal items could serve as an alternative method to prepare active and stable catalysts for the formation of carbon nanofibers via catalytic chemical vapor deposition. The metal dusting stage takes place during the induction period, when no noticeable weight changes can be seen. Under the action of aggressive medium containing hydrogen and chlorinated hydrocarbons, the metal surface undergoes restructuring and disintegration. The dispersed metal particles being formed catalyze the intensive growth of CNF. The catalytic performance of such systems depends on the alloying metal. Iron was found to worsen the activity of nickel. At the same time, its alloying with copper, chromium, cobalt, platinum, palladium, molybdenum, or tungsten shortens the induction period and increases the values of carbon yield and specific surface area of CNF. The addition of heteroatom-containing co-substrate to the reaction mixture, for an example of acetonitrile, allows producing of CNF functionalized with nitrogen-containing groups.

Acknowledgement

This work was by the Russian Foundation for Basic Research (project No. 18-29-19053_mk).

REFERENCES

[1] I.V. Mishakov, R.A. Buyanov, V.I. Zaikovskii, I.A. Strel'tsov, A.A. Vedyagin, Kinet. Catal., 2008, **49**, 868-872.

[2] I.V. Mishakov, Y.I. Bauman, D.V. Korneev, A.A. Vedyagin, Top. Catal. 2013, **56**, 1026-1032.

[3] Y.I. Bauman, A.S. Lysakova, A.V. Rudnev, I.V. Mishakov, Y.V. Shubin, A.A. Vedyagin, R.A. Buyanov, Nanotechnol. Russia, 2014, **9**, 380-385.

[4] Y.I. Bauman, A.A. Vedyagin, I.V. Mishakov, Protection of Metals and Physical Chemistry of Surfaces, 2016, **52**, 309-315.

[5] Y.I. Bauman, Y.V. Shorstkaya, I.V. Mishakov, P.E. Plyusnin, Y.V. Shubin, D.V. Korneev, V.O. Stoyanovskii, A.A. Vedyagin, Catal. Today, 2017, **293–294**, 23-32.

[6] Y.I. Bauman, I.V. Mishakov, A.A. Vedyagin, S. Ramakrishna, Mater. Lett., 2017, **201**, 70-73.

[7] Y.I. Bauman, I.V. Mishakov, Y.V. Rudneva, P.E. Plyusnin, Y.V. Shubin, D.V. Korneev, A.A. Vedyagin, Ind. Eng. Chem. Res., 2019, **58**, 685-694.

[8] Y.I. Bauman, Y.V. Rudneva, I.V. Mishakov, P.E. Plyusnin, Y.V. Shubin, D.V. Korneev, V.O. Stoyanovskii, A.A. Vedyagin, R.A. Buyanov, Heliyon, 2019, **5**, e02428:1-10.

[9] I.V. Mishakov, A.A. Vedyagin, Y.I. Bauman, A.R. Potylitsyna, A.S. Kadtsyna, V.V. Chesnokov, A.Y. Nalivaiko, A.A. Gromov, R.A. Buyanov, Catalysts, 2020, **10**, 1446:1-17.

[10] Y.V. Shubin, Y.I. Bauman, P.E. Plyusnin, I.V. Mishakov, M.S. Tarasenko, M.S. Mel'gunov, V.O. Stoyanovskii, A.A. Vedyagin, J. Alloys Compnd., 2021, **866**, 158778:1-12.

PEROXO-Zr/Hf CONTAINING POLYOXOMETALATES: SYNTHESIS, STRUCTURE AND DETAILED RAMAN SPECTROSCOPIC STUDIES

A. Sundar [1], B. S. Bassil [1,2], D. Bajuk-Bogdanović [3], G. Ćirić-Marjanović [3], O. V. Zalomaeva [4], N.V. Maksimchuk [4], O.A. Kholdeeva [4], and U. Kortz [1]

[1] Department of Life Sciences and Chemistry, Jacobs University, Campus Ring 1, 28759 Bremen, Germany, Email u.kortz@jacobs-university.de
[2] Department of Chemistry, Faculty of Arts and Sciences, University of Balamand, P.O. Box 100, Tripoli, Lebanon
[3] University of Belgrade-Faculty of Physical Chemistry, Studentski trg 12-16, 11158 Belgrade, Serbia
[4] Boreskov Institute of Catalysis, Lavrentieva Ave. 5, Novosibirsk, 630090, Russia.

ABSTRACT

Polyoxometalates (POM) are discrete anionic metal-oxo clusters of early *d*-block metal addenda ions in high oxidations states (e.g. W^{VI} Mo^{VI}, V^{V}). POMs exhibit a large variety of shapes, sizes and compositions with multiple associated physicochemical properties and potential applications in catalysis, biomedicine and material science. The substitution of addenda atoms by other d or f-block metals such as Zr or Hf can lead to novel compounds with unprecedented properties, and some peroxo-derivatives are also known. Here we report on the synthesis and structural characterization of four novel peroxo-Zr and Hf-containing polyanions of the Wells-Dawson type. The solution stability was investigated by multinuclear NMR and detailed Raman and IR spectroscopic studies were performed in the solid state. The catalytic activity of the novel POMs in the H_2O_2-based oxidation of organic substrates was also investigated.

CATALYTIC PROPERTIES OF CARBON NANOTUBES AND REDUCED GRAPHENE OXIDE IN ETHYLENE HYDROGENATION BY MOLECULAR HYDROGEN

P.E. Strizhak, A.A. Abakumov, I.B. Bychko

L. V. Pisarzhevsky Institute of Physical Chemistry of the National Academy of Sciences of Ukraine,
Prosp. Nauky, 31Kyiv 03028, Ukraine. (pstrizhak@hotmail.com)

ABSTRACT

In the last years, several studies dedicated to the carbon nanomaterials such as multi-walled carbon nanotubes (CNT) and reduced graphene oxide (rGO) catalytic activity in the hydrogenation reactions have been reported. Particularly, for the first time, we showed that rGO and CNTs are active in the gas-phase hydrogenation reactions with molecular hydrogen.

The work is dedicated to the determination of the influence of the structure and functionality of CNT and rGO on the catalytic activity in the hydrogenation of ethylene by molecular hydrogen. The ethylene hydrogenation is a simple model gas-phase reaction that convenient to establish a dependence between the method of catalyst activation, the diameter of CNT, and the procedure of rGO preparation and their catalytic activity.

The catalytic activity of rGO strongly depends on its structural characteristics. An increase in the surface area and a decrease in the oxygen content enhance the catalytic activity of rGO. The defectiveness and oxygen content are crucial for the catalytic performance of rGO obtained either by thermal reduction of graphene oxide in hydrogen or by reduction of graphene oxide with hydrazine. This conclusion has significant implications for the potential applications of rGO as a hydrogenation catalyst.

Obtained results show that non-activated carbon nanomaterials do not exhibit catalytic activity. Increasing the temperature of activation from 100°C to 400°C increases the catalytic activity by three orders of magnitude. Further temperature increase leads to a decrease in catalytic activity. An increase in the CNT diameter significantly decreases the catalytic activity. The highest obtained activity for CNT is $6.2 \bullet 10^{-6}$ $mol \bullet s^{-1} \bullet m^{-2}$ which is higher compared to rGO.

Our results indicate the high stability of CNT and rGO compared to the typical hydrogenation catalysts in hydrogen-rich and ethylene-rich atmospheres. That offers new opportunities for the application of nanocarbon-based catalysts in the hydrogenation reaction at high temperatures. That is extremely important to replace catalysts operating under conditions where the metal-containing catalysts deactivate due to the formation of the carbonaceous deposits.

This research received funding from the National Research Foundation of Ukraine, grant number 2020.02/0050.

PREDICTING PARTICLE SIZE DISTRIBUTION IN NANOPARTICLE FORMATION BY STOCHASTIC AND DETERMINISTIC APPROACHES

R. Szabó and G. Lente

University of Pécs, Institute of Chemistry, Department of Physical Chemistry and Materials Science,
Ijjúság útja 6, Pécs, 7624 Pécs, Hungary. (lenteg@gamma.ttk.pte.hu)

ABSTRACT

A class of nucleation-growth type models for nanoparticle formation were investigated by deterministic and stochastic kinetic methods. Four different kernel functions were used for characterizing the dependence of the reactivity of a nanoparticle on its size in the growth reaction. The final distribution of nanoparticles formed were determined as a function of the ratio of the rate constants characterizing nucleation and particle growth. It was found that the final size distributions predicted by the stochastic and deterministic approaches for the same model agree very well. Furthermore, it was also shown that the average size of nanoparticles formed can be given as a function of the rate constant ratio with a simple power expression, where the value of the exponent depends on the identity of the kernel function used.

INTRODUCTION

Nanoparticles play an increasingly significant role in chemistry research mostly because of their excellent catalytic properties [1-3]. By now, it has become clear that their usefulness (and also toxicity) is primarily determined by the particle size [1-3]. Therefore, controlling the average size and the distribution of particle size is one of the most important aspects of nanoparticle synthesis. It is also clear that these properties are determined by kinetic factors rather than thermodynamics [4-6].

In this paper, we report mathematical kinetic investigations on a class of models used to interpret nanoparticle formation. Both the deterministic and stochastic approaches were used and their results are compared with special emphasis on the particle size distribution, which is the most common characteristic determined in experimental works.

METHODS

The model studied in this work consist of two different kinds of steps. The first type is nucleation, in which *n* monomeric units come together to form a nanoparticle seed that is capable of later growth (*n* is a parameter, its value is an integer). The second reaction step type is the growth of a nanoparticle. In this step, one monomeric unit is added to a seed or nanoparticle of larger size. It is noted that the reaction of two nanoparticles (usually termed aggregation) is not present in this model. Although its role is known in many nanoparticle formation systems [1-3], the usual strategy of mathematical modeling is to start from the simplest models and consider more complicated aspects when necessary [7-11].

The model studied here can be represented by the following two generic reactions, both of which show mass action type kinetics. In this following equation, M denotes the monomeric unit, whereas C_i is a nanoparticle containing *i* monomeric units:

$$\begin{aligned} &n\mathrm{M} \xrightarrow{k_\mathrm{n}} \mathrm{C}_n \\ &\mathrm{C}_i + \mathrm{M} \xrightarrow{k_{\mathrm{g},i}} \mathrm{C}_{i+1} \qquad i \geq n \end{aligned} \tag{1}$$

This model gives rise to a set of simultaneous ordinary differential equations. Originally, the concentrations are the dependent variables in such equation and time is the independent variable, but it has been shown to be more advantageous to use dimensionless concentrations and dimensionless time instead [12-14]:

$$\begin{aligned}
&\frac{\mathrm{d}m}{\mathrm{d}\tau} = -n\alpha m^n - m\sum_{j=n}^{\infty} K\left(j\right)c_j \\
&\frac{\mathrm{d}c_n}{\mathrm{d}\tau} = \alpha m^n - K\left(n\right)mc_n \qquad\qquad\qquad\qquad\qquad\qquad (2)\\
&\frac{\mathrm{d}c_i}{\mathrm{d}\tau} = K\left(i-1\right)mc_{i-1} - K\left(i\right)mc_i \qquad\qquad i > n
\end{aligned}$$

Here m denotes the dimensionless concentration of the monomeric unit M, c_i is the dimensionless concentration of the nanoparticle containing i monomeric units (C_i). The additional physical quantities are dimensionless time τ, and the ratio of the nucleation and particle growth rate constants, which is denoted α. In this ratio, the dependence of the growth rate constants of the particle size must also be considered. This is done through the $K(i)$ kernel function, for which four possibilities are given in Table 1.

Table 1. Typical kernel functions in the nucleation-growth type nanoparticle formation model

Name	Kernel function
mass kernel	$K(i) = i$
surface kernel	$K(i) = i^{2/3}$
Brownian kernel	$K(i) = i^{1/3}$
diffusion kernel	$K(i) = 1$

In Table 1, the mass kernel implies that the growth rate constant is directly proportional to the mass of the particle (so in effect, the number of monomeric units in it). The surface kernel takes the growth rate constant as directly proportional to the surface of the nanoparticle. Without having to specify further shape parameters, the nanoparticles are assumed to have roughly spherical shape, the surface of which is proportional to the 2/3th power of the volume (which is directly proportional to the mass). The Brownian kernel works in a similar way, but here the rate constant is proportional to the linear size of the nanoparticle. Finally, the diffusion kernel implies that the growth rate constant is independent of the size of the particle. This is commonly rationalized by the fact that the diffusion controlled rate constant is also independent of the size of a species: a larger particle moves slower but it is also a larger target, and the two opposing effects cancel each other [15].

In the deterministic approach, the symbolic solution of Eq. 2 was sought. It is to be noted that numerical solutions are not really viable in this case because the number of dependent variables is infinitely high.

Stochastic calculations were done using Monte Carlo simulations [16-20], which is commonly called the Gillespie algorithm. In this method, the dimensionless concentrations are measured in absolute molecule number rather that molarity based values (this is emphasized by introducing a bar over the concentration symbols m and c_i), and a time-dependent propensity p_i, analogous to deterministic reaction rates, is defined for each step:

$$\begin{aligned} p_1(t) &= \binom{\overline{m}(t)}{n} \\ p_i(t) &= \alpha K(i)\,\overline{m}(t)\,\overline{c}_i(t) \qquad i \ge n \end{aligned} \tag{3}$$

The essence of the simulation is that in each step, two independent, uniformly distributed random numbers are generated between 0 and 1, these are rnd_1 and rnd_2. The first random number is used to increment the time according to the following equation [16-20]:

$$t^{\mathrm{new}} = t^{\mathrm{old}} - \frac{\ln rnd_1}{\sum_{j=1}^{n} p_j\left(t^{\mathrm{old}}\right)} \tag{4}$$

The second random number is used to decide which of the steps with non-zero propensity occurs. Step *i* occurs if and only if the following inequity is satisfied:

$$\frac{\sum_{j=1}^{i-1} p_j\left(t^{\mathrm{old}}\right)}{\sum_{j=1}^{n} p_j\left(t^{\mathrm{old}}\right)} \le rnd_2 < \frac{\sum_{j=1}^{i} p_j\left(t^{\mathrm{old}}\right)}{\sum_{j=1}^{n} p_j\left(t^{\mathrm{old}}\right)} \tag{5}$$

The occurrence of step *i* causes the following changes in the molecule numbers:

$$\begin{gathered} \overline{m}\left(t^{\mathrm{new}}\right) = \overline{m}\left(t^{\mathrm{old}}\right) - n; \quad \overline{c}_n\left(t^{\mathrm{new}}\right) = \overline{c}_n\left(t^{\mathrm{old}}\right) + 1 \quad \text{if } i = 1 \\ \left.\begin{array}{c} \overline{m}\left(t^{\mathrm{new}}\right) = \overline{m}\left(t^{\mathrm{old}}\right) - 1; \\ \overline{c}_i\left(t^{\mathrm{new}}\right) = \overline{c}_i\left(t^{\mathrm{old}}\right) - 1; \overline{c}_{i+1}\left(t^{\mathrm{new}}\right) = \overline{c}_{i+1}\left(t^{\mathrm{old}}\right) + 1 \end{array}\right\} \text{ if } i > n \end{gathered} \tag{6}$$

These steps are repeated until $c_1 = 0$, which means that all the propensities are zero, i.e. an unchangeable final state is reached.

RESULTS AND DISCUSSION

Full symbolic solutions were obtained for three different models [12, 14], which means that a formula was found to give the dependence of all dimensionless concentrations on dimensionless time. For other cases, some partial results are also reported in our earlier works [12-14].

For the diffusion kernel and $n = 1$, the following general formula has been found to be valid [14]:

$$c_i = \alpha - \alpha\,\mathrm{e}^{-\mu_0/\alpha} \sum_{j=0}^{i-1} \frac{1}{j!}\left(\frac{\mu_0}{\alpha}\right)^j \tag{7}$$

For the mass kernel and $n = 1$, the symbolic solution takes the following form [14]:

$$\begin{aligned} m &= \frac{\alpha + 1}{\alpha\,\mathrm{e}^{(\alpha+1)\tau} + 1} \\ c_i &= \frac{\alpha}{i}\left(\frac{1-m}{\alpha+1-m}\right)^i \end{aligned} \tag{8}$$

The symbolic solution has also been found for the mass kernel and $n = 2$, although this is somewhat more complicated than the previous ones [12]:

$$\begin{aligned} m &= \frac{1}{1-2\alpha+2\alpha\,\mathrm{e}^{\tau}} \\ c_i &= \frac{\alpha(i-1)!(-1)^{i-1}(m-1)}{\prod_{j=2}^{i}(2\alpha-j-1)} + \\ &\quad + \sum_{j=2}^{i} \frac{\alpha(j^2-1)}{j(2\alpha-j-1)} \binom{i-1}{j-1} (-1)^j \left[\left(\frac{1-m}{2\alpha} + m \right)^{j/(2\alpha-1)} - 1 \right] \end{aligned} \qquad (9)$$

In addition, a special numerical method was developed for the diffusion kernel and $n = 2$ [13], in which the individual c_i values could be calculated for $i = 2$ first and then for successively larger and larger i values.

Fortunately, programming the Gillespie algorithm in stochastic studies does not really depend on the complexity of the model, so these simulations could be carried out for every kernel and n value. We selected the range $n = 1–5$, so altogether did these calculations in 20 different models.

Since almost all earlier attempts on treating nanoparticle formation models involved the deterministic approach [1-3] only, it was important to compare the results from the two approaches. This is really essential because the typical particle numbers are very low in the system, which are the exact conditions where stochastic kinetics may describe behavior very different from the deterministic approximation.

Generally, it was found that the stochastic approach predicts substantial fluctuations in the time course of the reactions. However, when the final nanoparticle size distribution is concerned, the two approaches give essentially the same final results, which implies that even despite the anticipated problems, the deterministic approach is suitable for predicting size distributions. As an example, the two sets of data are compared for the diffusion kernel and $n = 2$ with $\alpha = 5 \times 10^{-7}$ in Figure 1. It is notable that in this graph, the x axis shows i values, which means that it is proportional to the mass of the nanoparticles rather than the linear size. The linear size would be obtained as the cube root of this axis. Also, the graph shows the cumulative distribution function (the probability that the size of the particle is smaller than i). From earlier examples, it is understood that this sort of representation is much better suited for comparison with experimental data than histograms, which tend to rely on the arbitrary categorization of data.

As already pointed out, the stochastic simulations could be done for every nucleation-growth type model. This means that the final distributions could be characterized for all these cases as a function of the rate constant ratio α.. Such a dependence is shown for different values of n of the Brownian kernel in Figure 2.

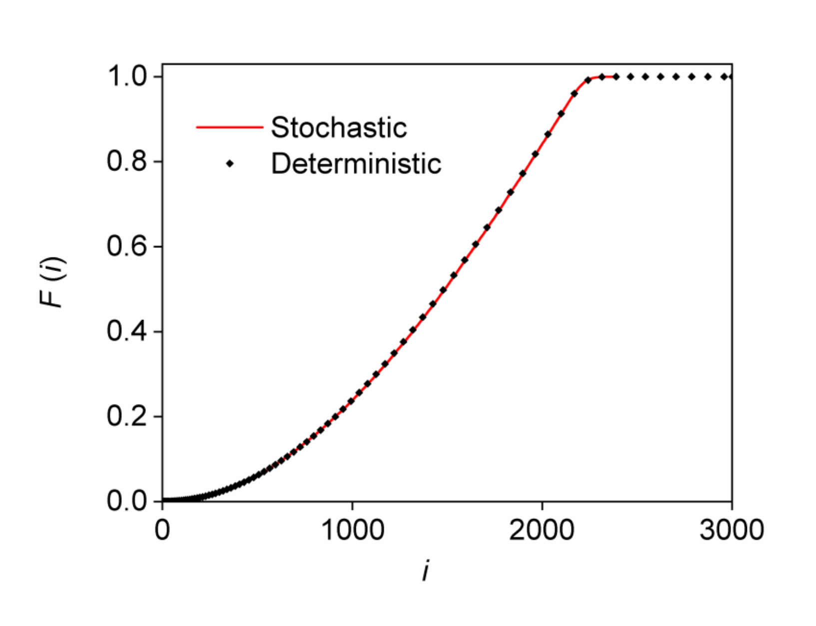

Figure 1. Final particle size distribution in stochastic simulations and the deterministic prediction for the diffusion kernel with $n = 2$ with $\alpha = 5 \times 10^{-7}$.

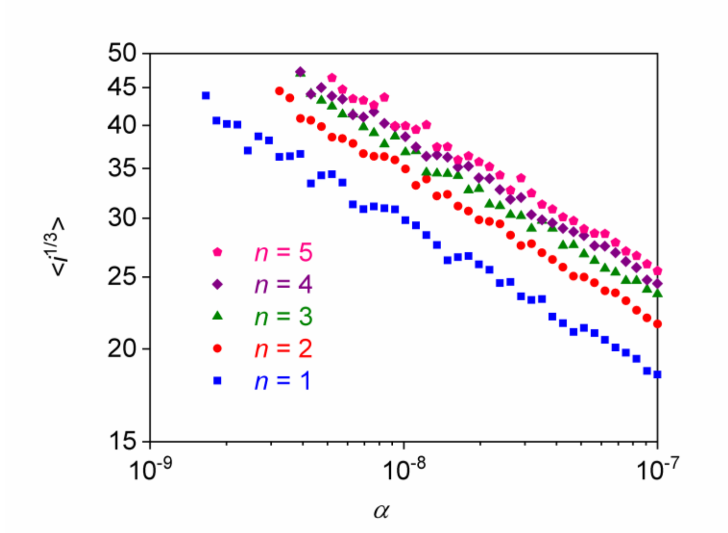

Figure 2. Dependence of average particle size on the value of α for different values of n with the Brownian kernel

A detailed analysis of the data showed that the average particle size (which is the average of the cube root of the monomeric units in the particles) can be given with a power function as follows:

$$\left\langle i^{1/3} \right\rangle = X\alpha^{\rho} \tag{10}$$

The values of the ρ exponents for the 20 different models studies in this work are given in Table 2.

Table 2. Power function exponents (ρ) for the dependence of average particle size on the value of α

Kernel	1	2	3	4	5
mass	0.258	0.249	0.241	0.235	0.230
surface	0.261	0.272	0.246	0.247	0.260
Brownian	0.200	0.201	0.200	0.194	0.197
diffusion	0.166	0.167	0.166	0.166	0.167

Table 2 shows that the exponent ρ only depends somewhat on the value of n for the mass kernel. This observation may be used to identify the suitable kernel functions for interpreting experimental data.

CONCLUSION

It is concluded that the mathematical methods developed in this work are capable of providing mechanism-based predictions for the size distributions of nanoparticles formed. The methods are readily extended to other models as well, so they will be directly suitable for comparing theoretical mechanistic considerations with experimental data.

Acknowledgement

This work was supported by the Higher Education Institutional Excellence Program of the Ministry of Human Capacities in Hungary, within the framework of the 1st thematic program of the University of Pécs. The National Research, Development, and Innovation Office of Hungary also supported this work under grant No. SNN 125739.

REFERENCES

[1] S. T. Hunt, Y. Román-Leshkov, Accounts of Chemical Research, 2018, 51, 1054-1062.
[2] I.V. Zibareva, L. Y. Ilina, A. A. Vedyagin, Reaction Kinetics Mechanisms and Catalysis. 2019, 127, 19-24.
[3] Z. Li, S. Ji, Y. Liu, X. Cao, S. Tian, Y. Chen, Z. Niu, Y. Li, Chemical Reviews, 2020, 120, 623-682.
[4] A. F: Lisovsky, Science of Sintering, 2010, 42, 15–24.
[5] L. M. Wheeler, N. J. Kramer, U. R. Kortshagen, Nano Letters, 2018, 18, 1888–1895.
[6] A. F: Lisovsky, Journal of Superhard Materials, 2020, 42, 9–17.
[7] G. Lente, I. Fábián, Inorganic Chemistry, 1998, 37, 4204-4209.
[8] G. Lente, I. Fábián, Inorganic Chemistry, 1999, 38, 603-605.
[9] G. Lente, J. H. Espenson, Inorganic Chemistry, 2000, 39, 4809-4814.
[10] G. Lente, Journal of Physical Chemistry A, 2006, 110, 12711-12713.
[11] G. Lente, Physical Chemistry Chemical Physics, 2007, 9, 6134-6141.
[12] R. Szabó, G. Lente, Journal of Mathematical Chemistry, 2019, 57, 616-631.
[13] R. Szabó, G. Lente, Chemistry of Materials, 2021, DOI: 10.1021/acs.chemmater.0c04688.
[14] R. Szabó, G. Lente, Journal of Mathematical Chemistry, 2021, 10.1007/s10910-021-01265-z.
[15] G. Lente, Current Opinion in Chemical Engineering, 2018, 21, 76-83.
[16] T. Sipos, J. Tóth, P. Érdi, Reaction Kinetics and Catalysis Letters, 1974, 1, 113-117.
[17] T. Sipos, J. Tóth, P. Érdi, Reaction Kinetics and Catalysis Letters, 1974, 1, 209-213.
[18] D. T. Gillespie, Journal of Computational Physics, 1976, 22, 403-434.
[19] D. T. Gillespie, Jornal of Physical Chemistry, 1977, 81, 2340-2361.
[20] D. T. Gillespie, A. Hellander, L. R. Petzold, Journal of Chemical Physics, 2014, 138, 270901

FREE RADICAL SCAVENGING POTENCY OF EQUOL

A. Amić [1], D. Milenković [2], J. M. Dimitrić Marković [3] and Z. Marković [2]

[1] Department of Chemistry, Josip Juraj Strossmayer University of Osijek, Ulica cara Hadrijana 8A, 31000 Osijek, Croatia (aamic@kemija.unios.hr).
[2]Institute of Information Technologies, Department of Science, University of Kragujevac, 34000 Kragujevac, Serbia.
[3]The Faculty of Physical Chemistry, University of Belgrade, Studentski trg 12-16, 11000 Belgrade, Serbia.

ABSTRACT

Kinetic analysis performed by using Transitivity Code indicates that phenolic hydrogens of physiologically active equol molecule are much more abstractable than C-ring hydrogens. Obtained results are opposite to very recently published statements that aliphatic C−H bonds of natural compounds may play significant role in antioxidant action. Unequivocally, phenolic O−H bonds are responsible for antiradical activity of equol. The contribution of equol's C-ring hydrogens to free radical scavenging is negligible.

INTRODUCTION

It is well-known that oxyl radicals (peroxyl radicals $ROO^{\bullet}$) react ~10^4 faster with O−H bonds than with C−H bonds of comparable strength [1]. A few decades ago breaking of phenolic O−H bond was recognized as a cornerstone of antioxidant (free radical scavenging) activity of polyphenolic compounds [2]. Such breaking may be homolytic (e.g., *via* hydrogen atom transfer (HAT) mechanism) or heterolytic (e.g., *via* sequential proton loss electron transfer (SPLET) mechanism) [3]. Despite that, very recently in several reports it has been claimed that C−H bond hydrogen abstraction may play notable role in free radical scavenging by natural compounds, even more significant than phenolic O−H bond hydrogen abstraction [4]. Such statements are mainly based on using of inappropriate level(s) of theory: B3LYP functional which underestimates barrier heights [5] and/or such tunneling corrections that highly overestimate importance of tunneling for C−H bond abstraction [6].

Equol, a product of human intestinal bacterial metabolism of soy isoflavones [7], is particularly suitable molecule to reinvestigate the role of C−H hydrogens in antiradical activity. Equol possesses five C-ring hydrogens which may compete with two phenolic hydrogens in free radical quenching (Fig. 1).

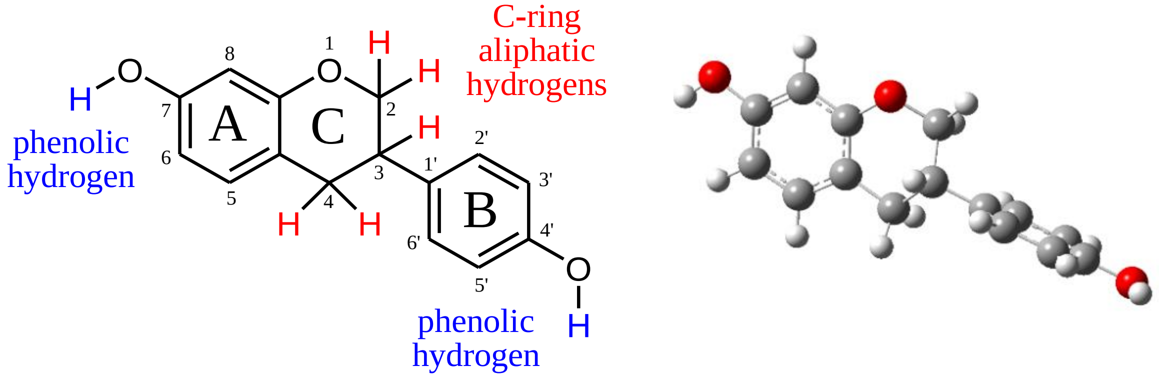

Figure 1. Structure of equol

METHODS

Geometry optimizations and frequency calculations for equol and all species involved in studied mechanism of hydroperoxyl ($HOO^{\bullet}$) scavenging were performed at M06-2X/6-311++G(d,p) level of theory in gas-phase at 298.15 K by using the Gaussian 09. Local minima and transition states (TS) were identified by the number of imaginary frequencies (0 and 1, respectively). IRC calculation was performed on both sides of the TS to confirm that it properly connects the corresponding reactants and products. The rate constants (k) were calculated by using transition state theory (TST) as implemented in the Transitivity Code [8]. For kinetic calculations, this code needs only the electronic structures of reactants, transition state and products.

For a general bimolecular reaction, the rate constant (k) is given by:

$$k = \kappa \frac{k_B T}{h} \frac{Q^{\neq}}{Q_1 Q_2} \exp\left(-\frac{\varepsilon^{\neq}}{k_B T}\right)$$

where, κ accounts for tunneling corrections, k_B is the Boltzmann constant, T is the temperature, h is the Planck constant, Q_1, Q_2 and $Q^{\neq}$ are partition functions of reactants and of the transition state, respectively, and $\varepsilon^{\neq}$ is the barrier height. The one-dimensional tunneling corrections in the Transitivity Code include Skodje-Truhlar (ST), Bell's and the deformed (*d*-TST) tunneling corrections.

The branching ratios (Γ, in %) calculated from rate constants can be used to identify the reaction pathways contributing the most to the total reaction:

$$\Gamma = (k_i/k_{overall}) \times 100$$

where k_i represents the rate constant of independent path. The overall rate constant ($k_{overall}$) is calculated as the sum of rate constants of all reaction paths.

RESULTS AND DISCUSSION

The simplest approach to study the rate constants is TST with one-dimensional tunneling corrections. Tunneling in HAT reactions is significant and must be taken into account. Results of performed calculations at the M06-2X/6-311++G(d,p) level of theory and kinetic calculations using the Transitivity Code are summarized in Table 1.

Table 1. TS imaginary frequency ν (cm^{-1}), barrier height $\varepsilon^{\neq}$ (kcal/mol) and rate constant k (M^{-1} s^{-1}) in HAT reaction of equol with $HOO^{\bullet}$ radical

path	ν	$\varepsilon^{\neq}$	k(TST)	k(d-TST)	k(ST)	k(Bell35)
C2-H	-1819	10.39	1.7×10^{0}	2.3×10^{1}	8.6×10^{2}	8.8×10^{2}
C3-H	-1919	10.93	6.2×10^{-1}	1.1×10^{1}	7.2×10^{2}	7.3×10^{2}
C4-H	-1740	7.08	3.7×10^{2}	3.5×10^{3}	2.8×10^{4}	2.9×10^{4}
7-OH	-2110	6.72	1.9×10^{3}	3.6×10^{4}	3.9×10^{5}	3.9×10^{5}
4'-OH	-2201	7.18	1.1×10^{3}	2.7×10^{4}	3.9×10^{5}	3.9×10^{5}
$k_{overall}$			3.5×10^{3}	6.6×10^{4}	8.1×10^{5}	8.2×10^{5}

As can be seen from Table 1, phenolic OH groups of equol are preferred sites for H-atom abstraction. Branching ratios clearly indicate major role of equol's phenolic C7-OH and C4'-OH groups (>90%) in $HOO^{\bullet}$ inactivation (Table 2). Amongst C-ring hydrogens, only those from C-4 site slightly contribute to the $HOO^{\bullet}$ scavenging (<10%).

Table 2. Branching ratios Γ (%) at 295.15 K

path	Γ_{TST}	$\Gamma_{d\text{-}TST}$	Γ_{ST}	Γ_{Bell35}
C2-H	0.0	0.0	0.1	0.1
C3-H	0.0	0.0	0.1	0.1
C4-H	10.7	5.3	3.5	3.6
7-OH	56.4	54.3	47.9	47.9
4’-OH	32.9	40.4	48.4	48.3

Without tunneling corrections, the k(TST) values for O−H paths are by ~10^3 (~10^1) higher then corresponding values for C2-H and C3-H (C4-H) paths, respectively. The same relationships remains by including tunneling corrections. Depending on applied tunneling corrections k_{overall} increase by ~10^1 (for d-TST) and by ~10^2 (for ST and Bell35). If we recall that phenolic O−H bonds are by a factor of ~10^4 more reactive than C−H bonds of similar strength [1], than it is obvious that used one-dimensional tunneling corrections are not fully appropriate. We suppose that more accurate results could be obtained by using canonical variational transition state theory (CVT) corrected by multidimensional small-curvature tunneling (SCT) [9]. The CVT/SCT method is successfully applied to the reactions of radical scavenging by natural antioxidants [10].

CONCLUSION

By using appropriate level of theory for electronic calculations and simple kinetic approach, we qualitatively found that phenolic hydrogens of equol are more abstractable than C-ring aliphatic hydrogens. To achieve reliable quantitative results more sophisticated kinetic approach (CVT/SCT) must be applied.

Acknowledgement

This work was partially supported by the Croatian Ministry of Science and Education, and the Ministry of Education, Science and Technological Development of Republic of Serbia (Contract number: 451-03-68/2020-14/200146).

REFERENCES

[1] J. M. Mayer, Acc. Chem. Res., 2011, **44**, 36-46.
[2] W. Bors, W. Heller, C. Michel, M. Saran, Method. Enzymol., 1990, **186**, 343-355.
[3] A. Galano, G. Mazone, R. Alvarez-Diduk, T. Marino, J. R. Alvarez-Idaboy, N. Russo, Annu. Rev. Food Sci. Technol., 2016, **7**, 335-352.
[4] see, for example: a) Q. V. Vo, P. C. Nam, N. M. Thong, N. T. Trung, C-T. D. Phan, A. Mechler, ACS Omega, 2019, **4**, 8935-8942; b) T. C. Ngo, T. H. Nguyen, D. Q. Dao, J. Chem. Inf. Model, 2019, **59**, 766-776; c) H. Boulebd, Free Radic. Res., 2020, **54**, in press.
[5] Y. Zhao, N. Gonzalez-Garcia, D. G. Truhlar, J. Phys. Chem. A, 2005, **109**, 2012-2018.
[6] E. Dzib, J. L. Cabellos, F. Ortiz-Chi, S. Pan, A. Galano, G. Merino, Int. J. Quantum. Chem., 2018, **119**, e25686.
[7] B.-J. Li, J. Food Process. Preserv., 2019, **43**, e14205.
[8] H. G. Machado, F. O. Sanches-Neto, N. D. Coutinho, K. C. Mundim, F. Palazzetti, V. H. Carvalho-Silva, Molecules, 2019, **24**, 3478.
[9] J. L. Bao, D. G. Truhlar, Chem. Soc. Rev., 2017, **46**, 7548-7596.
[10] S. G. Chiodo, M. Leopoldini, N. Russo, M. Toscano, Phys. Chem. Chem. Phys., 2010, **12**, 7662-7670.

APPLICATION OF QUANTUM CHEMICAL CALCULATION IN DEFINING PEAKS IN UV-VIS SPECTRA OF OXIDATIVE TARTRAZINE DEGRADATION

M. Popadić[1], S. Marinović[2], T. Mudrinić[2], A. Milutinović-Nikolić[2],
P. Banković[2], I. Đorđević[2] and G. Janjić[2]

[1]*University of Belgrade–Faculty of Chemistry, Studentski trg 12-16, 11000 Belgrade, Republic of Serbia.*
[2] *University of Belgrade, Institute of Chemistry, Technology and Metallurgy, National Institute, Njegoševa 12, 11000 Belgrade, Republic of Serbia (goran.janjic@ihtm.bg.ac.rs)*

ABSTRACT

Degradation of tartrazine in presence of cobalt activated Oxone® (potassium peroxymonosulfate) was investigated. Aluminium pillared clay acted as a support for catalytically active Co^{2+}. Oxone® was a precursor of $SO_4^{\cdot-}$ radical anions. Along with decolorization of tartrazine solution, the degradation of tartrazine and formation of oxidation products was monitored using UV-Vis spectroscopy. Quantum chemical calculations were performed in order to predict UV-Vis spectra. Different models were tested, and the results of calculation have shown that the combination of TPSS-D3 method and aug-cc-pVDZ basis set is quite satisfactory level of theory. The experimentally obtained peaks that arose during degradation were identified using this method.

INTRODUCTION

Catalytic oxidative degradation in the presence of sulfate radical anions ($SO_4^{\cdot-}$), has received much attention recently [1]. Oxone® ($KHSO_5 \cdot 0.5 \cdot KHSO_4 \cdot 0.5 \cdot K_2SO_4$) has been widely utilized as a source of HSO_5^- ions that yield into $SO_4^{\cdot-}$ radical anions. In order to be efficient, the Oxone® should be activated. In our previous work, pillared montmorillonite impregnated with cobalt, was found to be efficient catalyst in catalytic oxidation of tartrazine in the presence of Oxone® [2]. The process was monitored using UV-Vis spectroscopy. It was found that changes in UV-Vis spectra were the result of tartrazine decolorization as well as formation of oxidative products. In this paper quantum chemical calculation were applied in order to assign newly formed peaks in UV-Vis spectra to defined products of tartrazine degradation.

EXPERIMENTAL

The 2 µm fraction of clay rich in montmorilonite was pillared with aluminium, impregnated with cobalt. The obtained catalyst was fully characterized [2]. The catalytic test was performed by stirring (300 rpm) tartrazine solution (C_0 = 50 mg dm^{-3}) in the presence of 0.130 mmol Oxone® and 10 mg of catalyst [2]. The experiments were conducted at 50 °C at unadjusted pH (pH = 3.6). The sampling was performed at a predetermined periods of time (5, 10, 20, 30, 60, 120 and 240 min). The supernatant was separated from the catalyst by centrifugation and the obtained solution was monitored by using UV-Vis spectrophotometry (Thermo Scientific Evolution 220 UV-Vis Spectrophotometer).

All theoretical calculations were performed with the Gaussian 09 program package [3]. Structures of all investigated tartrazine forms were optimized with Density functional theory (DFT), by using the TPSS-D3 functional and 6-31g basis set. Time dependent density functional theory (TD-DFT) has been employed to compute the absorption spectra. To determine the level of theory which achieves the best agreement of experimental with calculated UV-Vis spectra, several functionals (cam-B3LYP, M06-2X, and TPSS-D3) and two basis sets (aug-cc-pVDZ and def2-TZVP) were used.

The calculations were performed using restricted formalism, the tight convergence criteria and without any symmetry constraints. The effect of water, as solvent, was simulated using the Solvation Model based on Density (SMD).

RESULTS AND DISCUSSION

Experimentally obtained UV-Vis spectra after selected reaction times are given in Figure 1a. The only change in spectra of starting solution (0 min) up to 60 min of reaction, was diminishing of the characteristic peaks at 257 nm and 426 nm. Besides these changes, a new peak at 231 nm appeared after 120 min of reaction, Later on, after 240 min of reaction the intensity of this peak decreased along with formation of another additional peak at 275 nm.

The possible reaction pathways were analyzed in order to estimate the origin of 231 nm and 275 nm peaks. Afterwards, for each potential product of the reaction, the theoretical UV-Vis spectra obtained by quantum chemical calculations were established (Figure 1b).

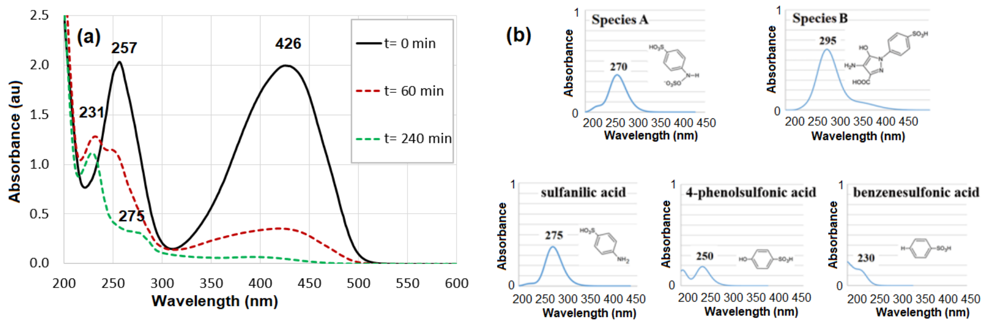

Figure 1. Experimental UV-Vis spectra for degradation of tartrazine (a) and calculated UV-Vis spectra of its oxidation products (b).

In the proposed mechanism $SO_4^{\cdot-}$ radical anion attacked the N atom of the azo group of tartrazine bonded to the benzene ring, producing a sulfate tartrazine derivative. Degradation started with the azo bond cleavage by $SO_4^{\cdot-}$ radical anion [4] (Figure 2). In this manner, two products were formed: sulfanilic acid derivative (species A) and the derivative of benzenesulfonic acid with pyrazole ring as substituent (species B).

After NH_3 and CO_2 release from species B and degradation of pyrazole ring, the sulfanilic acid might be formed. Further degradation sulfanilic acid can lead among other products into formation of 4-phenolsulfonic and benzenesulfonic acid. In calculated spectra of species B the peak was estimated at 300 nm. This peak was not pronounced in the experimental spectra, indicating the fast degradation of this product. The spectra of species A and sulfanilic acid have peaks at 270 nm and 275 nm, respectively. Therefore, the experimentally obtained peak at 275 nm can be assigned to these two species. The occurrence of the peak at 230 nm could be assigned to 4-phenolsulfonic and benzenesulfonic acid since they showed peak at around 230 nm in calculated spectra.

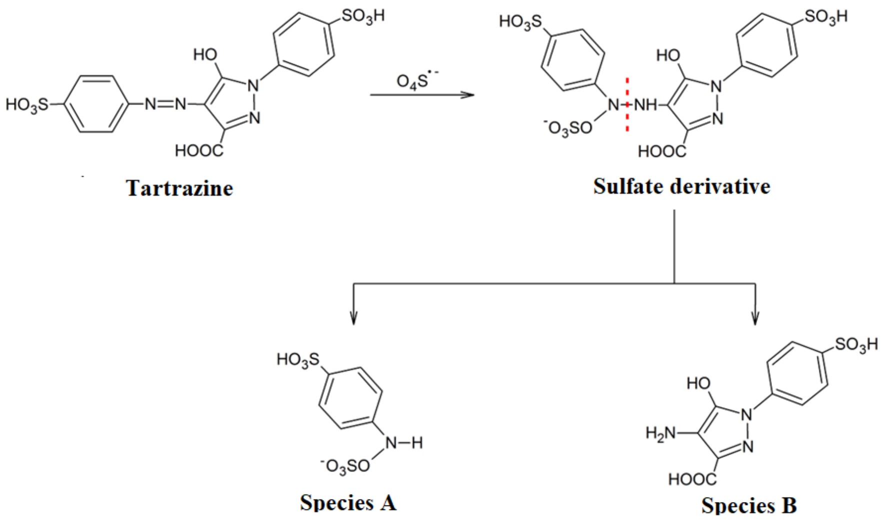

Figure 2. The first step of main reaction path of tartrazine degradation i.e. the azo bond cleavage.

CONCLUSION

Oxidative degradation of tartrazine by $SO_4^{\cdot-}$ radical anions was monitored by UV-Vis spectroscopy. In the first period of the reaction (up to 60 min) the only registered change in spectra was diminishing of the tartrazine originated characteristic peaks at 257 nm and 426 nm. After 120 min and 240 min of the catalytic reaction additional peaks at 231 nm and 275 nm, respectively, were monitored. The possible reaction pathways were analyzed in order to estimate the origin of 231 nm and 275 nm peaks. For each potential product of reaction quantum-chemical calculations were performed and theoretical UV-Vis spectra were calculated. The combination of TPSS-D3 method and aug-cc-pVDZ basis set was found to be the most appropriate. Based on calculated UV-Vis spectra peak at 275 nm can be assigned to sulfanilic acid derivatives. On the other hand, peak at 231 nm can be the result of further degradation of derivative of the benzenesulfonic acid with pyrazole ring as substituent. The products of degradation for which the calculated UV-Vis spectra had maxima in vicinity of 231 nm were 4-phenolsulfonic and benzenesulfonic acid. The quantum chemical calculations have proven beneficial for the identification of the products of tartrazine degradation.

Acknowledgement

This work was financially supported by the Ministry of Education, Science and Technological Development of the Republic of Serbia (Grant No: 451-03-9/2021-14/200026).

REFERENCES

[1] Y. Yang, J. Jiang, X. Lu, J. Ma, Y. Liu, Environ. Sci. Technol. 2015; 49: 7330–7339. doi.org/10.1021/es506362e
[2] M. Marković, S. Marinović, T. Mudrinić, M. Ajduković, N. Jović-Jovičić, Z. Mojović, J. Orlić, A. Milutinović-Nikolić, P. Banković, Appl Clay Sci 2019, **182**, 105276 (10 pages).
[3] M. J. Frisch et al., *Gaussian 09* (Gaussian, Inc., Wallingford CT, 2009).
[4] L. H. Mendoza-Huizar, J Mex Chem Soc 2014, **58**, 416–423.

KINETICS OF THE REDUCTION OF DICYANOBIS(2,2'-BIPYRIDYL)IRON(III) BY IODIDE IN AQUEOUS MEDIUM

R. Khattak [1] and M. S. Khan [2]

[1]Department of Chemistry, Shaheed Benazir Bhutto Women University, Peshawar 25000, Pakistan.
(rznkhattak@yahoo.com; rznkhattak@sbbwu.edu.pk)
[2]Department of Chemistry, University of Malakand, Chakdara 18800, Pakistan.

ABSTRACT

The redox reaction between dicyanobis(2,2'-bipyridyl)iron(III) and iodide may have potential application in dye-sensitized solar cells. In this study, kinetics of the reduction of dicyanobis(2,2'-bipyridyl)iron(III) was studied in aqueous medium. Iodide was used as a reducing agent at 60 mM ionic strength and a temperature of 293 ± 0.5 K. The reaction was of zero and fractional (0.5) order in the oxidant and reductant, respectively. The reaction was in general fractional (0.5) order. With increasing acidity in the reaction mixture, the measured zero order rate constant decreased, but was unaffected by increasing ionic strength. The thermodynamic parameters of activation were also computed for the redox process.

INTRODUCTION

Dicyanobis(2,2'-bipyridyl)iron(III) has potential application in the dye-sensitized solar cells (DSSCs). Its photosensitive nature and high reduction potential (0.76 V) make it a good candidate for DSSC to be used as a sensitizer [1]. It has been used as an oxidizing agent for several reductants that include hexacyanoferrate(II), glutathione, L-cystein and iodide in different solvent media [2-5]. We used this complex to oxidize iodide in binary solvent media (aqueous-alcohol) and studied the effect of ionic strength on the redox reaction [6]. In this study, we have been interested in the reduction of dicyanobis(2,2'-bipyridyl)iron(III) by using potassium iodide in aqueous medium. Potassium iodide is easily oxidized by our selected mixed ligand complex without any application of an external triggering such as catalyst or external factors including ultra sensitive experimental conditions. The electrochemical series shows iodine's reduction potential as 0.54 V. Oxidation of iodide is an important facet of solar cells such as perovskite and dye-sensitized solar cells where it is oxidized in different ways [7-10]. In the dye-sensitized solar cells, different complexes have been used to oxidize the iodide ion in order to improve the efficiency of the DSSCs [11-12]. We studied the kinetics of our selected redox reaction and determined the effect of various parameters on the rate constant of the reaction and deduced the rate law.

METHODS

Analar grade (Sigma-Aldrich) materials (dicyanobis(2,2'-bipyridyl)iron(III) nitrate, potassium iodide, potassium nitrate and nitric acid) were used in this study. The aqueous solutions were prepared in deionized water. The spectra of reactants and products were recorded in aqueous medium (Figure 1). The time course graph was monitored upon formation of dicyanobis(2,2'-bipyridyl)iron(II) and the increase in absorbance was recorded. While determining the order of reaction with respect to the reactants, the pseudo-first order condition was maintained by keeping the oxidant at a low concentration (0.08 mM) and the reductant at a high concentration (80 – 2400 μM). To evaluate the influence of H^+ ions and ionic strength, this ratio was kept at 80 μM : 800 μM (oxidant : reductant). Each experiment was repeated thrice to acquire accuracy. The integration method was implemented to determine the order of reaction and the rate constant. The observed rate constant was the average of three readings.

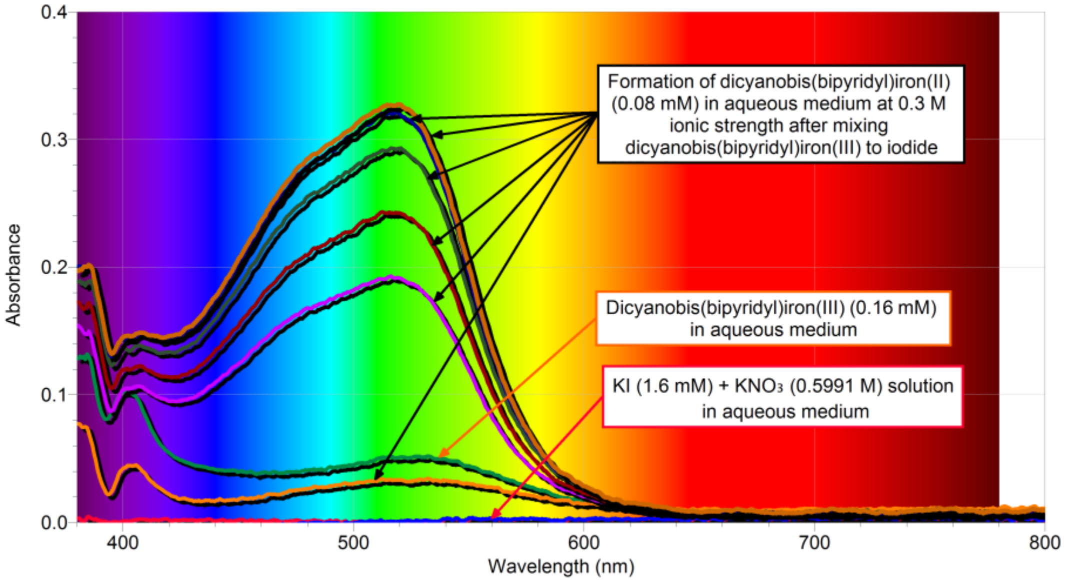

Figure 1. Spectral analysis (visible region) of reactants and product.

RESULTS AND DISCUSSION

The reaction was found to undergo the zero order kinetics in dicyanobis(2,2'-bipyridyl)iron(III) at 293 ± 0.5 K and 60 mM ionic strength (I) in aqueous medium. The observed zero order rate constant was determined at different concentration of iodide (0.08 – 2.4 mM) keeping all other parameters constant. The concentration of the oxidant was maintained at 80 μM. The plot of the observed rate constant versus the fractional (0.5) power of the concentration of iodide yielded a straight line passing through the origin (Figure 2). The slope of the plot provided the fractional order rate constant as 5×10^{-6} $M^{0.5}$ s^{-1}. The overall order of reaction was found fractional (0.5) consequently.

The effect of the increasing acidity was also studied on the observed rate constant by adding nitric acid to the reaction mixture. The value of the rate constant was decreased with increasing acidity that showed the rate resisting effect of the hydrogen ions on the rate constant (Figure 3). These results helped to conclude that the slow-step of the reaction involves the unprotonated iodide or triiodide ion. The results were refined by the neutral effect of the ionic strength on the observed zero order rate constant.

The effect of ionic strength was studied by increasing the concentration of potassium nitrate in the reaction mixture keeping all other parameters constant. The ionic strength was varied between 5 – 370 mM. The plot of log rate constant versus square root of ionic strength showed no effect according to the formulation of the primary salt effect (Figure 4). This confirms the formation of triiodide ion and its rate-leading effect in the reaction mechanism because the neutral iodine plays a vital role of limiting reactant in the formation of triiodide ion.

The activation parameters of the reaction were determined by varying the temperature between 10 – 40 °C. The Arrhenius and Eyring plots were drawn that yielded activation parameters such as activation energy; $E_a = 46.23$ kJ mol^{-1}, pre-exponential factor; $A = 24.62$ M s^{-1}, change in enthalpy of activation; $\Delta H^\# = 43.76$ kJ mol^{-1}, change in entropy of activation; $\Delta S^\# = -226.5$ J mol^{-1} K^{-1}, and change in Gibbs free energy of activation; $\Delta G^\# = 111.26$ kJ mol^{-1} (25 °C).

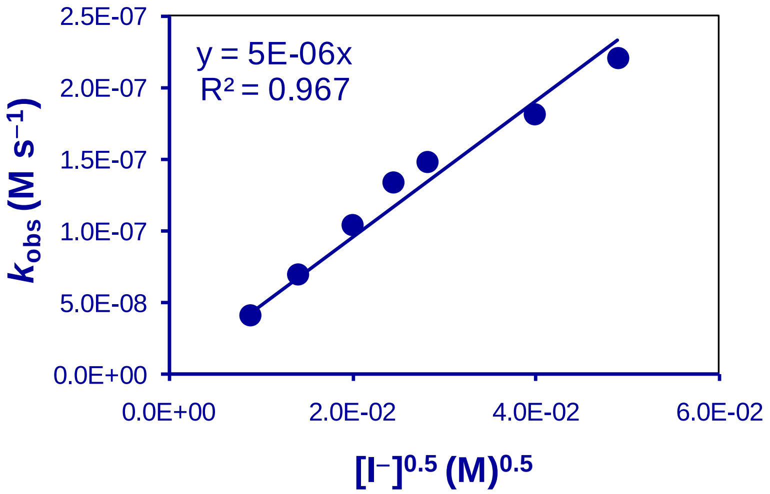

Figure 2. Fractional order with respect to reductant in aqueous medium.

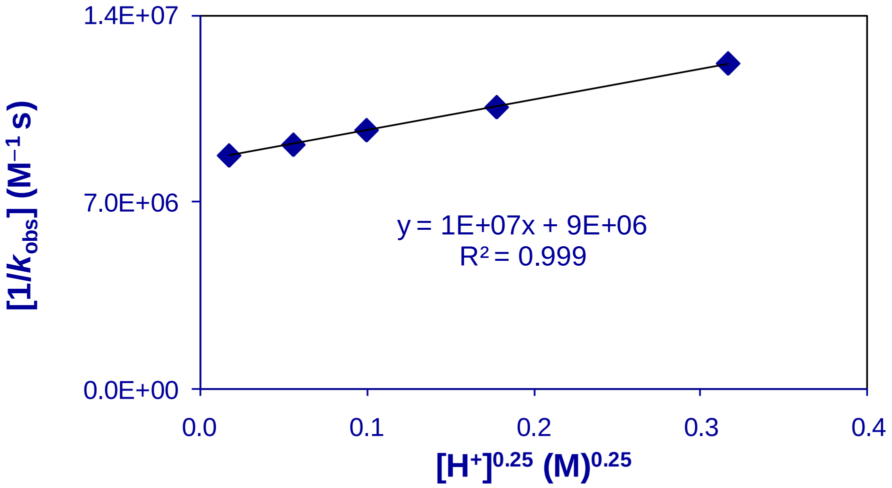

Figure 3. Rate resisting effect of H^+ ions on the rate constant in aqueous medium.

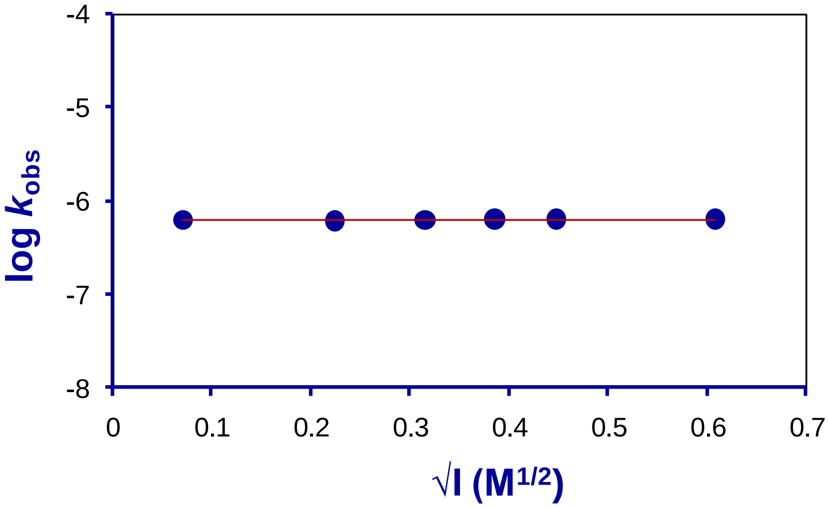

Figure 4. Primary salt effect in aqueous medium.

CONCLUSION

The reduction of dicyanobis(2,2'-bipyridyl)iron(III) by iodide conforms an overall fraction (0.5) order kinetics in aqueous medium. The reaction is zero order in oxidant and fractional order in reductant. The rate-determining step of the reaction is lead by the triiodide ion. The concentration of triiodide ion depends upon the concentration of the iodine in the reaction mixture. As a result, the concentration of iodine is limiting reactant for triiodide ion. The protonation of triiodide ion decelerates the reaction consequently as per our observations. The rate law of the reaction is proposed as follows.

$$Rate = [I^-]^{0.5}\left(k + \frac{k'}{[H^+]^{0.25}}\right)$$

REFERENCES

[1] R. Khattak, PhD, University of Karachi, **2011**.

[2] X. Wang, D. M. Stanbury *J. Phys. Chem. A.* **2004**, 108, 7637-7638.

[3] X. Wang, D. M. Stanbury *Inorg. Chem.* **2008**, 47, 1224-1236.

[4] X. Wang, D. M. Stanbury *Inorg. Chem.* **2006**, 45, 3415-3423.

[5] N. Bhattarai, D. M. Stanbury *Inorganic Chemistry*. **2012**, 51, 13303-13311.

[6] R. Khattak, M. S. Khan, R. Ullah, Zainab, Sony, M. Ali, W. Rahman, F. Hakeem, K. Ayaz, Z. Bibi *International Journal of Chemical Kinetics*. **2021**, 53, 16-26.

[7] M. Kokkonen, P. Talebi, J. Zhou, S. Asgari, S. A. Soomro, F. Elsehrawy, J. Halme, S. Ahmad, A. Hagfeldt, S. G. Hashmi *Journal of Materials Chemistry A*. **2021**, 9, 10527-10545.

[8] Y. Yang, L. Wu, X. Hao, Z. Tang, H. Lai, J. Zhang, W. Wang, L. Feng *RSC Advances*. **2019**, 9, 28561-28568.

[9] G. Boschloo, A. Hagfeldt *Acc. Chem. Res.* **2009**, 42, 1819-1826.

[10] M. Zhang, J. Bing, Y. Cho, Y. Li, J. Zheng, C. F. J. Lau, M. A. Green, S. Huang, A. W. Y. Ho-Baillie *Nano Energy*. **2019**, 63, 103853.

[11] C. A. Bignozzi, R. Argazzi, R. Boaretto, E. Busatto, S. Carli, F. Ronconi, S. Caramori *Coord. Chem. Rev.* **2013**, 257, 1472-1492.

[12] R. Khattak, M. S. Khan, S. Summer, R. Ullah, H. Afridi, Z. Rehman, S. Masood, H. Noreen, R. A. Qazi, B. Begum *International Journal of Chemical Kinetics*. **2021**, 53, 230-241.

MODELING OF THE LINSEED OIL EPOXIDATION: THE USE OF DIFFERENT EXPRESSIONS FOR THE REACTION RATE OF THE PERACETIC ACID FORMATION

O. Govedarica, M. Janković, S. Sinadinović-Fišer, J. Pavličević, V. Teofilović, N. Vukić, J. Blagojević

University of Novi Sad, Faculty of Technology, Bul. cara Lazara 1, 21000 Novi Sad, Serbia.
(ogovedarica@uns.ac.rs)

ABSTRACT

The published pseudohomogeneous model for the vegetable oil epoxidation with *in situ* formed peracetic acid in the presence of the ion exchange resin as a catalyst was modified considering, besides the heterogeneously catalyzed, previously neglected homogenously catalyzed peracetic acid formation. Comparison of the original and two proposed models shows that introduced modification improves the modeling of the epoxidation process.

INTRODUCTION

In industry, vegetable oils are epoxidized with percarboxylic acid formed *in situ* from carboxylic acid and hydrogen peroxide [1]. The formation of commonly applied peracetic acid is carried out in the presence of an acidic catalyst. When ion exchange resin Amberlite IR120-H is the catalyst, the formation of peracid is catalyzed heterogeneously, by the active sites of the resin [1,2], as well as homogenously, by hydronium ions originating from acetic acid dissociation [3]. The aim of the present work is to modify existing pseudohomogenous model of the vegetable oil epoxidation with peracetic acid [2] as to better describe changes of epoxy group and residual vegetable oil's unsaturation amounts. The model was modified by taking into consideration also homogenously catalyzed peracetic acid formation.

METHODS

The epoxidation of linseed oil with peracetic acid formed *in situ* from acetic acid and hydrogen peroxide in the presence of Amberlite IR120-H was carried out in a batch reactor as described in the literature [1]. The process was followed by determining the amount of residual unsaturation and the amount of epoxy group in the samples of epoxidized linseed oil. The experimental data of 96 epoxidation runs have been given previously [1].

RESULTS AND DISCUSSION

The epoxidation of vegetable oils involves peracetic acid (P) and water (W) formation from acetic acid (A) and hydrogen peroxide (H):

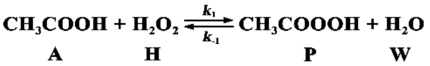

$$\underset{A}{CH_3COOH} + \underset{H}{H_2O_2} \underset{k_{-1}}{\overset{k_1}{\rightleftarrows}} \underset{P}{CH_3COOOH} + \underset{W}{H_2O} \qquad (1)$$

conversion of double bond in oil triglycerides (D) into epoxy group (E):

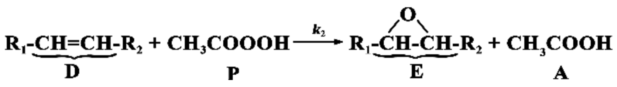

$$R_1\text{-}\underbrace{CH=CH}_{D}\text{-}R_2 + \underset{P}{CH_3COOOH} \xrightarrow{k_2} R_1\text{-}\underbrace{\overset{O}{CH\text{-}CH}}_{E}\text{-}R_2 + \underset{A}{CH_3COOH} \qquad (2)$$

and several side reactions of epoxy group, among which is prominent the one with acetic acid yielding the hydroxy acetate (HA) [1,2]:

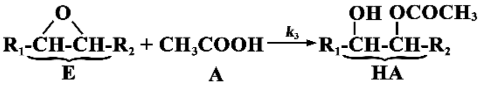

(3)

The reaction system of epoxidation process, conducted as the batch process, can be mathematically described with the pseudohomogenous model (Model 0) found in the literature [2]:

$$d[\text{A}]/dt = \left(d[\text{H}]/dt\right)_1 + k_2[\text{P}][\text{D}] - k_3[\text{E}][\text{A}]^n \tag{4}$$

$$d[\text{P}]/dt = -\left(d[\text{H}]/dt\right)_1 - k_2[\text{P}][\text{D}] \tag{5}$$

$$d[\text{W}]/dt = -\left(d[\text{H}]/dt\right)_1 \tag{6}$$

$$d[\text{D}]/dt = -k_2[\text{P}][\text{D}] \tag{7}$$

$$d[\text{E}]/dt = k_2[\text{P}][\text{D}] - k_3[\text{E}][\text{A}]^n \tag{8}$$

$$d[\text{HA}]/dt = k_3[\text{E}][\text{A}]^n \tag{9}$$

where square brackets denote amounts of compounds and functional groups as mole per 100 g oil. t (min) is the reaction time. k_2 (100 g oil/mol·min) and k_3 [(100 g oil)^n/(mol^n·min)] are the rate coefficients for the reactions (2) and (3), respectively. n is the order of the reaction (3) with respect to acetic acid. Model 0 takes into consideration only the consumption of H by heterogeneously catalyzed reaction of P formation:

$$\left(d[\text{H}]/dt\right)_1 = \left(d[\text{H}]/dt\right)_{1,\text{het}} = -m\cdot C_\text{s}\cdot k_{1,\text{het}}\left([\text{A}][\text{H}] - [\text{P}][\text{W}]/K_1\right) \tag{10}$$

where $k_{1,\text{het}}$ (100 g oil/mol^2·min) is the rate coefficient for heterogeneously catalyzed reaction (1). m_c (g) and C_s (mol/g cat) are the mass of the catalyst and the amount of sulpho groups in the catalyst, respectively. K_1 is the chemical equilibrium constant for the reaction (1) [1].

In this study, Model 0 was modified by taking into consideration the change of H amount caused by homogenously catalyzed P formation, $(d[\text{H}]/dt)_{1,\text{hom}}$. Therefore, the total consumption of H for P formation was considered as:

$$\left(d[\text{H}]/dt\right)_1 = \left(d[\text{H}]/dt\right)_{1,\text{het}} + \left(d[\text{H}]/dt\right)_{1,\text{hom}} \tag{11}$$

In Model 1, for the change of H amount caused by homogenously catalyzed P formation, expression proposed by Zhao et al [3] was used:

$$\begin{aligned}\left(dC_\text{H}/dt\right)_{1,\text{hom}} = -10^8\sqrt{K_{\text{D,A}}C_\text{A}}\Big[&6.83\cdot\exp\left(-57846.15/R\cdot T\right)C_\text{A}C_\text{H}\\ &-6.73\cdot\exp\left(-60407.78/R\cdot T\right)C_\text{P}C_\text{W}\Big]\end{aligned} \tag{12}$$

where C_i (mol/L) is the concentration of component i in the aqueous phase. $K_{\text{D,A}}$ is the dissociation constant of acetic acid [4].

In Model 2, for $\left(dC_\text{H}/dt\right)_{1,\text{hom}}$ the modification of Eq. (12) was proposed:

$$\left(dC_\text{H}/dt\right)_{1,\text{hom}} = k_{1,\text{hom}}\sqrt{K_{\text{D,A}}C_\text{A}}\left[C_\text{A}C_\text{H} - (C_\text{P}C_\text{W}/K_1)\right] \tag{13}$$

where $k_{1,\mathrm{hom}}$ ($\mathrm{L}^{1.5}/\mathrm{mol}^{1.5}\cdot\mathrm{min}$) is the rate coefficient for homogenously catalyzed reaction (1). Its temperature dependency was not taken from the expression (12); instead, it was determined by fitting the model to the experimental data.

In Eqs. (12) and (13) the concentrations of components in the aqueous phase were calculated as follows: $C_\mathrm{A} = [\mathrm{A}]/(K_\mathrm{A} v^\mathrm{o} + v^\mathrm{aq})$, $C_\mathrm{H} = [\mathrm{H}]/v^\mathrm{aq}$, $C_\mathrm{W} = [\mathrm{W}]/v^\mathrm{aq}$ and $C_\mathrm{P} = [\mathrm{P}]/(K_\mathrm{P} v^\mathrm{o} + v^\mathrm{aq})$. K_A and K_P are the partition coefficients for acetic acid and peracetic acid, respectively. v^o and v^aq (L/100 g oil) are the volumes of the aqueous and oil phases, respectively. Since the change of molar volume of aqueous phase with time was neglected, the expression $(d[\mathrm{H}]/dt)_{1,\mathrm{hom}} = v^\mathrm{aq}(dC_\mathrm{H}/dt)_{1,\mathrm{hom}}$ was used when fitting the proposed modified models to the experimental data. The expression for $k_{1,\mathrm{hom}}$ in Eq. (13) was presented, like the other reaction rate coefficients in all studied models, with the modified form of Arrhenius equation:

$$k_i = \exp\left[k_{i,0} - k_{i,\mathrm{E_a}} / \mathrm{R}\left(1/T - 1/T_\mathrm{ref}\right)\right] \tag{14}$$

where $k_{i,0}$ and $k_{i,\mathrm{Ea}}$ are the constants related to the frequency factor and the activation energy for reaction i, respectively. R [8.3143 J/(mol·K)] is the universal gas constant. T (K) is the temperature of the epoxidation process, whereas T_ref is the reference temperature (accepted as 346 K). $k_{i,0}$ and $k_{i,\mathrm{Ea}}$ for all reaction rate coefficients were obtained by fitting models to the experimental data obtained for the linseed oil epoxidation by applying the following objective function:

$$\mathrm{F} = \sum_{i=1}^{\mathrm{NE}}\left[\left([\mathrm{D}]_i^\mathrm{calc} - [\mathrm{D}]_i^\mathrm{exp}\right)^2 + \left([\mathrm{E}]_i^\mathrm{calc} - [\mathrm{E}]_i^\mathrm{exp}\right)^2\right]$$

where NE is the number of the experimental points.

Parameter estimation results with related statistics for fitting the models with different expressions for the reaction rate of the P formation to the experimental data for the linseed oil epoxidation are given in Table 1. All reaction rate coefficients, calculated using values of $k_{i,0}$ and $k_{i,\mathrm{Ea}}$ given in Table 1, have positive values and increase with rising in temperature. This confirms the validity of the proposed models as do the positive values of calculated amounts of all reactants and products.

Table 1. Comparison of the models with different P formation reaction rates

	Model 0 Ref. [2]		Model 1		Model 2	
	Order of the reaction (3) with respect to acetic acid, *n*					
	1	2	1	2	1	2
Error						
F	0.1492	0.1454	0.1436	0.1399	0.1173	0.1166
Constant of the reparameterized Arrhenius equation *i.e.* model parameter						
$(k_{1,\mathrm{het}}C_\mathrm{s})_0$	-11.26	-11.28	-11.44	-11.45	-12.43	-12.34
$(k_{1,\mathrm{het}}C_\mathrm{s})_\mathrm{Ea}$	20364	20875	15851	16543	50631	52142
$k_{1,\mathrm{hom},0}$	-	-	-	-	-2.292	-2.338
$k_{1,\mathrm{hom},\mathrm{Ea}}$	-	-	-	-	16389	13163
$k_{2,0}$	-2.348	-2.238	-2.122	-2.017	0.6635	0.6084
$k_{2,\mathrm{Ea}}$	82546	88860	94291	100715	215070	219520
$k_{3,0}$	-6.608	-5.744	-6.603	-5.745	-6.599	-5.773

$k_{3,Ea}$	35397	40086	34993	40095	35966	42396

According the lower F, n=2 and both modified models better describe the epoxidation process than published one, but in this work proposed Model 2 better than Model 1.

CONCLUSION

Improving of the model for the vegetable oil epoxidation with *in situ* formed peracetic acid in the presence of the heterogeneous catalyst by adding the parameter for the homogeneously catalyzed reaction of the peracetic acid formation was the best when the reaction rate coefficient constants for the latter reaction were determine by fitting the model to the epoxidation data.

Acknowledgement

The Ministry of Education, Science and Technological Development of Serbia (Project #451-03-9/2021-14/200134).

REFERENCES

[1] M. Janković, O. Govedarica, S. Sinadinović-Fišer, Ind. Crop Prod., 2020, **143**, 111881
[2] M. Janković, S. Sinadinović-Fišer, O. Govedarica, J. Pavličević, J. Budinski-Simendić, Chem. Ind. Chem Eng. Q., 2017, **23**, 97-111.
[3] X. Zhao, T. Zhang, Y. Zhou, D. Liu, J. Mol. Catal. A Chem., 2007, **271**, 246–252.
[4] K. Sue, F. Ouchi, K. Minami, K. Arai, J. Chem. Eng. Data, 2004, **49**, 1359–1363.

EFFICACY OF ZIRCONIA BASED NANOPOWDERS IN REMOVAL OF PHARMACEUTICALS USING SOLAR IRRADIATION

D. Šojić Merkulov [1], V. Despotović [1], S. Armaković [1], N Finčur [1], M Lazarević [1], M. Uzelac [1], N. D. Abazović [2], T. D. Savić [2], M. Čomor [2], and B. Abramović [1]

[1]*University of Novi Sad Faculty of Sciences, Trg D. Obradovića 3, 21000 Novi Sad, Serbia (biljana.abramovic@dh.uns.ac.rs).*
[2]*Vinča Institute of Nuclear Sciences, National Institute of RS, University of Belgrade, P. O. Box 522, 11001 Belgrade, Serbia.*

ABSTRACT

Photocatalytic/adsorption efficacy of pure ZrO_2 and ZrO_2 powders with incorporated Si^{4+} ions was obtained following kinetics of degradation reaction and adsorption/desorption of some pharmaceuticals under solar irradiation. All selected pharmaceuticals have been found in surface waters in Serbia as organic micropollutants with ability to impact water quality, ecosystems and human health. Removal efficacy was followed using UFLC technique. All used zirconia based nanopowders can be used for removal of selected pharmaceutical.

INTRODUCTION

Photocatalytic processes based on the application of oxide semiconductors (such as TiO_2, ZnO, ZrO_2) are among the most popular methods for removing pollutants from the environment by overcoming the shortcomings of conventional technologies [1]. A great deal of efforts has been made to improve the photocatalytic efficiency of different nanopowders by modifying the surface of the photocatalyst or by doping with various dopants [2]. In recent years, pharmaceuticals have been discovered in the environment, especially in surface waters. Some drugs were detected in concentrations of the order of μg/L, which are concentrations that may have a physiological effect on aquatic organisms [3]. Their presence and persistence is a very current environmental problem.

Within this study, the photolytic/photocatalytic degradations of three model pharmaceuticals are presented: amitriptyline, tricyclic antidepressant used in the treatment of psychiatric disorders, 4-amino-6-chlorobenzene-1,3-disulfonamide, stable hydrolysis product of frequently used pharmaceutical hydrochlorothiazide, and ceftriaxone, hemi-synthetic broad-spectrum third generation cephalosporin antibiotic. ZrO_2 and ZrO_2 nanopowders doped with Si^{4+} ions were used as photocatalysts with solar irradiation.

METHODS

All chemicals used in the investigation were of reagent grade and were used without further purification. Amitriptyline hydrochloride (AMI, $C_{20}H_{23}N$ x HCl, M_r=313.9, CAS No. 549-18-8, ≥ 98%), 4-amino-6-chlorobenzene-1,3-disulfonamide (ABSA, M_r=285.73, CAS No. 121-30-2, 98%), and ceftriaxone disodium salt hemi(heptahydrate) (CEF, $C_{18}H_{16}N_8Na_2O_7S_3$ x $3.5H_2O$, M_r=661.6, CAS No 104376-79-6) were purchased from Sigma–Aldrich.

ZrO_2 and ZrO_2 nanopowders doped with Si^{4+} ions were used as photocatalysts with solar irradiation. Nanopowders were synthesized using hydrothermal method; precursors were zirconyl chloride (Sigma Aldrich, 98%) without/with tetraethoxysilane (TEOS, Alfa Aeser, 98%). Assignation referred to quantity of used Si^{4+} precursor: ZrO_2-1 obtained with 0.5 mL and ZrO_2-2 obtained with 5 mL TEOS, detailed characterization presented in [4]. Experiments were performed at natural pH of suspensions (for ZrO_2 it was 6-7, for doped samples 9-10) and pH of dissolved pharmaceuticals.

Removal experiments were performed as previously described [5]. Solar irradiation was carried out using a 50 W halogen lamp (Philips) with the intensity of 0.1 W/cm^2 in the visible region and 2.2 x 10^{-4} W/cm^2 in the UV region. Experiments were performed using 20 mL of emerging pollutant aqueous solution, where their initial concentration in all experiments was 0.05 mM, while catalyst loading was 1.0 mg/mL.

To monitor the photodegradation of pharmaceuticals, high pressure liquid chromatography with a diode array detector (UFLC-DAD, Shimadzu Nexera, Tokyo, Japan) was used. Aliquots of the reaction mixture (0.5 mL) were taken before the start of irradiation and at specific time intervals during the irradiation (volume variation ca. 10%). All samples with photocatalyst were filtered through a Millipore (Millex-GV, MA, USA, 0.22 μm) membrane filter in order to separate the catalyst particles. Prepared aliquots were analyzed on UFLC-DAD as described previously in ref. [6] for AMI, [7] for ABSA, and [8] for CEF.

RESULTS AND DISCUSSION

Applied hydrothermal method for synthesis and Si^{4+} doping of zirconia powders produced crystalline powders: monoclinic in the case of pure ZrO_2 with particle diameter ~ 25 nm and doped samples with tetragonal crystalline phase and particles of 3-6 nm in diameter [4]. The presence of Si^{4+} ions in zirconia matrix induced decrease of effective band gap of doped samples: pure ZrO_2 had E_g ~ 5 eV, ZrO_2-1 had E_g ~ 4.7 eV and ZrO_2-2 had E_g ~ 3.8 eV. This method induced a great number of different intraband states in all nanopowders, defects like oxygen vacancies, resulting in the significant tailing of absorption in the visible part of the spectra. These findings were inspiration for to photocatalytic experimental setup with simulated Solar light source.

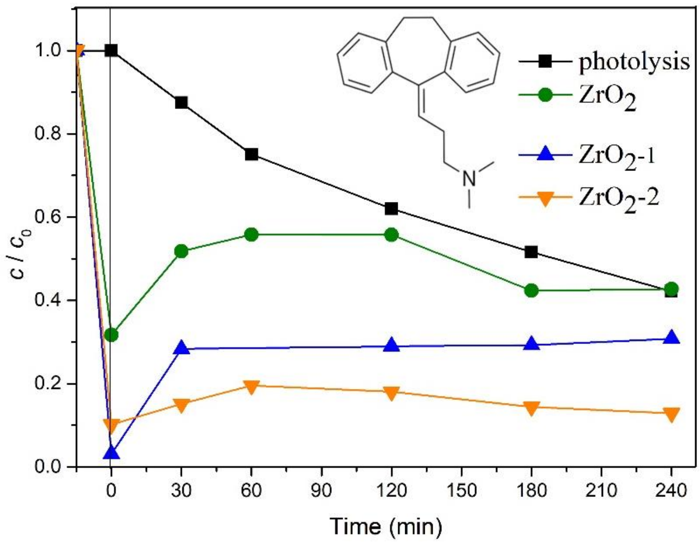

Figure 1. Kinetics of adsorption and photodegradation of AMI.

Among chosen pharmaceuticals only amitriptyline (AMI) has significant photolysis, after 240 min 57.3% (the same as with ZrO_2 nanopowder) was degraded (Fig. 1). The photocatalytic removal efficiency of AMI (Fig. 1) increases with increasing content of incorporated Si^{4+} ions in zirconia based photocatalyst. After 240 min of irradiation in the systems with ZrO_2-2, ZrO_2 and ZrO_2-1, 87.1%, 57.3 and 69.2% of AMI was removed, respectively. In the presence of the catalyst, after sonication in the dark, significant adsorption of AMI occurs on the catalyst surface. During irradiation, desorption occurs [9,10], as well as degradation of AMI. The degree of adsorption/desorption of AMI depends on the type of the catalyst. Since a significant adsorption of AMI on the tested nanopowders was found (Fig. 1), the effect of pH on adsorption of AMI using ZrO_2-2 was investigated. The pH of AMI suspension using ZrO_2-2 without pH adjustment was 10, and in order to test the effect of pH, it was adjusted to 5. It was found that with decreasing pH, the adsorption of AMI is significantly lower (only 30.3%), which indicates the importance of pH value. This finding can be assigned to differences in surface charges of ZrO_2, with IEP=6, negative at pH=10 and mainly positive at pH=5 and present forms of AMI in the solution, with pK_a=9.4 [11].

ZrO_2 and ZrO_2-2 nanopowders had slightly higher efficiency in the removal of ABSA, i.e. 9% of ABSA was removed after 120 min of irradiation, while only 5% when ZrO_2-1 was used (Fig. 2). When ABSA was removed in the presence of undoped ZrO_2, the initial pH was 7.7, but using ZrO_2-1 and ZrO_2-2 pH=9.8. Reduction of the initial pH to 7.4 upon removal of ABSA with ZrO_2-1 practically does not affect its efficacy, although the adsorption of ABSA on the nanopowder surface was slightly reduced. pK_a values for ABSA were estimated using DFT analysis, and were: 8.8, 10, 12.5 [12]. Bearing in mind that in all cases photocatalyst's surfaces were negatively charged obviously, adsorption was not crucial for photodegradation of ABSA.

In Fig. 3 results of adsorption, photolysis and photocatalysis of CEF are presented. Adsorption of CEF (pK_1=2.37, pK_2=3.03, pK_3=4.21 and pK_4=10.74 [13]; and natural pH of suspensions) is insignificant as in the case of ABSA. Namely, using ZrO_2, ZrO_2-1, and ZrO_2-2 percent of adsorption is only 7.2, 0.4, and 0.0, and the removal efficiency after 240 min of irradiation was 18.0%, 1.1%, and 7.9%, respectively. The most effective nanopowder was pure ZrO_2, either for adsorption and photodegradation.

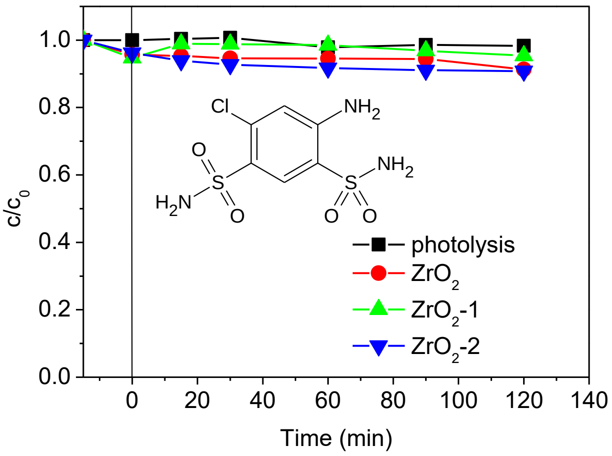

Figure 2. Kinetics of adsorption and photodegradation of ABSA.

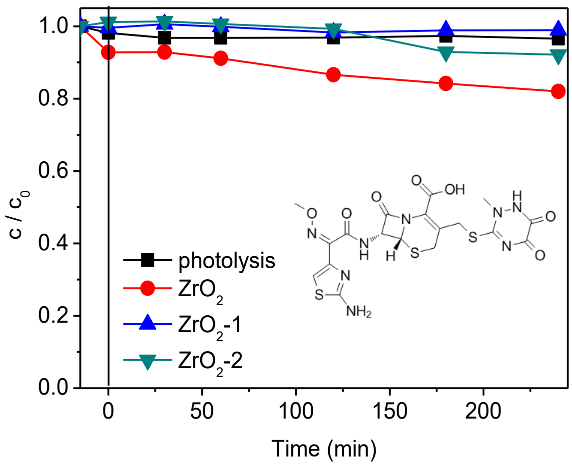

Figure 3. Kinetics of adsorption and photodegradation of CEF.

CONCLUSION

Presented results indicated that applied nanopowders are efficient adsorbents/photocatalysts for AMI, almost inactive for ABSA and slightly active for CEF. After 240 min of irradiation, 57.3% of AMI was removed by photolysis, while in the presence of ZrO_2-2 87.1% was removed. In the case of ABSA, the best photocatalysts were pure ZrO_2 and ZrO_2-2, although only 9% of starting concentration was removed. CEF was removed the most efficiently by pure ZrO_2, (7.2% after 240 min of process). pH of the suspensions was obviously important due to different ionic species present during irradiation and surface charges of the photocatalysts.

Acknowledgement

The authors acknowledge financial support of Ministry of Education, Science and Technological Development of the RS (Grant No. 451-03-9/2021-14/200125 and 451-03-9/2021-14/200017).

REFERENCES

[1] H. Dong, G. Zeng, L. Tang, C. Fan, C. Zhang, X. He, Y. He, Water Research, 2015, 79, 128-146.
[2] P. V. L. Reddy, K.-H. Kim, Journal of Hazardous Materials, 2015, 285, 325-335.
[3] J. S. Murray, P. Politzer, Wires Computational Molecular Science, 2011, 1, 153-163.
[4] M. V. Carević, N. D. Abazović, T. B. Novaković, V. B. Pavlović, M. I. Čomor, Applied Catalysis B: Environmental, 2016, 195, 112-120.
[5] B. F. Abramović; V. N. Despotović, D. V. Šojić, D. Z. Orčić, J. J. Csanádi, D. D. Četojević-Simin, Chemosphere, 2013, 93, 166-171.
[6] T. B. Ivetić, N. L. Finčur, B. F. Abramović, M. Dimitrievska, G. R. Štrbac, K. O. Čajko, B. B. Miljević, L. R. Đačanin, S. R. Lukić-Petrović, Ceramics International, 2016, 42, 3575-3583.
[7] S. J. Armaković, S. Armaković, D. D. Četojević-Simin, F. Šibul, B. F. Abramović, Environmental Pollution, 2018, 233, 916-924.
[8] B. F. Abramović, M. M. Uzelac, S. J. Armaković, U. Gašić, D. D. Četojević-Simin, S. Armaković, Science of the Total Environment, 2021, 768, No 144991.
[9] J. Zhu, F. Chen, J. Zhang, H. Chen, M. Anpo, Journal of Photochemistry and Photobiology A: Chemistry, 2006, 180, 196-204.
[10] D. V. Šojić, V. N. Despotović, N. D. Abazović, M. I. Čomor, B. F. Abramović, Journal of Hazardous Materials, 2010, 179, 49-56.
[11] B. Kasprzyk-Hordern, R. M. Dinsdale, A. J. Guwy, Analytical and Bioanalytical Chemistry, 2008, 39, 1293-1308.
[12] S. J. Armaković, Photocatalytic stability of selected active components of cardiovascular drugs: kinetics, mechanism and toxicity of the intermediates, PhD Thesis, Faculty of Sciences, Novi Sad, 2016.
[13] S. Budavari, The Merck Index, 13th ed., Merck & Co. Inc., Rahway, NJ, USA, 2001, p. 335.

ZIRCONIA BASED PHOTOCATALYSTS IN DEGRADATION OF SELECTED HERBICIDES

M. Čomor[1], N. Abazović[1], T. Savić[1], D. Šojić Merkulov[2], V. Despotović [2], S. Armaković[2], N Finčur[2], M Lazarević[2], M. Uzelac[2], and B. Abramović[2]

[1] *Vinča Institute of Nuclear Sciences, National Institute of RS, University of Belgrade, P.O. Box 522 11001 Belgrade, Serbia*
[2] *University of Novi Sad Faculty of Sciences, Trg D. Obradovića 3, 21000 Novi Sad, Serbia*

ABSTRACT

Hydrothermally synthesized zirconia nanopowders: pure and doped with Si^{4+} ions were spectroscopically characterized and used as photocatalysts for degradation of herbicides sulcotrione and fluroxypyr. Zirconia is wide band gap ceramic (E_g ~ 5 eV) however, synthesized nanopowders showed unexpected, modest absorbance in visible light range. That fact inspired photocatalytical degradation of herbicides with wide utilization, using solar irradiation (SI) in laboratory conditions. In the scope of this study, degradation of herbicides was only slightly achieved (irradiation time 2h).

INTRODUCTION

Zirconia (ZrO_2) is a member of transition metal oxides group of wide band gap materials. ZrO_2 is an important ceramic material widely used in variety of applications [1]. Due to its nature as n-type semiconductor, it has been considered as a photocatalyst in photocatalytical heterogeneous reactions. The values of the zirconia bandgap energy (E_g) is in the range between 3.25 and 5.1 eV, depending on the used preparation technique and the presence of dopants and defects, for the most usual value is $E_g = 5$ eV, conduction band potential would be −1.0 V and the valence band potential would be +4.0 V *vs*. NHE at pH 0, excellent values for variety of oxidation/reduction reactions in the solution. In the scope of this study, hydrothermal method for synthesis of zirconia nanopowders was chosen. In order to overcome necessity for UV irradiation, zirconia was doped with Si^{4+} ions. Literature already showed that Si^{4+} ions can introduce defects in zirconia matrix and change effective band gap. Simultaneously Si-doping process increase specific surface area of zirconia [2].

Both herbicides used as model molecules for photocatalytical degradation are widely used for control of grass and broad-leaf weeds in agriculture. Due to their solubility in water, they can be found in environment, especially in rivers and lakes. Sulcotrione belongs to class of triketone herbicides used for weed control in corn [3, 4]. Fluroxypyr is a selective post-emergent systemic herbicide widely used in agriculture. It was introduced in Europe for post-emergence control of annual and perennial broad-leaf weeds in small grains such as wheat, barley, oats and croplands [5].

METHODS

All chemicals were of reagent grade and used without further purification. Pesticides sulcotrione (CAS No. 99105-77-8, $C_{14}H_{13}ClO_5S$, $M_r = 328.8$, PESTANAL®, analytical standard, 99.9%) and fluroxypyr (CAS No. 99105-77-8, $C_7H_5Cl_2FN_2O_3$, $M_r = 255.03$, PESTANAL®, analytical standard, 99.9%) were purchased from Fluka.

Zirconia nanopowders were synthesized using hydrothermal method; precursors were zirconyl chloride (Sigma Aldrich, 98%) without/with tetraethoxysilane (TEOS Alfa Aeser, 98%). Assignation referred to quantity of used Si^{4+} precursor: ZrO_2-1 obtained with 0.5 mL and ZrO_2-2 obtained with 5 mL TEOS, detailed characterization presented in [1], as a part of this study, FTIR spectra (taken by using attenuated total reflection mode of a Nicolet 380 FTIR spectrometer) and UV/Vis absorption/ reflectance spectra (obtained using an Evolution 600 spectrophotometer Thermo Scientific, reflectance was converted to absorption using Kubelka-Munk method) are presented. Natural pH of suspensions was for ZrO_2 6-7, for doped samples 9-10.

Removal experiments were performed as previously described [6]. Solar irradiation was carried out using a 50 W halogen lamp (Philips) with the intensity of 0.1 W/cm^2 in the visible region and 2.2×10^{-4} W/cm^2 in the UV region. Experiments were performed using 20 mL of emerging pollutant solution, where their initial concentration in all experiments was 0.05 mM, while catalyst loading was 1.0 mg/mL. Photodegradation was monitored at natural pH values of the suspensions without adjustment.

To monitor the photodegradation of pesticides, high pressure liquid chromatography with a diode array detector (UFLC-DAD, Shimadzu Nexera, Tokyo, Japan) was used. Aliquots of the reaction mixture (0.5 mL) were taken before the start of irradiation and at specific time intervals during the irradiation (volume variation ca. 10%). All samples with photocatalyst were filtered through a Millipore (Millex-GV, MA, USA, 0.22 μm) membrane filter in order to separate the catalyst particles. Prepared aliquots were analyzed on UFLC-DAD. For the sulcotrione and fluroxypyr UV/Vis DAD detector was set at 231 and 212 nm (wavelength of maximum absorption), respectively. The mobile phase with flow rate of 1.0 mL/min was a mixture of ACN and water in ratio 50:50 (*v*/*v*).

RESULTS AND DISCUSSION

Hydrothermally synthesized zirconia nanopowders: pure and doped with Si^{4+} ions [1], were successfully synthesized. One of the easiest ways to prove presence of Si^{4+} ions in zirconia matrix is FTIR spectroscopy. A characteristic band at 950 cm^{-1} (Fig. 1a) can be seen; this band assigned to Zr-O-Si [2]. It is present only in doped samples with intensity that follows concentration of Si^{4+} ions in the samples. Also, UV/Vis spectra (Fig. 1b) show significant differences in reflection/absorption due to presence of dopant and, most probably, defects induced through synthesis. Even for pure ZrO_2 defect-related absorption can be seen at ~ 400 nm, in the visible light region. Doped samples showed higher absorption intensity at 400 nm and, especially ZrO_2-2, broad band from 400 nm to NIR region. This effect, absorption of visible light, by zirconia samples was inspiration for probing photocatalysis degradation reactions by solar irradiation in laboratory conditions.

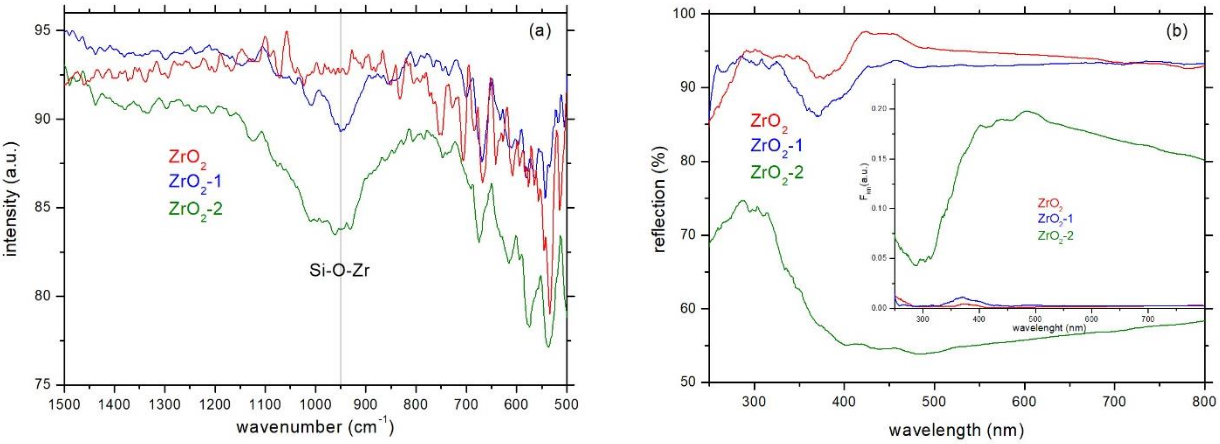

Figure 1. FTIR (a) and UV/Vis (b) reflection/absorption (inset) spectra of pure and Si^{4+} doped zirconia nanopowders.

In order to test the stability of sulcotrione, a direct photolysis experiment was performed (Fig. 2), where no degradation was observed after 120 min of irradiation, from which it can be concluded that the compound is stable. After that, the efficiency of photocatalytic degradation of sulcotrione using of ZrO_2, ZrO_2-1 and ZrO_2-2 nanopowders and solar irradiation was examined (Fig. 2a). As can be seen in the presence of these nanopowders, almost no degradation of sulcotrione occurs during 120 min of irradiation. Only about 4% of sulcotrione was degraded by using doped zirconia samples, pure ZrO_2 showed no photocatalytic efficacy.

The photocatalytic activity of pure ZrO_2, as well as ZrO_2 nanopowders doped with different content of Si^{4+} ions (ZrO_2-1 and ZrO_2-2) was investigated in the photodegradation of fluroxypyr using solar irradiation. The obtained results were compared with the results of direct photolysis (Fig. 2b). On the basis of the obtained results for the efficiency of photocatalytic degradation of fluroxypyr using solar irradiation, it can be concluded that the synthesized nanopowders slightly accelerate the degradation of fluroxypyr compared to the process of direct photolysis.

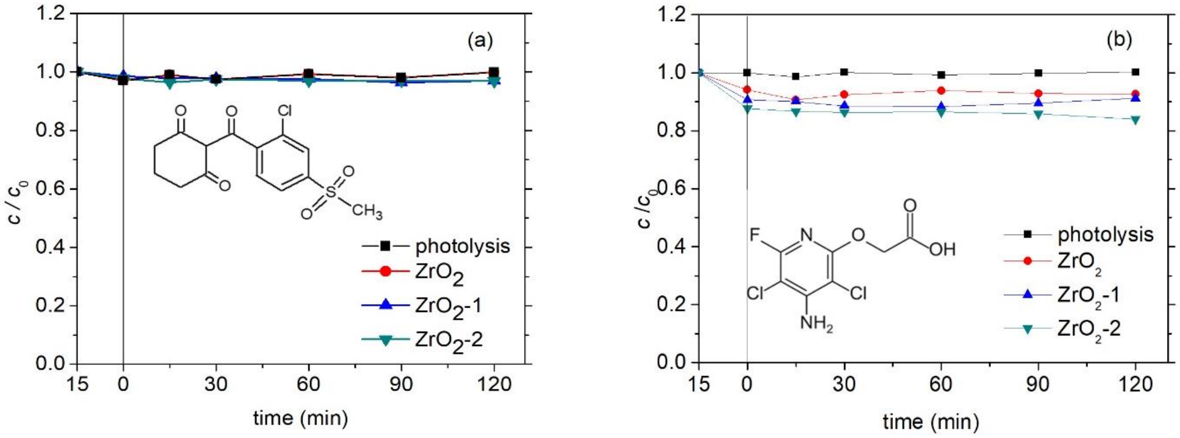

Figure 2. Adsorption and kinetics of photolysis and photocatalytical degradation of sulcotrione (a) and fluroxypyre (b).

Based on the obtained results, it was found that after 120 min irradiation in the presence of ZrO_2 and ZrO_2-1, respectively about 91% of fluroxypyr is still present in solution. ZrO_2-2 proved to be somewhat more efficient, with 17% of fluroxypyr being removed from solution after 120 min of irradiation. During equilibration of reaction dispersions, before irradiation, fluroxypyr was adsorbed at the surface of zirconia nanopowders; about 6% on ZrO_2, 9% on ZrO_2-1 and 12% on ZrO_2-2. Obviously more experimental optimization is needed for better application of zirconia nanopowders for removal/photodegradation of fluroxypyr.

CONCLUSION

Hydrothermal method for synthesis of pure and Si^{4+} doped zirconia nanopowders proved to be efficient. FTIR spectroscopy reveals presence of Si-O-Zr bonds in the doped samples. Also, improvement of UV/Vis absorption in visible part of the spectra for all samples can be ascribed to formation of defects and/or presence of dopant ions in the samples. Usage of Solar light for irradiation in photodegradation reactions of sulcotrione and fluroxypyr showed modest results in the scope of presented reaction conditions. These are not ideal photocatalysts for degradation of sulcotrione. Adsorption and photodegradation of fluroxypyre was achieved, best photocatalyst was ZrO_2-2 with 17% of degradation after 2 h of irradiation which was expected due to its UV/Vis absorption spectrum.

Acknowledgement

The authors acknowledge financial support of Ministry of Education, Science and Technological Development of the RS (Grant No. 451-03-9/2021-14/200125 and 451-03-9/2021-14/ 200017).

REFERENCES

[1] M. V. Carević, N. D. Abazović, T. B. Novaković, V. B. Pavlović, M. I. Čomor, Applied Catalysis B: Environmental, 2016, 195, 112-120.

[2] S. F. Yin, B. Q. Xu, ChemPhysChem, 2003, 277-281.

[3] H. Chaabane, E. Vulliet, F. Joux, F. Lantoine, P. Conan, J.-F. Cooper, C.-M. Coste, Water Research, 2007, 41, 1781-1789.

[4] https://sitem.herts.ac.uk/aeru/ppdb/en/Reports/600.htm

[5] J. Hu, T. Wang, J. Long, Y. Chen, International Journal Environmental Analytical Chemistry, 2014, 94, 211-222.

[6] B. F. Abramović; V. N. Despotović, D. V. Šojić, D. Z. Orčić, J. J. Csanádi, D. D. Četojević-Simin, Chemosphere, 2013, 93, 166-171.